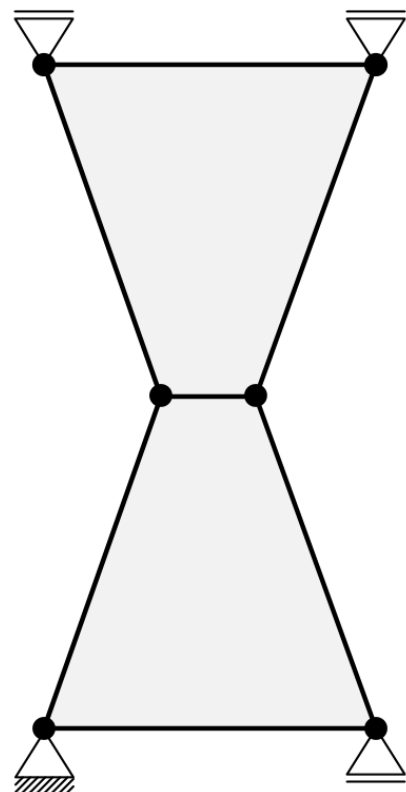
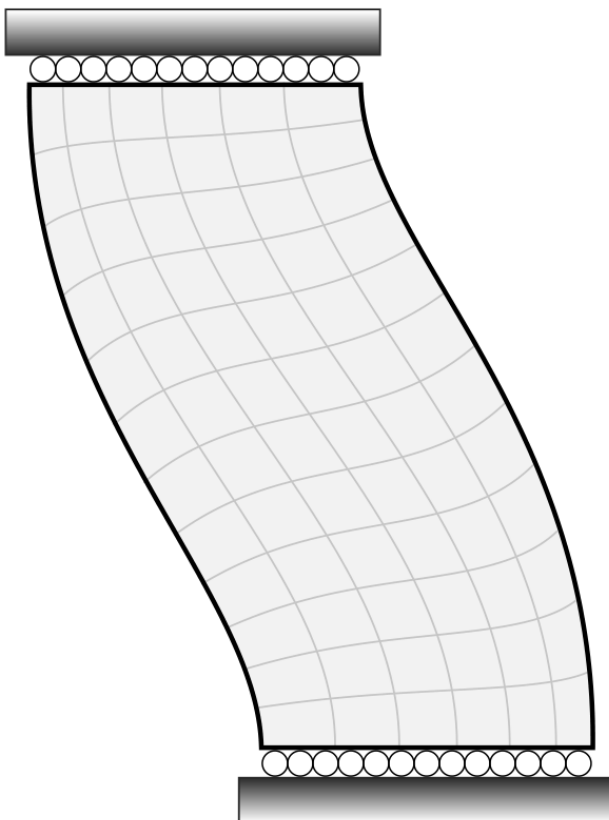


Locking and Hourglassing in Nonlinear Finite Element Technology

Simon Bieber



Locking and Hourglassing in Nonlinear Finite Element Technology

von

Simon Bieber

Bericht Nr. 76

Institut für Baustatik und Baudynamik der Universität Stuttgart

Professor Dr.-Ing. habil. M. Bischoff

2024



© Simon Bieber

Berichte können bezogen werden über:
Institut für Baustatik und Baudynamik
Universität Stuttgart
Pfaffenwaldring 7
70550 Stuttgart

Tel.: 0711 - 685 66123
Fax: 0711 - 685 66130
E-Mail: sekretariat@ibb.uni-stuttgart.de
<http://www.ibb.uni-stuttgart.de/>

Alle Rechte, insbesondere das der Übersetzung in andere Sprachen, vorbehalten. Ohne Genehmigung des Autors ist es nicht gestattet, diesen Bericht ganz oder teilweise auf photomechanischem, elektronischem oder sonstigem Wege zu kommerziellen Zwecken zu vervielfältigen.

D 93 - Dissertation an der Universität Stuttgart
ISBN 978-3-00-077649-6

Locking and Hourglassing in Nonlinear Finite Element Technology

Von der Fakultät Bau- und Umweltingenieurwissenschaften
der Universität Stuttgart zur Erlangung der Würde eines
Doktor-Ingenieurs (Dr.-Ing.) genehmigte Abhandlung

vorgelegt von

Simon Bieber

aus Backnang

Hauptberichter: Prof. Dr.-Ing. habil. Manfred Bischoff

Mitberichter: Prof. Ferdinando Auricchio

Mitberichter: Prof. Dr.-Ing. habil. Anton Tkachuk

Tag der mündlichen Prüfung: 6. April 2023

Institut für Baustatik und Baudynamik der Universität Stuttgart

2024

Kurzfassung

Die vorliegende Arbeit befasst sich mit Problemen, die ausschließlich bei der Finite-Elemente-Analyse nichtlinearer Probleme in der Festkörpermechanik auftreten. Ein besonderes Augenmerk liegt dabei auf künstlichen Versteifungseffekten (“Locking”) und künstlichen Instabilitäten (“Hourglassing”). Bei beiden Phänomenen lassen sich die Ursachen auf geometrische und materielle Nichtlinearitäten zurückführen. In diesem Zusammenhang wird auch die algorithmische Behandlung zur effizienten Berechnung von Instabilitätspunkten diskutiert.

Ein volumetrisches Lockingphänomen, das durch geometrisch nichtlineare Biegeverformungen hervorgerufen wird, wurde kürzlich in Willmann et al. 2022 entdeckt. Die Autoren untersuchten diesen Effekt im Zusammenhang mit 3d Schalenelementen. Auf der Grundlage dieser Arbeit wird das Problem des “nichtlinearen Lockings” weiter untersucht. Die Analyse wird auf gängige EAS-Volumenelemente erweitert. Mögliche Lösungsmethoden und die Bedeutung für praktische Anwendungen werden diskutiert. Darüber hinaus werden nichtlineare geometrische Lockingeffekte untersucht, die insbesondere bei der Analyse von Elementen mit großen und kleinen Seitenverhältnissen von Bedeutung sind. Eine besondere Herausforderung bei der Analyse von nichtlinearem Locking ist die Wahl geeigneter Benchmarks. Eine Voraussetzung der beschriebenen Effekte sind nichtlineare inhomogenen Elementdeformationen. Aus diesem Grund werden neben den numerischen auch analytischen Lösungen für Biegeprobleme mit großen Dehnungen untersucht.

Basierend auf der Arbeit von Bieber et al. 2022 wird das Problem des Hourglassing analysiert. Das Phänomen tritt bei kritischen Verformungszuständen auf, die auch potentiell anfällig für physikalische Instabilitäten sind. Die zugrundeliegenden Ursachen des Hourglassing lassen sich durch geometrie- und materialinduzierte physikalische Strukturinstabilitäten erklären. Aus diesem Grund und in Abgrenzung zur einschlägigen Literatur zu diesem Thema werden diese numerischen Artefakte in geometrisches und materielles Hourglassing klassifiziert. Auf der Grundlage dieser Untersuchung wird eine Lösung für geometrischen Hourglassing vorgestellt. Ein besonderes Merkmal dieser Methode ist die Einfachheit bei der Implementierung. Die Schwierigkeiten bei der Anwendung einer ähnlichen Strategie auf materielles Hourglassing werden diskutiert. Ähnliche zu dem Problem des nichtlinearen Lockings liegt ein besonderer Fokus auf das Entwickeln zuverlässiger und effizienter Benchmarks. Aus diesem Grund wird eine eingehende analytische Lösung eines Verzweigungsproblems mit großer Dehnung vorgestellt.

Der Erfolg einer effizienten Berechnung von Instabilitätspunkten ist stark problemabhängig. Die einschlägigen Methoden aus der Literatur und ihre Schwierigkeiten bei der Wahl eines geeigneten Lastschrittverfahrens werden diskutiert. Es wird eine methodische Idee vorgeschlagen, die diese Schwierigkeiten durch eine adaptive Laststeuerung abmindert. Für eine Reihe von Benchmarks wird die Effizienz und Praktikabilität dieses Ansatzes demonstriert.

Abstract

This thesis deals with issues that arise exclusively in the finite element analysis of nonlinear problems in solid mechanics. A particular focus is on locking and artificial instabilities (“Hourglassing”), both of which are inherently related to geometric and material nonlinearities. In connection therewith, the algorithmic treatment for efficient computation of instability points is discussed. The issues are investigated within the popular class of enhanced assumed strain (EAS) formulations.

A volumetric locking phenomenon that is induced by geometrically nonlinear bending deformations has been recently discovered in Willmann et al. 2022. The authors analyzed this effect in the context of 3d shell finite elements. Based on that work, the issue of “nonlinear locking” is further elaborated herein. The analysis is extended to popular EAS solid elements, including guidelines on possible remedies. The relevance for practical applications is highlighted. In addition, nonlinear geometric locking effects, especially important in the analysis of elements with large and small aspect ratios, are investigated. A particular challenge is the choice of suitable benchmarks, since these effects only occur under certain conditions. For this reason, the numerical and analytical solutions of large bending of rubber blocks are studied.

Based largely on the work of Bieber et al. 2022, the issue of artificial instabilities (hourglassing) is analyzed. It occurs under critical deformation states, which are also potentially prone to physical instabilities. The underlying causes of hourglassing can likewise be explained by geometry-induced and material-induced trigger mechanism of structural instabilities. For that reason, and in delineation from the pertinent literature on this topic, these pathologies are classified as geometric hourglassing and material hourglassing. Based on this analysis, an obvious remedy for the geometric hourglassing phenomenon is presented. A special feature of this method is the simplicity regarding the implementation of existing methods. The difficulties in applying a similar strategy to material hourglassing are discussed. As for nonlinear locking, a particularly challenging aspect is reliable and efficient benchmarking. Difficulties include the large parameter dependency as well as the absence of analytical reference solutions. For this reason, an analytical in-depth analysis of a large strain bifurcation problem is presented, tailored for benchmarking against hourglassing issues.

The success of an efficient computation of instability points is strongly problem-dependent. The pertinent methods from the literature and their difficulties in choosing a suitable load step are discussed. Proposed is a methodological idea that potentially alleviates these difficulties through an adaptive load-stepping approach. For a series of benchmarks, the efficiency and practicability is demonstrated and future work is discussed.

Danksagung

Die vorliegende Arbeit entstand als Dissertation während meiner Tätigkeit am Institut für Baustatik und Baudynamik der Universität Stuttgart. Ich bedanke mich ganz besonders bei meinem Doktorvater Professor Dr.-Ing. habil. Manfred Bischoff für die zahlreichen anregenden Gespräche und Diskussionen. Diese ragten auch weit in nicht fachliche Themenwelten hinein und werden mir in schöner Erinnerung bleiben. Ich hoffe sehr, dass noch weitere folgen werden und dass ich ihn von den Vorzügen eines Trollingers überzeugen kann.

I would also like to thank Professor Ferdinando Aurichhio for giving me the wonderful opportunity to do research at his institute in Pavia, for doing the co-report of this thesis and for his dedicated support in my research.

Ein herzliches Dankeschön gebührt auch Professor Dr. Ing. Anton Takchuk für sein großes Engagement in der fachlichen und mentalen Unterstützung meiner Forschungsarbeit am Institut, den durchweg kritischen Forschungsfragen und natürlich die Übernahme des Mitberichtes.

Unausweichlich, dass an dieser Stelle auch Robin Pfefferkorn einen eigenen Dankesabsatz bekommt. Ohne ihn hätte meine Doktorandenzeit nur halb so viel Spaß gemacht und der wissenschaftliche Output wäre ein anderer.

Ein ganz herzliches Dankeschön möchte ich meinen Eltern aussprechen für die bedingungslose Unterstützung in all den Jahren.

In der Kürze liegt die Würze: Ein riesen Dank gilt allen Kolleginnen und Kollegen des Instituts für das wunderbare Miteinander.

Dresden, im Februar 2024

Simon Bieber

Dai diamanti non nasce niente, dal letame nascono i fior.

- Fabrizio de André, Via del Campo -

Contents

Abbreviations and Nomenclature	ix
1 Introduction	1
1.1 The Big Picture	1
1.2 Objectives and Outline of this Work	5
2 Fundamentals of Finite Elasticity	9
2.1 Kinematics	10
2.1.1 Deformation of Elastic Bodies	10
2.1.2 Strain Measures	12
2.1.3 Incremental Kinematic Relations	13
2.2 Stress, Forces and Equilibrium	14
2.3 Constitutive Equations	15
2.3.1 Some Preliminary Aspects	15
2.3.2 Hyperelastic Materials	16
2.3.3 Incremental Constitutive Relations	17
2.3.4 Some Aspects on Local Uniqueness and Stability of Solutions	19
2.3.5 Examples of Strain Energy Functions	21
2.4 Boundary Value Problem and Variational Formulations	26
2.4.1 Boundary-Value Problem of Isotropic Finite Elasticity	26
2.4.2 Single-Field Variational Energy Principles	27
2.4.3 Multi-Field Variational Principles	29
3 A Family of Nonlinear Finite Element Formulations	31
3.1 Isoparametric Finite Element Procedure	31
3.2 Displacement-Based Finite Elements	33
3.2.1 Discretization	33
3.2.2 Fundamental Mathematical Properties	36
3.3 Enhanced Assumed Strain Finite Elements	39
3.3.1 A Lagrangian Formulation (Qp/Em)	39
3.3.2 Two-Point Formulations (Q1/Hm) and (Q1/HTm)	42
3.4 Assumed Stress Element (Q1/S5)	45

4	Analytical Solutions for Some Classical Problems in Finite Elasticity	47
4.1	Bifurcations in Plane Strain Tension and Compression	47
4.1.1	Problem Setup and Principal Solution	48
4.1.2	Euler Buckling – Introductory Example	49
4.1.3	Bifurcation Analysis	51
4.1.4	Example I: Geometric Instabilities	57
4.1.5	Example II: Material-Induced Instabilities	62
4.2	Finite Bending of a Rubber Block	64
4.2.1	Principal Solution	65
4.2.2	Example: Bending of a Neo-Hookean Block	69
4.2.3	Bending Instabilities	72
5	Nonlinear Locking Phenomena	75
5.1	Analysis of Nonlinear Locking Phenomena	76
5.1.1	Recap on Linear Locking	76
5.1.2	Model Problem	76
5.1.3	Deformation-Dependent Modal Analysis	77
5.1.4	Geometric Locking Phenomena	80
5.1.5	Volumetric Locking Phenomena	82
5.2	Remedies to Avoid Nonlinear Locking	85
5.2.1	Numerical Integration: Theory and Practice	85
5.2.2	Assumed Stress Elements	86
5.2.3	Novel Enhanced Assumed Strain Elements	86
5.3	Numerical Experiments	89
5.3.1	Finite Bending Problem – Displacement Controlled	90
5.3.2	Slender Beam Problem – Force Controlled	97
5.3.3	Comment on Further Numerical Results.	98
6	Physical and Artificial Instabilities of Nonlinear Finite Elements	99
6.1	Literature Review	99
6.2	Introductory Example – Ritz Method	101
6.2.1	Geometric Instability Mechanisms	102
6.2.2	Geometric Hourglassing Phenomenon	106
6.2.3	Material-Induced Structural Instability Mechanisms	108
6.2.4	Material Hourglassing	109
6.3	Approach to Avoid Hourglassing	110
6.4	Modal Analysis	113
6.5	Numerical Experiments	117
6.5.1	Euler Buckling: Coarse Mesh Accuracy	117
6.5.2	Block under Compression: Physical vs. Artificial Instabilities . . .	117

6.5.3	Compression and Tension of a Constrained Block	121
7	Algorithmic Aspects	125
7.1	Computational Aspects in the Determination of Critical Points	125
7.1.1	A Short Review On Nonlinear Solution Techniques	126
7.1.2	Pre- and Post-Critical Behaviour of Discrete Structures	128
7.1.3	Adaptive Load Control – Model Problem	132
7.1.4	Numerical Experiments	137
7.1.5	Open Issues	140
7.2	Robustness and Efficiency in the Newton-Raphson Scheme	145
8	Concluding Remarks and Outlook	149
A	Appendix	151
A.1	Technical Aspects of the Finite Element Method	151
A.1.1	Numerical Quadrature	151
A.1.2	Sobolev Spaces	152
A.2	Supplements to the Bifurcation Problem	152
A.2.1	Derivation of the Trigonometric Ansatz Functions	152
A.2.2	Elliptic-Complex Case – Coefficients	155
A.2.3	Bifurcation Modes – Coefficients	155
A.3	Finite Bending Problem – Stress Resultants	157
A.4	Constants	157
A.5	Adaptive Load Control – Technical Aspects	158
A.5.1	Quadratic Extrapolation	158
A.5.2	Supplements to Figure 7.7 and 7.8	159
	Bibliography	165
	Index	174

Abbreviations and Nomenclature

Abbreviations

ALC	Adaptive Load Control
BK	Blatz-Ko
BT	Boundary Terms
BVP	Boundary Value Problem
DOF	Degrees Of Freedom
EC	Elliptic-Complex
EI	Elliptic-Imaginary
EAS	Enhanced Assumed Strain Method
FEM	Finite Element Method
HR	Hellinger-Reissner
HW	Hu-Washizu
IBVP	Incremental Boundary Value Problem
NH	Neo-Hooke
ODG	Ogden
SVK	Saint-Venant Kirchhoff

Mathematical notation

$\text{DIV}(\bullet)$	divergence of (\bullet) w.r.t. the reference coordinates
$\text{div}(\bullet)$	divergence of (\bullet) w.r.t. the spatial coordinates
$\text{Grad}(\bullet)$	gradient of (\bullet) w.r.t. the reference coordinates
$\text{Grad}^s(\bullet)$	symmetric gradient of (\bullet) w.r.t. the reference coordinates
$\text{grad}(\bullet)$	gradient of (\bullet) w.r.t. the spatial coordinates
$\mathbf{a} \cdot \mathbf{b}$	scalar product between two vectors $(a_i b_i)$
$\mathbf{A} : \mathbf{B}$	double contraction between two second-order tensors $(A_{ij} B_{ij})$
\mathbf{AB}	dot product of two second-order tensors $(A_{ij} B_{jk})$
\mathbf{Ab}	linear transformation of \mathbf{b} $(A_{ij} b_j)$

$\mathbf{a} \times \mathbf{b}$	cross product $(a_i b_j)$
$(\bullet)^{-1}$	inverse of (\bullet)
\cup	set union symbol
\bigcup	union operator
\mathbf{A}	assembly operator
\cap	set intersection symbol
\emptyset	empty set
\mathbf{I}	identity
(x_1, x_2)	open interval
$[x_1, x_2]$	closed interval
\mathcal{S}^I	denotes symmetrical modes w.r.t. X_I -axis
\mathcal{A}^I	denotes antisymmetrical modes w.r.t. X_I -axis
\mathbb{R}	set of real numbers
\mathbb{R}^+	set of positive real numbers with zero
\mathbb{N}	set of natural numbers
\mathbb{N}_0	set of natural numbers with zero
\mathcal{C}	set of complex numbers
\mathcal{B}_0	reference configuration
Γ_0	boundary of \mathcal{B}_0
\mathcal{B}	spatial configuration
Γ	boundary of \mathcal{B}
$\mathbf{E}_{(\bullet)}$	reference base vector
$\mathbf{e}_{(\bullet)}$	spatial base vector
\mathbb{E}^3	Euclidean space
\mathcal{H}^s	Sobolev space of order s
$\mathcal{SO}(3)$	special orthogonal rotation group
n_{no}	Number of element nodes
n_e	Total number of elements
$n_e^{X_i}$	Number of elements in direction X_i

Chapter 1

Introduction

1.1 The Big Picture

Nonlinear deformation processes of solid bodies are omnipresent in everyday life. The term “nonlinear” refers to the underlying mathematical model that is used to characterize the relation of the body’s structural response to a loading scenario. Nonlinearity can originate from the kinematic description of the deformation process itself and from the material model. This is usually referred to as geometric nonlinearity and material nonlinearity, respectively. Figure 1.1 sketches examples of nonlinear deformations such as large bending of metal sheets, large stretching of resistance rubber bands or snapping mechanism of a carnivorous plant. Moreover, nonlinearities are closely related to geometry-induced and material-induced structural instability phenomena. These are often characterized by large abrupt deformations upon small load changes and cause, in the worst case, catastrophic structural failure. A typical example from everyday life is the structural instability (buckling) of an axially loaded ruler, see Figure 1.1 (f). The engineer’s task is to understand these processes, e.g., predict stresses, forces or deformations of structures, and analyze their load-carrying behavior. For many problems, it is nowadays well established to solve the underlying boundary value problem with the finite element method. It is a simulation tool that is tailored for solid mechanics problems and main subject of the present thesis.

For half a century, enormous research efforts were devoted to the development of reliable finite element formulations. Nowadays, its theoretical and practical maturity is indisputable and, also in the nonlinear regime, established formulations perform well for a wide range of (nonlinear) problem types. Particularly prominent examples for solid finite elements are the displacement-pressure formulation of Simo et al. 1985, reduced integrated elements with hourglass stabilization, see among others, Kosloff and Frazier 1978, or the incompatible mode elements by Wilson et al. 1973. In view of that, it is crucial to discuss the need for further research on this topic. The step from linear

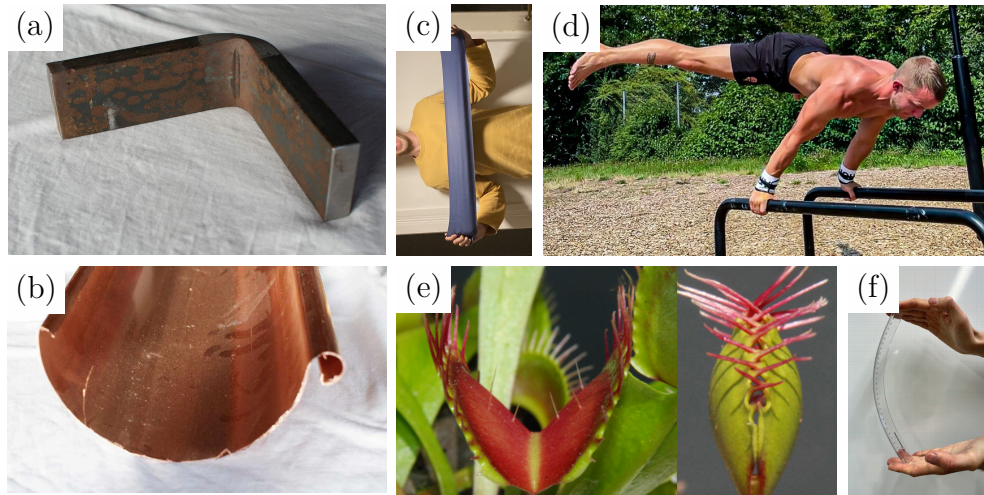


Figure 1.1: Examples of nonlinear deformation processes: (a,b) nonlinear bending of a 15 mm iron sheet (large strain) and a 1.5 mm copper gutter (moderately small strain); (c) stretching of a latex resistance band; (d) straining of the athlete’s soft biological tissues, i.e., muscles and tendons, during an intense workout (with permission from Calisthanik 2022); (e) large deformation snapping mechanism of a carnivorous plant (with permission from A. Westermeier, see also Sachse et al. 2020); (f) post-buckling deformation of a ruler.

to nonlinear finite elements introduces additional problems. One aspect is, that under *certain conditions*, established finite element formulations do not perform satisfactorily. This concerns, on the one hand, accuracy of the simulation results and, on the other hand, robustness of the solution processes. Both are specified below. Another aspect is the difficulty in doing a reliable *analysis*, crucial for assessing the aforementioned issues. Many contributions, in particular the mathematically oriented ones, deal with linear problems. The analysis of nonlinear finite element formulations, however, receives less attention. Here, it becomes more difficult to make general statements about the element’s properties. One reason for that is the lack of mathematical theory, such as the celebrated inf-sup condition in the linear regime (Brezzi 1974). Therefore, nonlinear benchmark problems are gaining in importance. To some extent, they can be used to evaluate the element performance. However, compared to linear problems, nonlinear problems are inherently more complex: solutions may be non-unique, the assessment of solutions requires physical insights, analytical solutions are rarely available, etc.

This work deals with unresolved issues that arise exclusively in *nonlinear* finite element simulations. It follows a list of properties that, at best, a nonlinear finite element should satisfy:

- (i) simple to implement,
- (ii) computationally inexpensive,
- (iii) based on a strain-driven format,
- (iv) satisfy the patch test and objectivity requirement,
- (v) accurate for coarse meshes and in particular locking-free,
- (vi) insensitive to mesh distortion,
- (vii) free from artificial instabilities (hourglassing),
- (viii) algorithmic robustness.

An all-in-one formulation¹ that fulfills properties (i)-(viii) is naturally hard to achieve. Of course, all properties mutually influence each other and, furthermore, specific practical requirements may differently weight the importance of each of the properties.

To a certain degree, it remains a subjective perception whether an element is simple to implement or not. In the authors opinion, Properties (i)-(iii) are of crucial importance with respect to the acceptance (of newly designed element formulations) within a broader community. However, regardless of whether Properties (i)-(viii) are met, existing nonlinear advanced finite elements have barely entered commercial finite element codes. In this sense, the driving motivation of this work is to “redesign” established popular finite elements, instead of developing completely new formulations. The popular class of Enhanced Assumed Strain (EAS) formulations introduced by Simo and Rifai 1990 will play a central role in this context.

Properties (iv)-(vi) are a prerequisite for proper convergence of finite elements, see for instance the textbooks of Hughes 2012 and Zienkiewicz et al. 2014 for the linear and nonlinear case, respectively. Property (v) describes an element, that performs well for nearly incompressible materials as well as slender elements (i.e. small and large aspect ratios). If not, the element performs too stiff and “locks”. These properties were exhaustively studied in the context of linear finite elements. However, locking in the nonlinear regime appears to be poorly understood as shown by recent work of Willmann et al. 2022 in the context of shell analysis. Figure 1.2 (a) shows a sketch of the pathological stiffening effect due to nonlinear locking. A beam-like structure is subjected to a follower load such that it should approximately coils up to a circle. The

¹I.e., a Swiss Army knife, also aptly described by the german phrase “eierlegende Wollmilchsau”.

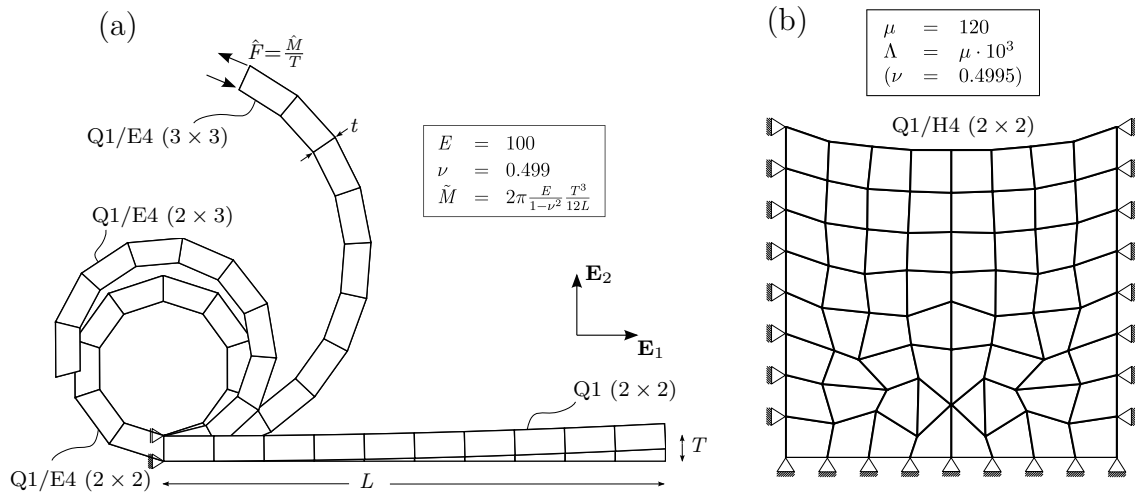


Figure 1.2: Illustration of numerical pathologies of EAS formulations: (a) coiling of a plane strain beam-like structure with $L/T = 20$ using a nearly incompressible Saint-Venant Kirchhoff material; Brackets indicate the number of Gauss quadrature points used; (b) plane strain compression of a severely constrained Neo-Hookean block under self-weight $\hat{\mathbf{B}} = -\gamma\mu\mathbf{E}_2$; depict is the deformed mesh at $\gamma = 1.88$ (immediately before reaching the critical point); the problem is adopted from Auricchio et al. 2005.

results obtained with EAS element Q1/E4, which is known to be free of locking in the linear regime, exhibit locking for this nonlinear simulation. The solution depends on the quadrature rules used as well as Poisson's ratio ν and thickness T (not shown). The former is related to volumetric locking and the latter to geometric locking, including shear locking and trapezoidal locking as special cases.

Property (vii) is a direct result of remedies against locking. Locking-free elements are softer and more flexible and thus, in turn, can suffer from artificial instabilities (the term hourglassing is used synonymously). This usually goes along with deformation states that are also potentially prone to physical instabilities. As shown in Korelc et al. 2010, Auricchio et al. 2013 and Pfefferkorn and Betsch 2020, the development of elements that are physically stable without exhibiting artificial instabilities is still not fully satisfying. A particular issue is the reverse behavior: elements that are stable for compression problems are prone to show hourglassing under critical tensile deformation states, and vice versa. The former case is related to geometric instabilities and the latter one to material-induced structural instabilities. Figure 1.2 (b) depicts simulation results with incompatible mode element Q1/H4 of a hyperelastic block under self-weight $\hat{\mathbf{B}}$. Shortly before the structure becomes unstable at $\gamma = 1.88$, the deformed mesh exhibits the typical hourglass pattern. This is a numerical pathology and does not reflect the physically correct solution to the problem.

Property (viii) describes in a broader sense all algorithmic related difficulties encountered within the nonlinear solution process. Algorithms should be robust with respect to varying input parameters. Two issues appeared to be particularly pronounced for the problems in this thesis: on one hand, the robustness of the Newton-Raphson process with respect to critical parameters (e.g., Poisson’s ratio or element slenderness). The problem depends on the considered element formulations and is discussed in Pfefferkorn et al. 2021. On the other hand, with established methods (Wriggers 2008), calculating stability points efficiently can be difficult. The critical point should be approached cautiously to avoid numerical problems. This requires problem-specific, user-defined load step sizes and mitigates an efficient computation.

In a nutshell, those properties are (not) related to the content of this thesis as follows: Property (ii) and (vi) are not examined within the scope of this work. Reference is made to the textbook of Wriggers 2008 and Zienkiewicz et al. 2014 as well as the recent contribution of Pfefferkorn and Betsch 2021. The main goals of the present work are related to Property (v), (vii) and (viii).

1.2 Objectives and Outline of this Work

Figure 1.3 illustrates an overview of the thesis’ content. The topics are mainly considered under the framework of two-dimensional finite elasticity. The majority of numerical issues are discussed in the context of EAS finite elements.

Chapter 2 and 3 provide the theoretical foundation of this work. Its content is the basic prerequisite for a deeper understanding of the following chapters.

Chapter 4 provides purely analytical solutions of two nonlinear problems, which serve as a benchmark throughout this thesis. The main features of a reliable benchmark is the *isolation of individual phenomena* and their clear *reproducibility* for other researchers. Both are crucial, since a benchmark’s main purpose is to promote the comparability of numerical methods. Of course, developing simple benchmarks, e.g., with respect to the material or geometry, increases acceptance within the research community. In addition to that, providing numerical or, in the best case, analytical reference solutions is crucial. The development of benchmarks that represent a compromise between those aspects and the increasing complexity of nonlinear problems is a primary goal in this work. The theoretical aspects of two problems are described. In Figure 1.3 it is classified as a “Review” topic as it does, to a large extent, not contain novel results by the author but rather a summary of an intense literature study. Nevertheless, it is not considered within the “preliminaries” since the corresponding literature appears to be barely considered in the computational-oriented research community.

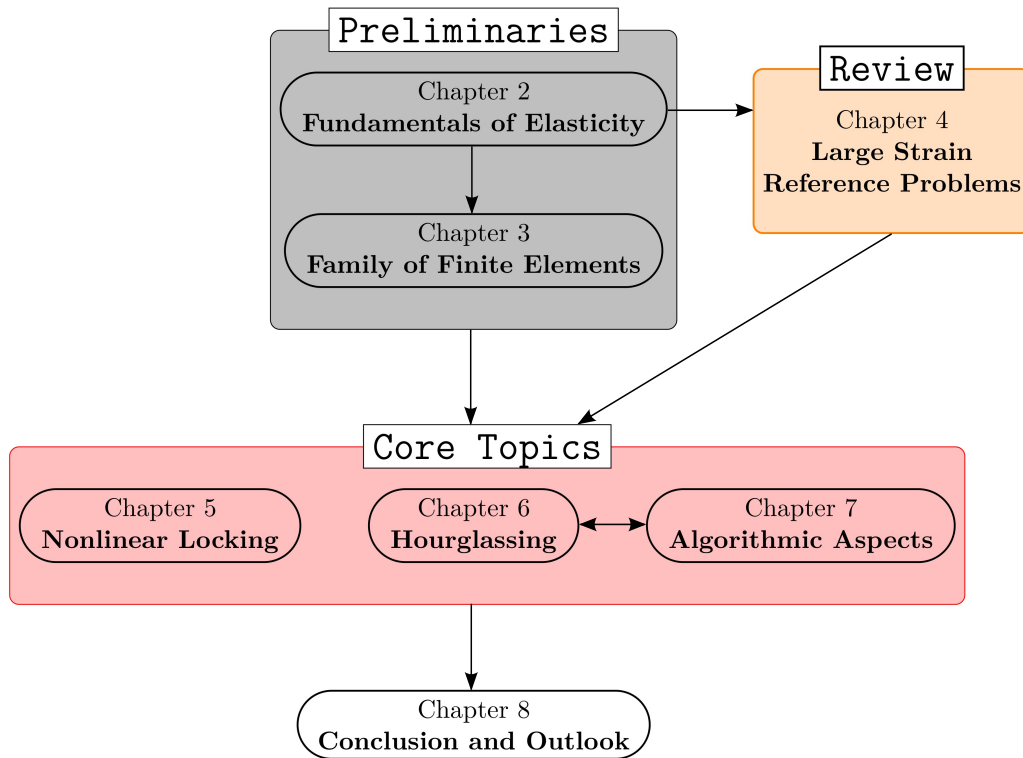


Figure 1.3: Outline of this work.

Chapter 5 presents a study on locking effects that are induced by geometric nonlinearity, including the development of remedies against it. Recently, Willmann et al. 2022 presented the first investigations of nonlinear volumetric locking.² It has been shown that an artificial stiffening occurs under the *joint interaction* of nearly incompressible materials, large bending deformations and higher-order integration. For a total Lagrangian EAS formulation, a higher-order strain enhancement was introduced to overcome the undesired stiffening effect. The two main goals are the extension of these investigations to other nonlinear solid finite element formulations and to nonlinear *geometric* locking effects. Special attention is paid to the development of a suitable benchmark.

Chapter 6 provides a further discussion on the investigations of physical and artificial stability by Bieber et al. 2022. In delineation from this publication, the present studies focus on a deeper understanding of the hourglassing phenomena. The goal is to provide physical insights into the geometric and material instability mechanisms by means of the Ritz method. In addition, further numerical examples are given that illustrate the interplay between stabilizing and destabilizing stiffness contributions. The advantages and limitations of stabilization concepts are discussed.

²In Willmann et al. 2022 the authors use the denomination “nonlinear Poisson stiffening” instead of (volumetric) nonlinear locking, since the mesh is not refined in shell thickness-direction.

Chapter 7 focuses on two algorithmic issues. The problems that arise in the computation of stability points are discussed. Ideas for *adaptive load control methods* are presented and numerically tested. A discussion on open issues and possible future developments closes this section. Followed by that, based on Pfefferkorn et al. 2021, a brief recap on the robustness issues within Newton-Raphson schemes is provided. The goal is to show that a good performance can also be obtained for the newly proposed EAS elements from Chapter 5 and 6.

Chapter 8 provides a summary and concluding remarks of the thesis' results, including open issues and possible future research directions.

Chapter 2

Fundamentals of Finite Elasticity

This chapter provides the theoretical concepts that are required to describe the behavior of elastic bodies undergoing large deformations. As is common in many engineering approaches, the real structure is modeled as a continuum whose constitutive equations are based on a purely phenomenological description. The problems covered in this work are restricted to:

- quasi-static deformations,
- isotropic homogeneous elastic materials,
- isothermal processes.

In most situations, plane strain deformations with unit thickness in the third dimension are considered.

The content of this chapter is well-established and is covered in numerous textbooks. In particular, the following books have proven to be helpful and serve as the primary references of this chapter. From a purely mechanical perspective, the textbooks of Holzapfel 2010, Ogden 1997 and Bigoni 2012 provide clear insight. Moreover, the latter complements the theory with illustrative experiments from real-world problems. An excellent review focusing on hyperelastic material can be found in Beatty 1987. A more engineering-oriented approach to structural and continuum mechanics, including many descriptive examples, is given in Hjelmstad 2005. Ciarlet 1986 provides a mathematical perspective that is accessible to engineers. A delightful presentation of the geometrical description of finite deformations is given in the dissertation of Miehe 1988.

2.1 Kinematics

2.1.1 Deformation of Elastic Bodies

The configurations $\mathcal{B}_\gamma \subset \mathbb{E}^3$ of an elastic body are treated mathematically as an accumulation of points in Euclidean space. Here, $\gamma \in [0, \hat{\gamma}]$ refers to a load factor (pseudo-time) and defines a one-parameter family of intermediate configurations. The stress-free initial configuration \mathcal{B}_0 and the deformed current configuration $\mathcal{B} \equiv \mathcal{B}_{\hat{\gamma}}$ are of particular interest. The deformation is described by the function $\varphi : \mathcal{B}_0 \rightarrow \mathcal{B}$, a bijective twice-continuously differentiable map that relates each point in the initial configuration to the deformed one. The position of these points is represented by

$$\mathbf{x} = \varphi(\mathbf{X}) \quad \text{and} \quad \mathbf{X} = \varphi^{-1}(\mathbf{x}), \quad (2.1)$$

where \mathbf{X} establishes the material (Lagrangian) and \mathbf{x} the spatial (Eulerian) description.¹ In line with standard notation from literature, material quantities (e.g., tensors, indices or derivative operators) are equipped with upper case letters and spatial quantities with lower ones. Position vectors (2.1) may also be expressed as

$$\mathbf{X} = X_A \mathbf{E}_A \quad \text{and} \quad \mathbf{x} = x_a \mathbf{e}_a, \quad (2.2)$$

where \mathbf{E}_A and \mathbf{e}_a denote the material and spatial reference system.

The essential quantities to describe a finite deformation of a body are the (material) deformation gradient

$$\mathbf{F} = \text{Grad } \mathbf{x} \quad \text{or} \quad F_{aB} = \frac{\partial x_a}{\partial X_B}, \quad (2.3)$$

its determinant

$$J = \det \mathbf{F} \quad (2.4)$$

and cofactor

$$\text{cof } \mathbf{F} = J \mathbf{F}^{-\text{T}}. \quad (2.5)$$

To prevent self-penetration of matter and ensure the invertibility of φ , J must be greater than zero. A deformation where $J = 1$ is *isochoric* and, if enforced by the constitutive law, the material is said to be *incompressible*. The deformation gradient establishes the

¹A descriptive geometrical illustration is given for a finite bending deformation in Section 4.2, Figure 4.9

crucial transformations of infinitesimal material line elements $d\mathbf{X}$, volume elements dV and oriented area elements $d\mathbf{A} = dA \mathbf{N}$ in the current configuration (or vice versa)

$$d\mathbf{x} = \mathbf{F}d\mathbf{X}, \quad (2.6a)$$

$$dv = JdV, \quad (2.6b)$$

$$d\mathbf{a} = \text{cof } \mathbf{F} d\mathbf{A}. \quad (2.6c)$$

Here, the last map is known as Nanson's formula. In general, $\varphi(\mathbf{X})$ is nonlinear in \mathbf{X} , in which case the corresponding deformation is said to be *inhomogeneous*. In case \mathbf{F} is constant in all positions \mathbf{X} , and consequently in all transformations (2.6) as well, the deformation is called *homogeneous*.

In some cases, it appears practical to describe certain field quantities with spatial coordinates. From Equation (2.3) follows the spatial deformation gradient as

$$\mathbf{F}^{-1} = \text{grad } \mathbf{x} \quad \text{or} \quad F_{Ba}^{-1} = \frac{\partial X_B}{\partial x_a}. \quad (2.7)$$

Since \mathbf{x} depends on the deformation process, the spatial derivatives of other quantities are usually not directly available. Fortunately, the chain rule provides the following relations for smooth scalar, vector and second-order tensor fields

$$\text{grad } a = \mathbf{F}^{-T} \text{Grad } a, \quad (2.8a)$$

$$\text{grad } \mathbf{a} = \text{Grad } \mathbf{a} \mathbf{F}^{-1}, \quad (2.8b)$$

$$\text{div } \mathbf{A} = \text{Grad } \mathbf{A} : \mathbf{F}^{-T}. \quad (2.8c)$$

Alternatively, the deformation can be described by means of the displacement vector

$$\mathbf{u} = \mathbf{X} - \mathbf{x}. \quad (2.9)$$

This gives rise to the material and spatial displacement gradient

$$\mathbf{H} = \text{Grad } \mathbf{u} = \mathbf{F} - \mathbf{I} \quad \text{and} \quad \mathbf{h} = \text{grad } \mathbf{u} = \mathbf{I} - \mathbf{F}^{-1}, \quad (2.10)$$

respectively, with the identity tensor \mathbf{I} . Furthermore, two multiplicative splits of the deformation gradient are introduced: Firstly, the polar decompositions

$$\mathbf{F} = \mathbf{R}\mathbf{U} = \mathbf{v}\mathbf{R} \quad \text{or} \quad F_{aB} = R_{aC} U_{CB} = v_{ab} R_{bB}, \quad (2.11)$$

with the orthogonal rotation tensor \mathbf{R} and the positive definite symmetric tensors \mathbf{U} and \mathbf{v} , known as right and left stretch tensor, respectively. The rotation tensor provides a rotation of infinitesimal material line elements and the stretch tensors a pure stretch

in the respective configuration. The second split decomposes \mathbf{F} into a purely deviatoric part \mathbf{F}_d and a purely volumetric part \mathbf{F}_v , i.e

$$\mathbf{F} = \mathbf{F}_v \mathbf{F}_d, \quad (2.12)$$

where

$$\mathbf{F}_v = J^{\frac{1}{3}} \mathbf{I} \quad \text{and} \quad \mathbf{F}_d = J^{-\frac{1}{3}} \mathbf{F}. \quad (2.13)$$

In case $\det \mathbf{F}_d = 1$ the deviatoric part represents a purely *isochoric* deformation.

Furthermore, the *principal stretches* $\lambda_i \equiv \lambda_{(i)}$ (no tensorial index notation) are relevant quantities within this work. Based on the polar decomposition (2.11) they appear within the spectral representation of the right and left stretch tensor

$$\mathbf{U} = \sum_{i=1}^3 \lambda_i \mathbf{N}^{(i)} \otimes \mathbf{N}^{(i)} \quad \text{and} \quad \mathbf{v} = \sum_{i=1}^3 \lambda_i \mathbf{n}^{(i)} \otimes \mathbf{n}^{(i)}, \quad (2.14)$$

with orthonormal and normalized eigenvectors, also referred to as Lagrangian and Eulerian principle axes, $\mathbf{N}^{(i)}$ and $\mathbf{n}^{(i)}$. This constitutes the spectral form of the deformation gradient and rotation tensor as

$$\mathbf{F} = \sum_{i=1}^3 \lambda_i \mathbf{n}^{(i)} \otimes \mathbf{N}^{(i)} \quad \text{and} \quad \mathbf{R} = \sum_{i=1}^3 \mathbf{n}^{(i)} \otimes \mathbf{N}^{(i)}. \quad (2.15)$$

2.1.2 Strain Measures

So far, the mapping of material points through φ and the transformation of material elements via \mathbf{F} have been introduced. To compute the internal work, it is relevant to measure the relative length change of material fibers in the course of a deformation. Besides the stretch tensors in (2.11) numerous other definitions are possible. The important ones will be presented.

The right and left Cauchy-Green deformation tensor

$$\mathbf{C} = \mathbf{F}^T \mathbf{F} = \mathbf{U}^2 \quad \text{and} \quad \mathbf{b} = \mathbf{F} \mathbf{F}^T = \mathbf{v}^2 \quad (2.16)$$

provide a measure of squared length in the material and spatial setting. The Green-Lagrange and Almansi strain tensor read

$$\mathbf{E} = \frac{1}{2} (\mathbf{C} - \mathbf{1}) \quad \text{and} \quad \mathbf{e} = \frac{1}{2} (\mathbf{I} - \mathbf{b}^{-1}). \quad (2.17)$$

Here, the Green-Lagrange strain may also be expressed via the displacement gradient as

$$\mathbf{E} = \underbrace{\frac{1}{2}(\mathbf{H}^T + \mathbf{H})}_{\boldsymbol{\varepsilon}} + \underbrace{\frac{1}{2}(\mathbf{H}^T \mathbf{H})}_{\mathbf{E}_{\text{nl}}}, \quad (2.18)$$

providing a split into symmetric parts which are linear and nonlinear in \mathbf{H} . Due to round-off errors it is advantageous to use (2.18) instead of (2.17)₁ for the numerical implementation.

2.1.3 Incremental Kinematic Relations

The concept of *variation* and *linearization* of functions is crucial in the numerical treatment of nonlinear problems. It is important for variational calculus but also in numerics for the construction of incremental-iterative solution schemes, which are typically employed in implicit solution processes. Furthermore, the linearization of weak form equilibrium equations can provide useful mechanical insights, like the concept of stiffness.

The increment $\Delta_{\mathbf{u}}a(\bar{\mathbf{u}}, \Delta\mathbf{u})$ of a differentiable scalar function $a(\bar{\mathbf{u}})$ can be interpreted as the linear change – or derivative – of the respective function at a fix state $\mathbf{u} = \bar{\mathbf{u}}$, while moving in the direction of $\Delta\mathbf{u}$.

This can be formalized via the directional derivative (Gateaux derivative) as

$$\Delta_{\mathbf{u}}a := \left[\frac{d}{d\varepsilon} a(\bar{\mathbf{u}} + \varepsilon\Delta\mathbf{u}) \right] \Big|_{\varepsilon=0} = \frac{\partial a}{\partial \mathbf{u}} \Big|_{\mathbf{u}=\bar{\mathbf{u}}} \cdot \Delta\mathbf{u}. \quad (2.19)$$

Here, a may also be replaced by vector-valued functions \mathbf{a} or second-order tensor functions \mathbf{A} . Technically, a variation is equivalent to Equation (2.19) and denoted with symbol δ , e.g., $\delta_{\mathbf{u}}\alpha$.

For the sake of convenience, the fixed quantities are not further assigned, i.e. $\bar{\mathbf{u}}$ is replaced by \mathbf{u} . The subsequent material and spatial forms of the incremental kinematic relations are given as

$$\begin{aligned} \Delta_{\mathbf{u}}\mathbf{F} &= \Delta_{\mathbf{u}}\mathbf{H} = \text{Grad } \Delta\mathbf{u}, \\ \Delta_{\mathbf{u}}\mathbf{E} &= \text{sym}(\mathbf{F}^T \text{Grad } \Delta\mathbf{u}), \\ \Delta_{\mathbf{u}}\mathbf{C} &= 2 \text{sym}(\mathbf{F}^T \text{Grad } \Delta\mathbf{u}), \\ \Delta_{\mathbf{u}}J &= J\mathbf{F}^{-T} : \Delta_{\mathbf{u}}\mathbf{F} = J \text{div } \Delta\mathbf{u} \\ &= JF_{Ba}^{-1} \Delta_{\mathbf{u}}F_{aB} = J\Delta u_{a,a}, \\ \Delta_{\mathbf{u}}\mathbf{C}^{-1} &= -\mathbf{F}^{-1} \left(\text{grad } \Delta\mathbf{u} + (\text{grad } \Delta\mathbf{u})^T \right) \mathbf{F}^{-T}. \end{aligned} \quad (2.20)$$

and

$$\begin{aligned}\Delta_{\mathbf{u}}\mathbf{e} &= \text{sym}(\text{grad } \Delta\mathbf{u}), \\ \Delta_{\mathbf{u}}\mathbf{h} &= \text{grad } \Delta\mathbf{u}.\end{aligned}\tag{2.21}$$

2.2 Stress, Forces and Equilibrium

Considered is the deformed configuration \mathcal{B} of a body that is subjected to a body load $\hat{\mathbf{b}}$ in its interior and to surface tractions $\hat{\mathbf{t}}$ on the Neumann boundary Γ^σ . Following the stress principle of Euler and Cauchy, the bodies' response to $\hat{\mathbf{b}}$ is characterized by a force vector \mathbf{t} that carries the loading through the body. It acts between each neighboring isolated subdomain \mathcal{B}^{sub} of \mathcal{B} and provides the description in the form of a free body diagram that satisfies the linear force and angular momentum balance

$$\int_{\Gamma^{\text{sub}}} \mathbf{t} \, da + \int_{\mathcal{B}^{\text{sub}}} \hat{\mathbf{b}} \, dv = 0 \quad \text{and} \quad \int_{\Gamma^{\text{sub}}} \mathbf{x}_o \times \mathbf{t} \, da + \int_{\mathcal{B}^{\text{sub}}} \mathbf{x}_o \times \hat{\mathbf{b}} \, dv = 0,\tag{2.22}$$

respectively, with arbitrary origin \mathbf{x}_o . For a descriptive geometrical illustration of a free body diagram, it is referred to the finite bending deformation in Section 4.2, Figure 4.11. The Cauchy theorem states the existence of a tensor $\boldsymbol{\sigma}(\mathbf{x})$ such that $\mathbf{t}(\mathbf{x}, \mathbf{n}) = \boldsymbol{\sigma}\mathbf{n}$, where $\mathbf{n}(\mathbf{x})$ is the unit normal vector on Γ^{sub} . Cauchy's three assertions are: (i) \mathbf{t} depends only linearly on \mathbf{n} , (ii) $\boldsymbol{\sigma} = \boldsymbol{\sigma}^T$ and thus fulfills (2.22)₂ and (iii) via the divergence theorem the global force balance (2.22)₁ yields the local form

$$\left. \begin{aligned}\text{div } \boldsymbol{\sigma} + \hat{\mathbf{b}} &= \mathbf{0} && \text{in } \mathcal{B} \\ \boldsymbol{\sigma}\mathbf{n} - \hat{\mathbf{t}} &= \mathbf{0} && \text{on } \Gamma^\sigma\end{aligned}\right\}.\tag{2.23}$$

This provides the so-called *Cauchy stress tensor* $\boldsymbol{\sigma}$. The fully spatial nature is often not practical and prompts a reformulation of the force balance momentum in the reference configuration. The area transformation (2.6c) yields $\boldsymbol{\sigma} \, da = J\boldsymbol{\sigma}\mathbf{F}^{-T}d\mathbf{A} = \mathbf{P}d\mathbf{A}$ and provides

$$\left. \begin{aligned}\text{Div } \mathbf{P} + \hat{\mathbf{B}} &= \mathbf{0} && \text{in } \mathcal{B}_0 \\ \mathbf{P}\mathbf{N} - \hat{\mathbf{T}} &= \mathbf{0} && \text{on } \Gamma_0^\sigma\end{aligned}\right\},\tag{2.24}$$

where $\mathbf{N}(\mathbf{X})$ denotes the unit normal vector in the reference configuration. This establishes the non-symmetric *first Piola-Kirchhoff stress tensor* \mathbf{P} that provides the pseudo or nominal force vector $\mathbf{T} = \mathbf{P}\mathbf{N}$, parallel to \mathbf{t} but measuring force related to the reference area. Angular momentum balance (2.22)₂ is fulfilled via symmetry in $\mathbf{P}\mathbf{F}^T = \mathbf{F}\mathbf{P}^T$. Further useful stress measures are the symmetric *second Piola-Kirchhoff stress* \mathbf{S} and

	$\boldsymbol{\sigma}$	$\boldsymbol{\tau}$	\mathbf{P}	\mathbf{S}
$\boldsymbol{\sigma}$	σ_{ab}	$J^{-1}\boldsymbol{\tau}$	$J^{-1}\mathbf{P}\mathbf{F}^T$	$J^{-1}\mathbf{F}\mathbf{S}\mathbf{F}^T$
$\boldsymbol{\tau}$	$J\boldsymbol{\sigma}$	τ_{ab}	$\mathbf{P}\mathbf{F}^T$	$\mathbf{F}\mathbf{S}\mathbf{F}^T$
\mathbf{P}	$J\boldsymbol{\sigma}\mathbf{F}^{-T}$	$\boldsymbol{\tau}\mathbf{F}^{-T}$	P_{aB}	$\mathbf{F}\mathbf{S}$
\mathbf{S}	$J\mathbf{F}^{-1}\boldsymbol{\sigma}\mathbf{F}^{-T}$	$\mathbf{F}^{-1}\boldsymbol{\tau}\mathbf{F}^{-T}$	$\mathbf{F}^{-1}\mathbf{P}$	S_{AB}

Table 2.1: Various stress tensors and their relations.

the symmetric Kirchhoff stress $\boldsymbol{\tau}$. An overview of transformations of these stress tensors is provided in Table 2.1.

2.3 Constitutive Equations

2.3.1 Some Preliminary Aspects

The relation between kinematic quantities and stresses (constitutive equations) is determined by the material behavior. The phenomenological abstraction of the real material's response involves the fitting of a constitutive model, e.g., the fitting of a response function to experimental data. This provides the constitutive equation (material law) and completes the set of required equations to solve the BVP.

For large strain problems, the field of application of a constitutive law should naturally be confined by mathematical and physical restrictions. These are formulated in the form of inequalities, which constrain the range of possible deformations. *Mathematical restrictions* concern the uniqueness and existence of solutions to the governing BVP and are discussed further in Section 2.3.4. *Physical restrictions*, on the other hand, are related to the fact that the experiments to which the equations of a constitutive model are fitted are based on a selected set of \mathbf{F} .² This naturally raises the question of physical and numerical reliability when simulations are done for arbitrary deformations \mathbf{F} , see the discussion in Section 3.1 of Ciarlet 1986. The simulation may show results that would not be covered by experiments.

The focus of this work lies on mathematical and numerical aspects of large strain problems and the selected “model problem” materials are chosen to be *as simple as possible* but still cover ubiquitous response patterns, such as strain softening or strain stiffening. Attention is paid to the mathematical restrictions, whereas physical meaningfulness with respect to the specific material model is not a prior focus.

²Typically this experimental data emanates from simple deformation states, in particular homogeneous stretch and shear states.

2.3.2 Hyperelastic Materials

A material is called hyperelastic (or Green elastic) if there exists a stored energy function $W(\mathbf{F})$ that defines energy per unit volume in such a way that

$$\mathbf{P} = \frac{\partial W(\mathbf{F})}{\partial \mathbf{F}} \quad \text{or} \quad P_{aB} = \frac{\partial W}{\partial F_{aB}}. \quad (2.25)$$

In mathematical terms this establishes a one to one stress-strain correspondence. Relation (2.25) can be derived by the entropy-free (equal sign) case of the second law of thermodynamics

$$\left(\mathbf{P} - \frac{\partial W}{\partial \mathbf{F}} \right) : \frac{d}{dt} \mathbf{F} = 0, \quad (2.26)$$

also called Coleman-Noll procedure. For more details it is referred to Section 6.1 of Holzapfel 2010.

Requirements. Some physically motivated requirements have to be fulfilled by the strain energy function. In the large strain regime, this concerns the growth condition, which implies infinite energy for extreme deformations, i.e.

$$W(\mathbf{F}) \rightarrow \infty \quad \text{for} \quad \begin{cases} J \rightarrow \infty \\ J \rightarrow 0^+ \end{cases} \quad (2.27)$$

This plays a particularly important role in the context of existence theorems in finite elasticity; see Ciarlet 1986 for further details. Furthermore, it is convenient to require $W(\mathbf{I}) = 0$, i.e. no energy and zero stress in the undeformed state, as well as $W(\mathbf{F}) > 0$.

Another important aspect is material objectivity with respect to the coordinate system (frame invariance) and superimposed rigid body motions. Both should not affect the constitutive response:

$$W(\mathbf{QF}) = W(\mathbf{F}) \quad \forall \mathbf{Q} \in \mathcal{SO}(3). \quad (2.28)$$

From this follows, with a slight abuse of notation,

$$W(\mathbf{F}) = W(\mathbf{U}) = W(\mathbf{C}) \quad (2.29)$$

and consequently

$$\mathbf{S} = \frac{\partial W(\mathbf{E})}{\partial \mathbf{E}} = 2 \frac{\partial W(\mathbf{C})}{\partial \mathbf{C}}. \quad (2.30)$$

Furthermore the assumption of an isotropic material response yields

$$W(\mathbf{F}) = W(\mathbf{F}\mathbf{Q}^T) \quad \forall \mathbf{Q} \in \mathcal{SO}(3). \quad (2.31)$$

In this case, the stored energy can also be expressed in terms of the principal stretches as

$$W(\mathbf{F}) = W(\lambda_\alpha) \quad \alpha = 1,2,3, \quad (2.32)$$

from which the principal stresses can be deduced as

$$S_{(\alpha)} = \frac{1}{\lambda_\alpha} \frac{\partial W}{\partial \lambda_\alpha}, \quad P_{(\alpha)} = \frac{\partial W}{\partial \lambda_\alpha}, \quad \sigma_{(\alpha)} = J^{-1} \lambda_\alpha \frac{\partial W}{\partial \lambda_\alpha}. \quad (2.33)$$

Here, similar to the principal stretches, the parentheses will be skipped in the sequel, i.e. $S_i \equiv S_{(i)}$ (no tensorial index notation).

Incompressible materials. The isochoric constraint is implemented in the stored energy as

$$W(\mathbf{F}, p) = W_d(\mathbf{F}) - p(J - 1), \quad (2.34)$$

where W_d is a deviatoric stored energy defined for $J = 1$ and p a Lagrange multiplier that enforces the isochoric constraint $J = 1$. Exemplified for the Cauchy stress and using $\partial J / \partial \mathbf{F} = J^{-1} \mathbf{F}^{-T}$ it follows directly that

$$\boldsymbol{\sigma} = -p\mathbf{I} + \frac{\partial W(\mathbf{F})}{\partial \mathbf{F}} \mathbf{F}^T, \quad (2.35)$$

or, in terms of the principal stretches,

$$\sigma_i = -p + J^{-1} \lambda_i \frac{\partial W}{\partial \lambda_i}. \quad (2.36)$$

2.3.3 Incremental Constitutive Relations

In analogy to the incremental kinematic quantities introduced in Section 2.1.3, incremental stress-strain relations are obtained in a similar manner.

Material constitutive tensor. The chain rule provides the incremental second Piola-Kirchhoff stress relation

$$\Delta_{\mathbf{u}}\mathbf{S} = \frac{\partial \mathbf{S}}{\partial \mathbf{E}} \frac{\partial \mathbf{E}}{\partial \mathbf{u}} \cdot \Delta \mathbf{u} = \frac{\partial \mathbf{S}}{\partial \mathbf{E}} : \Delta_{\mathbf{u}}\mathbf{E} \quad (2.37)$$

and establishes, using (2.30), the *material constitutive tensor*

$$\mathbb{C} = \frac{\partial^2 W}{\partial \mathbf{E} \partial \mathbf{E}} = 4 \frac{\partial^2 W}{\partial \mathbf{C} \partial \mathbf{C}} \quad \text{or} \quad C_{ABCD} = \frac{\partial^2 W}{\partial E_{AB} \partial E_{CD}}. \quad (2.38)$$

Symmetry of S_{AB} and E_{CD} yields the minor symmetry $C_{ABCD} = C_{BACD} = C_{ABDC}$ and the existence of an energy functional W provides $C_{ABCD} = C_{CDAB}$. Thus, the fourth order tensor \mathbb{C} possesses major symmetry (21 coefficients remain).

With the spectral decomposition (2.15) and the constitutive relation (2.33) the second Piola-Kirchhoff stress can be expressed as

$$\mathbf{S} = \sum_{i=1}^3 S_i \mathbf{N}^{(i)} \otimes \mathbf{N}^{(i)}. \quad (2.39)$$

This furnishes the spectral representation of the material constitutive tensor

$$\begin{aligned} \mathbb{C} &= \sum_{i,j=1}^3 \frac{1}{\lambda_j} \frac{\partial W}{\partial \lambda_j} \mathbf{N}^{(i)} \otimes \mathbf{N}^{(i)} \otimes \mathbf{N}^{(j)} \otimes \mathbf{N}^{(j)} \\ &+ \sum_{\substack{i,j=1 \\ i \neq j}}^3 \frac{S_j - S_i}{\lambda_j^2 - \lambda_i^2} \mathbf{N}^{(i)} \otimes \mathbf{N}^{(j)} \otimes (\mathbf{N}^{(i)} \otimes \mathbf{N}^{(j)} + \mathbf{N}^{(j)} \otimes \mathbf{N}^{(i)}) \end{aligned} \quad (2.40)$$

in terms of the eigenvalues λ_i^2 and eigenvectors $\mathbf{N}^{(i)}$ of \mathbf{C} . Here the special case $\lambda_i = \lambda_j$ requires the second factor to be replaced by the limit value

$$\lim_{\lambda_j \rightarrow \lambda_i} \frac{S_j - S_i}{\lambda_j^2 - \lambda_i^2} = \frac{\partial S_j}{\partial \lambda_j} - \frac{\partial S_i}{\partial \lambda_i}. \quad (2.41)$$

For further details it is referred to Example 6.8 in Holzapfel 2010.

Spatial and two-point constitutive tensors. Based on \mathbb{C} , the spatial constitutive tensor \mathbb{c} is obtained by a push-forward operation

$$c_{abcd} = J^{-1} C_{ABCD} F_{aA} F_{bB} F_{cC} F_{dD} \quad (2.42)$$

providing the incremental stress relation

$$\Delta_{\mathbf{u}}\boldsymbol{\sigma} = \mathbb{c} : \text{grad } \Delta\mathbf{u}. \quad (2.43)$$

The two-point constitutive tensor \mathbb{A} is obtained by

$$\mathbb{A} = \frac{\partial^2 W}{\partial \mathbf{F} \partial \mathbf{F}} \quad \text{or} \quad A_{aBcD} = \frac{\partial^2 W}{\partial F_{aB} \partial F_{cD}} \quad (2.44)$$

and provides the incremental stress relation

$$\Delta_{\mathbf{u}}\mathbf{P} = \mathbb{A} : \text{Grad } \Delta\mathbf{u}. \quad (2.45)$$

Furthermore, the tensor \mathbb{A} can be split into a material contribution \mathbb{A}^m and geometric contribution \mathbb{A}^g , with

$$A_{aBcD}^m = C_{ABCD} F_{aA} F_{cC} \quad \text{and} \quad A_{aBcD}^g = \delta_{ac} S_{BD}. \quad (2.46)$$

2.3.4 Some Aspects on Local Uniqueness and Stability of Solutions

Large strain structural analysis can result in (extreme) deformation states where the global and local uniqueness of the solution is lost.

Global uniqueness, closely related to *structural* stability, regards the structure as a whole and is determined by the structural topology, material model and boundary conditions. It is extensively discussed in Section 4.1.

The local aspects of stability, on the other hand, focus on the material behavior at the continuum point. Local instability often indicates the onset of structural failure.³ It is often discussed in the context of plasticity; see e.g., the survey article of Petryk 2000. However, as exemplified later, this topic can also become relevant in the analysis of elastic materials. Within this work, the particularly important cases are:

- material instability (loss of ellipticity of the underlying equilibrium equations),
- loss of positive definiteness of \mathbb{C} ,
- loss of positive definiteness of \mathbb{A} .

These cases are closely connected to the physical and numerical (artificial) instability problems in the subsequent sections.

³However, not always. A typical counterexample is the formation of plastic hinges in statically indeterminate truss systems or in an ideally elastic-plastic beam-like structure subjected to pure bending; see e.g., Chen and Baker 2003.

Loss of ellipticity and material instability. Strong ellipticity of the underlying system is defined by the Legendre-Hadamard condition

$$(\mathbf{a} \otimes \mathbf{B}) : \mathbb{A} : (\mathbf{a} \otimes \mathbf{B}) \geq 0 \quad \forall \mathbf{a}, \mathbf{B} \quad (2.47)$$

with nonzero vectors \mathbf{B} and \mathbf{a} connected to the rank-one tensor $\bar{\mathbf{F}} = (\mathbf{a} \otimes \mathbf{B})$. From the perspective of elastodynamics, this conditions admits the well-known interpretation via the wave propagation problem

$$(\mathbf{Q} - \rho_0 c^2 \mathbf{I}) \mathbf{a} = \mathbf{0} \quad \text{with } Q_{ac} = A_{aBcD} B_B B_D. \quad (2.48)$$

Here \mathbf{Q} denotes the acoustic tensor, ρ_0 the density and c the wave speed in direction \mathbf{B} . The material is stable when it allows for every direction \mathbf{B} a propagation with real wave speed, i.e.

$$\rho_0 c^2 \geq 0. \quad (2.49)$$

For a detailed discussion it is referred to Section 6.2.7 in Ogden 1997.

As shown in Knowles and Sternberg 1975, loss of ellipticity indicates the onset of *weak discontinuities*, i.e. deformation gradients that are discontinuous in time but still obey a continuous displacement field. A violation of Equation (2.47) is usually associated with the term (local) *material instability* or *material failure* and indicates the onset of possible strain localizations, e.g., the formation of shear bands.

Loss of positive definiteness of constitutive operators. Positive definiteness of the two-point constitutive tensor \mathbb{A} is a necessary condition for ellipticity. It also excludes any form of global material-induced instabilities; see Bigoni 2012. In contrast to that, the non-positive definiteness of the material constitutive tensor \mathbb{C} does not admit any physical interpretation. For the uniaxial stress case, it can be associated with strain softening of the first and second Piola-Kirchhoff stress tensors, as shown in Figure 2.1 (b).

The constitutive operators in the homogeneous plane strain case are considered. The required coefficients of the tangents \mathbb{C} and \mathbb{A} (or $\hat{\mathbf{C}}$ and $\hat{\mathbf{A}}$ in Voigt notation) are defined via the incremental stress-strain relations

$$\begin{bmatrix} \Delta P_{11} \\ \Delta P_{22} \\ \Delta P_{12} \\ \Delta P_{21} \end{bmatrix} = \hat{\mathbf{A}} \Delta \mathbf{F} = \begin{bmatrix} A_{11}^n & A_{12}^n & 0 & 0 \\ A_{12}^n & A_{22}^n & 0 & 0 \\ 0 & 0 & A_{11}^s & A_{12}^s \\ 0 & 0 & A_{12}^s & A_{22}^s \end{bmatrix} \begin{bmatrix} \Delta F_{11} \\ \Delta F_{22} \\ \Delta F_{12} \\ \Delta F_{21} \end{bmatrix} \quad (2.50)$$

	(E, ν)		(Λ, μ)
Young's modulus	E	—	$\frac{\mu(3\Lambda+2\mu)}{\Lambda+\mu}$
Poisson's ratio	ν	—	$\frac{\Lambda}{2(\Lambda+\mu)}$
1 st Lamé constant	Λ	$\frac{\mu(E-2\mu)}{3\mu-E}$	—
2 nd Lamé constant (shear modulus G)	μ	$\frac{E}{2(1+\nu)}$	—
Longitudinal modulus	M	$\frac{E(1-\nu)}{(1+\nu)(1-2\nu)}$	$\Lambda + 2\mu$
Bulk modulus	K	$\frac{E}{3(1-\nu)}$	$\Lambda + \frac{2\mu}{3}$

Table 2.2: Pairs of linear elasticity constants and their relations.

and

$$\begin{bmatrix} \Delta S_{11} \\ \Delta S_{22} \\ \Delta S_{12} \end{bmatrix} = \hat{\mathbf{C}} \Delta \mathbf{E} = \begin{bmatrix} C_{11}^n & C_{12}^n & 0 \\ C_{12}^n & C_{22}^n & 0 \\ 0 & 0 & C_{12}^s \end{bmatrix} \begin{bmatrix} \Delta E_{11} \\ \Delta E_{22} \\ 2\Delta E_{12} \end{bmatrix}. \quad (2.51)$$

Required in the sequel are the sub-matrices \mathbf{A}_n , \mathbf{A}_s and \mathbf{C}_n , defined by the respective 2×2 blocks as

$$\mathbf{A}_n = \begin{bmatrix} A_{11}^n & A_{12}^n \\ A_{12}^n & A_{22}^n \end{bmatrix}, \quad \mathbf{A}_s = \begin{bmatrix} A_{11}^s & A_{12}^s \\ A_{12}^s & A_{22}^s \end{bmatrix}, \quad \mathbf{C}_n = \begin{bmatrix} C_{11}^n & C_{12}^n \\ C_{12}^n & C_{22}^n \end{bmatrix}. \quad (2.52)$$

2.3.5 Examples of Strain Energy Functions

The strain energy functions that are required in this thesis are collected in the following. All hyperelastic materials under consideration can be expressed in terms of two linear elasticity constants. In order to simplify expressions, it will become advantageous to switch between constants. Table 2.2 shows the relationships between the six elasticity constants.

Saint-Venant Kirchhoff (SVK). The SVK model is the simplest hyperelastic material. The stored energy function is typically expressed with the Lamé constants as

$$W(\mathbf{E}) = \frac{\Lambda}{2} (\text{tr } \mathbf{E})^2 + \mu \text{tr } \mathbf{E}^2, \quad (2.53)$$

providing the second Piola-Kirchhoff stress

$$\mathbf{S} = \frac{\partial W}{\partial \mathbf{E}} = \Lambda \operatorname{tr} \mathbf{E} \mathbf{I} + 2\mu \mathbf{E}. \quad (2.54)$$

The SVK material meets the objectivity requirement (2.28) and isotropy condition (2.31) and is a suitable choice for problems involving *large deformation* but only *small strain*. An appealing property is that the material's constitutive tensor \mathbb{C} is equivalent to the linear elastic one and thus independent of the deformation. Exemplified for the plane strain case, tensor \mathbb{C} in Voigt notation reads

$$\hat{\mathbf{C}} = \begin{bmatrix} \Lambda + 2\mu & \Lambda & 0 \\ \Lambda & \Lambda + 2\mu & 0 \\ 0 & 0 & \mu \end{bmatrix} = \frac{E}{(1 + \nu)(1 - 2\nu)} \begin{bmatrix} 1 - \nu & \nu & 0 \\ \nu & 1 - \nu & 0 \\ 0 & 0 & 2(1 + \nu) \end{bmatrix}. \quad (2.55)$$

According to Ciarlet 1986 (p. 184), Equation (2.53) can also be expressed in terms of the right Cauchy-Green tensor as

$$W(\mathbf{C}) = -\frac{3K}{4} \operatorname{tr} \mathbf{C} + \frac{M}{8} \operatorname{tr} \mathbf{C}^2 + \frac{\lambda}{4} \operatorname{tr} \operatorname{cof} \mathbf{C} + \frac{9K}{8}. \quad (2.56)$$

Due to the minus sign in the first expression, it can be shown that W is not polyconvex. It also violates the constitutive growth condition (2.27)₁, for example, uniform volumetric compression $\lambda_i \rightarrow 0^+$ yields $\operatorname{tr} \mathbf{C} \rightarrow 0$ and produces stress that tends to zero. It is also worth noting that the leading terms of all hyperelastic strain energy functions coincide with (2.53) near to the undeformed state $\mathbf{F} \rightarrow \mathbf{I}$.

Neo-Hooke (NH). The NH model is physically motivated by networks of chain molecules and developed in view of experiments on vulcanized rubber sheets by Treloar 1944. The suffix “Neo” emphasizes the generalization of Hooke's law and can be traced back to the seminal work of Rivlin 1948. For the incompressible case, its strain energy function constitutes the simple form

$$W_d(\mathbf{C}) = \frac{\mu}{2} (\operatorname{tr} \mathbf{C} - 3) = \frac{\mu}{2} (\lambda_1^2 + \lambda_2^2 + \lambda_3^2 - 3). \quad (2.57)$$

For two-dimensional axial extension, the model is in good agreement with experimental results, but less suitable for modeling shear and three-dimensional states of strain, as already noted in the early work of Treloar 1944.⁴

⁴For these cases the Mooney-Rivlin model is more suited, since the model includes also a dependence on the second invariant $\frac{1}{2} (\operatorname{tr}^2 \mathbf{C} - \operatorname{tr} \mathbf{C}^2)$.

For the compressible case an extension of the form

$$W(\mathbf{C}) = \frac{\mu}{2} (\text{tr } \mathbf{C} - 3) - \mu \ln J + \underbrace{\frac{\Lambda}{2} \ln^2 J}_{U(J)}, \quad (2.58)$$

is used. Here, the term $\mu \ln J$ is a prerequisite to ensure the stress-free reference state and $U(J)$ represents the energy contribution related to the volume change J . However, the definition of $U(J)$ in the context of the NH model is not explicitly defined in literature and various choices, with potential consequences for numerical, mathematical and physical behavior are possible; see Hartmann and Neff 2003. A further choice that will partially be used in this work is

$$U(J) = \frac{\Lambda}{4} (J^2 - 1 - 2 \ln J). \quad (2.59)$$

“Special” Blatz-Ko rubber (BK). Blatz and Ko 1962 proposed the BK model, which is a constitutive relation tailored for the modeling of compressible rubber materials. In the present work, the focus lies on the so-called *special* BK rubber, a variant for modeling foamed polyurethane elastomers. It is characterized by the remarkably simple strain-energy function

$$W(\lambda_1, \lambda_2) = \frac{\mu}{2} \left(\frac{1}{\lambda_1^2} + \frac{1}{\lambda_2^2} + 2\lambda_1\lambda_2 - 4 \right). \quad (2.60)$$

The only material parameter is the shear modulus of linear elasticity. It can be demonstrated that $\lim_{\lambda_i \rightarrow 1} \nu = 1/4$ for the Poisson’s ratio. For an in-depth discussion, it is referred to Beatty 1987, specifically Section 8.1.

The constitutive model appears to be popular for analytical investigations. For instance in the closed form solutions, usually rarely available for compressible materials, of the finite strain problems presented in Carroll 1988. Furthermore, Knowles and Sternberg 1975 demonstrated that the ellipticity condition (2.47) holds if and only if

$$2 - \sqrt{3} < \frac{\lambda_1}{\lambda_2} < 2 + \sqrt{3}. \quad (2.61)$$

A simple derivation of this equation can be found in Horgan 1996.

Ogden material (OGD). The last considered material was proposed by Ogden 1972. It is based on the principal stretches and takes the form

$$W(\lambda_1, \lambda_2, \lambda_3) = \sum_{i=1}^N \left[\frac{\mu_p}{\alpha_p} \left(\lambda_i^{\alpha_p} + \lambda_2^{\alpha_p} + \lambda_3^{\alpha_p} - 3 \right) \right] + U(J), \quad (2.62)$$

with material constants α_p and μ_p . Good agreement with experimental results is possible (see the discussion in Section 6.5 in Holzapfel 2010). Parameters $N = 1$, $\mu_1 = \mu$ and $\alpha_1 = 2.0$ recovers the NH material. Only the special variant with $N = 1$, $\alpha_1 = 0.5$, and $\mu_1 = \mu$ in combination with the volumetric part of (2.58) is used in this work. The material is denoted as ‘‘OGD’’.

Examples. The vanishing determinant of the constitutive operator’s submatrices (Equation (2.38) and (2.44)) of BK and a compressible NH are illustrated in Figure 2.1 (a,c). Furthermore, the dashed lines represent the uniaxial and equibiaxial stress states. Both plots show that the definiteness of the constitutive tensors depends on the stretch state. For the uniaxial stress states, only the BK model shows instabilities. This circumstance is later intensively exploited. However, depending on the biaxial stress state and on $U(J)$, also compressible NH models can exhibit instabilities.

For a uniaxial stress state the constraint $S_1(\lambda_1, \lambda_2) = 0$ is used to express λ_1 as a function of λ_2 . For the materials herein this relation is given as

$$\text{BK:} \quad \lambda_1 = 3\lambda_2^{-1/3}, \quad (2.63a)$$

$$\text{NH:} \quad \lambda_1 = \exp \left(\frac{\mu}{\Lambda} - \frac{W_L \left(\frac{2\mu \exp(2\mu/\Lambda)}{\Lambda \lambda_2^2} \right)}{2} \right) \frac{1}{\lambda_2}, \quad (2.63b)$$

$$\text{OGD:} \quad \lambda_1 = \left[W_L \left(\frac{\sqrt{\mu^2/\lambda_2} \exp(\frac{\mu}{2\Lambda})}{2\Lambda} \right) \right]^2 \frac{4\Lambda^2}{\mu^2}, \quad (2.63c)$$

$$\text{SVK:} \quad \lambda_1 = \frac{\sqrt{-(\Lambda + 2\mu)(\Lambda \lambda_2^2 - 2\Lambda - 2\mu)}}{\Lambda + 2\mu}. \quad (2.63d)$$

Here, W_L denotes the Lambert W function. Now the vertical stress S_1 and constitutive tensor \mathbb{C} can be expressed as a function of λ_2 only. Figure 2.1 (b,d) depicts the uniaxial stress-stretch curves for various materials. A typical strain softening behavior under tension is observed for BK (b) and OGD (d). In each case, the onset of softening goes hand in hand with the indefiniteness of the corresponding constitutive operator (dashed vertical lines in (b)) but occurs before ellipticity is lost. It is observed that S_2 softens prior to P_2 . This becomes particularly important for the analysis of material hourglassing.

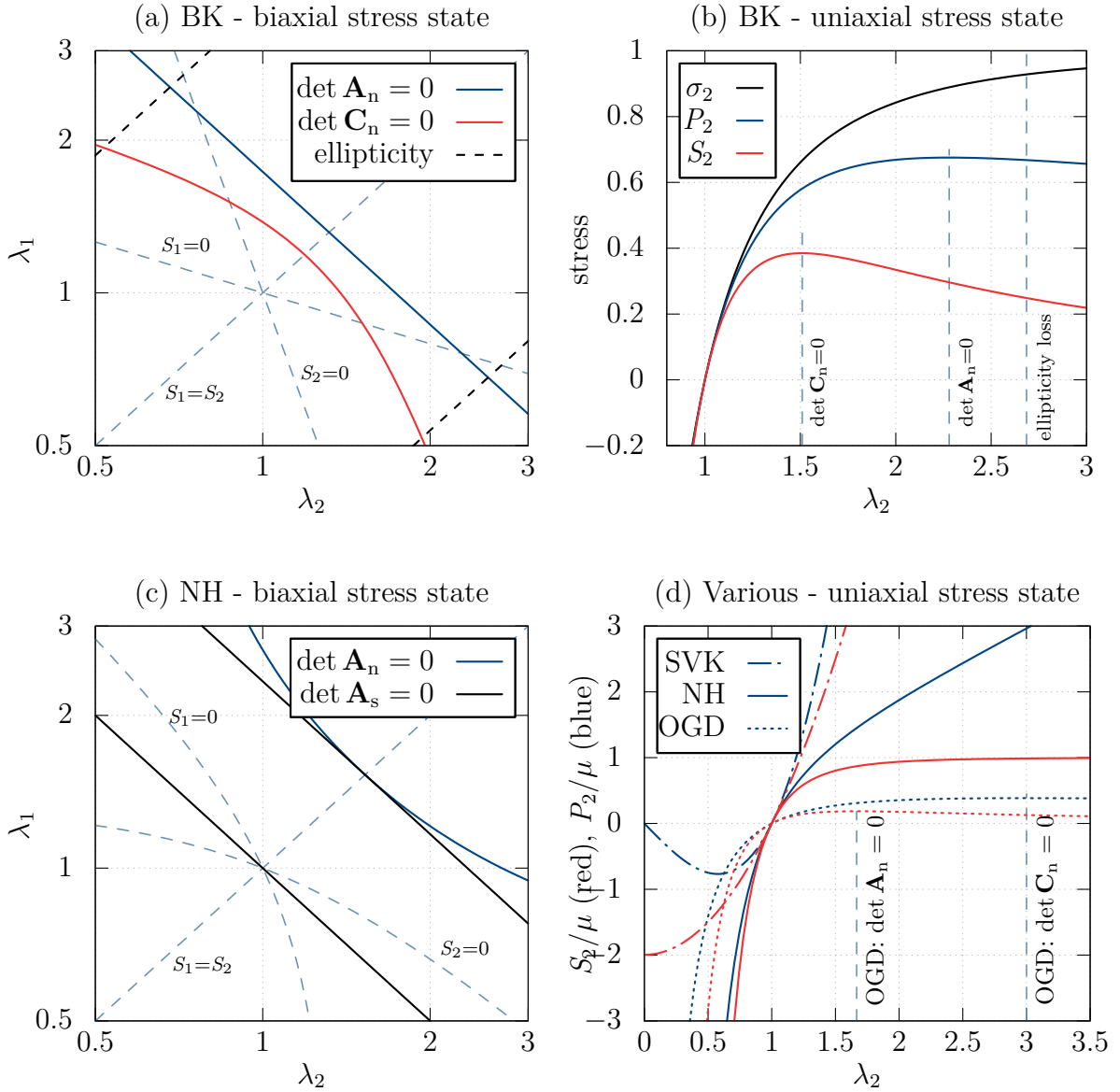


Figure 2.1: Left: respective quantities for a biaxial stress state; right: various stress measures for a uniaxial stress state with $S_1 = 0$; (a,b) Blatz-Ko rubber with $\mu = 1$; (c) a compressible Neo-Hookean model with $\nu = 0.3$, $E = 1000$ and $U(J) = \frac{\Lambda}{4}(J^2 - 1 - 2 \ln J)$; (d) nearly incompressible models with $\nu = 0.499$ and $E = 1000$ or $\Lambda = 166444.30$ and $\mu = 333.56$; NH with $U(J) = \frac{\Lambda}{4} \ln^2 J$; S_2 (red) and P_2 (blue).

Remark 2.3.1. Real-world tensile material-induced instabilities and strain softening behaviour are rather associated with plastic materials. Nevertheless, to a certain extent, theoretically derived tensile instabilities of simple hyperelastic materials have also

been reproduced by experiments. Examples are the equibiaxial stretching experiments by Overvelde et al. 2016 or the set of elastic instability experiments in Gent 2005.

2.4 Boundary Value Problem and Variational Formulations

A variational perspective on the underlying Boundary Value Problem (BVP) is required to solve problems using the finite element method. Some classical variational principles within the framework of quasi-static elastic problems are presented. Figure 2.2 provides an overview of the principles and their connections. They provide a variational basis for the finite element formulations in the remainder of this work. For further details and references, it is referred to the textbook of Washizu 1975 and, with a focus on nonlinear elasticity, to the review article by Guo 1980. Without loss of generality, the subsequent equations are primarily illustrated for the two-point setting with stress and strain variable \mathbf{P} and \mathbf{F} , respectively.

2.4.1 Boundary-Value Problem of Isotropic Finite Elasticity

The general BVP is governed by the following set of equations

$$\left. \begin{array}{ll} \text{Equilibrium} & \text{Div } \mathbf{P} = -\hat{\mathbf{B}} \\ \text{Kinematic} & \mathbf{F} = \mathbf{I} + \text{Grad } \mathbf{u} \\ \text{Constitutive} & \mathbf{P} = \frac{\partial W}{\partial \mathbf{F}} \text{ or } \mathbf{F} = \frac{\partial W_c}{\partial \mathbf{P}} \end{array} \right\} \text{ in } \mathcal{B}_0 \quad (2.64)$$

subjected to the essential (displacement) and natural (force) boundary conditions

$$\begin{aligned} \mathbf{u} &= \hat{\mathbf{u}} & \text{on } \Gamma_0^u, \\ \mathbf{P}\mathbf{N} &= \hat{\mathbf{T}} & \text{on } \Gamma_0^\sigma. \end{aligned} \quad (2.65)$$

Here, the body's reference surface is decomposed into $\Gamma_0 = \Gamma_0^u \cup \Gamma_0^\sigma$ with $\Gamma_0^u \cap \Gamma_0^\sigma = \emptyset$ and W_c denotes the complementary strain energy function. This completes the *boundary value problem* of finite elasticity. The corresponding *incremental boundary value problem*

(IBVP) can be formulated in a similar manner as

$$\left. \begin{aligned} \text{Div } \Delta \mathbf{P} &= -\Delta \hat{\mathbf{B}} \\ \Delta \mathbf{F} &= \text{Grad } \Delta \mathbf{u} \\ \Delta \mathbf{P} &= \mathbb{A} : \Delta \mathbf{F} \end{aligned} \right\} \text{ in } \mathcal{B}_0 \quad (2.66)$$

with

$$\begin{aligned} \Delta \mathbf{u} &= \mathbf{0} & \text{on } \Gamma_0^u, \\ \Delta \mathbf{P} \mathbf{N} &= \Delta \hat{\mathbf{T}} & \text{on } \Gamma_0^\sigma. \end{aligned} \quad (2.67)$$

A solution of the BVP or IBVP will provide a \mathbf{u} or $\Delta \mathbf{u}$, respectively, that solves the differential equations at *every* point of the body. This however is, besides a few special cases, of which some are presented in Chapter 4, difficult to obtain in closed form.

2.4.2 Single-Field Variational Energy Principles

For a conservative system, the total potential energy functional is given as

$$\Pi(\mathbf{u}) = \underbrace{\int_{\mathcal{B}_0} W(\mathbf{F}(\mathbf{u})) \, dV}_{\Pi_{\text{int}}} - \underbrace{\int_{\mathcal{B}_0} \hat{\mathbf{B}} \cdot \mathbf{u} \, dV - \int_{\Gamma_0^\sigma} \hat{\mathbf{T}} \cdot \mathbf{u} \, dA}_{\Pi_{\text{ext}}}, \quad (2.68)$$

with displacement as independent variable. The *principle of minimum potential energy* states that equilibrium of the deformed body is met when, among all admissible displacements that satisfy the essential boundary conditions, the actual displacement field makes Π a minimum. This implies that the first variation vanishes, i.e.

$$\begin{aligned} \delta_{\mathbf{u}} \Pi(\mathbf{u}) &= \int_{\mathcal{B}_0} \frac{\partial W(\mathbf{F}(\mathbf{u}))}{\partial \mathbf{F}} : \delta_{\mathbf{u}} \mathbf{F} \, dV - \int_{\mathcal{B}_0} \hat{\mathbf{B}} \cdot \delta_{\mathbf{u}} \, dV - \int_{\Gamma_0^\sigma} \hat{\mathbf{T}} \cdot \delta_{\mathbf{u}} \, dA \\ &= - \int_{\mathcal{B}_0} (\text{Div } \mathbf{P} + \hat{\mathbf{B}}) \cdot \delta_{\mathbf{u}} \, dV + \int_{\Gamma_0^\sigma} (\mathbf{P} \mathbf{N} - \hat{\mathbf{T}}) \cdot \delta_{\mathbf{u}} \, dA = 0. \end{aligned} \quad (2.69)$$

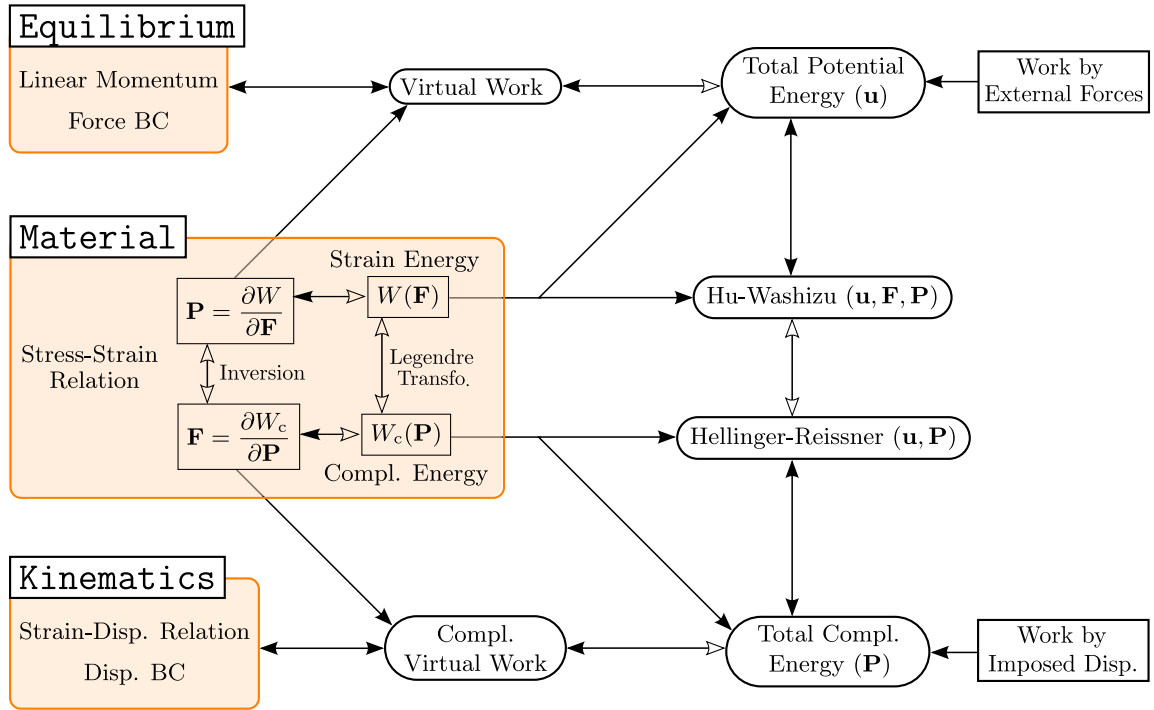


Figure 2.2: Illustration of interconnections of variational principles in the large strain theory of finite elastostatics. The figuration is inspired by Washizu 1975. Curved boxes represent variational principles. Non-filled arrows indicate directed relations, which are less common or not necessarily available.

Here, the application of the divergence theorem⁵

$$\int_{\mathcal{B}_0} \mathbf{P} : \text{Grad } \delta \mathbf{u} \, dV = - \int_{\mathcal{B}_0} \text{Div } \mathbf{P} \cdot \delta \mathbf{u} \, dV + \int_{\Gamma_0^c} \mathbf{P} \mathbf{N} \cdot \delta \mathbf{u} \, dA \quad (2.70)$$

provides the lower part of (2.69). An interpretation of $\delta \mathbf{u}$ as *virtual displacement* constitutes equivalence with the *principle of virtual work*. The terms in parenthesis in (2.69) show that the virtual work principle includes the weak form of the equilibrium equations in (2.64) and the force boundary conditions in (2.65). The internal virtual work contribution may also be expressed with other pairs of work-conjugated stress-strain measures as

$$\delta_{\mathbf{u}} \Pi_{\text{int}} = \int_{\mathcal{B}_0} \mathbf{S} : \delta_{\mathbf{u}} \mathbf{E} \, dV = \int_{\mathcal{B}_0} \mathbf{P} : \text{Grad } \delta \mathbf{u} \, dV = \int_{\mathcal{B}} \boldsymbol{\sigma} : \text{grad } \delta \mathbf{u} \, dv, \quad (2.71)$$

see Holzapfel 2010 for further details.

⁵Using chain rule as intermediate step: $\int_{\mathcal{B}_0} \mathbf{P} : \text{Grad } \delta \mathbf{u} \, dV = \int_{\mathcal{B}_0} (\text{Div } (\mathbf{P} \delta \mathbf{u}) - \text{Div } \mathbf{P} \cdot \delta \mathbf{u}) \, dV$.

Assumed is the existence of a unique inverse constitutive relation of (2.31), i.e.

$$\mathbf{F}(\mathbf{P}) = \frac{\partial W_c}{\partial \mathbf{P}}, \quad (2.72)$$

with complementary energy density $W_c(\mathbf{P})$, related to the strain energy via the Legendre transformation

$$W_c(\mathbf{P}) + W(\mathbf{F}) = \mathbf{F} : \mathbf{P}. \quad (2.73)$$

This furnishes the complementary potential energy functional

$$\Pi_c(\mathbf{P}) = \int_{\mathcal{B}_0} W_c(\mathbf{P}) \, dV - \int_{\Gamma_0^u} \mathbf{P}\mathbf{N} \cdot \hat{\mathbf{u}} \, dA, \quad (2.74)$$

with stress tensor \mathbf{P} as independent variable. The *principle of minimum complementary energy* states that equilibrium of the deformed body is met when, among all admissible stress fields that satisfy the equilibrium equations in the domain as well as the force boundary conditions, the actual stress field makes Π_c a minimum. This implies⁶

$$\begin{aligned} \delta_{\mathbf{P}} \Pi_c(\mathbf{P}) &= \int_{\mathcal{B}_0} \frac{\partial W_c(\mathbf{P})}{\partial \mathbf{P}} : \delta \mathbf{P} \, dV - \int_{\Gamma_0^u} \delta \mathbf{P}^T \mathbf{N} \cdot \hat{\mathbf{u}} \, dA \\ &= \int_{\mathcal{B}_0} (\mathbf{F}(\mathbf{P}) - \text{Grad } \mathbf{u}) : \delta \mathbf{P} \, dV + \int_{\Gamma_0^u} (\mathbf{u} - \hat{\mathbf{u}}) \cdot \delta \mathbf{P}\mathbf{N} \, dA = 0. \end{aligned} \quad (2.75)$$

An interpretation of $\delta \mathbf{P}$ as *virtual stress field* constitutes the equivalence with the *complementary virtual work principle*. The bracket terms show that it includes the kinematic equations (2.10) and the displacement boundary conditions in (2.65). In a similar manner, the IBVP can also be considered within a variational description.

2.4.3 Multi-Field Variational Principles

Based on the preceding single-field formulations, the method of Lagrangian multipliers can be used to include further governing equations in a variational weak form. The *three-field Hu-Washizu functional* (HW) has displacements as well as stresses and strains as independent variables. The starting point is a total potential energy expression like (2.68), but with an internal energy computed by the independent deformation gradient

⁶Using $\int_{\mathcal{B}_0} \text{Div}(\delta \mathbf{P}\mathbf{u}) \, dV = \underbrace{\int_{\mathcal{B}_0} \text{Div} \delta \mathbf{P} \cdot \mathbf{u} \, dV}_{=0} + \int_{\mathcal{B}_0} \delta \mathbf{P} : \text{Grad } \mathbf{u} \, dV = \int_{\Gamma_0^u} \delta \mathbf{P}\mathbf{N} \cdot \mathbf{u} \, dA$.

F. The Lagrangian multiplier \mathbf{P} can be used to incorporate the kinematic equation and the essential boundary conditions as

$$\begin{aligned} \Pi_{\text{HW}}(\mathbf{u}, \mathbf{P}, \mathbf{F}) &= \Pi_{\text{int}}(\mathbf{F}) + \Pi_{\text{ext}}(\mathbf{u}) \\ &+ \int_{\mathcal{B}_0} (\text{Grad } \mathbf{u} - \mathbf{F}) : \mathbf{P} \, dV - \int_{\Gamma_0^{\mathbf{u}}} (\mathbf{u} - \hat{\mathbf{u}}) \cdot \mathbf{P} \mathbf{N} \, dA. \end{aligned} \quad (2.76)$$

The principle of Hu-Washizu states that the actual solution is given by stationarity of (2.76), i.e. $\delta \Pi_{\text{HW}} = 0$. The *two-field Hellinger-Reissner functional* (HR) includes the displacements and stresses as independent variable. It can be interpreted as an extension of the preceding complementary energy functional via

$$\Pi_{\text{HR}}(\mathbf{u}, \mathbf{S}) = \Pi_{\text{c}}(\mathbf{S}) + \int_{\mathcal{B}_0} (\text{Div}(\mathbf{F}\mathbf{S}) + \hat{\mathbf{B}}) \cdot \mathbf{u} \, dV - \int_{\Gamma_0^{\sigma}} (\mathbf{F}\mathbf{S}\mathbf{N} - \hat{\mathbf{T}}) \cdot \mathbf{u} \, dA. \quad (2.77)$$

Here, in view of the next chapter, a total Lagrangian formulation is considered. This time the Lagrange multiplier \mathbf{u} is used to incorporate the equilibrium equations and the natural boundary conditions into the functional.

Remark 2.4.1. Within the small strain regime, the complementary energy principle as well as the Hellinger-Reissner principle are widely present in engineering applications. A classical example is the force method for statically indeterminate structures; see Argyris and Kelsey 1960 for an excellent overview, or the equilibrium finite element formulations in Moitinho de Almeida and Maunder 2017. However, for large strain regimes, the constitutive relation (2.72) is in general not unique (e.g., the same stress state can be found under various rotations) nor is it established that complementary strain energy functions are defined without referring to W , see the discussion in Section 6.2.2 in Ogden 1997. This is an enormous drawback in terms of generality for all principles in the lower half of Figure 2.2. However, it is pointed out that stress-strain relations other than \mathbf{P} - \mathbf{F} may be more suitable in this context. See for instance the discussion in Guo 1980 on Fraeijs de Veubeke's principle with independent \mathbf{P} and independent rotation tensor \mathbf{R} .

Chapter 3

A Family of Nonlinear Finite Element Formulations

The purpose of this chapter is twofold: first, the basic concept, notation and the fundamental mathematical properties of standard displacement-based finite elements are covered. Second, two concepts of mixed formulations are presented: various nonlinear variants of the enhanced assumed strain (EAS) formulations and assumed stress formulations. For a more detailed discussion on nonlinear finite elements, reference is made to the textbooks of Wriggers 2008 and Zienkiewicz et al. 2014.

3.1 Isoparametric Finite Element Procedure

The technical implementation of the finite element formulations herein relies on the isoparametric concept. It was proposed in the seminal work of Irons 1966 and constitutes a partition of the physical body \mathcal{B}_0 into a finite set of elements with subdomain Ω_e . Inside the elements, the geometry as well as the compatible displacement field are approximated by the same ansatz functions. This provides an approximation of the domain and the boundary as

$$\mathcal{B}_0 \approx \mathcal{B}_0^h = \bigcup_{e=1}^{n_e} \Omega_e, \quad \text{and} \quad \Gamma_0 \approx \Gamma_0^h = \bigcup_{e=1}^{n_e} \partial\Omega_e, \quad (3.1)$$

respectively. Here, superscript “h” is used to indicate the finite element approximation of the respective quantity, n_e denotes the number of elements and $\Omega_e \subset \mathcal{B}_0^h$ represents the element’s undeformed configuration. The global boundary element edges are identified with $\partial\Omega_e \subset \Gamma_0^h$ (not to be confused with the interface edges $\partial\Omega_i$). Plane quadrilateral Qp -elements are considered, with bilinear shape functions for $p = 1$ and biquadratic

shape functions for $p = 2$. The geometry approximation is given by

$$\mathbf{X} \approx \mathbf{X}^h = \bigcup_{e=1}^{n_e} \mathbf{X}_e \quad \text{and} \quad \mathbf{x} \approx \mathbf{x}^h = \bigcup_{e=1}^{n_e} \mathbf{x}_e, \quad (3.2)$$

with element approximations

$$\mathbf{X}_e = \sum_{A=1}^{n_{no}} N^A \mathbf{X}_e^A \quad \text{and} \quad \mathbf{x}_e = \sum_{A=1}^{n_{no}} N^A \mathbf{x}_e^A. \quad (3.3)$$

Here, n_{no} denotes the number of element nodes, $N^A(\xi, \eta)$ the Lagrangian shape function of node A and \mathbf{X}_e^A and \mathbf{x}_e^A the respective nodal position vectors. The natural element coordinates ξ and η are defined in the parent reference element $\Omega_{\text{par}} = [-1, 1]^2$. The mapping between the physical space and parameter space is given by the element Jacobians

$$\mathbf{J}_e = \frac{\partial \mathbf{X}_e}{\partial \boldsymbol{\xi}} \quad \text{and} \quad \mathbf{j}_e = \frac{\partial \mathbf{x}_e}{\partial \boldsymbol{\xi}}, \quad (3.4)$$

with $\boldsymbol{\xi} = [\xi \ \eta]^T$. This allows an elegant implementation of the material and spatial gradient

$$\text{Grad } N^A = \mathbf{J}_e^{-T} \frac{\partial N^A}{\partial \boldsymbol{\xi}} \quad \text{and} \quad \text{grad } N^A = \mathbf{j}_e^{-T} \frac{\partial N^A}{\partial \boldsymbol{\xi}}, \quad (3.5)$$

as well as the infinitesimal volume approximations (with out-of-plane unit thickness)

$$dV_e = \det \mathbf{J}_e d\xi d\eta \quad \text{and} \quad dv_e = \det \mathbf{j}_e d\xi d\eta. \quad (3.6)$$

An illustration of these transformations is given in Figure 3.1. For ease of readability the following notational specifications will be used in the subsequent finite element related sections:

- Indices e and h are mostly skipped and, if not otherwise stated, discretized quantities refer to one generic element: e.g., $\mathbf{d}_e = \mathbf{d}$ or $\mathbf{u}^h = \mathbf{u}$.
- Upper case letters used as superscripts refer to element nodes.
- Tensor and matrix notation are not distinguished and should become clear from the context.
- With few exceptions, numerical quadrature provides only an approximation. Nonetheless, it is symbolized by the integral operator: $\int_{\Omega_e} N(\boldsymbol{\xi}) dV \equiv \sum_{i=1}^{N_{\text{QP}}} N(\boldsymbol{\xi}_i) \omega_i dV$, with quadrature points $\boldsymbol{\xi}_i$ and weights ω_i (Appendix A.1.1).

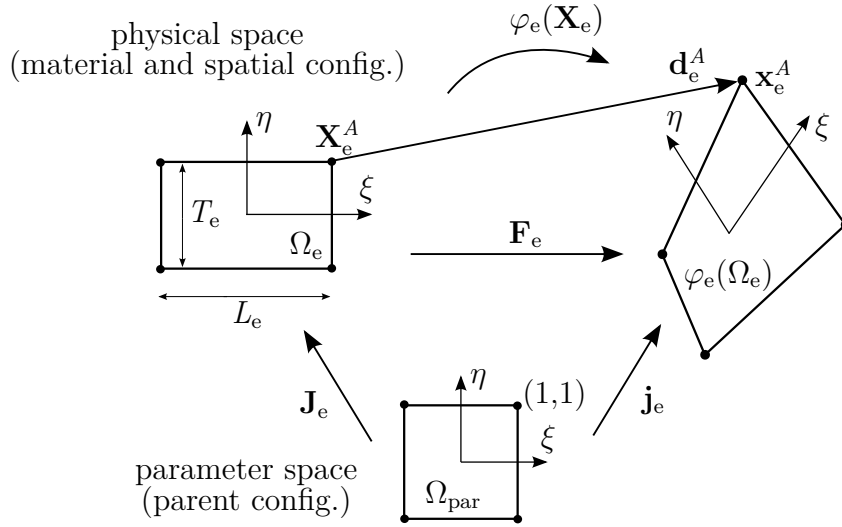


Figure 3.1: Element configurations within the isoparametric concept.

- Material derivatives are abbreviated as: $(\bullet)_{,I} := \frac{\partial(\bullet)}{\partial X_I}$.

Remark 3.1.1. In a fascinating manner, the development of the finite element method was shaped by *mathematical* and *engineering* contributions. In the first half of the 20th century, the works of Ritz, Galerkin and Courant are often associated with the first FEM related contributions. However, the conceptual idea of the FEM can also be found in much earlier works, such as the paper of Schellbach 1851. According to Clough 1990, the breakthrough in the engineering community was made in 1953 at the Boeing company, where access to the best computers was available. The need to model the increasing complexity of airplane structures yielded the idea that “deformations of any plane stress element be approximated by assuming a combination of simple strain fields” (Clough 1990, p. 93). These results were published in the seminal work of Turner et al. 1956. Due to Clough, the review of Argyris and Kelsey 1960 on matrix formulation of force and displacement methods is the “by far (...) most significant contribution”.

3.2 Displacement-Based Finite Elements

3.2.1 Discretization

This formulation – also denoted as *irreducible displacement method* – uses the compatible displacement field as primary variable. Within the element, the Bubnov-Galerkin

approximation of the actual, virtual and incremental displacement field is given by

$$\{\mathbf{u}, \delta\mathbf{u}, \Delta\mathbf{u}\} = \sum_{A=1}^{n_{no}} N^A \{\mathbf{d}^A, \delta\mathbf{d}^A, \Delta\mathbf{d}^A\}, \quad (3.7)$$

where $\{\mathbf{d}^A, \delta\mathbf{d}^A, \Delta\mathbf{d}^A\}$ is the respective nodal vector. The basis of a nonlinear finite element procedure is the incremental representation of weak form expression (2.69) in terms of the assembled element approximations (3.7). Linearization yields a system of n_{dof} equations

$$\delta\mathbf{D}^T (\mathbf{R} + \mathbf{K}\Delta\mathbf{D}) = \mathbf{0} \quad \forall \delta\mathbf{D} \quad \Rightarrow \quad \boxed{\mathbf{K}\Delta\mathbf{D} = -\mathbf{R}} \quad (3.8)$$

with global displacement vector

$$\{\mathbf{D}, \delta\mathbf{D}, \Delta\mathbf{D}\} = \mathbf{A} \{\mathbf{d}_e, \delta\mathbf{d}_e, \Delta\mathbf{d}_e\}, \quad (3.9)$$

and global stiffness matrix and residual vector

$$\mathbf{K} = \mathbf{A} \begin{matrix} n_e \\ \mathbf{A} \end{matrix} (\mathbf{k}_m + \mathbf{k}_g)_e \quad \text{and} \quad \mathbf{R} = \mathbf{A} \begin{matrix} n_e \\ \mathbf{A} \end{matrix} \mathbf{r}_e, \quad (3.10)$$

respectively. Here, the matrices and the vectors on element-level are denoted with lowercase symbols.

Finite element operators. The discretized counterparts of the strain measures presented in Section 2.1 are

$$\mathbf{H}^c = \text{Grad } \mathbf{u}, \quad \mathbf{F}^c = \mathbf{I} + \mathbf{H}^c \quad \text{and} \quad \mathbf{E}^c = \frac{1}{2} \left(\mathbf{H}^{cT} + \mathbf{H}^c + (\mathbf{H}^c)^T \mathbf{H}^c \right). \quad (3.11)$$

Here, superscript ‘‘c’’ refers to the fact that they are derived by the compatible displacement approximation (3.7) and helps later to distinguish between other strain interpolations. Using Voigt notation, the virtual and incremental Green-Lagrange strain approximations on element level read

$$\delta_{\mathbf{u}}\mathbf{E}^c = \sum_{A=1}^{n_{no}} \mathbf{B}^A \delta\mathbf{d}^A \quad \text{and} \quad \Delta_{\mathbf{u}}\mathbf{E}^c = \sum_{A=1}^{n_{no}} \mathbf{B}^A \Delta\mathbf{d}^A, \quad (3.12)$$

with nodal strain-displacement operator

$$\mathbf{B}^A = \frac{\partial\mathbf{E}^c}{\partial\mathbf{d}^A} = \begin{bmatrix} F_{11}^c N_{,1}^A & F_{21}^c N_{,1}^A \\ F_{12}^c N_{,2}^A & F_{22}^c N_{,2}^A \\ F_{12}^c N_{,1}^A + F_{11}^c N_{,2}^A & F_{21}^c N_{,2}^A + F_{22}^c N_{,1}^A \end{bmatrix}. \quad (3.13)$$

This operator can also be split into $\mathbf{B}^A = \mathbf{B}_{\text{lin}}^A + \mathbf{B}_{\text{nl}}^A$, where $\mathbf{B}_{\text{lin}}^A$ is the operator from linear theory and \mathbf{B}_{nl}^A the nonlinear remainder, i.e.

$$\mathbf{B}_{\text{lin}}^A = \begin{bmatrix} N_{,1}^A & N_{,1}^A \\ N_{,2}^A & N_{,2}^A \\ N_{,1}^A + N_{,2}^A & N_{,2}^A + N_{,1}^A \end{bmatrix} \quad \text{and} \quad \mathbf{B}_{\text{nl}}^A = \begin{bmatrix} H_{11}^c N_{,1}^A & H_{21}^c N_{,1}^A \\ H_{12}^c N_{,2}^A & H_{22}^c N_{,2}^A \\ H_{12}^c N_{,1}^A + H_{11}^c N_{,2}^A & H_{21}^c N_{,2}^A + H_{22}^c N_{,1}^A \end{bmatrix}. \quad (3.14)$$

Further introduced is the nodal strain-displacement operator

$$\mathbf{B}_{\text{H}}^A = \begin{bmatrix} N_{,1}^A & 0 \\ 0 & N_{,2}^A \\ N_{,2}^A & 0 \\ 0 & N_{,1}^A \end{bmatrix}, \quad (3.15)$$

associated with the displacement gradient $\begin{bmatrix} H_{11}^c & H_{22}^c & H_{12}^c & H_{21}^c \end{bmatrix}^T$ and providing

$$\delta_{\mathbf{u}} \mathbf{H}^c = \sum_{A=1}^{n_{\text{no}}} \mathbf{B}_{\text{H}}^A \delta \mathbf{d}^A \quad \text{and} \quad \Delta_{\mathbf{u}} \mathbf{H}^c = \sum_{A=1}^{n_{\text{no}}} \mathbf{B}_{\text{H}}^A \Delta \mathbf{d}^A. \quad (3.16)$$

Linearization of the virtual Green-Lagrange strain expression (3.12) double contracted with the second Piola-Kirchhoff stress yields

$$\Delta_{\mathbf{u}} \delta_{\mathbf{u}} \mathbf{E}^c : \mathbf{S} = \delta \mathbf{d}^T \left(\frac{\partial^2 \mathbf{E}^c}{\partial \mathbf{d} \partial \mathbf{d}} : \mathbf{S} \right) \Delta \mathbf{d} := \delta \mathbf{d}^T \mathbb{G}(\mathbf{E}^c, \mathbf{S}) \Delta \mathbf{d}. \quad (3.17)$$

Here, \mathbb{G} represents the integrand of the geometric element stiffness matrix, referred to as *geometric operator*. It depends only on the nonlinear part $\mathbf{E}_{\text{nl}} = \frac{1}{2} (\mathbf{H}^c)^T \mathbf{H}^c$ of the Green Lagrange strain and may be further specified as

$$\mathbb{G}((\mathbf{H}^c)^T \mathbf{H}^c, \mathbf{S}) = [G^{AB}] \quad \text{with} \quad G^{AB} = \frac{1}{2} \frac{\partial^2 H_{iI}^c H_{iJ}^c}{\partial d_j^A \partial d_k^B} S_{IJ} = N_{,I}^A N_{,J}^B S_{IJ} \delta_{jk}^AB \quad (3.18)$$

Here, lower indices i, j, \dots and I, J, \dots refer to the spatial and material coordinates, respectively.

Element stiffness matrix and residual vector. Substituting (3.7) and (3.12) into the weak form (2.71) yields $\delta \mathbf{d}^T \mathbf{r}$, with virtual element displacement vector $\delta \mathbf{d}$ and element residual vector

$$\mathbf{r} = \underbrace{\int_{\Omega} \mathbf{B}^T \mathbf{S} \, dV}_{\mathbf{f}_{\text{int}}} - \underbrace{\left(\int_{\Omega} \mathbf{N}^T \hat{\mathbf{B}} \, dV + \int_{\partial\Omega^{\sigma}} \mathbf{N}^T \hat{\mathbf{T}} \, dA \right)}_{\mathbf{f}_{\text{ext}}} - \underbrace{\int_{\partial\Omega_i} \mathbf{N}^T \mathbf{T}_i \, dA}_{\mathbf{f}_i} \quad (3.19)$$

Here, $\partial\Omega^{\sigma} \subset \Gamma$, $\partial\Omega_i$ represents the interelement edges and \mathbf{T}_i the interelement contact forces. The resulting force vector \mathbf{f}_i vanishes after assembly, i.e. $\sum_{e=1}^{n_e} \mathbf{f}_i^e = \mathbf{0}$. The nonlinear solution process is typically based on a Newton-Raphson scheme and requires a linearization (3.19). The increment of the virtual work $\delta \mathbf{d}^T \mathbf{r}$ reads $\delta \mathbf{d}^T (\mathbf{k}_m + \mathbf{k}_g) \Delta \mathbf{d}$, with material element stiffness matrix

$$\mathbf{k}_m = \int_{\Omega} \mathbf{B}^T \hat{\mathbf{C}} \mathbf{B} \, dV = \int_{\Omega} \mathbf{B}_H^T \hat{\mathbf{A}}_m \mathbf{B}_H \, dV \quad (3.20)$$

and geometric element stiffness matrix

$$\mathbf{k}_g = \int_{\Omega} \mathbb{G}(\mathbf{E}^c, \mathbf{S}) \, dV = \int_{\Omega} \mathbf{B}_H^T \hat{\mathbf{A}}_g \mathbf{B}_H \, dV. \quad (3.21)$$

Here, $\hat{\mathbf{A}}_m$ and $\hat{\mathbf{A}}_g$ represent the constitutive tensors (2.46) in Voigt notation.

3.2.2 Fundamental Mathematical Properties

The basic mathematical properties of displacement-based finite elements in the context of linear elasticity, i.e. linear elliptic BVPs, are summarized. These properties become particularly helpful in the assessment of finite element results. However, the transfer to nonlinear problems should be treated with caution and is only applicable to the corresponding incremental problem. For further engineering-oriented references, the reader is referred to the textbooks of Hughes 2012, Bathe 1996 and Babuska et al. 2011.

Approximation properties. A BVP with homogeneous Dirichlet and Neumann conditions on Γ_0 is considered. Introduced are the *inner product* and the *strain energy inner product*

$$(\hat{\mathbf{b}}, \delta \mathbf{u})_{L_2} = \int_{\tilde{\mathcal{B}}_0} \hat{\mathbf{b}} \cdot \delta \mathbf{u} \, dV \quad \text{and} \quad a(\mathbf{u}, \mathbf{u}) = \int_{\tilde{\mathcal{B}}_0} \text{Grad}^s \mathbf{u} : \mathbb{C}_{\text{lin}} : \text{Grad}^s \mathbf{u} \, dV, \quad (3.22)$$

respectively, both representing symmetric bilinear forms. Herein, unlike the notation from the previous section, \mathbf{u} represents the continuous solution and \mathbf{u}^h the finite element approximation. The weak form of the mathematical problem can be stated as: find the *exact solution* $\mathbf{u} \in \mathcal{U}$ such that

$$a(\mathbf{u}, \delta \mathbf{u}) = (\hat{\mathbf{b}}, \delta \mathbf{u})_{L_2} \quad \forall \delta \mathbf{u} \in \mathcal{U}, \quad (3.23)$$

with

$$\mathcal{U} = \left\{ \mathcal{H}^1(\Omega); \mathbf{u} = \mathbf{0} \text{ on } \Gamma^u \right\} \quad (3.24)$$

and \mathcal{H}^s being the Sobolev space defined in Appendix A.1.2. The finite-dimensional approximation to \mathcal{U} is given by $\mathcal{U}^h \subset \mathcal{U}$ and furnishes the discrete problem: Find the finite element solution $\mathbf{u}^h \in \mathcal{U}^h$ such that

$$a(\mathbf{u}^h, \delta \mathbf{u}^h) = (\hat{\mathbf{b}}, \delta \mathbf{u}^h)_{L_2} \quad \forall \delta \mathbf{u}^h \in \mathcal{U}^h. \quad (3.25)$$

For a sequence of uniformly refined spaces \mathcal{U}^h (until theoretically $\mathcal{U}^h = \mathcal{U}$), the standard finite element method yields

$$\|\mathbf{u} - \mathbf{u}^h\|_{\mathcal{H}^1} \rightarrow 0 \quad \text{for } \bar{h} \rightarrow 0, \quad (3.26)$$

where \bar{h} is a characteristic element size measure. Monotonic convergence of the form (3.26) is ensured by *compatibility* and *completeness* of the element ansatz. Compatibility requires the displacement ansatz (3.7) to be at least C^0 -continuous across the element boundaries (no gaps between adjacent elements). The correct representation of constant strain modes (including rigid body displacements) is meant by the completeness requirement.

The error in the finite element approximation $\mathbf{e} = \mathbf{u} - \mathbf{u}^h$ gives rise to the following statements:

(i) *Galerkin error orthogonality:*

$$\boxed{a(\mathbf{e}, \delta \mathbf{u}^h) = 0 \quad \forall \delta \mathbf{u}^h \in \mathcal{U}^h} \quad (3.27)$$

The error is orthogonal to \mathcal{U}^h , i.e. \mathbf{u}^h is the projection of the exact solution onto \mathcal{U}^h .

(ii) *Best approximation property:*

$$\boxed{a(\mathbf{e}, \mathbf{e}) \leq a(\mathbf{u} - \mathbf{w}^h, \mathbf{u} - \mathbf{w}^h) \quad \forall \mathbf{w}^h \in \mathcal{U}^h} \quad (3.28)$$

From all possible solutions \mathbf{w}^h in \mathcal{U}^h , \mathbf{u}^h is the one which approximates \mathbf{u} best. Here, “best” refers to the energy norm, i.e. the best approximation of the first derivative (strain and stress) in a weighted least-squares sense.

(iii) “Underestimation” of the exact solution:

$$\boxed{a(\mathbf{u}_h, \mathbf{u}_h) \leq a(\mathbf{u}, \mathbf{u})} \quad (3.29)$$

The strain energy of the finite element solution always underestimates the exact strain energy. Consequently the (finite) discrete structure performs stiffer and displacements are underestimated.

Remark 3.2.1. For stress driven “equilibrium” finite elements based on complementary energy principles (see Section (2.4.2)) with a direct approximation of stress fields, Statement (iii) is just the opposite. The strain energy is larger than the exact value, the corresponding displacement solution is overestimated and the discrete structure performs softer. The established error bounds become particularly useful in the context of a dual error analysis. See the textbook of Moitinho de Almeida and Maunder 2017.

A priori error estimates. Considered is a variational problem with highest order of derivative m and a smooth (exact) solution $\mathbf{u} \in \mathcal{H}^{p+1}$. Furthermore a (p, m) -regular mesh¹ is assumed. The *standard error estimate* for elliptic BVP’s is given as

$$\hat{C}_2 \|\mathbf{e}\|_{\mathbb{E}} \leq \|\mathbf{e}\|_{\mathcal{H}^m} \leq \hat{C} \bar{h}^{p+1-m} \|\mathbf{u}\|_{\mathcal{H}^{p+1}}. \quad (3.30)$$

Here, \hat{C}_2 is a constant and \hat{C} is a constant that is *independent* of \bar{h} but dependent on the material properties, the finite element mesh and the exact solution \mathbf{u} . Estimate (3.30) is a direct consequence of the the best approximation property (3.28). The result holds, since the Sobolev norm of order m is equivalent to the energy norm $\|\mathbf{e}\|_{\mathbb{E}}$. Using $C = \hat{C} \|\mathbf{u}\|_{\mathcal{H}^{p+1}}$, the natural logarithm of the right hand side of (3.30) yields

$$\ln(C \bar{h}^\beta) = \beta \ln \bar{h} + \ln C \approx -\beta \ln \sqrt{n_{\text{no}}} + \ln C. \quad (3.31)$$

Here, the last term holds for uniform two-dimensional meshes and is used typically for convergence plots. For further details and references it is referred to Babuska et al. 2011. For linear elasticity $m = 1$, it can be shown that displacement and first derivative quantities follow

$$\begin{aligned} \|\mathbf{u} - \mathbf{u}^h\|_{L_2} &\leq C \bar{h}^{p+1}, \\ \|\text{Grad } \mathbf{u} - \text{Grad } \mathbf{u}^h\|_{L_2} &\leq \|\mathbf{u} - \mathbf{u}^h\|_{\mathcal{H}^1} \leq C \bar{h}^p. \end{aligned} \quad (3.32)$$

¹A mesh where the aspect ratio of all elements remains sufficiently uniform $\mathcal{U}^h \in \mathcal{H}^m$.

Details on that can be found in Hughes 2012 (p. 190). In other words, the L_2 -norm of the displacement error is $p + 1$, whereas the L_2 -norm of the displacement gradient quantities (e.g., strain, stress, or energy) is p . The latter is true because derivatives dominate the \mathcal{H}^1 -norm of the error. However, these are optimal estimates that depend on the nature of the solution \mathbf{u} as well as the material properties via constant \hat{C} . This latter gives rise to the volumetric locking phenomenon; see for instance Suri 1996.

3.3 Enhanced Assumed Strain Finite Elements

3.3.1 A Lagrangian Formulation (Qp/Em)

The simplest type of nonlinear EAS formulation is based on an additive enhancement of the compatible Green-Lagrange strain expression (3.11)₃ of the form

$$\boxed{\mathbf{E}(\mathbf{d}, \boldsymbol{\alpha}) = \mathbf{E}^c(\mathbf{d}) + \tilde{\mathbf{E}}(\boldsymbol{\alpha})} \quad (3.33)$$

where $\tilde{\mathbf{E}}$ is the strain enhancement which depends linear on m enhanced mode degrees of freedom which are collected in the vector $\boldsymbol{\alpha}$. The enhanced strain expression then provides

$$\mathbf{S}_E := \frac{\partial W(\mathbf{E})}{\partial \mathbf{E}} \quad \text{and} \quad \mathbb{C}_E := \frac{\partial^2 W(\mathbf{E})}{\partial \mathbf{E} \partial \mathbf{E}}. \quad (3.34)$$

This formulation is closely related to the original work of Simo and Rifai 1990 and is especially popular for the membrane part of shell elements; see references Betsch et al. 1996 and Bischoff and Ramm 1997. For three-dimensional brick elements it is referred to the work of Klinkel and Wagner 1997. The reason for its simplicity is twofold: first, the Green-Lagrange strain is a total Lagrangian-type tensor and consequently objectivity is ensured a priori. Second, since (3.33) depends linearly on $\boldsymbol{\alpha}$, its linearization is trivial and close to the geometrically linear framework.

A variationally sound basis was provided by Simo and Rifai 1990. Inserting (3.33) and (3.7) into the total Lagrangian version of the three-field Hu-Washizu functional (2.76) yields

$$\Pi_{\text{HW}}(\mathbf{d}, \boldsymbol{\alpha}, \mathbf{S}) = \int_{\tilde{B}_0} \left(W(\mathbf{E}^c + \tilde{\mathbf{E}}) - \underline{\mathbf{S}} : \tilde{\mathbf{E}} - \hat{\mathbf{B}} \cdot \mathbf{u} \right) dV + \text{BT}. \quad (3.35)$$

Applying the Hu-Washizu principle $\delta\Pi_{\text{HW}} = 0$ provides the global and local Euler equations

$$\int_{\tilde{\mathcal{B}}_0} \left(\frac{\partial W(\mathbf{E})}{\partial \mathbf{E}} : \delta_{\mathbf{u}} \mathbf{E} - \hat{\mathbf{B}} \cdot \delta \mathbf{u} \right) dV = 0 \quad \Rightarrow \text{Div}(\mathbf{F}^c \mathbf{S}_E) + \hat{\mathbf{B}} = \mathbf{0}, \quad (3.36a)$$

$$- \int_{\tilde{\mathcal{B}}_0} \tilde{\mathbf{E}} : \delta \mathbf{S} dV = 0 \quad \Rightarrow \tilde{\mathbf{E}} = \mathbf{0}, \quad (3.36b)$$

$$\int_{\tilde{\mathcal{B}}_0} \left(\frac{\partial W(\mathbf{E})}{\partial \mathbf{E}} - \mathbf{S} \right) : \delta \tilde{\mathbf{E}} dV = 0 \quad \Rightarrow \mathbf{S}_E = \mathbf{S}. \quad (3.36c)$$

The weak form does not contain derivatives on the enhanced strain field and the independent stress field and, consequently, they do not have to be continuous. In fact, they will be defined as discontinuous across element boundaries. The specific design feature of EAS elements is based on the enforcement of L_2 -orthogonality between the discrete stresses and the enhanced strain interpolation. Exploiting this orthogonality removes the underlined term in (3.35) and consequently the weak form expressions

$$\int_{\Omega} \tilde{\mathbf{E}} : \delta \mathbf{S} dV = 0 \quad \text{and} \quad \int_{\Omega} \mathbf{S} : \delta \tilde{\mathbf{E}} dV = 0 \quad (3.37)$$

vanish. The Euler equation in (3.36a) reveals an obvious kinematic ambiguity. While the Lagrangian stress tensor \mathbf{S}_E is based on the enhanced Green-Lagrange strain, its two-point analogue emanates from a transformation with (only) the compatible deformation gradient, i.e. $\mathbf{P}_E = \mathbf{F}^c \mathbf{S}_E$. This questions the consistency of the formulations with respect to transformations into the spatial setting or two-point setting. Another issue is consistency of stress recovery since the independent stress field is eliminated on theory level. As shown by Bischoff et al. 1999 for the linear case, stress recovery can be accomplished by exploiting the equivalence to assumed stress formulations, see also Klinkel and Wagner 1997 for geometrically nonlinear problems (restricted to the SVK material). However, this issue is not further discussed herein and stresses are recovered via (3.34)₁ in this work.

Discretization. The enhanced strain interpolation is constructed as

$$\tilde{\mathbf{E}} = \frac{\det \mathbf{J}_0}{\det \mathbf{J}} \mathbf{J}_0^{-T} \tilde{\mathbf{E}}^{\text{par}} \mathbf{J}_0^{-1}, \quad (3.38)$$

where $\tilde{\mathbf{E}}^{\text{par}}$ is defined in the parent element configuration. In Voigt notation it is expressed as

$$\tilde{\mathbf{E}} = \frac{\det \mathbf{J}_0}{\det \mathbf{J}} \mathbf{T}_0^{-T} \mathbf{M}_E^{\text{par}} \boldsymbol{\alpha} = \mathbf{M}_E \boldsymbol{\alpha} \quad \text{with} \quad \int_{\Omega} \mathbf{M}_E \, dV = \mathbf{0}. \quad (3.39)$$

Here, similar to \mathbf{B} , \mathbf{M}_E is the respective enhanced strain operator in Voigt notation. Here, \mathbf{T}_0 resembles the transformation in (3.38) in matrix form, see Equation (4.1) in Andelfinger and Ramm 1993. Both, the manipulation with the element Jacobian in Equation (3.38) as well as the vanishing integral in (3.39) are fundamental requirements for passing the patch test. Furthermore, the space of the enhanced strain interpolation has to be independent of the compatible strain approximation. For further details it is referred to Section 2.2 in Simo and Rifai 1990.

Linearization of (3.36) provides, for arbitrary $\delta \mathbf{d}$ and $\delta \boldsymbol{\alpha}$, the discrete set of element equations

$$\begin{bmatrix} \mathbf{k}_m + \mathbf{k}_g & \mathbf{L} \\ \mathbf{L}^T & \mathbf{D} \end{bmatrix} \begin{bmatrix} \Delta \mathbf{d} \\ \Delta \boldsymbol{\alpha} \end{bmatrix} = - \begin{bmatrix} \mathbf{r} \\ \tilde{\mathbf{r}} \end{bmatrix}, \quad (3.40)$$

where \mathbf{r} and $\mathbf{k}_m + \mathbf{k}_g$ are computed using (3.34). The EAS residual vector reads

$$\tilde{\mathbf{r}} = \int_{\Omega} \mathbf{M}_E^T \mathbf{S}_E \, dV \quad (3.41)$$

and the material EAS tangents are

$$\mathbf{L} = \int_{\Omega} \mathbf{B}^T \hat{\mathbf{C}}_E \mathbf{M}_E \, dV \quad \text{and} \quad \mathbf{D} = \int_{\Omega} \mathbf{M}_E \hat{\mathbf{C}}_E \mathbf{M}_E \, dV. \quad (3.42)$$

The enhanced strain parameters can be eliminated on element level via static condensation

$$\underbrace{(\mathbf{k}_m + \mathbf{k}_g - \mathbf{L} \mathbf{D}^{-1} \mathbf{L}^T)}_{\mathbf{k}_{\text{red}}} \Delta \mathbf{d} = - \underbrace{(\mathbf{r} - \mathbf{L} \mathbf{D}^{-1} \tilde{\mathbf{r}})}_{\mathbf{r}_{\text{red}}}, \quad (3.43)$$

with \mathbf{k}_{red} and \mathbf{r}_{red} being the reduced element stiffness matrix and element residual vector. For details on efficient update procedures within the Newton-Raphson scheme it is referred to Klinkel and Wagner 1997.

Q1/E4, Q1/E2n and Q1/E2s. A popular formulation for plane solid elements is the Q1/E4 element. It is defined by the enhancement

$$\tilde{\mathbf{E}}^{\text{par}} = \begin{bmatrix} \xi\alpha_1 & \xi\alpha_3 + \eta\alpha_4 \\ \xi\alpha_3 + \eta\alpha_4 & \eta\alpha_2 \end{bmatrix}. \quad (3.44)$$

Provided that the element is *undistorted* (rectangular shaped) and subjected to *homogeneous deformations*, parameter α_1 and α_2 remove volumetric locking and α_3 and α_4 remove shear locking. The element formulations that only handle one of the two locking issues are denoted as Q1/E2n (using only α_1 and α_2) and Q1/E2s (using only α_3 and α_4).

Q2/E11. Another element that will be considered in the subsequent analysis is the Q2/E11 element proposed by Bischoff and Ramm 1997. It is designed to remove “higher-order” volumetric locking and shear locking, present in the displacement-based nine-noded Q2. The strain enhancement reads

$$\begin{aligned} \tilde{E}_{11}^{\text{par}} &= \alpha_1(1 - 3\xi^2) + \alpha_2(\eta - 3\xi^2\eta) + \alpha_3(\eta^2 - 3\xi^2\eta^2) \\ \tilde{E}_{22}^{\text{par}} &= \alpha_4(1 - 3\eta^2) + \alpha_5(\xi - 3\xi\eta^2) + \alpha_6(\xi^2 - 3\xi^2\eta^2) \\ \tilde{E}_{12}^{\text{par}} &= \alpha_7(1 - 3\xi^2) + \alpha_8(1 - 3\eta^2) + \alpha_9(\eta - 3\xi^2\eta) \\ &\quad + \alpha_{10}(\xi - 3\xi\eta^2) + \alpha_{11}(1 - 3(\xi^2 + \eta^2) + 9\xi^2\eta^2). \end{aligned} \quad (3.45)$$

3.3.2 Two-Point Formulations (Q1/Hm) and (Q1/HTm)

This nonlinear EAS formulation is based on an additive enhancement of the compatible displacement gradient (3.11)₁ of the form

$$\boxed{\mathbf{H}(\mathbf{d}, \boldsymbol{\alpha}) = \mathbf{H}^c(\mathbf{d}) + \tilde{\mathbf{H}}(\mathbf{d}, \boldsymbol{\alpha})} \quad (3.46)$$

and provides via $\mathbf{F} = \mathbf{I} + \mathbf{H}$

$$\mathbf{P}_{\mathbf{H}} := \frac{\partial W(\mathbf{F})}{\partial \mathbf{F}} \quad \text{and} \quad \mathbb{A}_{\mathbf{H}} := \frac{\partial^2 W(\mathbf{F})}{\partial \mathbf{F} \partial \mathbf{F}}. \quad (3.47)$$

This enhancement, often referred to as a “fully nonlinear” EAS formulation, was first proposed by Simo and Armero 1992. Important further developments regarding element

stability and frame invariance can be found in Simo et al. 1993, Glaser and Armero 1997 and Pfeifferkorn and Betsch 2019. Inserting (3.46) and (3.7) into the the three-field Hu-Washizu functional (2.76) yields

$$\Pi_{\text{HW}}(\mathbf{d}, \boldsymbol{\alpha}, \mathbf{P}) = \int_{\tilde{\mathcal{B}}_0} \left(W(\mathbf{F}^c + \tilde{\mathbf{H}}) - \underline{\mathbf{P}} : \tilde{\mathbf{H}} - \hat{\mathbf{B}} \cdot \mathbf{u} \right) dV + \text{BT}. \quad (3.48)$$

The stationary condition $\delta\Pi_{\text{HW}} = 0$ provides the global and local Euler equations

$$\int_{\tilde{\mathcal{B}}_0} \left(\frac{\partial W(\mathbf{F})}{\partial \mathbf{F}} : \delta_{\mathbf{u}} \mathbf{F} - \hat{\mathbf{B}} \cdot \delta \mathbf{u} \right) dV = 0 \quad \Rightarrow \text{Div}(\mathbf{P}_{\text{H}}) + \hat{\mathbf{B}} = \mathbf{0}, \quad (3.49a)$$

$$- \int_{\tilde{\mathcal{B}}_0} \tilde{\mathbf{H}} : \delta \mathbf{P} dV = 0 \quad \Rightarrow \tilde{\mathbf{H}} = \mathbf{0}, \quad (3.49b)$$

$$\int_{\tilde{\mathcal{B}}_0} \left(\frac{\partial W(\mathbf{F})}{\partial \mathbf{F}} - \mathbf{P} \right) : \delta \tilde{\mathbf{H}} dV = 0 \quad \Rightarrow \mathbf{P}_{\text{H}} = \mathbf{P}. \quad (3.49c)$$

As before, L_2 -orthogonality between the enhanced strain and stress interpolation removes the underlined term in (3.48) and consequently

$$\int_{\Omega} \tilde{\mathbf{H}} : \delta \mathbf{P} dV = 0 \quad \text{and} \quad \int_{\Omega} \mathbf{P} : \delta \tilde{\mathbf{H}} dV = 0. \quad (3.50)$$

In contrast to the total Lagrangian formulation, the present formulation allows to recast the enhanced strain in other geometric settings. Based on (3.46), the resulting Green-Lagrange strain may be expressed as

$$\mathbf{E}_{\text{H}}(\mathbf{d}, \boldsymbol{\alpha}) = \mathbf{E}^c + \frac{1}{2} \left(\tilde{\mathbf{H}}^{\text{T}} + \tilde{\mathbf{H}} + \tilde{\mathbf{H}}^{\text{T}} \tilde{\mathbf{H}} + (\mathbf{H}^c)^{\text{T}} \tilde{\mathbf{H}} + \mathbf{H}^c \tilde{\mathbf{H}}^{\text{T}} \right). \quad (3.51)$$

The total Lagrangian stress tensor and constitutive tangent read

$$\mathbf{S}_{\text{H}} := \frac{\partial W(\mathbf{E}_{\text{H}})}{\partial \mathbf{E}_{\text{H}}} = \mathbf{F}^{-1} \mathbf{P}_{\text{H}} \quad \text{and} \quad \mathbb{C}_{\text{H}} := \frac{\partial^2 W(\mathbf{E}_{\text{H}})}{\partial \mathbf{E}_{\text{H}} \partial \mathbf{E}_{\text{H}}}. \quad (3.52)$$

Discretization of Q1/H4. The enhanced strain interpolation of this element reads

$$\tilde{\mathbf{H}}(\boldsymbol{\alpha}) = \frac{\det \mathbf{J}_0}{\det \mathbf{J}} \mathbf{J}_0^{-\text{T}} \tilde{\mathbf{H}}^{\text{par}} \mathbf{J}_0^{-1}, \quad (3.53)$$

with

$$\tilde{\mathbf{H}}^{\text{par}} = \begin{bmatrix} \xi \alpha_1 & \eta \alpha_3 \\ \xi \alpha_4 & \eta \alpha_2 \end{bmatrix}. \quad (3.54)$$

This enhancement allows an interpretation as a nonlinear version of the incompatible mode element by Wilson et al. 1973. The corresponding EAS element operators are defined as

$$\mathbf{M}_H = \frac{\partial \mathbf{E}_H}{\partial \boldsymbol{\alpha}}, \quad \mathbb{G}^{\text{d}\alpha} = \frac{\partial^2 \text{sym}(H_{iI}^c \tilde{H}_{iJ})}{\partial d_k^B \partial \alpha_C} S_{H|IJ}, \quad \mathbb{G}^{\alpha\alpha} = \frac{\partial^2 \frac{1}{2}(\tilde{H}_{iI} \tilde{H}_{iJ})}{\partial \alpha_C \partial \alpha_D} S_{H|IJ}, \quad (3.55)$$

where $(C, D) = 1, \dots, m$ refers to the enhanced parameters. This provides the EAS tangents

$$\mathbf{L} = \underbrace{\int_{\Omega} \mathbf{B}^T \hat{\mathbf{C}}_H \mathbf{M}_H \, dV}_{\mathbf{L}_m} + \underbrace{\int_{\Omega} \mathbb{G}^{\text{d}\alpha}(\mathbf{E}_H, \mathbf{S}_H) \, dV}_{\mathbf{L}_g} \quad (3.56)$$

and

$$\mathbf{D} = \underbrace{\int_{\Omega} \mathbf{M}_H^T \hat{\mathbf{C}}_H \mathbf{M}_H \, dV}_{\mathbf{D}_m} + \underbrace{\int_{\Omega} \mathbb{G}^{\alpha\alpha}(\mathbf{E}_H, \mathbf{S}_H) \, dV}_{\mathbf{D}_g}. \quad (3.57)$$

Unlike for Qp/Em , EAS-related geometric contributions occur.

Discretization of Q1/HT4. An alternative enhancement is given by the following simple modification

$$\mathbf{H} = \mathbf{I} + \mathbf{H}^c + \mathbf{F}_0^c \tilde{\mathbf{H}}^T. \quad (3.58)$$

Here, $\tilde{\mathbf{H}}(\boldsymbol{\alpha})$ is defined in (3.53) and $\mathbf{F}_0^c(\mathbf{d})$ denotes the compatible deformation gradient at the element centroid. This enhancement was proposed by Glaser and Armero 1997 and the corresponding element is denoted as Q1/HT4. As shown by Bieber et al. 2022, the transposition has a beneficial effect on the geometric stiffness matrix such that artificial instabilities for compression problems are fully removed, see Section 6.2.3 for further details. The strain enhancement can not be interpreted by the incompatible mode ansatz, which is why the modification with \mathbf{F}_0^c is a prerequisite for frame-invariance. Detailed derivations and an overview of alternative transformations are given in the review article by Pfefferkorn and Betsch 2019.

3.4 Assumed Stress Element (Q1/S5)

This type of element can be derived on the basis of the two-field Hellinger-Reissner functional (2.77). Considered is the stress interpolation proposed by Pian and Sumihara 1984

$$\mathbf{S} = \mathbf{J}_0^T \mathbf{S}^{\text{par}} \mathbf{J}_0, \quad (3.59)$$

with

$$\tilde{\mathbf{S}}^{\text{par}} = \begin{bmatrix} \beta_1 + \eta\beta_4 & \beta_3 \\ \beta_3 & \beta_2 + \xi\beta_5 \end{bmatrix}. \quad (3.60)$$

In Voigt notation it is expressed as

$$\mathbf{S} = \mathbf{T}_0 \mathbf{Q}^{\text{par}} \boldsymbol{\beta} = \mathbf{Q} \boldsymbol{\beta}. \quad (3.61)$$

The independent stress field provides

$$\mathbf{E}_S := \frac{\partial W_c(\mathbf{S})}{\partial \mathbf{S}} \quad \text{and} \quad \mathbb{D}_S := \frac{\partial^2 W_c(\mathbf{S})}{\partial \mathbf{S} \partial \mathbf{S}}. \quad (3.62)$$

Inserting (3.61) and (3.7) into the weak form of (2.77) provides the global and local Euler equations

$$\int_{\mathcal{B}_0} (\mathbf{S} : \delta_{\mathbf{u}} \mathbf{E}^c - \hat{\mathbf{B}} \cdot \delta \mathbf{u}) \, dV = 0 \quad \Rightarrow \text{Div}(\mathbf{F}^c \mathbf{S}) + \hat{\mathbf{B}} = \mathbf{0}, \quad (3.63a)$$

$$\int_{\mathcal{B}_0} (\mathbf{E}^c - \mathbf{E}_S) : \delta \mathbf{S} \, dV = 0 \quad \Rightarrow \mathbf{E}^c = \mathbf{E}_S, \quad (3.63b)$$

Linearization of (3.63) provides, for arbitrary $\delta \mathbf{d}$ and $\delta \boldsymbol{\beta}$, the discrete set of element equations

$$\begin{bmatrix} \mathbf{k}_g & \mathbf{G} \\ \mathbf{G}^T & \mathbf{V} \end{bmatrix} \begin{bmatrix} \Delta \mathbf{d} \\ \Delta \boldsymbol{\beta} \end{bmatrix} = - \begin{bmatrix} \mathbf{r} \\ \mathbf{r}_{\text{kin}} \end{bmatrix}, \quad (3.64)$$

where \mathbf{r} and \mathbf{k}_g are computed on the basis of (3.59). The kinematic element residual vector reads

$$\mathbf{r}_{\text{kin}} = \int_{\Omega} \mathbf{Q}^T (\mathbf{E}^c - \mathbf{E}_S) \, dV, \quad (3.65)$$

and tangents are

$$\mathbf{G} = \int_{\Omega} \mathbf{B}^T \mathbf{Q} \, dV \quad \text{and} \quad \mathbf{V} = \int_{\Omega} \mathbf{Q}^T \hat{\mathbf{D}}_S \mathbf{Q} \, dV. \quad (3.66)$$

Q1/S5 based on SVK. For the SVK case the element designer is fortunate. From the corresponding strain energy function (2.53) it follows

$$W_c(\mathbf{S}) = \frac{\Lambda}{4\mu(3\Lambda + 2\mu)} (\text{tr } \mathbf{S})^2 + \frac{1}{4\mu} \text{tr } \mathbf{S}^2 = \frac{1}{2} \mathbf{S}^T \hat{\mathbf{C}}^{-1} \mathbf{S} \quad (3.67)$$

providing

$$\mathbf{S}_S = \hat{\mathbf{C}}^{-1} \mathbf{S} \quad \text{and} \quad \hat{\mathbf{D}}_S = \hat{\mathbf{C}}^{-1} \quad (3.68)$$

Here $\hat{\mathbf{C}}$ is defined in (2.55), see also Gao and Hajilarov 2017 for a mathematical background.

Q1/S5 based on NH. Following Wriggers 2008, a finite element formulation can be derived directly on the basis of the weak-form expression (3.63b). By that, one can circumvent the need for a complementary strain energy function by using the inverse of the stress-strain relation. For the Neo-Hookean material based on the volumetric strain energy in (2.58) an explicit inversion of the stress-relation is given in Appendix 2 in Pfefferkorn et al. 2021.² The constitutive tensor is obtained via

$$\mathbb{C}(\mathbf{E}_S) = \frac{\partial^2 W(\mathbf{E}_S)}{\partial \mathbf{E}_S \partial \mathbf{E}_S} \quad \Rightarrow \quad \hat{\mathbf{D}}_S = \hat{\mathbf{C}}_S^{-1}. \quad (3.69)$$

²See also Wriggers 2008 for a Neo-Hookean material based on the volumetric part of Equation (2.59). An algorithmic treatment of the inversion is also given in Viebahn et al. 2019. However, both have the same limitations as discussed in Section 2.2.

Chapter 4

Analytical Solutions for Some Classical Problems in Finite Elasticity

The purpose of this chapter is to present some of the rare problems in finite elasticity for which analytical solutions are available. For the remainder of this work, these solutions serve as a basis for the analysis and development of advanced nonlinear finite elements. The pioneering works originate mainly from the 50s and 60s where the lack of numerical simulation methods promoted the development of analytical solutions. These examples are nowadays well established (in the respective scientific community) and found their way into standard textbooks, such as Ogden 1997 or Bigoni 2012. In this sense, the subsequent derivations of analytical solutions do not claim novelty but rather keep the problem descriptions within this work as self-contained as possible.

4.1 Bifurcations in Plane Strain Tension and Compression

Euler's celebrated "Elastica" provided the first sound analysis of axially loaded thin structural members. His formulae became an essential tool in structural engineers' everyday lives. While Euler's focus lied on the axial compression case, the pioneering work of Considère 1885 dealt with the necking instabilities of columns under tension¹. Both, however, restricted their analysis to one-dimensional problems.

The first successful attempt to consider a more general large strain continuum case, namely two-dimensional plane strain bodies, can be traced back to Biot 1963a and his monograph Biot 1965. Based on that, a more general analysis of incompressible solids is presented in the work of Hill and Hutchinson 1975 and Young 1976, which focus on

¹This is, compared to Euler's buckling cases, less intuitive and the interested reader is referred to the recent contribution by Audoly and Hutchinson 2016.

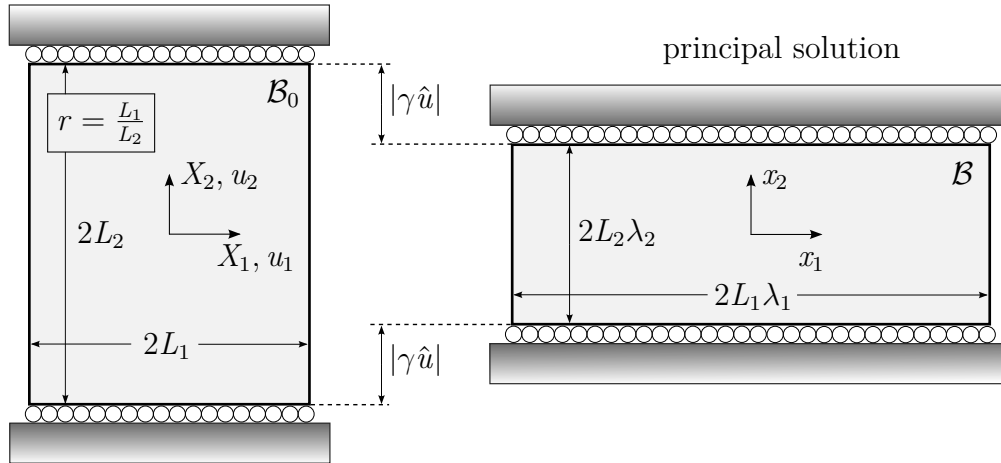


Figure 4.1: Bifurcation problem; deformation exemplified for a compression test.

uniaxial tension and compression, respectively. Both references provide an asymptotic analysis for slender blocks and thus a link of the general approach to the known structural approximations. It is also worth noting the extensions to elasto-plastic solids by Needleman 1979, as well as the analysis of surface instabilities of compressible solids in Bardet 1990a and Bardet 1990b. To the best of the author's knowledge, the latter reference is the only one where analytical solutions are compared with finite element results for that specific problem. For a general overview it is referred to Chapter 6.3 of Ogden 1997.

It is pointed out that the above-mentioned references leave out a post-bifurcation analysis. An important case that bears great difficulties in the analytical treatment. However, Triantafyllidis et al. 2007 discusses aspects of post-bifurcation behavior via a Lyapunov-Schmidt-Koiter expansion. The notation of this paper is adopted subsequently.

4.1.1 Problem Setup and Principal Solution

The stress-free reference configuration \mathcal{B}_0 consists of an isotropic compressible elastic $2L_1 \times 2L_2$ block under plane strain conditions, see Figure 4.1. Here, L_I are aligned to the Cartesian reference coordinates X_I and define the block's aspect ratio as $r = L_1/L_2$. The deformation is controlled at the top and bottom edges, at $X_2 = \pm L_2$, by a uniformly vertically displaced roller support (no shear is transmitted), whereas the lateral edges, at $X_1 = \pm L_1$, remain traction-free. The corresponding essential and natural boundary conditions read

$$u_2(X_1, \pm L_2) = \pm \gamma \hat{u}, \quad u_1(0,0) = 0 \quad (4.1)$$

and

$$P_{11}(\pm L_1, X_2) = 0, \quad P_{21}(\pm L_1, X_2) = 0, \quad P_{12}(X_1, \pm L_2) = 0. \quad (4.2)$$

Here, $\gamma \in \mathbb{R}_0^+$ is the load factor, $u_i(X_1, X_2)$ is the respective displacement component and P_{ij} denotes the first Piola-Kirchhoff stress. The second part of (4.1) is imposed for definiteness. With these boundary conditions at hand, the solution of the displacement-controlled problem is governed by the weak equilibrium equation

$$\Pi_{,\mathbf{u}}[\mathbf{u}, \gamma] \delta \mathbf{u} = \int_{\mathcal{B}_0} \delta_{\mathbf{u}} \mathbf{F} : \mathbf{P}(\mathbf{u}, \gamma) \, dV = 0, \quad (4.3)$$

with admissible virtual displacements $\delta \mathbf{u}$ and elastic potential Π . For a sufficiently small load factor $\gamma \in [0, \gamma_c^{(1)})$ a unique solution (i.e., a minimizer of Π) is given by the deformed configuration $2L_1\lambda_1 \times 2L_2\lambda_2$. The homogeneous stress and strain tensor become

$$\mathbf{P} = \text{diag}(0, P_{22}) \quad \text{and} \quad \mathbf{F} = \text{diag}(\lambda_1, \lambda_2), \quad (4.4)$$

respectively, describing a uniaxial stress and a biaxial stretch state. Here the loading directly determines the vertical stretch as $\lambda_2 = 1 + \gamma \hat{u}/L_2$. Moreover, the constraint $P_{11} = 0$ provides $\lambda_1(\lambda_2)$ and $P_2(\lambda_2)$ as a function of the vertical stretch via the constitutive law; see Section 2.3.5. The corresponding displacement field

$$\mathbf{u}_0(\lambda_2) = [(\lambda_1 - 1)X_1 \quad (\lambda_2 - 1)X_2]^T \quad (4.5)$$

is denoted as *principal solution* \mathbf{u}_0 . Since the elastic potential depends directly on the vertical stretch it is convenient to use the stretches λ_2 (instead of the load factor) as quantity of interest.

4.1.2 Euler Buckling – Introductory Example

The purpose of this section is to provide a smooth transition to the more general case. For a block with sufficient slenderness $r \ll 1$ the problem setup described before depicts the special case of Euler's column buckling. The onset of buckling occurs at small strain and thus the block is considered as a slice (with a unit thickness in third dimension) of an infinitely wide plate² with deflection $w \equiv u_1$ as only degree of freedom. Elasticity constants E and ν provide the bending and axial stiffness

$$EI = \frac{E}{1 - \nu^2} \frac{(2L_1)^3}{12} = \tilde{E} \frac{2L_1^3}{3} \quad \text{and} \quad EA = \tilde{E} 2L_1, \quad (4.6)$$

²With a slight misuse of the terminology: the wording “beam” or “column” will also be used.

respectively, with modified Young's modulus $\tilde{E} = E/(1 - \nu^2)$. Figure 4.2 sketches the thin beam-equivalent to the previously introduced general problem setup. Small deflections are assumed, such that $w' \ll 1$, with $w' = dw/dX_2$. Equilibrium is governed by the linearized virtual work principle

$$\int_{-L_2}^{L_2} (\delta w'' EI w'' - \delta w' P w') dX_2 = 0, \quad (4.7)$$

subject to boundary conditions

$$w'(\pm L_2) = 0, \quad Q(\pm L_2) = 0, \quad w(0) = 0. \quad (4.8)$$

Here, P denotes the axial force and $Q = -EIw''' - Pw'$ denotes the shear force. The Euler equation of (4.7) yields Euler's buckling criterion

$$\boxed{w'''' + \tilde{p}_2 w'' = 0} \quad \text{with } \tilde{p}_2 = \sqrt{\frac{P}{EI}}. \quad (4.9)$$

The general solution of (4.9) is provided by

$$w(X_2) = A \cos(\tilde{p}_2 X_2) + B \sin(\tilde{p}_2 X_2) + C \tilde{p}_2 X_2 + D. \quad (4.10)$$

This ansatz together with boundary conditions (4.8) yields the coefficient matrix

$$\mathbf{M} = \begin{bmatrix} p_2 \sin(\tilde{p}_2 L_2) & \tilde{p}_2 \cos(\tilde{p}_2 L_2) & \tilde{p}_2 & 0 \\ -\tilde{p}_2 \sin(\tilde{p}_2 L_2) & \tilde{p}_2 \cos(\tilde{p}_2 L_2) & \tilde{p}_2 & 0 \\ 0 & 0 & EI \tilde{p}_2^3 & 0 \\ 1 & 0 & 0 & 1 \end{bmatrix} \quad (4.11)$$

with respect to the coefficient vector $[A \ B \ C \ D]^T$. The non-trivial solution is determined by $\det \mathbf{M} = 0$, providing

$$\sin(\tilde{p}_2 L_2) \cos(\tilde{p}_2 L_2) = 0 \quad \Rightarrow \quad \tilde{p}_2 = n \frac{\pi}{L_2} \quad \text{or} \quad \tilde{p}_2 = (n - \frac{1}{2}) \frac{\pi}{L_2}, \quad (4.12)$$

with $n \in \mathbb{N}$. This gives rise to the following two classes of buckling cases

$$\mathcal{S}^1 : \begin{cases} w = A \cos(\tilde{p}_2 X_2) - A \\ \tilde{p}_2 = n\pi/L_2 \end{cases} \quad \text{and} \quad \mathcal{A}^1 : \begin{cases} w = B \sin(\tilde{p}_2 X_2) \\ \tilde{p}_2 = (n - \frac{1}{2})\pi/L_2 \end{cases} \quad (4.13)$$

Here, in view of the next section, the solutions are divided into buckling modes which are symmetric \mathcal{S}^1 and antisymmetric \mathcal{A}^1 with respect to the X_1 -axis. The critical axial

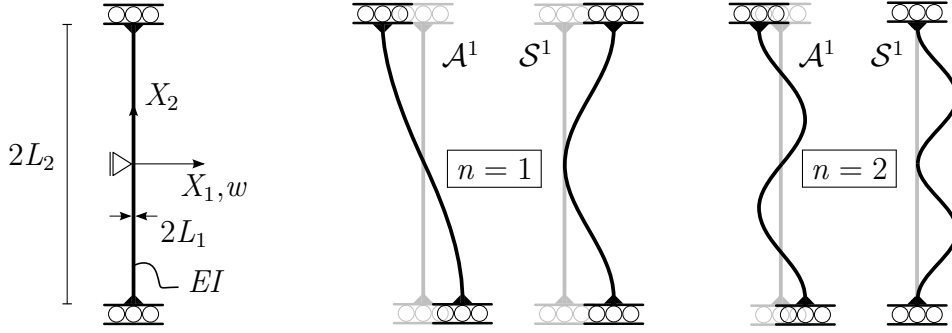


Figure 4.2: Left: beam-equivalent to the general setup of Figure 4.1; middle to right: a sketch of the first four buckling modes.

force is then given by

$$P_c^{(j)} = \tilde{p}_2^2 EI \text{ (compression)} \quad (4.14)$$

with the critical stress component

$$\sigma_{22,c} = -\frac{P_c^{(j)}}{2L_1} = -\frac{1}{3}\tilde{E}n^2\pi^2r^2 \quad \text{or} \quad \sigma_{22,c} = -\frac{1}{3}\tilde{E}\left(n - \frac{1}{2}\right)^2\pi^2r^2. \quad (4.15)$$

Here, the integer j denotes the $P^{(j)}$ -value sorted in ascending order. In view of the next section, the critical state may also be expressed in terms of a “post-processed” critical axial stretch. Using $P = (\lambda_2 - 1)EA = \varepsilon EA$, where the axial strain $\varepsilon = \gamma \hat{u}/L_2$ is induced by the (small) prescribed displacement, the critical stretch reads

$$\lambda_c^{(j)} = 1 - \frac{\tilde{p}_2^2 EI}{EA}. \quad (4.16)$$

It is obvious that the assumed small strain condition is only met for small ratio's of EI/EA . The subsequent derivation aims to provide a more general results, also valid for bulky structures. For an excellent review on thin column buckling, it is referred to the book of Hjelmstad 2005.

4.1.3 Bifurcation Analysis

As for the simple Euler buckling case from before, the interest lies in the onset of critical deformation states where - apart from the principal solution - bifurcated equilibrium branches emerge. The theory of incremental deformations by Biot 1965 is used to analyze this problem.

Incremental problem. Starting point for the stability analysis is the frozen set of deformed configurations along the primary path. Each set, i.e., each prescribed $\lambda_2(\gamma)$, is checked for the existence of bifurcated incremental equilibrium states. The corresponding criterion for a critical point is described by the *incremental* eigenvalue problem

$$(\Pi_{,\mathbf{u}}\delta\mathbf{u})_{,\mathbf{u}} \cdot \Delta\mathbf{u}^{(j)} = \int_{\mathcal{B}_0} \delta\mathbf{u} \mathbf{F} : \mathbb{A}(\mathbf{u}_0(\lambda_c^{(j)})) : \text{Grad} \Delta\mathbf{u}^{(j)} \, dV = 0, \quad (4.17)$$

where \mathbb{A} is the two-point constitutive tensor of the current principal deformation state and $\Delta\mathbf{u}^{(j)}$ is the (unknown) incremental bifurcation mode (“buckling mode”), which obeys the boundary conditions below. In ascending order, the integer j denotes the j th bifurcation point with critical stretch $\lambda_2 = \lambda_c^{(j)}$. Once a critical mode is found, the presence of a bifurcation point, rather than a limit point, is ensured by the orthogonality condition

$$\Pi_{,\mathbf{u}}\Delta\mathbf{u}^{(j)} = \int_{\mathcal{B}_0} \text{Grad} \Delta\mathbf{u}^{(j)} : \mathbf{P}(\mathbf{u}_0, \lambda_c^{(j)}) \, dV = 0. \quad (4.18)$$

The superscript j is skipped subsequently for readability reasons, keeping in mind that infinitely many bifurcations can occur. The incremental equivalent to the set of boundary conditions (4.1) and (4.2) reads

$$\Delta u_2(X_1, \pm L_2) = 0, \quad \Delta u_1(0,0) = 0 \quad (4.19)$$

and

$$\Delta P_{11}(\pm L_1, X_2) = 0, \quad \Delta P_{12}(\pm L_1, X_2) = 0, \quad \Delta P_{21}(X_1, \pm L_2) = 0. \quad (4.20)$$

With $\mathbb{A}(\mathbf{u}_0)$, the explicit form of the incremental stress-strain relation reads

$$\left. \begin{aligned} \Delta P_{11} &= A_{1111}\Delta u_{1,1} + A_{1122}\Delta u_{2,2}, & \Delta P_{12} &= A_{1212}\Delta u_{1,2} + A_{1221}\Delta u_{2,1}, \\ \Delta P_{21} &= A_{2121}\Delta u_{2,1} + A_{2112}\Delta u_{1,2}, & \Delta P_{22} &= A_{2222}\Delta u_{2,2} + A_{2211}\Delta u_{1,1}. \end{aligned} \right\} \quad (4.21)$$

Providing the Euler equation

$$\text{Div}(\Delta\mathbf{P}) = \text{Div}(\mathbb{A}(\mathbf{u}_0, \lambda_c) : \text{Grad}\Delta\mathbf{u}) = \mathbf{0} \quad (4.22)$$

of the incremental stability criterion (4.17). With Equation (4.21), the governing partial differential equation can be specified as

$$A_{1111}\Delta u_{1,11} + A_{1122}\Delta u_{2,21} + A_{1212}\Delta u_{1,22} + A_{1221}\Delta u_{2,12} = 0, \quad (4.23a)$$

$$A_{2222}\Delta u_{2,22} + A_{2211}\Delta u_{1,12} + A_{2121}\Delta u_{2,11} + A_{2112}\Delta u_{1,21} = 0. \quad (4.23b)$$

Elimination of either u_1 or u_2 from (4.23) yields the characteristic equation

$$\boxed{a\Delta u_{\alpha,1111} + 2b\Delta u_{\alpha,1122} + c\Delta u_{\alpha,2222} = 0} \quad (4.24)$$

with $\alpha = 1, 2$ and coefficients

$$\begin{aligned} a &:= A_{1111}A_{1212}, & c &:= A_{2222}A_{2121}, \\ 2b &:= A_{1111}A_{2222} + A_{1212}A_{2121} - (A_{1122}A_{2112})^2. \end{aligned} \quad (4.25)$$

General solution and local uniqueness. Following Ogden 1997 (p. 415) a general ansatz for the incremental displacements of the form

$$\Delta u_{\alpha} = m_{\alpha} f_{\alpha}(p_1 X_1 + p_2 X_2), \quad \alpha = 1, 2 \quad (4.26)$$

is adopted. Here, m_{α} and p_{α} are constants and f_{α} is a sufficiently differentiable function. Substitution into (4.24) provides the characteristic equation

$$\boxed{a \left(\frac{p_1}{p_2} \right)^4 + 2b \left(\frac{p_1}{p_2} \right)^2 + c = 0} \quad (4.27)$$

which has the four roots

$$\frac{p_1}{p_2} = \pm \sqrt{\frac{-b \mp \sqrt{b^2 - ac}}{a}}. \quad (4.28)$$

Real, imaginary, and complex solutions are all possible depending on the elastic constants, specifically the sign of $b^2 - ac$. This work is restricted to cases where the material remains strongly elliptic and therefore

$$a > 0, \quad c > 0, \quad b > -\sqrt{ac}. \quad (4.29)$$

This is a direct result of the ellipticity condition (2.47) (see Equation (6.2.151) in Ogden 1997). The solutions of p_1/p_2 can be found in the following regimes:

- The *Elliptic-Imaginary regime* (EI) occurs for $b^2 > ac$ and provides four purely imaginary roots

$$\frac{p_1}{p_2} = \pm i\alpha \quad \text{and} \quad \frac{p_1}{p_2} = \pm i\beta, \quad (4.30)$$

with the real constants

$$\alpha = \sqrt{\frac{b + \sqrt{b^2 - ac}}{a}} \quad \text{and} \quad \beta = \sqrt{\frac{b - \sqrt{b^2 - ac}}{a}}. \quad (4.31)$$

Here $i = \sqrt{-1}$ denotes the imaginary unit.

- The *Elliptic-Complex regime* (EC) occurs for $b^2 < ac$ and provides four complex roots

$$\frac{p_1}{p_2} = \pm i(\gamma + i\delta) \quad \text{and} \quad \frac{p_1}{p_2} = \pm i(\gamma - i\delta), \quad (4.32)$$

with the real constants

$$\gamma = \sqrt{\frac{\sqrt{ac} + b}{2a}} \quad \text{and} \quad \delta = \sqrt{\frac{\sqrt{ac} - b}{2a}}. \quad (4.33)$$

Both cases complete the required classifications within this work. The case where the ellipticity assumption (4.29) does not hold brings up two additional cases. For sake of completeness, these are briefly sketched: the hyperbolic regime with $-b/a > 0$, $b^2 > ac$ and $ac > 0$ yields four real roots and the parabolic regime with $ac < 0$ has two real and two imaginary roots. These cases allow for localized solutions such as shear bands, which are not present in the elliptic regime, see the discussion in Hill and Hutchinson 1975.

Buckling ansatz. The ansatz for the incremental bifurcation components Δu_α must be constructed in such a way that dependence of the argument $p_1 X_1 + p_2 X_2$ in (4.26) and the essential boundary conditions (4.19) are ensured. This is achieved with an exponential ansatz, and it is referred to Appendix A.2.1 for technical details. A set of solutions that comply with these criteria is of the form

$$\mathcal{S}^1 : \begin{cases} \Delta u_1 = v_1(X_1) \cos(p_2 X_2) - v_1(0) \\ \Delta u_2 = -v_2(X_1) \sin(p_2 X_2) \\ p_2 = n\pi/L_2 \end{cases} \quad (4.34a)$$

or

$$\mathcal{A}^1 : \begin{cases} \Delta u_1 = v_1(X_1) \sin(p_2 X_2) \\ \Delta u_2 = -v_2(X_1) \cos(p_2 X_2) \\ p_2 = (n - \frac{1}{2})\pi/L_2 \end{cases} \quad (4.34b)$$

Here, n is an arbitrary integer and \mathcal{S}^1 and \mathcal{A}^1 designate modes where Δu_1 is symmetric and antisymmetric with respect to the X_1 -axis. The functions $v_\alpha(X_1)$ are determined for each regime individually.

EI case. The four purely imaginary solutions (4.30) of Equation (4.27) provide³

$$p_1 = p_2 \cdot \{+i\alpha, -i\alpha, +i\beta, -i\beta\} \quad (4.35)$$

and require the X_1 -dependent part of ansatz (4.34) to be of the form

$$\mathcal{S}^2 : \begin{cases} v_1 = B_1 \sinh(\alpha p_2 X_1) + D_1 \sinh(\beta p_2 X_1) \\ v_2 = B_2 \cosh(\alpha p_2 X_1) + D_2 \cosh(\beta p_2 X_1) \end{cases} \quad (4.36a)$$

$$\mathcal{A}^2 : \begin{cases} v_1 = A_1 \cosh(\alpha p_2 X_1) + C_1 \cosh(\beta p_2 X_1) \\ v_2 = A_2 \sinh(\alpha p_2 X_1) + C_2 \sinh(\beta p_2 X_1) \end{cases} \quad (4.36b)$$

Here, \mathcal{S}^2 and \mathcal{A}^2 denote modes in which v_1 is symmetric or antisymmetric with respect to the X_2 -axis. For the antisymmetric case \mathcal{A}^2 , the incremental equilibrium equations (4.23a) together with natural boundary conditions (4.20) provide the coefficient matrix

$$\mathbf{M} = \begin{bmatrix} A_{1111}\alpha\mathbf{f}_\alpha & A_{1111}\beta\mathbf{f}_\beta & b_1 A_{1122}\mathbf{f}_\alpha & b_1 A_{1122}\mathbf{f}_\beta \\ b_1 A_{2112}\mathbf{c}_\alpha & b_1 A_{2112}\mathbf{c}_\beta & -A_{2121}\alpha\mathbf{c}_\alpha & -A_{2121}\beta\mathbf{c}_\beta \\ \alpha^2 A_{1111} - A_{1212} & 0 & b_1\alpha(A_{1122} + A_{1221}) & 0 \\ 0 & \beta^2 A_{1111} - A_{1212} & 0 & b_1\beta(A_{1122} + A_{1221}) \end{bmatrix} \quad (4.37)$$

with respect to coefficient vector $[A_1 \ C_1 \ A_2 \ C_2]^\top$, correspondence

$$\begin{cases} \mathcal{S}^1 & \rightarrow b_1 = -1 \\ \mathcal{A}^1 & \rightarrow b_1 = +1 \end{cases} \quad (4.38)$$

and abbreviated hyperbolic functions

$$\mathbf{c}_{\{\alpha,\beta\}} = \cosh(\{\alpha,\beta\} p_2 L_1) \quad \text{and} \quad \mathbf{f}_{\{\alpha,\beta\}} = \sinh(\{\alpha,\beta\} p_2 L_1). \quad (4.39)$$

The results for the symmetric case \mathcal{S}^2 are obtained simply by swapping all hyperbolic functions in (4.37) and (A.15). Of interest are the non-trivial solutions that require

³Notation: curly brackets are used to shorten the representation of a set of relations, e.g. $z = \{x, y\} \Rightarrow z = x$ or $z = y$ and $\{w, z\} = \{x, y\} \Rightarrow w = x$ and $z = y$.

$\det \mathbf{M} = 0$. After some algebraic manipulations and using

$$\begin{aligned} s_{\{\alpha, \beta\}} &= A_{1111}A_{1221} \{\alpha, \beta\}^2 + A_{1122}A_{1212}, \\ t_{\{\alpha, \beta\}} &= A_{2121}(A_{1111} \{\alpha, \beta\}^2 - A_{1212}) + A_{2112}(A_{1122} + A_{1221}), \end{aligned} \quad (4.40)$$

the critical stretches are obtained by

$$\frac{\tanh(\beta p_2 L_1)}{\tanh(\alpha p_2 L_1)} = \left(\frac{\beta s_\alpha t_\beta}{\alpha s_\beta t_\alpha} \right)^{b_2}, \quad (4.41)$$

with

$$\begin{cases} \mathcal{S}^2 & \rightarrow b_2 = -1 \\ \mathcal{A}^2 & \rightarrow b_2 = +1 \end{cases}. \quad (4.42)$$

Here the \mathcal{S}^1 and \mathcal{A}^1 cases are not directly present but come into play via the odd or even values for p_2 in (4.34). The critical stretch is then calculated by taking the first root (starting from the reference state $\lambda_2 = 1$) for all four combinations $\mathcal{S}^j \mathcal{A}^i$ and all integers n .

EC case. The four complex solutions (4.32) of Equation (4.27) provide

$$p_1^j = p_2 \cdot \{i\gamma - \delta, -i\gamma - \delta, i\gamma + \delta, -i\gamma + \delta\} \quad (4.43)$$

and requires the X_1 -dependent part of ansatz (4.34) to be of the form

$$\mathcal{S}^2 : \begin{cases} v_1 = B_1 \sinh(\gamma p_2 X_1) \cos(\delta p_2 X_1) + D_1 \cosh(\gamma p_2 X_1) \sin(\delta p_2 X_1) \\ v_2 = B_2 \cosh(\gamma p_2 X_1) \cos(\delta p_2 X_1) + D_2 \sinh(\gamma p_2 X_1) \sin(\delta p_2 X_1) \end{cases} \quad (4.44a)$$

$$\mathcal{A}^2 : \begin{cases} v_1 = A_1 \cosh(\gamma p_2 X_1) \cos(\delta p_2 X_1) + C_1 \sinh(\gamma p_2 X_1) \sin(\delta p_2 X_1) \\ v_2 = A_2 \sinh(\gamma p_2 X_1) \cos(\delta p_2 X_1) + C_2 \cosh(\gamma p_2 X_1) \sin(\delta p_2 X_1) \end{cases} \quad (4.44b)$$

As for the previous EI case, the non-trivial solutions provide the equation for the critical stretches

$$\frac{\sinh(2\gamma p_2 L_1)}{\sin(2\delta p_2 L_1)} = \frac{b_2 \mathfrak{B}}{\mathfrak{U}}, \quad (4.45)$$

where \mathfrak{U} and \mathfrak{B} are defined in Appendix A.2.

	ν	elliptic domain	PDE classification		1 st singularity	
			EI	EC	A	C
NH	$0.\bar{3}$	$(0, \infty)$	$(0, \infty)$	-	-	-
	0.499	$(0, \infty)$	$(0, \infty)$	-	-	-
SVK	$0.\bar{3}$	$(0.613, 1.732)$	$(1.701, 1.732)$	$(0.613, 1.701)$	1.732	-
	0.499	$(0.632, 1.415)$	-	$(0.632, 1.415)$	1.415	-
OGD	$0.\bar{3}$	$(0.230, 3.925)$	-	$(0.230, 3.925)$	3.151	1.690
	0.499	$(0.267, 3.732)$	-	$(0.267, 3.732)$	3.000	1.666
BK	0.25	$(0.372, 2.685)$	-	$(0.372, 2.685)$	2.279	1.509

Table 4.1: Vertical stretch values λ_2 or intervals in λ_2 of the *local constitutive behavior* for a uniaxial stress state. Various hyperelastic materials are examined. Singularity of the constitutive operators refers to the first singularity encountered in the tension loading program ($\lambda_2 > 1$). The situations at the regime boundaries are not discussed, see the general treatment in Ogden 1997.

4.1.4 Example I: Geometric Instabilities

The first set of examples covers the class of instabilities that appear under compressive deformation states, i.e., $\lambda_2 < 1$. These instabilities are driven by the geometric term \mathbb{A}^g (Equation (2.46)) in the incremental eigenvalue problem (4.17). A descriptive engineering interpretation is the “continuum version” of the P - Δ effect studied in Section 6.2. The roots of transcendental equations (4.41) and (4.45) are calculated with the computer algebra system Maple via the built-in root-finding algorithm “fsolve”. Hereby, a specification of a sufficiently narrow interval via a predictor calculation proved useful.

Table 4.1 shows the stretch domains of interest of the local stability behavior for the uniaxial tension/compression case: the column “elliptic domain” provides the interval where ellipticity holds. This determines the stretch-domain for the subsequent analysis. Moreover, the EI and EC regimes as well as possible singularities of the constitutive operators are shown.

Overview and principal solution procedure. First, a compressible Neo-Hookean (NH) material with $\nu = 1/3$ is considered. Figure 4.3 depicts 20 branches of critical stretches plotted over the block’s aspect ratio $r = L_1/L_2$. The curves correspond to all symmetric/antisymmetric mode combinations for the first five mode numbers n . The “most critical curve”, which corresponds to the maximum stretch value in the compression case, is usually of primary interest in engineering problems. However, the purpose of this plot is to provide a deeper insight into the general stability behavior, which is why

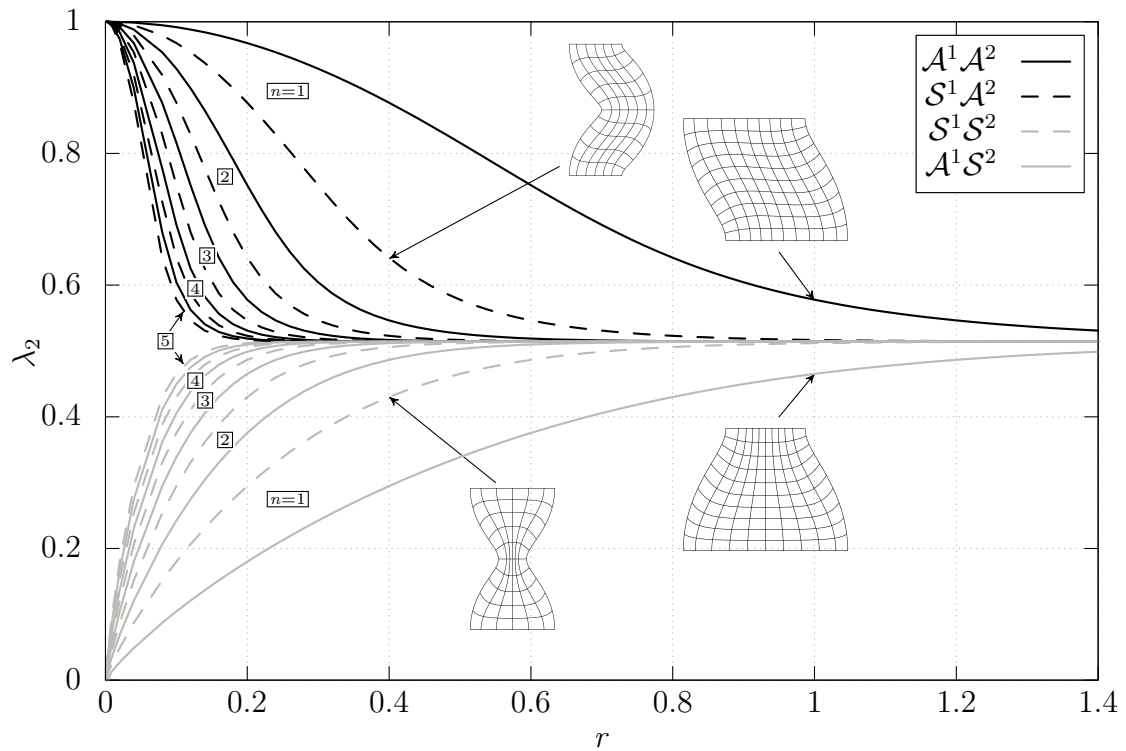


Figure 4.3: Critical stretches for all mode combinations up to $n = 5$. Neo-Hookean material with $\nu = 1/3$. The boxed numbers between two curves indicate their corresponding mode number.

several solution branches are considered independent of their magnitude. As expected, the results are sensitive with respect to the block's aspect ratio, the mode number n and the chosen symmetric/antisymmetric buckling mode ansatz. Combinations with \mathcal{A}^2 modes buckle earlier in the compression state than combinations with \mathcal{S}^2 modes. On one hand, the limit cases of r include $r \rightarrow 0$, which corresponds to the classical Euler buckling cases of Section 4.1.2. On the other hand, for $r \rightarrow \infty$, all critical curves accumulate around a halfway compressed block, a phenomenon that physically characterizes surface buckling. Both cases will be dealt with separately later.

Selected materials. Next, the influence of the aspect ratio on the stability behavior of various compressible hyperelastic blocks is considered. The first four critical stretches are plotted in Figure 4.4. The following graphs can be read from “top to bottom”, i.e., onset of compression ($\lambda_2 = 1$) until bifurcations occur.

Figure 4.4 (a) shows the results of three hyperelastic materials. The critical stretches of all materials coincide with the linear theory in the thin limit $r \rightarrow 0$ and reproduce Euler's buckling solution. The branches of the NH block, which correspond to the

first four curves in Figure 4.3, are \mathcal{A}^2 -antisymmetric but alternate between \mathcal{A}^1 ($\lambda_c^{\{1,3\}}$) and \mathcal{S}^1 ($\lambda_c^{\{2,4\}}$). They follow the same order as for the Euler case, see Figure 4.2. In contrast to that, the results based on the Blatz-Ko rubber (BK) and Saint-Venant Kirchhoff material (SVK) show alternating hierarchies with respect to the mode-type of the critical stretches (see the enlarged detail for BK). For the BK rubber this is also observed in the work of Triantafyllidis et al. 2007.

The same curves, but with an extended aspect ratio, are depicted in Figure 4.4 (b). All critical branches of each material converge towards the same value for the limit $r \rightarrow \infty$. This physically characterizes the surface buckling phenomenon, in which deformations are concentrated at the traction-free boundary surface and decay towards the inside of the block; see the buckling modes in Figure 4.5. Figure 4.4 (c) is concerned with the influence of Poisson's number. An interesting observation is that thin blocks buckle earlier (i.e., larger stretches) for "more compressible" materials, whereas bulky blocks buckle later. For the nearly incompressible case, surface buckling accumulates around $\lambda_2 = 0.5436$, a value also documented in Biot 1965, Equation (6.25).⁴

Asymptotic analysis. Similar to Biot 1965, the limit cases of the block's aspect ratio are considered. The EI case is used for the analysis. However, in a similar manner the asymptotic results can also be derived for the EC case. For the sequel it is convenient to introduce the wave number

$$\kappa = p_2 L_1 = \left\{ n, n - \frac{1}{2} \right\} \pi r. \quad (4.46)$$

Block's thin limit - Euler buckling. The general solution naturally raises the question if or how the general solution is linked to Euler's buckling results. To gain insights, an asymptotic analysis of the EI solution is considered. Only the left hand side of Equation (4.41) is affected by the geometry of the block, i.e., κ , whereas the right hand side is affected only by the material. A Maclaurin series in κ yields

$$\frac{\tanh(\beta\kappa)}{\tanh(\alpha\kappa)} = \frac{\beta}{\alpha} + \frac{\beta\alpha^2 - \beta^3}{3\alpha} \kappa^2 + \mathcal{O}(\kappa^4). \quad (4.47)$$

For small strain, the linearized constitutive two-point tangent reads $C_{IJKL}|_{\mathbf{F}=\mathbf{I}} + \delta_{IK}\sigma_{JL}$, with $\sigma = \text{diag}(0, \sigma_{22})$ being the linear stress tensor. For the antisymmetric \mathcal{A}^2 -case it

⁴Biot gives the stretch as 0.544 (presumably rounded) for the incompressible case. Herein, numerical calculations show that for the "quasi" incompressible case $0.499 < \nu < 0.5$, this value does not change up to the fifth digit.

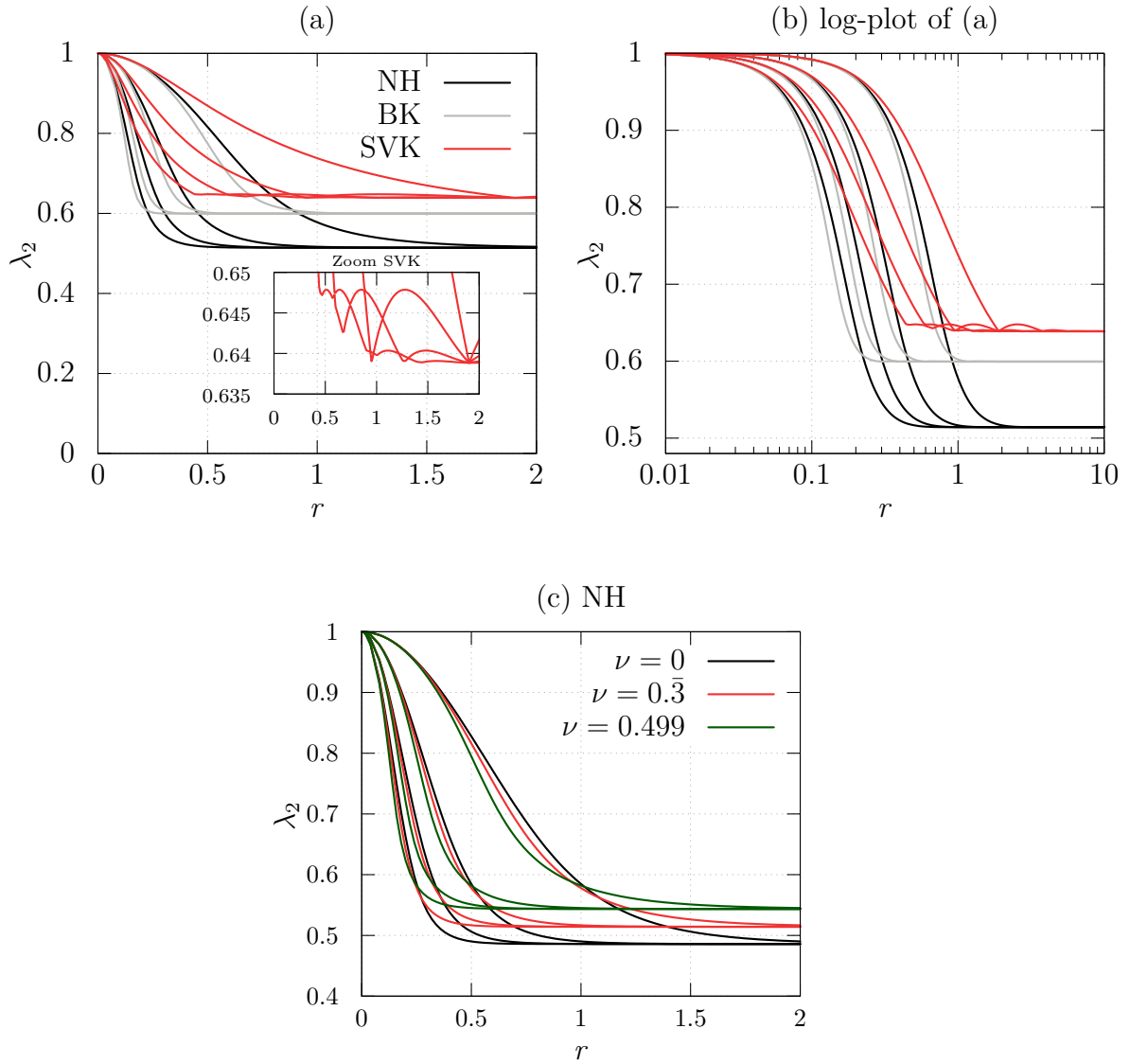


Figure 4.4: First four critical stretches, i.e., the four largest critical stretches in the compression loading program ($\lambda_2 < 1$), for various materials and varying aspect ratio.

follows the critical compressive stress as

$$\sigma_{22} = -\frac{E}{3(1-\nu^2)}\kappa^2 + \mathcal{O}(\kappa^4), \quad (4.48)$$

reproducing, for small κ , Euler's beam results of (4.15). In contrast, the symmetric modes \mathcal{S}^2 do not allow for a solution within the small strain regime. In fact, the linear solution estimates a fully compressed block. Both results are indicated on the very left of Figure 4.3. Therefore, the smallest critical stress is always one with an antisymmetric

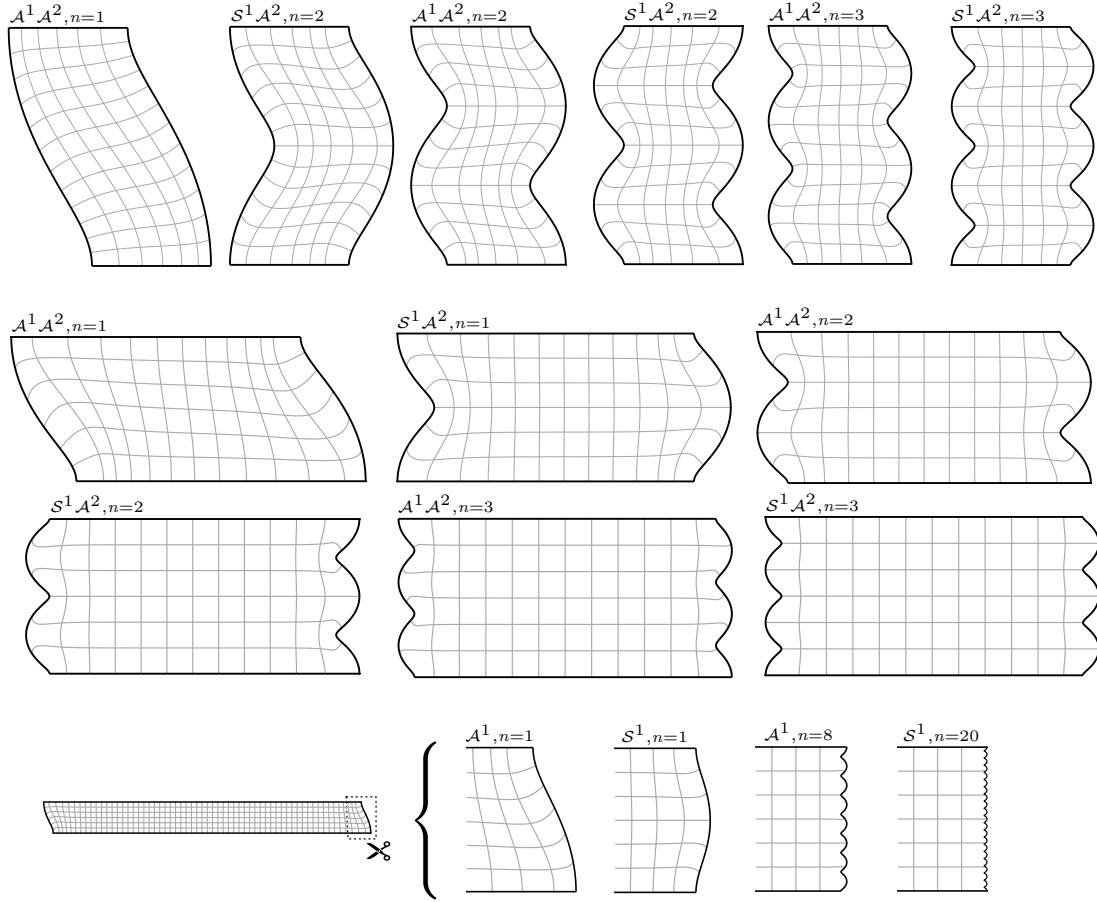


Figure 4.5: Buckling modes due to compression, superimposed onto the reference configuration, NH with $\nu = 1/3$; top and middle: first six buckling modes for aspect ratio $r = 1/2$ and $r = 2$; bottom: detail of four selected modes for a bulky block with $r = 10$.

bending-type buckling mode and not with a symmetric barreling-type mode. This is also true for finite r in the incompressible limit; see Section 6.2 in Young 1976.

Block's thick limit - surface buckling. For the limit case $r \rightarrow \infty$ the block can be considered as a semi-infinite elastic half-space. This was investigated in the contribution of Biot 1963b for a Neo-Hookean block. Now, the left hand side of Equation (4.41) yields

$$\lim_{\kappa \rightarrow \infty} \frac{\tanh(\beta\kappa)}{\tanh(\alpha\kappa)} = 1, \quad (4.49)$$

leaving a surface buckling criterion which only depends on the material-dependent right hand side of (4.41), i.e.,

$$\beta s_\alpha t_\beta = \alpha s_\beta t_\alpha. \quad (4.50)$$

This implies that surface buckling occurs *independently* of the geometry parameters (e.g. r , n or mode shape type) and can be regarded as purely material dependent local stability criterion.⁵ The exponential decay of the hyperbolic functions in X_1 also indicates that the buckling patterns will only appear in a narrow region at the boundary. This is demonstrated by the buckling modes at the bottom of the Figure 4.5.

4.1.5 Example II: Material-Induced Instabilities

The second set of examples covers the class of instabilities that appear under tensile deformation states, i.e., $\lambda_2 > 1$. These instabilities are caused by the material term \mathbb{A}^m of the incremental eigenvalue problem (4.17) (Equation (2.46)).

Selected materials. Focus lies on the BK and OGD materials, since NH does not exhibit instabilities under this loading scenario (see Hill and Hutchinson 1975, however, not necessarily for biaxial stress states, see Figure 2.1). As exemplarily shown in Table 4.1, both materials exhibit strain softening at a certain stretch level, i.e., a singularity of the constitutive operator. The interval between the onset of strain softening and the loss of ellipticity, aka material instability, is the domain of interest. In Figure 4.6 the interval is indicated by blue dash-dotted lines. Similarly as before, 20 branches of critical stretches are shown. A multitude of mode jumps govern the instability behavior, particularly for larger r . The dominant modes for small r 's are the symmetric modes \mathcal{S}^2 , as opposed to the compression problem.

Figure 4.7 shows the first four critical stretches for BK and a quasi incompressible Ogden material. Both materials show qualitatively a similar bifurcation behavior. Some buckling modes for the BK material are shown in Figure 4.8. The modes are often denoted as *diffuse bifurcations*.

Asymptotic analysis. Similarly as before, an asymptotic analysis for small and large r is considered. The left hand side of (4.45) provides the two limits

$$\lim_{\kappa \rightarrow 0} \frac{\sin(2\delta\kappa)}{\sinh(2\gamma\kappa)} = \frac{\delta}{\gamma} \quad \text{and} \quad \lim_{\kappa \rightarrow \infty} \frac{\sin(2\delta\kappa)}{\sinh(2\gamma\kappa)} = 0. \quad (4.51)$$

The *block's thin limit* is then determined by

$$\frac{\mathbf{u}\delta}{b_2\mathfrak{B}\gamma} - \frac{\delta}{\gamma} = 0 \quad \Leftrightarrow \quad \mathbf{u} = b_2\mathfrak{B}. \quad (4.52)$$

⁵It can be shown that for isotropic hyperelastic materials surface buckling *always* occurs before ellipticity is lost, see Bigoni 2012, Section 12.2.3.

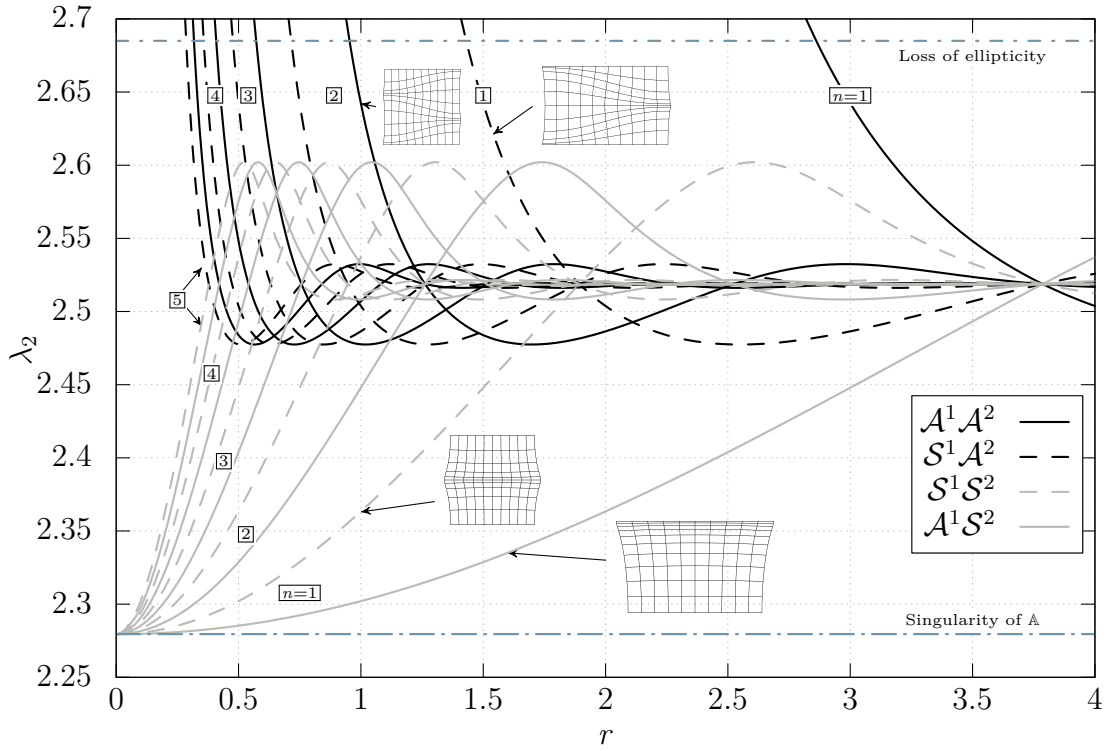


Figure 4.6: Critical stretches for all mode combinations up to $n = 5$. Special Blatz-Ko material with an implicit $\nu = 1/4$. The boxed numbers between two curves indicate their corresponding mode number n .

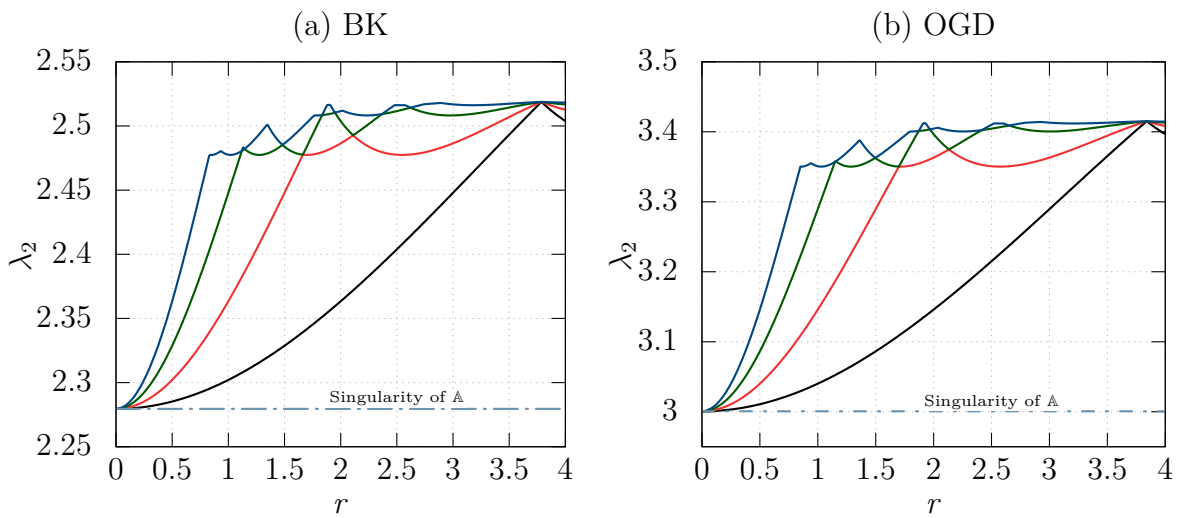


Figure 4.7: First four critical stretches versus the aspect ratio. (a) Blatz-Ko and (b) Ogden with $\alpha = 0.5$, $\nu = 0.499$.

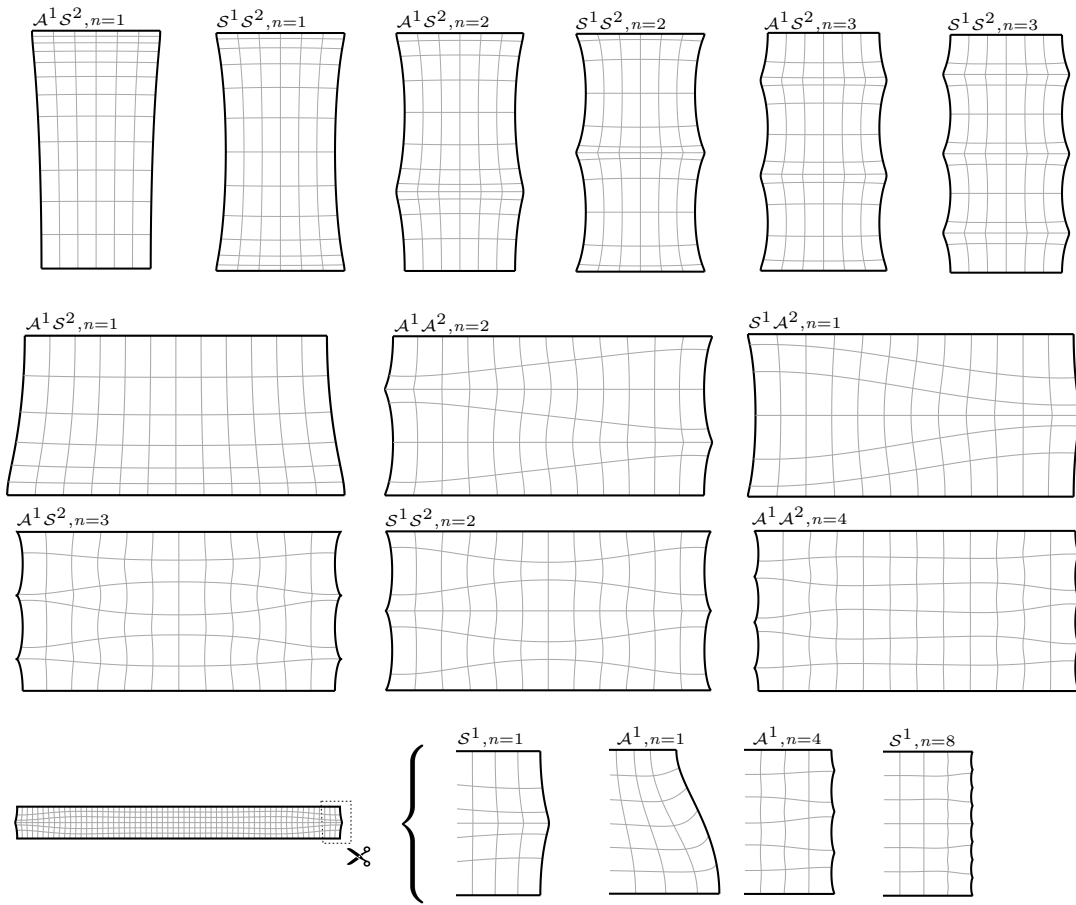


Figure 4.8: Buckling modes due to tension, superimposed onto the reference configuration; top and middle: first six buckling modes for aspect ratio $r = 1/2$ and $r = 2$; bottom: detail of four selected modes for a bulky block with $r = 10$.

It can be shown that a solution is given by $\det \mathbf{A} = 0$ and corresponds to *necking of a axially-loaded column*. The *Block's thick limit* simply requires

$$\mathbf{u}\delta = 0 \quad \Rightarrow \quad \mathbf{u} = 0 \quad \text{or} \quad \delta = 0. \quad (4.53)$$

This corresponds to a purely material-induced *surface buckling*. As before, this implies that surface buckling is *independent* of the geometry parameters and can be regarded as a local instability.

4.2 Finite Bending of a Rubber Block

Pure bending of beam-like specimens is a classical problem in the field of finite elasticity. Typically considered are plane strain deformations of elastic rectangular blocks

subjected to terminal moments. Under the premise of an *incompressible, homogeneous* and *isotropic* hyperelastic material, an analytical solution was presented in the seminal work of Rivlin 1949. As elaborated by Ericksen 1954, this is one of the few examples where so called controllable universal solutions are possible for *inhomogeneous* deformations. Within this special class of materials, involving a strongly elliptic strain energy function, the solutions characterize deformation states that can be maintained by surface tractions alone, independent of the considered material.

Since Rivlin’s original work, various aspects of this problem type have been studied, such as the case of compressible materials⁶, bending instabilities, and related deformations like the unbending (straightening) of circular tubes. Some of these aspects are discussed in the subsequent sections. For more details and references, the interested reader is referred to the recent overview by Sigaeva 2018 as well as Sections 5.5 and 12.4 in Bigoni 2012.

The motivation to deal with this problem concerns its application as a benchmark for numerical methods. For the sake of a general understanding, it is also noted that large bending appears in many engineering applications or natural processes. For instance, the modeling of bending instabilities of gastrointestinal tracts by Balbi et al. 2015, the bio-inspired study of elasmoid fish scales in Rudykh and Boyce 2014 or the structural analysis of offshore pipelines in Kyriakides and Corona 2007.

4.2.1 Principal Solution

Besides Rivlin’s original work, the subsequent derivations follow partly Bigoni 2012 (Section 5.5 therein) and Destrade et al. 2010.

Geometry and kinematics. Starting point is the semi-inverse⁷ approach of the pioneering work of Rivlin 1949. Assumed is a plane strain flexural deformation of an incompressible hyperelastic rectangular $L \times T$ block into a sector of cylindrical tube, with opening angle α and inner and outer radii r_i and r_o , see Figure 4.9. The stress-free reference configuration is described with Cartesian coordinates as

$$\mathbf{X} = X_i \mathbf{E}_i, \quad \text{with } X_1 \in [-T/2, T/2] \text{ and } X_2 \in [-L/2, L/2], \quad (4.54)$$

⁶Unlike for incompressible materials, the underlying equations become far more elaborated due to the absence of the volume constraint. The rare studies are restricted to a specific material such as the “special” Blatz-Ko rubber in Horgan and Murphy 2005.

⁷In contrast to inverse methods, the prefix “semi” implies that certain parts of the assumed displacement field are arbitrary parameters which have to be determined by the underlying differential equations, see the dissertation of De Pascalis 2010 for further details.

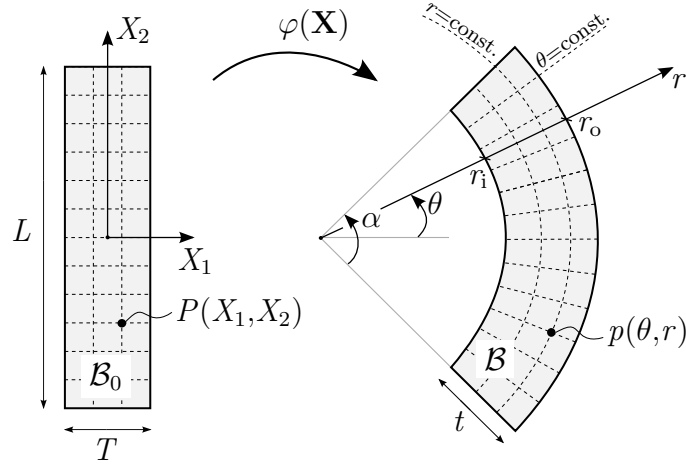


Figure 4.9: Finite bending deformation of a 4×1 rubber block. The figuration is adapted from Bigoni 2012.

where \mathbf{E}_i are the material base vectors. It is convenient to use cylindrical coordinates (r, θ) for the deformed configuration

$$\mathbf{x} = r\mathbf{e}_r = r \begin{bmatrix} \cos \theta \\ \sin \theta \end{bmatrix} \quad \text{with} \quad \begin{cases} r \in [r_i, r_o] \\ \theta \in [-\alpha/2, \alpha/2] \end{cases} \quad (4.55)$$

and spatial base vectors \mathbf{e}_r and $\mathbf{e}_\theta = -\sin \theta \mathbf{E}_1 + \cos \theta \mathbf{E}_2$. The assumed deformation can be interpreted as follows: planes normal to X_1 deform to sectors of cylindrical surface that are constant in r and planes normal to X_2 remain planes that are constant in θ . This implies a deformation field of the form

$$r = f(X_1) \quad \text{and} \quad \theta = g(X_2), \quad (4.56)$$

with unknown functions f and g . The deformation gradient follows as

$$\mathbf{F} = \frac{\partial f}{\partial X_1} \mathbf{e}_r \otimes \mathbf{E}_1 + f \frac{\partial g}{\partial X_2} \mathbf{e}_\theta \otimes \mathbf{E}_2, \quad (4.57)$$

directly providing the principal stretches $\lambda_r = \partial f / \partial X_1$ and $\lambda_\theta = f \partial g / \partial X_2$. The incompressibility constraint yields

$$J = \lambda_r \lambda_\theta = \frac{\partial f}{\partial X_1} \left(f \frac{\partial g}{\partial X_2} \right) = 1 \quad \Rightarrow \quad \frac{\partial}{\partial X_1} \left(\frac{1}{\frac{\partial f}{\partial X_1} f} \right) = 0. \quad (4.58)$$

This is fulfilled by the ansatz

$$f(X_1) = \sqrt{2AX_1 + B} \quad \text{and} \quad g(X_2) = \frac{X_2}{A} + C, \quad (4.59)$$

with real constants A, B and C . Obvious geometrical considerations provide

$$g(+L/2) \stackrel{!}{=} g(-L/2) \quad \Rightarrow \quad C = 0, \quad (4.60a)$$

$$g(\pm L/2) \stackrel{!}{=} \pm \alpha/2 \quad \Rightarrow \quad A = L/\alpha, \quad (4.60b)$$

$$f(-T/2) \stackrel{!}{=} r_i \quad \Rightarrow \quad B = r_i^2 + \frac{LT}{\alpha} = \frac{1}{2} (r_o^2 + r_i^2). \quad (4.60c)$$

Without loss of generality, Equation (4.60a) exploits the symmetry of the deformed block with respect to the X_1 -axis. The last term in Equation (4.60c) uses the isochoric relation $LT/\alpha = (r_o^2 - r_i^2)/2$, which constitutes that the bodies deformed and undeformed volume are identical.

In summary, it can be concluded that deformation (4.55) or, more specifically, ansatz (4.59) is determined by two of the three variables r_i, r_o and α . Following Destrade et al. 2010, the opening angle α is chosen as a *prescribed* variable⁸, leaving, due to relation (4.60c), either r_i or r_o as unknown. The functions (4.59) can be specified as

$$f(X_1) = \sqrt{\frac{2L}{\alpha}X_1 + \frac{1}{2}(r_i^2 + r_o^2)} \quad \text{and} \quad g(X_2) = \frac{\alpha}{L}X_2. \quad (4.61)$$

Equilibrium. Using the correspondence $r \rightarrow 1$ and $\theta \rightarrow 2$, the principal components of the deformation gradient are

$$\mathbf{F} = \text{diag}(\lambda, \lambda^{-1}, 1) \quad \text{with} \quad \lambda := \lambda_1 = \frac{1}{\lambda_2} = \frac{L}{\alpha r}. \quad (4.62)$$

Using Equation (2.36), the principal Cauchy stresses are given as

$$\sigma_{jj}(r) = -p + \lambda_j W_{,j} \quad (\text{no summation}) \quad (4.63)$$

with an arbitrary scalar pressure field $p(r, \theta)$ and $(\bullet)_{,j} = \partial(\bullet)/\partial\lambda_j$. With the absence of body forces, equilibrium in radial and circumferential direction reads

$$\frac{\partial \sigma_{rr}}{\partial r} + \frac{\sigma_{rr} - \sigma_{\theta\theta}}{r} = 0 \quad \text{and} \quad \frac{\partial \sigma_{\theta\theta}}{\partial \theta} = 0. \quad (4.64)$$

⁸More common in literature is to prescribe a terminal moment.

The second term provides $p = p(r)$, then solving (4.64)₁ for p yields

$$p(r) = \int \frac{1}{r} (\lambda_1 W_{,1} - \lambda_2 W_{,2}) \, dr + \lambda_1 W_{,1} + D, \quad D \in \mathbb{R}. \quad (4.65)$$

Following Destrade et al. 2010 (see Equation (3.5) and (3.6) therein) a modified strain energy function is introduced as

$$\tilde{W}(\lambda) = W(\lambda, \frac{1}{\lambda}) \quad \Rightarrow \quad \lambda \tilde{W}' = \lambda W_{,1} + \frac{1}{\lambda} W_{,2}, \quad (4.66)$$

where the prime denotes the derivative with respect to λ . Together with (4.65), (4.66) and relation $dr = -L/(\alpha\lambda^2) \, d\lambda$, the stress components can be simplified to

$$\sigma_{rr} = - \int \frac{1}{\lambda} (\lambda_1 W_{,1} - \lambda_2 W_{,2}) \frac{-L}{\alpha\lambda^2} \, d\lambda - D = \tilde{W} - D, \quad (4.67a)$$

$$\sigma_{\theta\theta} = \tilde{W} - \lambda \tilde{W}' - D. \quad (4.67b)$$

With $\lambda_i = L/(\alpha r_i)$ and $\lambda_o = L/(\alpha r_o)$, the stress-free boundaries at the inner and outer curved edges dictate

$$\sigma_{rr}(\lambda_i) = 0 \quad \text{and} \quad \sigma_{rr}(\lambda_o) = 0, \quad (4.68a)$$

and determine

$$D = \tilde{W}(\lambda_i) = \tilde{W}(\lambda_o) \quad (4.69)$$

in dependency of either r_i or r_o . This allows to write the stress in a simple form as

$$\sigma_{rr} = \tilde{W} - \tilde{W}(\lambda_i), \quad (4.70a)$$

$$\sigma_{\theta\theta} = \tilde{W} - \lambda \tilde{W}' - \tilde{W}(\lambda_i). \quad (4.70b)$$

For a more concrete solution, material symmetry provides

$$W(\lambda_i, \frac{1}{\lambda_i}) = W(\frac{1}{\lambda_i}, \lambda_i) = W(\lambda_o, \frac{1}{\lambda_o}) = W(\frac{1}{\lambda_o}, \lambda_o). \quad (4.71)$$

It follows

$$r_o = \frac{L^2}{r_i \alpha^2} \quad (4.72)$$

and substituting that into the expression for B , Equation (4.60c), yields

$$r_i^2 - \frac{L^4}{\alpha^4 r_i^2} + \frac{2LT}{\alpha} = 0. \quad (4.73)$$

The physically meaningful solution provides the inner radii

$$r_i^2 = -\frac{LT}{\alpha} + \frac{L\sqrt{T^2\alpha^2 + L^2}}{\alpha^2}, \quad (4.74)$$

and thus

$$B = \frac{L\sqrt{T^2\alpha^2 + L^2}}{\alpha^2}. \quad (4.75)$$

For a prescribed α this fully determines the deformed configuration.

4.2.2 Example: Bending of a Neo-Hookean Block

The behavior of the stress states is discussed for the Neo-Hookean strain energy function (2.57). Using the simplifications (4.62) and (4.66) it can be expressed as

$$\tilde{W}(\lambda) = \frac{\mu}{2} \left(\lambda^2 + \frac{1}{\lambda^2} - 2 \right) \quad (4.76)$$

and provides the principal Cauchy stresses

$$\sigma_{rr} = \mu \frac{\lambda^4 \lambda_i^2 - \lambda^2 \lambda_i^4 - \lambda^2 + \lambda_i^2}{2\lambda^2 \lambda_i^2}, \quad (4.77a)$$

$$\sigma_{\theta\theta} = -\mu \frac{(\lambda^2 \lambda_i^4 + (\lambda^4 - 3)\lambda_i^2 + \lambda^2)}{2\lambda^2 \lambda_i^2}. \quad (4.77b)$$

Here, using Equation (4.74), the inner radial stretch is given by $\lambda_i = L/(\alpha r_i)$. A block with initial dimensions $L = 4$ and $T = 1$ is considered. Figure 4.10 shows the principal Cauchy stress for various bended block configurations. The purpose of these plots is to illustrate the influence of nonlinearity on the stress state. On the top, both principal stresses are plotted onto the deformed geometry. Here, the dash-dotted line represents the neutral fibre, i.e. the radial location where $\sigma_{\theta\theta} = 0$. The neutral fiber moves inwards as the deformation progresses. This effect is explained by the strain-stiffening in the compression zone of the NH model, see also the discussion in Kanner and Horgan 2008. The stress distribution in thickness direction is depicted by the graphs at the bottom of Figure 4.10. As expected, the smallest angle $\alpha = \pi/3$ resembles a good approximation to a linear circumferential stress distribution across the thickness.

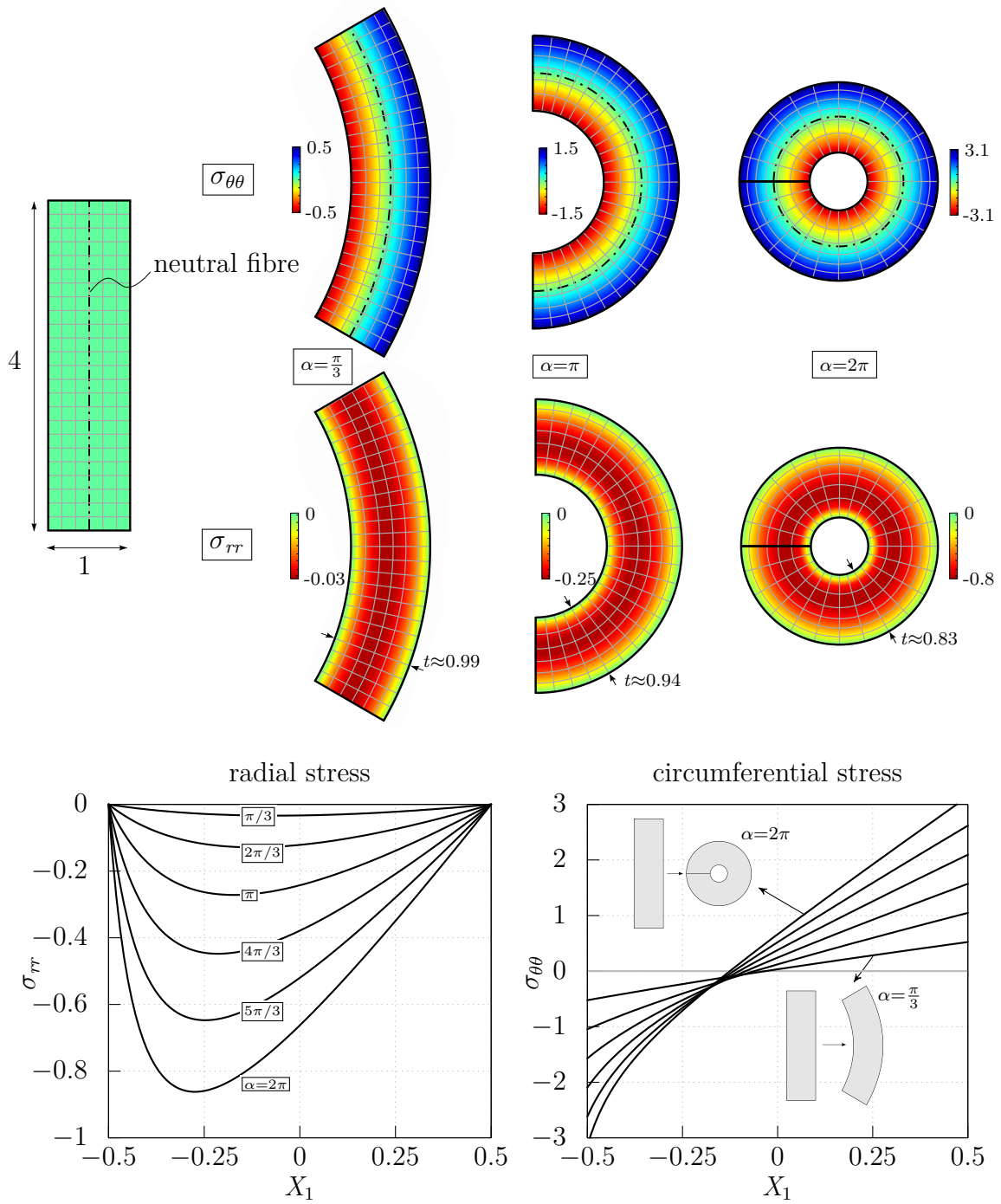


Figure 4.10: Principal Cauchy stress for NH and parameters $L = 4$, $T = 1$ and $\mu = 1$; top: Cauchy stress plotted onto the deformed configuration; bottom: stress distribution over the referential thickness for various opening angles.

Stress resultants. The available stress components give rise to consider the underlying structural problem. It consists of an “out-of-plane” infinitely wide plate. The corresponding stress resultants are obtained via integration over the thickness. The normal force reads

$$N = \int_{r_i}^{r_o} \sigma_{\theta\theta} dr = 0 \quad (4.78)$$

and the bending moment is

$$M = \int_{r_i}^{r_o} \sigma_{\theta\theta} r dr = \frac{\mu L^2}{4\alpha^2} \left(2 \ln \frac{\lambda_o}{\lambda_i} - \frac{\lambda_i^2}{\lambda_o^2} + \frac{3}{2\lambda_o^4} - \frac{1}{\lambda_i^2 \lambda_o^2} - \frac{1}{2\lambda_i^4} + 1 \right). \quad (4.79)$$

Technical details of both integrals are provided in Appendix A.3. The bending moment M can be related to the well-known linear bending moment

$$M_{\text{lin}} = \alpha \frac{EI}{L} = \alpha \frac{E/(1-\nu^2) T^3}{12L} \stackrel{\nu=0.5}{=} \frac{\alpha \mu T^3}{3L}, \quad (4.80)$$

valid for the thin limit $T \rightarrow 0$. Inspired by Destrade et al. 2010 (Section 5 therein), the non-dimensional parameter $\epsilon = \alpha T/L$ is introduced. It contains *all* parameters that describe the nonlinear deformation. With $\lambda_i^2 = \sqrt{1 + \epsilon^2} + \epsilon$ an alternative representation of the bending moment is

$$M = M_{\text{lin}} \left(\frac{\ln(\sqrt{\epsilon^2 + 1} - \epsilon)}{\epsilon^3} + \frac{\sqrt{\epsilon^2 + 1}}{\epsilon^2} \right). \quad (4.81)$$

Expansion in ϵ yields

$$\frac{M}{M_{\text{lin}}} = 1 - \frac{3}{10} \epsilon^2 + \frac{9}{56} \epsilon^4 + \mathcal{O}(\epsilon^6) \quad (4.82)$$

and recovers the thin limit for small ϵ , i.e. small bending angles $\alpha \ll 1$ or a thin block’s aspect ratio $T/L \ll 1$.

To enhance the understanding of nonlinear bending, the interplay of both principal stress components is illustrated in Figure 4.11. The physical need for the less intuitive radial stress becomes obvious from the free body diagram of a $(r_o - r_n) \times \bar{\alpha}$ cylindrical sector. The resulting radial and circumferential stresses, as shown in Figure 4.11, are as follows:

$$R_r = \int_{-\bar{\alpha}/2}^{\bar{\alpha}/2} \cos \frac{\theta}{2} \sigma_{rr} r_n d\theta \quad \text{and} \quad R_\theta = \int_{r_n}^{r_o} \sigma_{\theta\theta} dr. \quad (4.83)$$

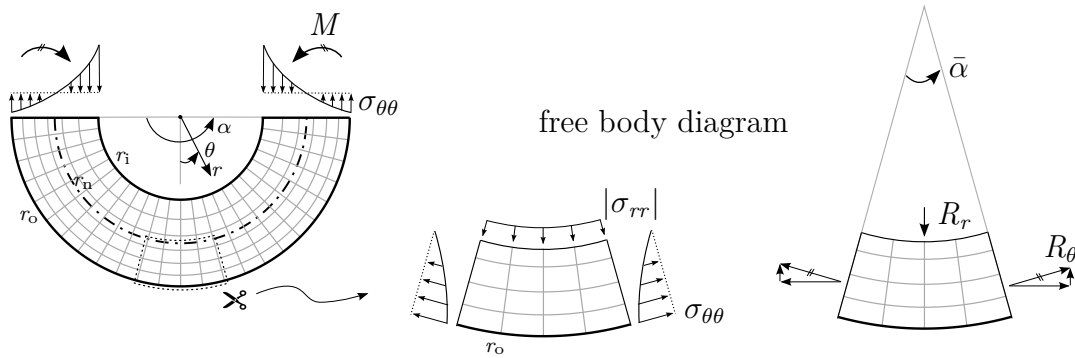


Figure 4.11: Illustration of the load-carrying behaviour of large bending equilibrium. The neutral fibre is located at $r = r_n$.

The radial resultant R_r contributes to equilibrium by “eating up” the vertical components $R_\theta \sin(\bar{\alpha}/2)$ of the circumferential resultant. Of course, at the inner boundary r_i the radial stress becomes obsolete, since $R_\theta = N = 0$, see Equation (4.78).

4.2.3 Bending Instabilities

For a small ϵ , that is, a small bending angle α or a small aspect ratio T/L , the solution to the bending problem remains unique. For sufficiently large ϵ , on the other hand, one can expect a critical deformed state where buckling occurs. To avoid this in the numerical studies, it becomes crucial to deal with this issue.

The incremental analysis of, among others, Coman and Destrade 2008 predicts a surface-type buckling pattern in the form of smooth sinusoidal wrinkles at the compressed side. However, these types of instabilities are not directly observed in rubber experiments or finite element simulations; see Gent and Cho 1999 or Sigaeva et al. 2018. The development of creases (Sulci⁹) is observed as actual instability mode, earlier than the predicted wrinkles. As remarked in Sigaeva 2018 the critical predictions of the incremental theory are nonetheless close to the finite element results (a deviation of 4% was observed for the eversion of a cylindrical tube). However, as shown by Cao and Hutchinson 2012, wrinkling modes may be viewed as an incipient form of creasing deformations and the number of predicted wrinkles appear to be similar to the developed number of creases, see the discussion in Sigaeva 2018.

From these observations, a surface buckling criterion is assumed to be sufficient as an estimation for the critical bending angle α . As shown in Section 4.1.4 the critical stretch

⁹Typically observed on the surface of greasy arms of infants or on the inner side of the reader’s elbow while flexing the arm; see also Hohlfeld and Mahadevan 2011.

of $\lambda_c = 0.544$ yields surface buckling. For thick (nearly) incompressible NH blocks, an estimation of the critical bending angle is given by

$$\lambda_i \stackrel{!}{=} 0.544 \quad \Rightarrow \quad \boxed{\alpha_c \approx 0.77 \frac{L}{T}} \quad (4.84)$$

This formula will be used for the finite element simulations in the next section.¹⁰

¹⁰A similar formula is given in Bigoni 2012, Equation (12.146) in Section 12.4.

Chapter 5

Nonlinear Locking Phenomena

Since the early days of the finite element method, research efforts have been devoted to locking and unlocking of elements. The majority of publications either deal with geometrically linear problems or apply unlocking schemes known from linear theory to the nonlinear case, without special regard to geometrically nonlinear aspects. In the following, locking effects that are induced by geometric nonlinearity are discussed. They are referred to as *nonlinear locking* as opposed to locking from the linear theory.

In the context of three-dimensional shell formulations, Willmann et al. 2022 showed that higher-order integration in combination with large bending deformations can trigger a nonlinear Poisson stiffening effect. This effect is called *nonlinear volumetric locking* in this work. It was identified as a deformation-dependent phenomenon with similar characteristics as the volumetric locking effect known from linear theory. The reason why this topic barely received attention in literature is related to numerical integration. Standard rank sufficient integration, usually referred to as “full integration” (e.g. 2×2 Gauss points for a Q1 element), does automatically avoid nonlinear locking. It may be interpreted as “reduced integration” with respect to critical nonlinear locking terms. The purpose of this chapter is to answer the question, to what extent geometric nonlinearity influences the volumetric and geometric locking behavior of the plane solid elements described in Chapter 3.

Based on that, a model problem for the analysis of nonlinear locking is investigated and possible remedies for nonlinear locking are discussed. Finally, a set of benchmarks shows the effects of nonlinear locking on large deformation finite element simulations.

5.1 Analysis of Nonlinear Locking Phenomena

5.1.1 Recap on Linear Locking

Locking manifests itself in *reduced preasymptotic convergence rates*, smaller than the optimal predicted one in error estimate (3.30). This effect depends on a critical parameter, such as a material parameter describing the degree of incompressibility or the aspect ratio of the element. The related locking phenomena are denoted as geometric locking and volumetric locking, respectively. From a practical engineering perspective, a locking-free response can be related to the *ability to represent simple inhomogeneous deformation states*. For the present Q1 element variants this means that constant bending states should be represented without showing parasitic stress/strain terms. This approach is also used in the following nonlinear analysis. For further details, reference is made to the dissertation of Koschnick 2004 as well as the mathematical oriented article by Suri 1996.¹

5.1.2 Model Problem

Inspired by Andelfinger and Ramm 1993, Table 5.1 shows the displacement modes and the resulting Green-Lagrange strain of a Q1 element. Terms added due to nonlinearity are underlined. The modes 1-6 represent *constant strain modes* and are a prerequisite for passing the nonlinear patch test. Modes 7-8 represent the *hourglass modes*, sometimes referred to as linear bending modes. Focus lies on the approximation properties of a single Q1 element to represent pure bending. The analytical solution of the finite bending problem from Section 4.2 serves as a reference for the locking analysis. Figure 5.1 sketches the deformed and undeformed configuration of a bent block for the analytical case (top) and discrete case (bottom). Due to the symmetry of the problem, only modes 3, 6 and 7 contribute to the element deformation. The best approximation, a single displacement based element can provide, is given by

$$\mathbf{u} = \begin{bmatrix} u \\ v \end{bmatrix} = \frac{1}{2} \begin{bmatrix} c_3\xi + c_7\xi\eta \\ c_6\eta \end{bmatrix}. \quad (5.1)$$

Here, c_i denote coefficients of generalized modal degrees of freedom of a Q1 element. The coefficients of the bilinear bending mode 7 and the homogeneous stretch modes 3 and 6

¹In Suri 1996, the authors proposed a definition of (volumetric) locking via a “locking ratio” that compares the energy norm of the error $\mathbf{e} = \mathbf{u}^h - \mathbf{u}$ of a compressible ($\nu = 0.3$) finite element solution with the one of nearly incompressible ($\nu \rightarrow 0.5$) one. This definition takes into account non-locking-related effects, such as the smoothness of solution \mathbf{u} , which can also deteriorate the convergence.

depend on α_e , the block's aspect ratio r_e and the material properties. The compatible displacement gradient of the displacement field given in Equation (5.1) reads

$$\mathbf{H}^c = \begin{bmatrix} (c_3 + c_7\eta)/L_e & c_7\xi/T_e \\ 0 & c_6/T_e \end{bmatrix} \quad (5.2)$$

and provides the Green-Lagrange strain tensor $\mathbf{E}^c = \frac{1}{2} [(\mathbf{H}^c)^T + \mathbf{H}^c + (\mathbf{H}^c)^T \mathbf{H}^c]$. A square element ($r_e = 1$) yields

$$\begin{bmatrix} E_{11}^c \\ E_{22}^c \\ 2E_{12}^c \end{bmatrix} = \underbrace{\begin{bmatrix} c_3 + c_7\eta \\ c_6 \\ c_7\xi \end{bmatrix}}_{\boldsymbol{\varepsilon}^c} + \frac{1}{2} \underbrace{\begin{bmatrix} c_3^2 + c_7c_3\eta + c_7^2\eta^2 \\ c_7^2\xi^2 + c_6^2 \\ c_7^2\xi\eta + 2c_7c_3\xi \end{bmatrix}}_{\mathbf{E}_{\text{nl}}^c}, \quad (5.3)$$

with a split into a linear part $\boldsymbol{\varepsilon}^c$ and nonlinear part \mathbf{E}_{nl}^c .

5.1.3 Deformation-Dependent Modal Analysis

Before considering an actual analysis, the effects of nonlinear locking are illustrated by means of a modal analysis of the element stiffness matrix. This is a typical way to analyze the locking behavior of elements. However, the major difficulty encountered in the analysis of nonlinear locking is its deformation-dependent nature. As described later, nonlinear locking is triggered by *inhomogeneous element deformations*. This means that the eigenvalue analysis must involve an element deformation with nonzero displacement mode 7 and/or mode 8. As a result of this, various deformed bending states with $\alpha_e = \{0, 0.2, 0.4, 0.8\}$ are considered. Figure 5.1 shows an example of such a deformation for $\alpha_e = \pi/2$. The compressible Neo-Hookean (NH) strain energy function (2.58) is used. The bending angle α_e imposes an inhomogeneous Dirichlet constraint on the lateral edges of the element. This is realized via Lagrangian multipliers; for technical details, see Section 5.3.1. After the converged solution is obtained, an eigenvalue analysis of the unconstrained 8×8 stiffness matrix² is conducted. Apart from the increasing stiffness, which affects the eigenvalues of the volumetric mode in the incompressible limit ($\Lambda \rightarrow \infty$), both hourglass eigenvalues of a locking-free stiffness matrix should remain finite - independent of any parameter. Thus, a bending-like eigenvalue ω_b is computed for each set of eigenvalues. It is defined as the eigenvalue whose normed eigenvector Φ_i is closest to the bending vector Φ_b^{lin} from linear theory:

$$\min_{i=1,\dots,8} \{|\Phi_i^T \Phi_b^{\text{lin}} - 1|\} \quad \text{with } \Phi_b^{\text{lin}} = \frac{1}{2} \begin{bmatrix} -1 & 0 & 1 & 0 & -1 & 0 & 1 & 0 \end{bmatrix}^T. \quad (5.4)$$

²For EAS elements the enhanced parameters are eliminated via static condensation.

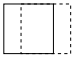
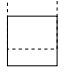
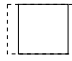

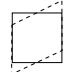
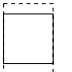
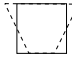
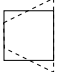
modes								
u	c_1	0	$c_3\xi$	$c_4\eta$	0	0	$c_7\xi\eta$	0
v	0	c_2	0	0	$c_5\xi$	$c_6\eta$	0	$c_8\xi\eta$
E_{11}^c	0	0	$c_3 + \frac{1}{2}c_3^2$	0	$\frac{1}{2}c_5^2$	0	$c_7\eta + \frac{1}{2}c_7^2\eta^2$	$\frac{1}{2}c_8^2\eta^2$
E_{22}^c	0	0	0	$\frac{1}{2}c_4^2$	0	$c_6 + \frac{1}{2}c_6^2$	$\frac{1}{2}c_7^2\xi^2$	$c_8\xi + \frac{1}{2}c_8^2\xi^2$
$2E_{12}^c$	0	0	0	c_4	c_5	0	$c_7\xi + \frac{1}{2}c_7^2\xi\eta$	$c_8\eta + \frac{1}{2}c_8^2\xi\eta$

Table 5.1: Green-Lagrange strain space of the displacement based Q1 modes (Andelfinger and Ramm 1993). Nonlinear strain terms are underlined. Possible mixed strain terms due to mode interactions are not shown.

This cumbersome procedure is necessary since the bending-like mode of the nonlinear stiffness matrix is not known a priori. The modal stiffness $(\Phi_b^{\text{lin}})^T \mathbf{K} \Phi_b^{\text{lin}}$, typically used in the linear case, turns out to be a combination of the eigenvalues of different strain modes. These can deteriorate the desired bending-like modal stiffness, in particular through the volumetric strain energy for nearly incompressible scenarios.

Figure 5.2 shows the eigenvalue ω_b versus a critical parameter: (a) the element aspect-ratio r_e and (b) the first Lamé constant Λ . The solid lines correspond to the eigenvalues of the geometrically linear stiffness matrix of Q1 (black) and Q1/E4 (red). These are given as

$$\omega_b^{\text{lin,Q1}} = \frac{\Lambda + 2\mu}{3r_e} + \frac{\mu r_e}{3}, \quad \omega_b^{\text{lin,EAS}} = \frac{E}{3r_e(1-\nu^2)} = \frac{\tilde{E}}{3r_e}. \quad (5.5)$$

Volumetric locking and shear locking are related to the incompressible limit $\Lambda \rightarrow \infty$ and the thin limit $r_e \rightarrow \infty$, respectively. The triangles on the lines represent the calculated eigenvalues of the (statically condensed) stiffness matrix of Q1/E4.

Although Q1/E4 is free from locking in the geometrically linear case, an artificial stiffening is observed. In situations where $\alpha_e \neq 0$ and more than 2×2 Gauss points are used, the eigenvalues critically depend on the parameters Λ and r_e . Furthermore, the effect depends on α_e , i.e., the degree of nonlinearity. Similar results to Q1/E4 are obtained for Q1/H4 (not shown). Interestingly, Q1/HT4 only suffers from nonlinear volumetric

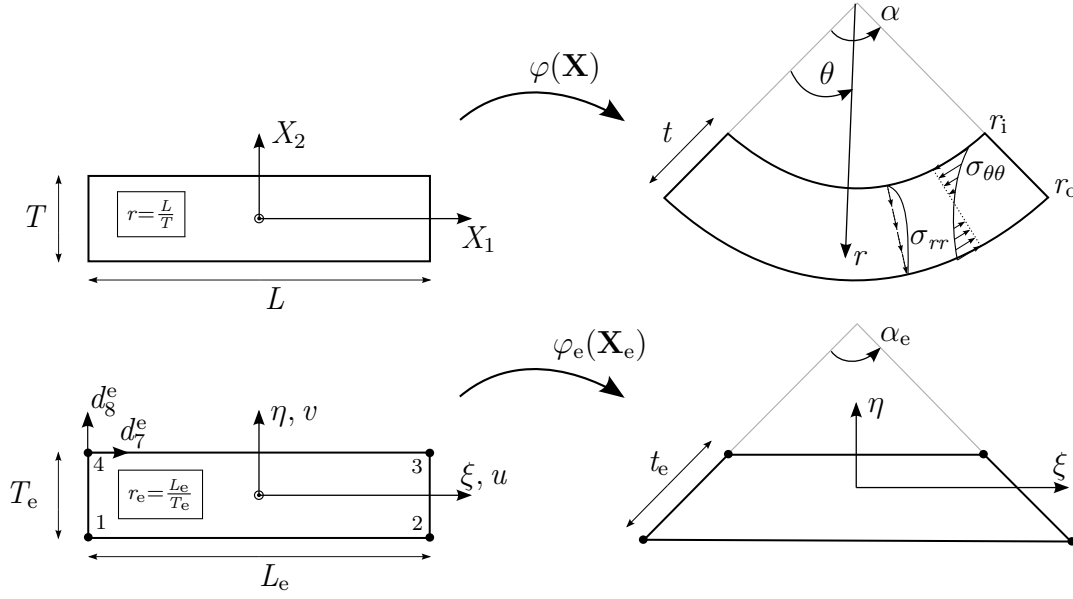


Figure 5.1: Finite bending deformation of a an incompressible rectangular rubber block exemplified for $\alpha = \alpha_e = \frac{\pi}{2}$; top: reference solution; bottom: element approximation.

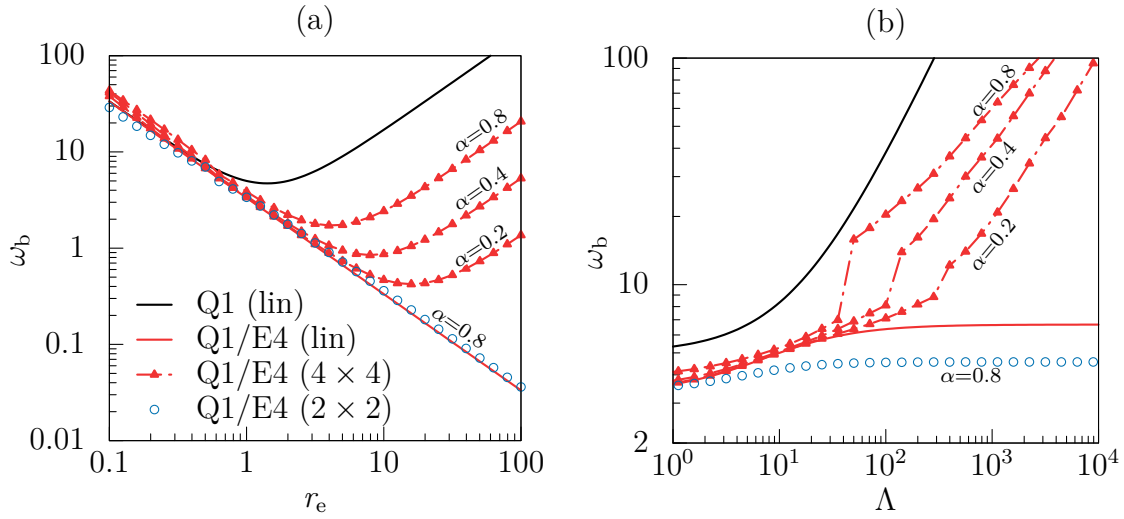


Figure 5.2: Bending eigenvalue ω_b according to Equation (5.4); left: geometric locking test with $\mu = 5$, $\Lambda = 0$ ($\nu = 0$) and variable r_e ; right: volumetric locking test with $\mu = 5$, $r_e = 1$ and variable Λ . Here, $(b \times \sharp)$ denotes the number of Gauss quadrature points in ξ - and η -direction.

locking, whereas the thin limit case does not yield locking. The reasons for these observed phenomena are discussed in the sequel.

5.1.4 Geometric Locking Phenomena

The generic term *nonlinear geometric locking* is used to describe locking that is induced by geometric nonlinearity and related to the geometric properties of the element, namely the aspect ratio. This issue becomes especially relevant for the modeling of thin-walled structures, where the element dimension in thickness direction is significantly smaller than it is in-plane.

Q1. Considered is the bending scenario of the model problem from before. The Green-Lagrange tensor $2\mathbf{E} = \text{diag}(\lambda^2, \lambda^{-2}) - \mathbf{I}$ is obtained from the reference deformation gradient (4.62). Two simple observations can be made: first, the in-plane shear component E_{12} is zero and second, the normal strain E_{11} and E_{22} depend only on X_2 , i.e., strain and stress quantities are constant in X_1 . This is obviously not possible for the nonlinear part of the strain approximation (5.3): E_{12}^c has a bilinear term and E_{22}^c has a quadratic term in ξ , accounting for the stretch of transverse fibers. The latter is illustrated in Figure 5.1 by the length change of the deformed and undeformed thickness fibers t_e and T_e , respectively.

To gain further insights, the stiffness matrix

$$\check{\mathbf{K}}_m = \int_{\Omega} \check{\mathbf{B}}^T \mathbf{C} \Big|_{\mathbf{u}=0} \check{\mathbf{B}} \, dV \quad (5.6)$$

is considered. Here, $\check{\mathbf{B}}(c_i)$ is the nonlinear (Green-Lagrange) strain-displacement operator in terms of the modal degrees of freedom c_i . The modal stiffness matrix $\check{\mathbf{K}}_m$ can be interpreted as the material part of the element stiffness based on the Saint-Venant Kirchhoff model. Focus is put on the stiffness associated with the linear bending mode 7, i.e., stiffness entry³

$$\check{\mathbf{K}}_{m,77} = \underbrace{\frac{M}{3r_e}}_{(i)} + \underbrace{\frac{r_e \mu}{3}}_{(ii)} + c_7^2 \left(\underbrace{\frac{T_e M}{5L_e^3}}_{(iii)} + \underbrace{\frac{2\Lambda}{9L_e T_e}}_{(iv)} + \underbrace{\frac{L_e M}{5T_e^3}}_{(v)} + \underbrace{\frac{4\mu}{9L_e T_e}}_{(vi)} \right) + k(c_3, c_6). \quad (5.7)$$

Here, $M = \Lambda + 2\mu$ is the longitudinal modulus and k a stiffness contribution that comes from the constant stretch modes. Geometric locking concerns the following terms in Equation (5.7): The contribution (ii) in (5.7) is well known from linear theory and related to linear shear locking. It is independent of the deformation state but scales linearly with the element's aspect ratio r_e ; see the black curve in Figure 5.2 (a). Contribution (v) originates from the quadratic ξ -term in E_{22}^c . Using $r_e = L_e/T_e$, its denominator

³This is related to the nodal stiffness matrix \mathbf{K}_m , i.e., the equivalent to (5.6), via $\check{\mathbf{K}}_{m,77} = (\Phi_b^{\text{lin}})^T \mathbf{K}_m \Phi_b^{\text{lin}}$, with Φ_b^{lin} defined in (5.4).

contains the thickness T_e raised to the third power. This produces severe stiffening in the thin limit. Furthermore, the term depends on the “amount” of bending deformation c_7^2 , hence locking becomes more intense with increasing nonlinearity. However, for the linear case as well as for nonlinear homogeneous deformations $c_7 = 0$ and nonlinear locking does not occur. This phenomenon is related to E_{22}^c and denoted as *nonlinear trapezoidal locking* in analogy to the linear locking phenomenon described in Macneal 1987. Finally, contribution (vi) comes from the bilinear term in E_{12}^c and scales linearly with $1/(L_e T_e)$. Therefore, it does not cause “nonlinear shear locking”, since it does not depend critically on r_e . However, parasitic shear strain/stress will occur. The remaining terms (i, iii, iv) are discussed in the context of volumetric locking.

Q1/E4. In the context of geometric locking, the enhancement of this element removes linear shear locking, such that term (ii) cancels. However, the nonlinear contributions, in particular (v), remain. The results of the modal analysis, namely the gap between the nonlinear branches and the linear one in Figure 5.2 (a), can be interpreted as the impact of nonlinear geometric locking due to (v). Here, the Poisson’s ratio is set to zero (i.e., $\Lambda = 0$ and $M = 2\mu$) in order to exclude any effects that are related to volumetric locking. Nonlinear geometric locking shows up for the 4×4 integrated elements. At a specific slenderness the eigenvalues become larger as the aspect ratio r_e increases. This effect is more pronounced for larger α . In contrast to that, the “reduced” integrated version of Q1/E4 provides reasonable results, i.e., reduced bending stiffness in the thin limit. This is due to the fact that the quadratic ξ -terms that cause (v) are not covered by the 2×2 quadrature.

Q1/H4. By assigning $\alpha_3 = -c_7/T_e$, the parasitic shear terms in (5.3) are cancelled. For $\alpha_1 = 0$ and $\alpha_4 = 0$ (these parameters are required for the rotated bending case $c_8 \neq 0$) the remaining Green-Lagrange strain expression then reads

$$\begin{bmatrix} E_{11} \\ E_{22} \\ 2E_{12} \end{bmatrix}^{\text{H4}} = \begin{bmatrix} c_7\eta + c_3 \\ c_6 + \alpha_2\eta \\ 0 \end{bmatrix} + \frac{1}{2} \begin{bmatrix} c_7^2\eta^2 + c_7c_3\eta + c_3^2 + c_7^2\xi^2 \\ \alpha_2\eta^2 + 2\alpha_2c_6\eta + c_6^2 + c_7^2\xi^2 \\ -c_7\alpha_2\xi\eta + c_7^2\xi\eta - c_6c_7\xi + c_7c_6\xi \end{bmatrix}. \quad (5.8)$$

The enhancement of Q1/H4 does not improve with respect to the nonlinear locking terms. In addition to Q1/E4 there even appears a ξ^2 -term in E_{11} . However, the behavior of the eigenvalues ω_b (not shown) are comparable to the ones of Q1/E4 in Figure 5.2.

Q1/HT4. The enhancement of Q1/HT4 directly influences the locking behavior in a favorable way. Again, by assigning $\alpha_3 = -c_7/T_e$, the parasitic shear terms in (5.2)

are cancelled. As a result, the parasitic ξ^2 -term and thus stiffness contribution (v) are automatically avoided and the element is free from nonlinear geometric locking. For $\alpha_1 = 0$ and $\alpha_4 = 0$ the remaining Green-Lagrange strain expression reads

$$\begin{bmatrix} E_{11} \\ E_{22} \\ 2E_{12} \end{bmatrix}^{\text{HT}^4} = \begin{bmatrix} c_7\eta + c_3 \\ c_6 + \alpha_2\eta \\ 0 \end{bmatrix} + \frac{1}{2} \begin{bmatrix} c_7^2\eta^2 + 2c_7c_3\eta + c_3^2 \\ \alpha_2\eta^2 + 2\alpha_2c_6\eta + c_6^2 \\ 0 \end{bmatrix}. \quad (5.9)$$

The corresponding eigenvalues ω_b (not shown) for all integration variants are comparable to the ones in Figure 5.2 (a) for Q1/E4 with 2×2 quadrature points.

5.1.5 Volumetric Locking Phenomena

The term *nonlinear volumetric locking* is used to describe volumetric locking that is induced by geometric nonlinearity. In order to analyze the locking issue, the incompressible limit $\nu \rightarrow 0.5$ (or equivalently $\Lambda \rightarrow \infty$) is studied. This is rather a thought experiment, since full incompressibility is not possible for the present strain driven formulations. The nonlinear isochoric volume constraints can be expressed via

$$\det \mathbf{F} = 1 \quad \text{and} \quad \det \mathbf{C} = 1. \quad (5.10)$$

For the energy to remain finite, (5.10) must be met exactly. The approximation properties to reproduce this volume constraint determine the locking behavior in the quasi-incompressible case. However, this is required only at the integration points and gives rise to advantageous integration schemes, see the later discussion in Section 5.2.1. This topic, however, is not taken into account in the analysis that follows.

Q1. The right Cauchy-Green tensor based on (5.3) is given as $\mathbf{C}^c = \mathbf{1} + 2\mathbf{E}^c$. It follows that the approximation of nonlinear volume constraint (5.10)₂ is

$$\det \mathbf{C}^c = A_1 + A_2\eta + A_3\eta^2 \stackrel{!}{=} 1, \quad (5.11)$$

where the deformation-dependent coefficients A_i are given in Appendix A.4. Assumed is the correct representation of the constant part of the isochoric strain state, i.e., $A_1 = 1$. This yields

$$c_3 = -c_6/(c_6 + 1), \quad (5.12)$$

and Equation (5.11) simplifies to

$$\det \mathbf{C}^c = 1 + 2(c_6 c_7 + c_7) \eta + (c_6^2 + 2c_6 + 1) c_7^2 \eta^2 \stackrel{!}{=} 1. \quad (5.13)$$

In comparison with the linear volume constraint $\text{tr } \boldsymbol{\varepsilon}^c = 0$, Equation (5.13) contains additional nonlinear terms, which give rise to term (iii), (iv) and (v) in Equation (5.7). They spoil the element's ability to represent the volume constraint exactly and are the reason for nonlinear locking. However, it has been shown in Willmann et al. 2022 that the locking behavior is, first of all, dominated by the linear terms. Thus, it becomes interesting to study elements that are *locking-free* in the linear case. This is approached next.

Q1/E4. The right Cauchy-Green tensor is given as $\mathbf{C}^{\text{E4}} = \mathbf{1} + 2(\mathbf{E}^c + \tilde{\mathbf{E}}_4)$. The approximation of the nonlinear volume constraint (5.10)₂ is

$$\det \mathbf{C}^{\text{E4}} = A_1 + B_2 \eta + B_3 \eta^2 + B_4 \xi^2 + B_5 \xi^2 \eta + B_6 \eta^3 \stackrel{!}{=} 1. \quad (5.14)$$

Here, $B_i(c_7, c_3, c_6, \alpha_2, \alpha_3)$ are further nonlinear deformation-dependent constants provided in Appendix A.4. In addition to (5.12), the relations

$$\alpha_3 = -\frac{c_7(c_3 + 1)}{2}, \quad \alpha_2 = -c_7 c_6^3 - 3c_7 c_6^2 - 3c_7 c_6 - c_7, \quad (5.15)$$

are assumed. By that, shear locking as well as a violation of the volume constraint for linear kinematics are avoided. Now, Equation (5.14) can be expressed as

$$\det \mathbf{C}^{\text{E4}} = 1 + \frac{c_7^2}{(1 + c_6)^2} \xi^2 - 3(1 + c_6)^2 c_7^2 \eta^2 + \frac{2c_7^3}{1 + c_6} \eta \xi^2 - 2(1 + c_6)^3 c_7^3 \eta^3. \quad (5.16)$$

Remarkably, the comparison with the Q1 element shows that this strain enhancement yields additional nonlinear terms. The terms with ξ^2 and $\xi^2 \eta$ are caused by α_3 and the η^3 -term by α_2 .

Figure 5.2 (b) shows the impact of nonlinear volumetric locking on the stiffness matrix of Q1/E4. It is less severe than linear volumetric locking, but it also depends critically on Λ and on the degree of nonlinearity, i.e., the value of α_e . The sudden increase of eigenvalues is caused by the fact that the eigenvalue of the homogeneous stretch mode (which remains finite at around ten, not shown) continuously merges with the bending mode over a certain range of Λ . It can also be seen that the eigenvalues for “reduced” 2×2 Gauss integration and $\alpha_e = 0.8$ do not depend critically on Λ . The reason for that is that all non-constant terms in (5.16) are not “seen” by the quadrature rule used.

Q1/H4. Again, using (5.12), the discrete version of volume constraint (5.10)₁ reads

$$\det \mathbf{F}^{\text{H4}} = 1 + (\alpha_2 c_3 + c_7 c_6 + \alpha_2 + c_7) \eta + \alpha_2 c_7 \eta^2 - \alpha_3 c_7 \xi^2 \stackrel{!}{=} 1. \quad (5.17)$$

The enhanced coefficients

$$\alpha_3 = -\frac{c_7}{2}, \quad \alpha_2 = -\frac{c_7 + c_6 c_7}{c_3 + 1}, \quad (5.18)$$

provide

$$\det \mathbf{F}^{\text{H4}} = 1 - (c_6^2 - 2c_6 - 1) c_7^2 \eta^2 + \frac{1}{2} \xi^2 c_7^2 \stackrel{!}{=} 1. \quad (5.19)$$

Similar to Equation (5.16), the presence of nonlinear terms prevents a correct representation of the volume constraint.

Q1/HT4. A favorable behavior is observed for the enhancement (5.23c). It is possible to eliminate the parasitic shear term for this formulation at the displacement gradient level. Thus, the element does not suffer from nonlinear ξ -terms and the locking issue reduces to

$$\det \mathbf{F}^{\text{HT4}} = 1 - (c_6^2 - 2c_6 - 1) c_7^2 \eta^2 \stackrel{!}{=} 1. \quad (5.20)$$

The behavior of the eigenvalues ω_b for both (not shown), Q1/HT4 and Q1/H4, are qualitatively comparable the one of Q1/E4 in Figure 5.2 (b).

Special case: Saint-Venant Kirchhoff material. The locking behavior in the context of the widely used SVK material with a strain energy function (2.53) is somewhat different compared to the NH material. The trace of the Green-Lagrange strain tensor governs the volumetric part of the strain energy and the incompressibility constraint is modeled by

$$\text{tr } \mathbf{E} = 0. \quad (5.21)$$

As before, linear shear locking and volumetric locking are avoided by assigning specific values to α_2 and α_3 . This yields the expressions

$$2\text{tr } \mathbf{E}^{\text{E4}} = c_7^2 \eta^2 + \xi^2 c_7^2, \quad (5.22a)$$

$$2\text{tr } \mathbf{E}^{\text{H4}} = D_1 \eta^2 + \xi^2 c_7^2, \quad (5.22b)$$

$$2\text{tr } \mathbf{E}^{\text{HT4}} = D_1 \eta^2. \quad (5.22c)$$

with $D_1 = c_7^2 + [-c_7(c_3 + 1)/(c_6 + 1)]^2$. The results of Q1/H4 and Q1/HT4 are similar to the fully nonlinear analysis from before. However, the results of Q1/E4 only contains quadratic terms in ξ and η .

5.2 Remedies to Avoid Nonlinear Locking

5.2.1 Numerical Integration: Theory and Practice

The locking analysis of the previous section is based on the premise that exact integration is used. However, in practice, it is common to use numerical integration schemes. Typically, the number of Gauss points is chosen such that a rank sufficient element stiffness matrix is ensured, e.g., 2×2 Gauss points for bilinear quadrilaterals. In the context of reduced integration techniques, the number of Gauss points may even be further decreased. In both cases, the issue of nonlinear locking is *avoided a priori*. This naturally raises the question:

Is nonlinear locking a purely academic artefact – not relevant in practice?

The answer to that depends on the application. For most cases, however, this issue is not relevant, since standard or reduced integration schemes are common practice. Furthermore, the phenomenon becomes only relevant for scenarios with large inhomogeneous deformations in combination with a critical parameter. Such situations appear only in a minority of solid mechanic problems.

Nevertheless, scenarios exist where higher-order integration is demanded. As shown in Willmann et al. 2022, a typical example is the simulation of a sheet metal forming process with 3d shell elements. Large bending scenarios require higher-order integration in shell thickness directions in order to capture plastic effects. Another example is the EAS formulation proposed in Simo et al. 1993. Here, higher-order integration was proposed to alleviate hourglassing under plane strain tension. Both examples fulfill the conditions that yield nonlinear volumetric locking, i.e., the presence of large strain in combination with a quasi-incompressible material.

To understand the impact of higher-order integration, the previous analysis of the EAS formulations provides useful insights. Exemplified is a quasi-incompressible bending scenario of Q1/E4. The constraint (5.14) contains quadratics and cubics in ξ and η and thus quartic and sextic functions in the energy expression, e.g., in the integrand of residual vector and stiffness matrix. Standard Gauss-Legendre integration, which is exact up to a polynomial degree $p = 2N_{QP} - 1$, requires at least 3×3 Gauss points to capture the quadratic expressions in (5.14).

5.2.2 Assumed Stress Elements

The assumed stress element Q1/S5 from Section 3.4 fully avoids nonlinear locking. In a nutshell, the problematic strain terms in \mathbf{E}^c are projected onto the stress-based strain $\mathbf{E}(\mathbf{S})$ via the kinematic constraint (3.63b). Theoretically, nonlinear locking can be reintroduced by enhancing the stress ansatz (3.60) with higher-order polynomials. Numerical experiments have shown that equivalent (up to machine precision) results to Q1/Em versions can be obtained. This analogy to EAS elements is also known from linear theory; see Andelfinger and Ramm 1993. Similar to that, it can be shown that displacement-pressure element formulations can avoid nonlinear volumetric locking.

5.2.3 Novel Enhanced Assumed Strain Elements

In Section 3.3, various EAS formulations are presented that use an enhanced compatible displacement gradient (5.2) as well as an enhanced compatible Green-Lagrange strain (5.3). The following extended versions of these formulations are introduced as:

$$\text{Q1/Em:} \quad \mathbf{E}^{\text{Em}} = \mathbf{E}^c + \tilde{\mathbf{E}}_m, \quad (5.23a)$$

$$\text{Q1/Hm:} \quad \mathbf{H}^{\text{Hm}} = \mathbf{H}^c + \mathbf{F}_0^c \tilde{\mathbf{H}}_m, \quad (5.23b)$$

$$\text{Q1/HTm:} \quad \mathbf{H}^{\text{HTm}} = \mathbf{H}^c + \mathbf{F}_0^c \tilde{\mathbf{H}}_m^T. \quad (5.23c)$$

Here, m indicates the number of enhanced strain modes. For $m = 4$, the elements resemble the classical formulations Q1/E4, Q1/H4 and Q1/HT4 presented in Section 3.3, with

$$\tilde{\mathbf{E}}_4^{\text{par}} = \begin{bmatrix} \alpha_1 \xi & \alpha_3 \xi + \alpha_4 \eta \\ \alpha_3 \xi + \alpha_4 \eta & \alpha_2 \eta \end{bmatrix} \quad \text{and} \quad \tilde{\mathbf{H}}_4^{\text{par}} = \begin{bmatrix} \alpha_1 \xi & \alpha_4 \eta \\ \alpha_3 \xi & \alpha_2 \eta \end{bmatrix}. \quad (5.24)$$

The \mathbf{F}_0 -modification for Q1/H4 is the only exception, as it is required to ensure frame invariance for arbitrary strain enhancements. Due to the orthogonality condition of the enhanced strain, see Bischoff et al. 1999, Legendre polynomials are used for the enhanced strain interpolation functions. They are defined as

$$L_k^\xi = \frac{1}{2^k k!} \frac{d^k}{d\xi^k} (\xi^2 - 1)^k, \quad L_l^\eta = \frac{1}{2^l l!} \frac{d^l}{d\eta^l} (\eta^2 - 1)^l, \quad L_{kl}^{\xi\eta} = L_k^\xi(\xi) L_l^\eta(\eta). \quad (5.25)$$

Q1/Em. Considered is the model problem from before for the derivation of novel strain enhancements. To overcome nonlinear locking, the additive extension of enhance-

ment (5.24)₁ is further specified as

$$\tilde{\mathbf{E}}_{\text{Em}}^{\text{par}} = \tilde{\mathbf{E}}_{\text{E4}}^{\text{par}} + \begin{bmatrix} \tilde{e}(\xi, \eta) & \alpha_5 \xi \eta \\ \alpha_5 \xi \eta & \alpha_6 L_2^\xi \end{bmatrix}. \quad (5.26)$$

Here, \tilde{e} is introduced as a (still unknown) function that will be used to alleviate volumetric locking. The enhanced mode $\alpha_5 \xi \eta$ is introduced to eliminate the parasitic shear term $c_7^2 \xi \eta$ and $\alpha_6 L_2^\xi$ eliminates the nonlinear trapezoidal locking term $\frac{1}{2} c_7^2 \xi^2$ in the Green-Lagrange strain expression (5.3). They effectively eliminate the nonlinear parasitic contributions (v) and (vi) of the material stiffness (5.7). Enhancement \tilde{e} is constructed such as to avoid the issue of nonlinear volumetric locking. With (5.12) and (5.15) the volume constraint $\det \mathbf{C}^{\text{Em}} \stackrel{!}{=} 1$ is solved for \tilde{e} . Transforming the equation provides

$$\begin{aligned} \tilde{e} &= \frac{2c_1^3 c_3 \eta^3 + 2c_1^3 \eta^3 + 3c_1^2 \eta^2}{-2 + 4c_1(1 + c_3)\eta} \\ &= (3c_1^2 \eta^2)/2 + 4c_1^3(1 + c_3)\eta^3 + 8c_1^4(1 + c_3)^2 \eta^4 + \mathcal{O}(\eta^5) \\ &= (3c_1^2 \eta^2)/2 + \sum_{n=2}^{\infty} 2^n c_1^{n+1} (1 + c_3)^{n-1} \eta^{n+1}. \end{aligned} \quad (5.27)$$

Depending on the numerical integration scheme, this provides clear guidance on how to construct an ansatz for \tilde{e} in order to avoid nonlinear volumetric locking. Introduced is $\tilde{e} = \tilde{e}_n$ as a set of n enhanced interpolation functions. Exemplified for N_{QP} Gauss-Legendre points in η -direction, the terms in the expansion of (5.27) must be covered up to $\eta^{(N_{\text{QP}}-1)}$. Thus $N_{\text{QP}} > 2$ requires

$$\tilde{e}_{(N_{\text{QP}}-1)} = \alpha_7 L_2^\eta + \alpha_8 L_3^\eta + \dots + \alpha_{(N_{\text{QP}}+4)} L_{(N_{\text{QP}}-1)}^\eta. \quad (5.28)$$

The preceding considerations are based on a special case of the previous model problem, in which only bending mode c_7 is active. More generally, it is desired to cover bending in both directions. Switching to Voigt notation, the following enhanced strain interpolation matrix is introduced

$$\mathbf{M}_{\text{Em}}^{\text{par}} = \begin{bmatrix} \xi & 0 & 0 & 0 & 0 & 0 & L_2^\eta & \dots & 0 & L_{n+1}^\eta \\ 0 & \eta & 0 & 0 & 0 & L_2^\xi & 0 & \dots & L_{n+1}^\xi & 0 \\ 0 & 0 & \xi & \eta & \xi \eta & 0 & 0 & \dots & 0 & 0 \end{bmatrix}, \quad (5.29)$$

with $m = 5 + 2n$. The corresponding element formulations which will be used in the remainder of the work are Q1/E7, Q1/E9 and Q1/E11.

Q1/HTm. An additive extension of the enhancement (5.24)₃ is considered

$$\tilde{\mathbf{H}}_{\text{HT}m}^{\text{par}} = \left(\tilde{\mathbf{H}}_4^{\text{par}} \right)^{\text{T}} + \begin{bmatrix} \tilde{h}(\xi, \eta) & 0 \\ 0 & 0 \end{bmatrix}. \quad (5.30)$$

Introducing $\tilde{h} = \tilde{h}_n$ and using the simplification (5.12) and (5.18), the volume constraint $\det \mathbf{F}^{\text{HT}m} \stackrel{!}{=} 1$ requires

$$\begin{aligned} \tilde{h} &= \frac{\alpha_2^2 \eta^2}{(1+c_3)^3} - \frac{\alpha_2^3 \eta^3}{(1+c_3)^4} + \frac{\alpha_2^4 \eta^4}{(1+c_3)^5} + \mathcal{O}(\eta^5) \\ &= \sum_{n=2}^{\infty} \frac{(-\alpha_2 \eta)^n}{(1+c_3)^{n+1}} \end{aligned} \quad (5.31)$$

Thus, for $N_{\text{QP}} > 2$ the enhanced ansatz is given by

$$\tilde{h}_{(n_{\text{QP}}-1)} = \alpha_5 L_2^\eta + \alpha_6 L_3^\eta + \dots + \alpha_{(n_{\text{QP}}+2)} L_{(n_{\text{QP}}-1)}^\eta. \quad (5.32)$$

Again, the general strain interpolation matrix is given by

$$\mathbf{M}_{\text{HT}m}^{\text{par}} = \begin{bmatrix} \xi & 0 & 0 & 0 & 0 & L_2^\eta & \dots & 0 & L_{n+1}^\eta \\ 0 & \eta & 0 & 0 & L_2^\xi & 0 & \dots & L_{n+1}^\xi & 0 \\ 0 & 0 & \xi & 0 & 0 & 0 & \dots & 0 & 0 \\ 0 & 0 & 0 & \eta & 0 & 0 & \dots & 0 & 0 \end{bmatrix} \quad (5.33)$$

with $m = 4 + 2n$. In this case, $\mathbf{M}_{\text{HT}m}^{\text{par}}$ is related to the displacement gradient, as opposed to (3.55). The corresponding element formulations, that will be used in the remainder of the work, are Q1/HT6 and Q1/HT8.

Q1/Hm. In analogy to Equation (5.30), and using (5.12) and (5.18), the volume constraint $\det \mathbf{F}^{\text{H}m} \stackrel{!}{=} 1$ requires

$$\begin{aligned} \tilde{h} &= \frac{\alpha_3 c_1 \xi^2}{1+c_3} + \frac{\alpha_2^2 \eta^2}{(1+c_3)^3} - \frac{\alpha_3 c_1 \alpha_2 \eta \xi^2}{(1+c_3)^2} - \frac{\alpha_2^3 \eta^3}{(1+c_3)^4} + \mathcal{O}(\eta^4, \eta^2 \xi^2) \\ &= \sum_{n=2}^{\infty} \frac{\alpha_2^n \eta^n}{(1+c_3)^{n+1}} + \sum_{m=1}^{\infty} \frac{\alpha_3 c_1 (-\alpha_2 \eta)^{m-1} \xi^2}{(1+c_3)^m}. \end{aligned} \quad (5.34)$$

Compared to (5.31), additional mixed terms appear. These arise due to the ξ -terms enhanced displacement gradient. Proposed is a strain interpolation matrix of the form

$$\mathbf{M}_{\text{H10}} = \begin{bmatrix} \xi & 0 & 0 & 0 & L_2^\xi & L_2^\eta & L_{12}^{\xi\eta} & 0 & 0 & 0 \\ 0 & \eta & 0 & 0 & 0 & 0 & 0 & L_2^\eta & L_2^\xi & L_{21}^{\xi\eta} \\ 0 & 0 & \eta & 0 & 0 & 0 & 0 & 0 & 0 & 0 \\ 0 & 0 & 0 & \xi & 0 & 0 & 0 & 0 & 0 & 0 \end{bmatrix}, \quad (5.35)$$

with $m = 10$. The corresponding element, that will be used in the remainder of the work, is Q1/H10.

5.3 Numerical Experiments

Various simulations are performed to highlight the impact of nonlinear locking. All simulations are performed under the following technical specifications:

- *Numerical integration* crucially influences the locking behaviour. For that reason, various scenarios with Gauss-Legendre as well as Gauss-Lobatto⁴ quadrature schemes are considered.
- *Stress resultants*, e.g., the bending moment, are calculated with the same integration points that are used for the computation of the stiffness matrix.
- *Stress recovery* is based on the stress values at the integration points. Stress-plots are produced via bilinear interpolation between these points. Therefore, the presented results may differ from simulations with “standard” finite element routines, where special stress recovery techniques (see for instance Chapter 13 in Zienkiewicz and Taylor 2000) are used.
- The considered element formulations are:
 - **Qp**: Displacement-based quadrilateral with polynomial degree p .
 - **Q1/Em**: EAS formulation based on enhanced Green-Lagrange strain. Here m denotes the number of enhanced modes according to Equation (5.29).
 - **Q1/Hm**: EAS formulation based on enhanced displacement gradient with the incompatible “Wilson” modes. Here m denotes the number of enhanced modes according to Equation (5.35).

⁴They have the special feature that the outer points are always located at the element boundary at $(\xi, \eta) = \pm 1$.

- **Q1/HT m** : EAS formulation based on enhanced displacement gradient with the transposed of the Wilson modes. Here m denotes the number of enhanced modes according to Equation (5.33).
- **Q1/S5**: Assumed stress element according to Section 3.4.

The results of Q1/S5 are considered to be, besides the analytical solution, a numerical reference solution. Its performance can be considered a “target” for all other Q1-based formulations.

5.3.1 Finite Bending Problem – Displacement Controlled

First, the bending problem of Section 4.2 is considered. The isochoric analytical solution of the principal stress components serves as a reference solution. Figure 5.3 sketches the deformed and undeformed mesh configuration of an exemplary finite element model. The left and right edge, are supported with a roller support, whereas the lower and upper edges remain traction-free. The deformation is controlled by the opening angle α , which prescribes the inclination of the right support axis, i.e. each element edge at $\partial\Omega^\alpha$. This is computationally realized via the method of Lagrangian multipliers, incorporating the constraints

$$\hat{\mathbf{n}}(\alpha) \cdot \mathbf{n}_e(\mathbf{d}_e) = 0 \quad e \in \hat{\mathcal{E}}. \quad (5.36)$$

Here, $\hat{\mathcal{E}}$ denotes the set of elements with edges at $\partial\Omega^\alpha$, \mathbf{n}_e the corresponding outward normal vector and $\hat{\mathbf{n}}$ the normal with the desired inclination.

The compressible Neo-Hookean strain energy (2.58) is used for the numerical computations. To reproduce a quasi-incompressible material response, Young’s modulus $E = 100$ and Poisson’s ratio $\nu = 0.499$ (cf. $\Lambda \approx 16644.42$ and $\mu \approx 33.356$) are used unless otherwise stated. The mesh is $n_e^{X_1} \times n_e^{X_2}$, where $n_e^{X_i}$ is the number of elements in the X_i -direction. In most cases, square-shaped elements are considered, i.e., $n_e^{X_1} = \lceil T/L \rceil \cdot n_e^{X_2}$. Quadrature with 5×5 Gauss-Lobatto points (comparable to 4×4 Gauss points) is used. Depending on α and aspect ratio T/L , physical instabilities and artificial instabilities (“hourglassing”) can occur. As elaborated previously, a rough estimate for the critical opening angle is given in Equation (4.84), i.e., $\alpha_c = 0.77L/T$. In the subsequent analysis α is chosen to be below that value. However, depending on the element’s aspect ratio, some formulations also suffer from artificial instabilities. These may occur before α_c is reached.

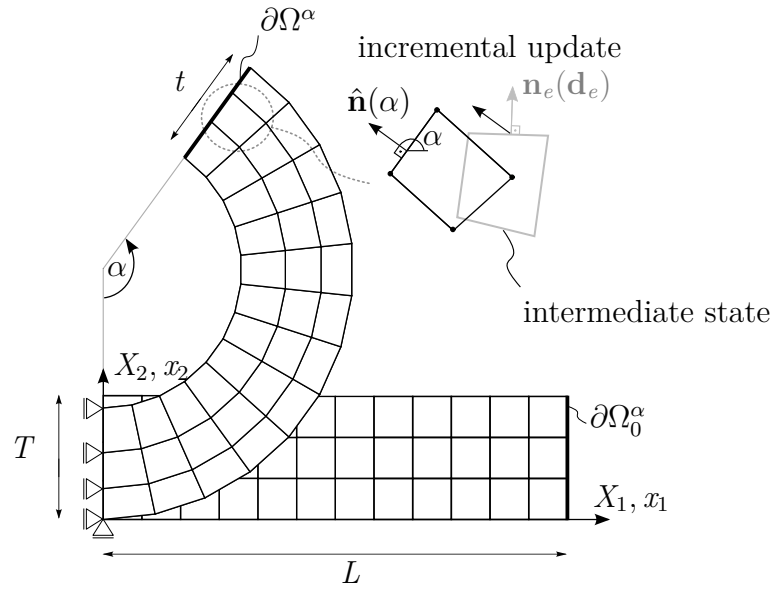


Figure 5.3: Finite bending problem; example of a FE model with a (3×12) mesh and parameters $\{L = 4, T = 1, \alpha = 4\pi/5\}$.

Stress quality. The geometric parameters $L = 4$, $T = 1$ and $\alpha = \pi/2$ are considered. Figure 5.4 and 5.5 show the normal components of the second Piola-Kirchhoff stress \mathbf{S} (using correspondence $X_1 \rightarrow 1$ and $X_2 \rightarrow 2$), plotted on the deformed mesh configuration. For reasons of simplicity and reproducibility, this stress measure is preferred (instead of the Cauchy stress), since no coordinate transformation on element level is required. Moreover, the results of S_{11} and S_{22} coincide qualitatively with the circumferential and radial Cauchy stresses, respectively.

Figure 5.4 shows the analytical solution as well as various finite element results. The results of Q1 show severe (mainly linear) volumetric locking and shear locking. The stress oscillations show high deviations to the analytical solution. The effect of nonlinear volumetric locking is observed for Q1/E4 and Q1/HT4. Both show milder oscillations than Q1, but still fail to reproduce the analytical solution properly, in particular at the element boundaries. As predicted, the oscillations of Q1/H4 are constant in X_1 -direction (ξ -direction within the element), whereas Q1/E4 oscillates in both directions. The stress results of Q1/H4 (not shown) are similar to the ones of Q1/E4.

Figure 5.5 depicts the results of elements that avoid or alleviate nonlinear locking. In contrast to the standard EAS results, Q1/S5 shows a good agreement with the analytical solution (within the limits of coarse mesh accuracy). The results of the novel EAS formulations show great improvements compared to the standard versions. Q1/HT6, Q1/E7, and Q1/E9 stresses are visually comparable to Q1/S5, with only minor oscillations in S_{22} .

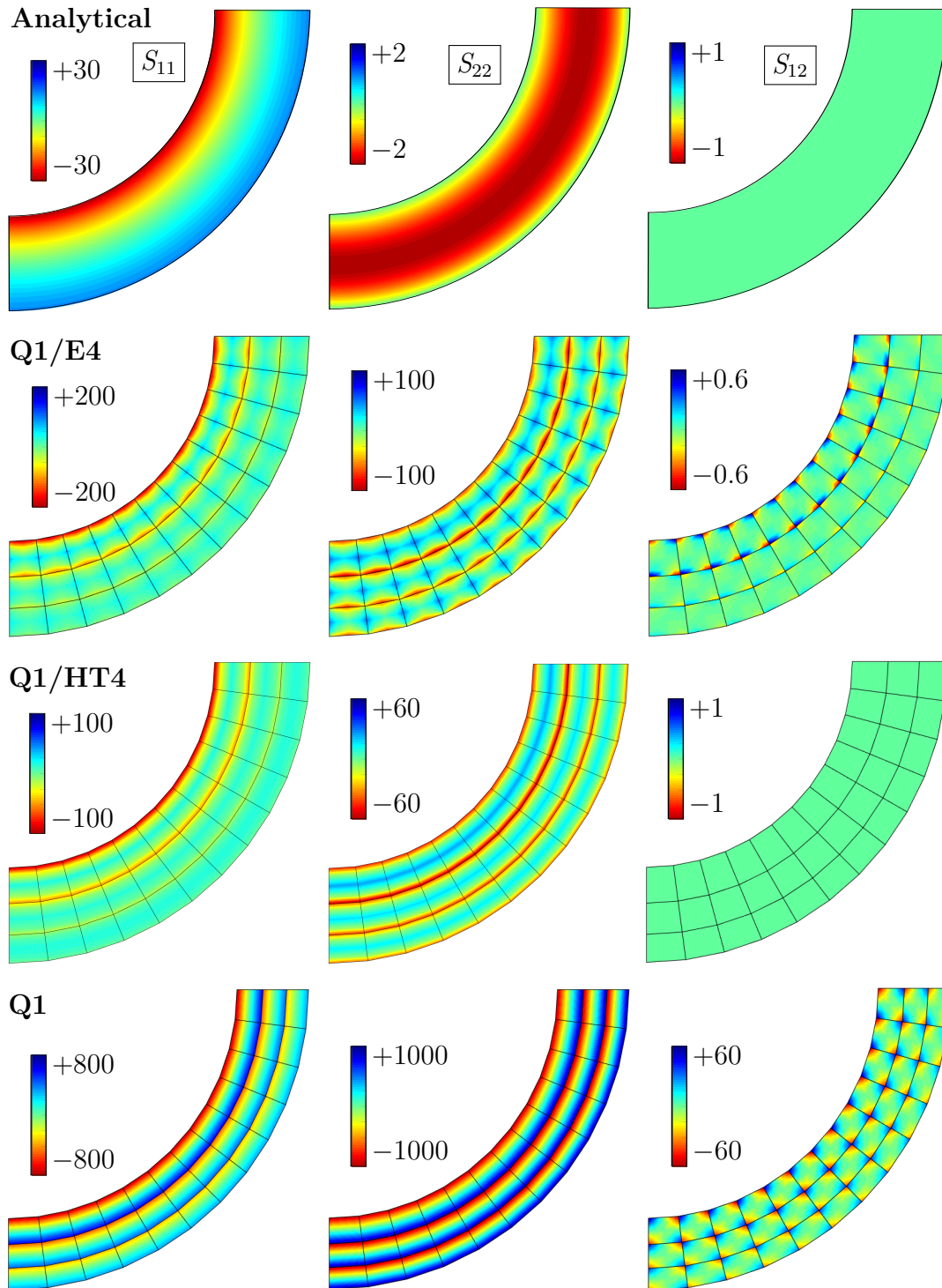


Figure 5.4: Stress quality; finite bending problem $\{L = 4, T = 1, \alpha = \pi/2, \nu = 0.499$ ($\nu = 0.5$ analytical) $\}$. Second Piola-Kirchhoff stress plotted onto the deformed configuration. Colour plots are produced with bilinear interpolation between the 5×5 Gauss-Lobatto points inside each element.

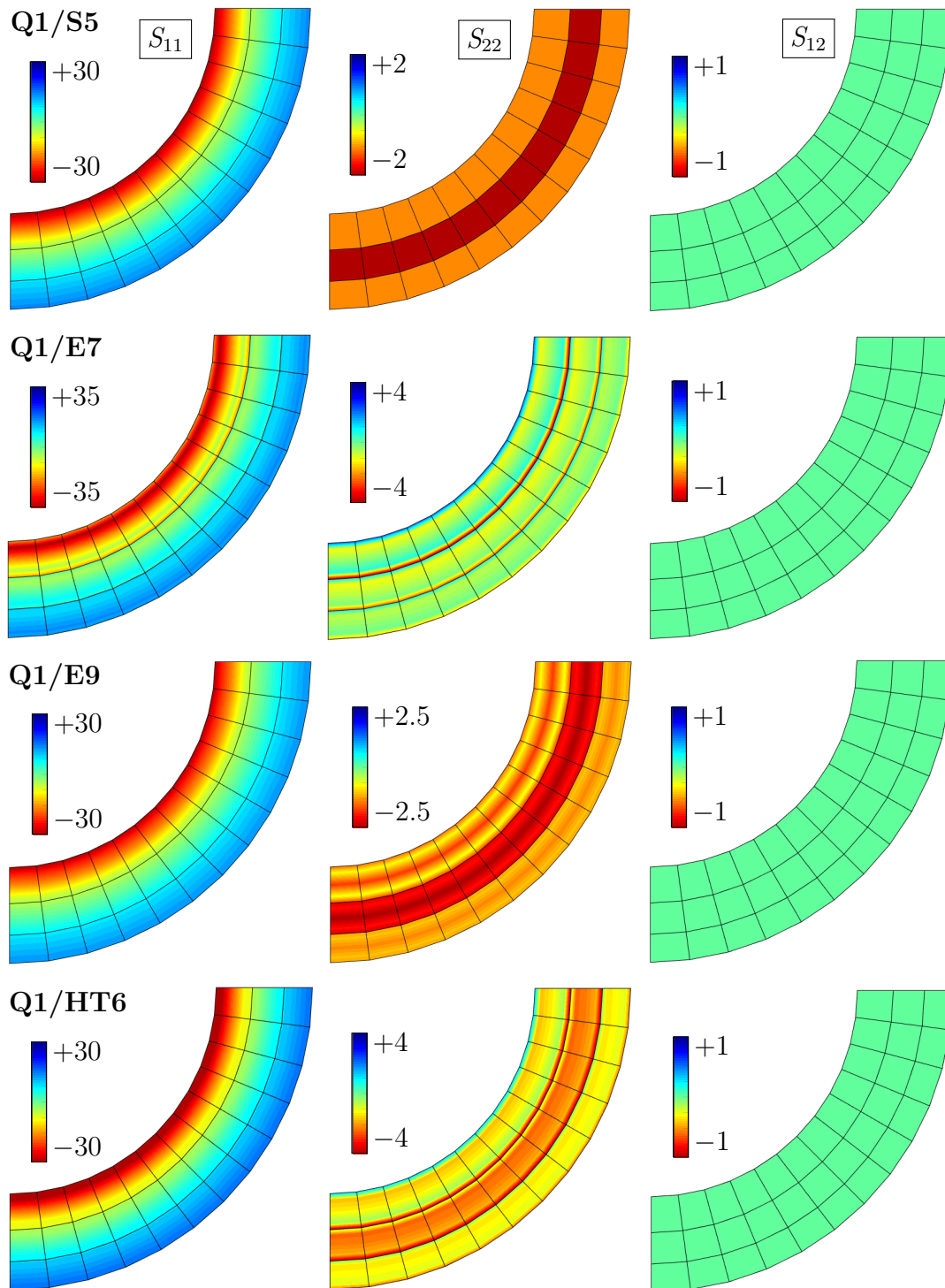


Figure 5.5: Stress quality; finite bending problem $\{L = 4, T = 1, \alpha = \pi/2, \nu = 0.499$ ($\nu = 0.5$ analytical) $\}$. Second Piola-Kirchhoff stress plotted onto the deformed configuration. Colour plots are produced with bilinear interpolation between the 5×5 Gauss-Lobatto points inside each element.

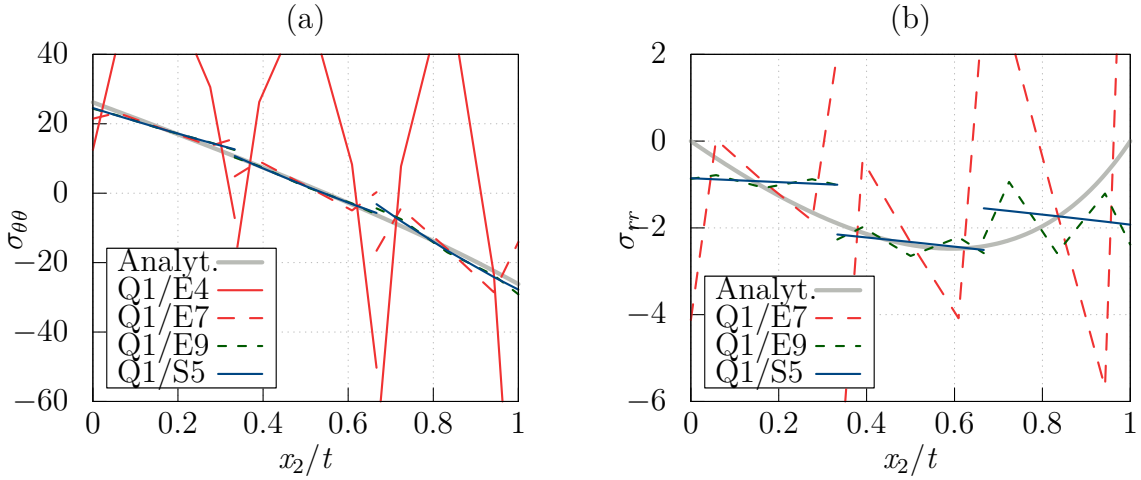


Figure 5.6: Cauchy stress at the clamped edge at $x_1 = 0$; (a) circumferential stress and (b) radial stress; numerical results are computed with three elements in thickness direction; finite bending problem $\{L = 4, T = 1, \alpha = \pi/2, \nu = 0.499$ (FEM), $\nu = 0.5$ (analytical) $\}$. Note: at the clamped edge $\sigma_{\theta\theta} = \sigma_{11}$ and $\sigma_{rr} = \sigma_{22}$, plots are produced with linear interpolation between the five Gauss-Lobatto points at the corresponding each element edge.

Figure 5.6 shows the principal Cauchy stress distribution along the radial section at the clamped edge. The analytical solution and linear interpolated stress values for various Q1/ E_m formulations are plotted. The plots show the dominant order, that degrades the accuracy; for example, Q1/E7 is free of quadratic oscillations, which are present in Q1/E4, but still shows cubic oscillations. These are not present for Q1/E9, where, on the other hand, quartic oscillations appear.

Convergence study. For various input parameters the relative L_2 -error

$$e(\sigma_{ij}) = \frac{\int_0^t (\sigma_{ij} - \sigma_{ij}^h)^2 dx_2}{\int_0^t (\sigma_{ij})^2 dx_2} \quad (5.37)$$

of the Cauchy stress at the clamped edge (at $X_1 = 0$) is computed. The error will not converge to zero because the numerical results are based on a quasi-compressible material. However, for the present investigations this is not relevant for the mesh-sizes used herein.

For $\alpha = \pi/2$, $L = 4$ and $T = 1$, Figure 5.7 (a,b) plots the relative error of the circumferential stress σ_{11} and radial stress σ_{22} , respectively, over the number of elements in X_2 -direction. The standard Q1 element shows the typical locking symptoms. Reduced preasymptotic convergence behaviour as well as a larger error than the fully locking-free

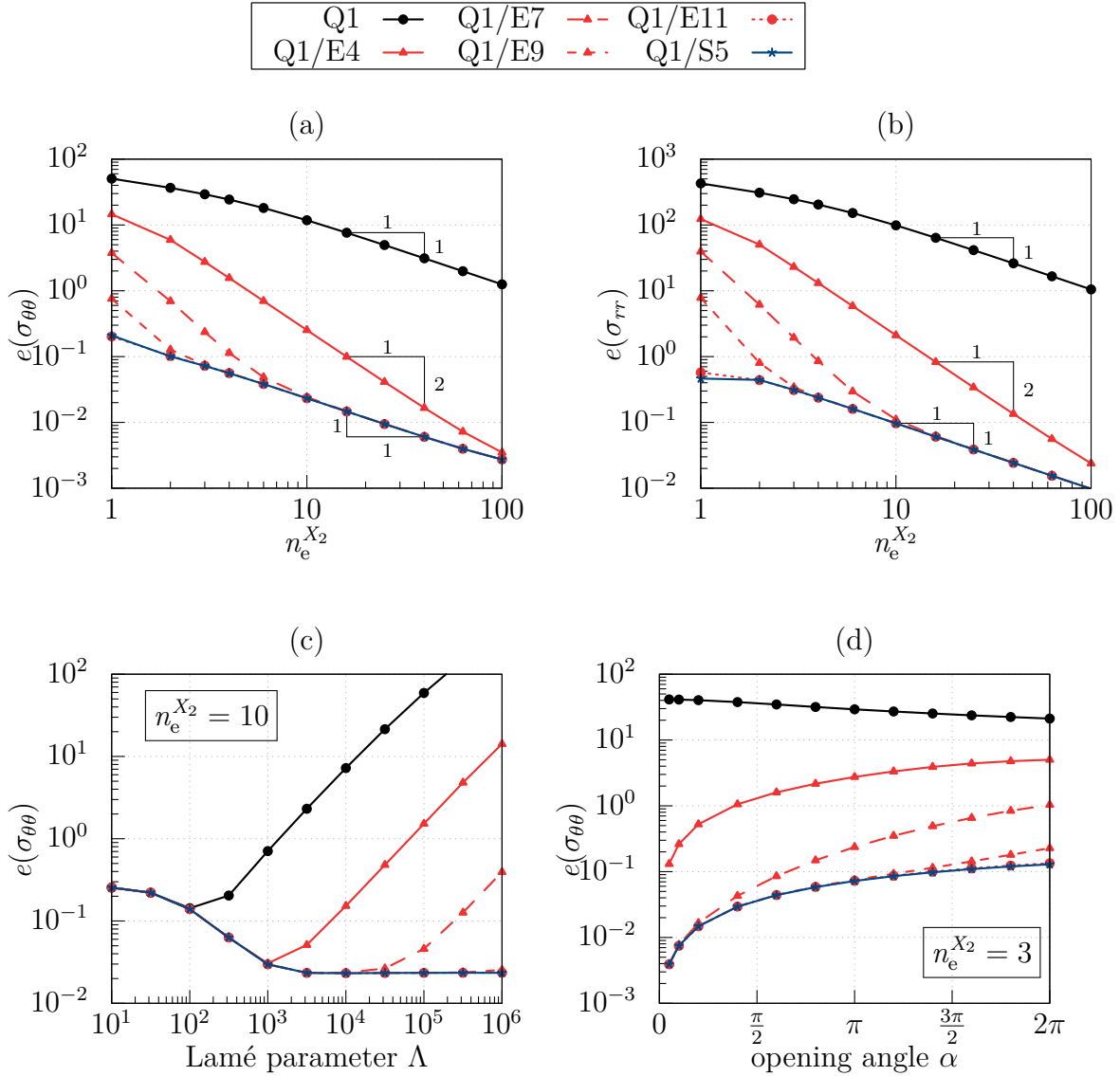


Figure 5.7: Finite bending problem (a,b,c) $\{\alpha = \pi/2, L = 4, T = 1\}$ and (d) $\{L = 8, T = 1\}$. Stress convergence.

assumed stress element Q1/S5. The results of the Q1/E m versions are visible between those curves. They lack linear locking but suffer from nonlinear locking that is inversely proportional to m . As expected, the nonlinear locking pathology is reduced by the higher order EAS elements Q1/E(7,9,11), each of which improves the error. Interestingly, the results of all Q1/E m show *higher preasymptotic convergence rates* than theoretically predicted. These rates eventually fit into the curve of the “target” Q1/S5. This be-

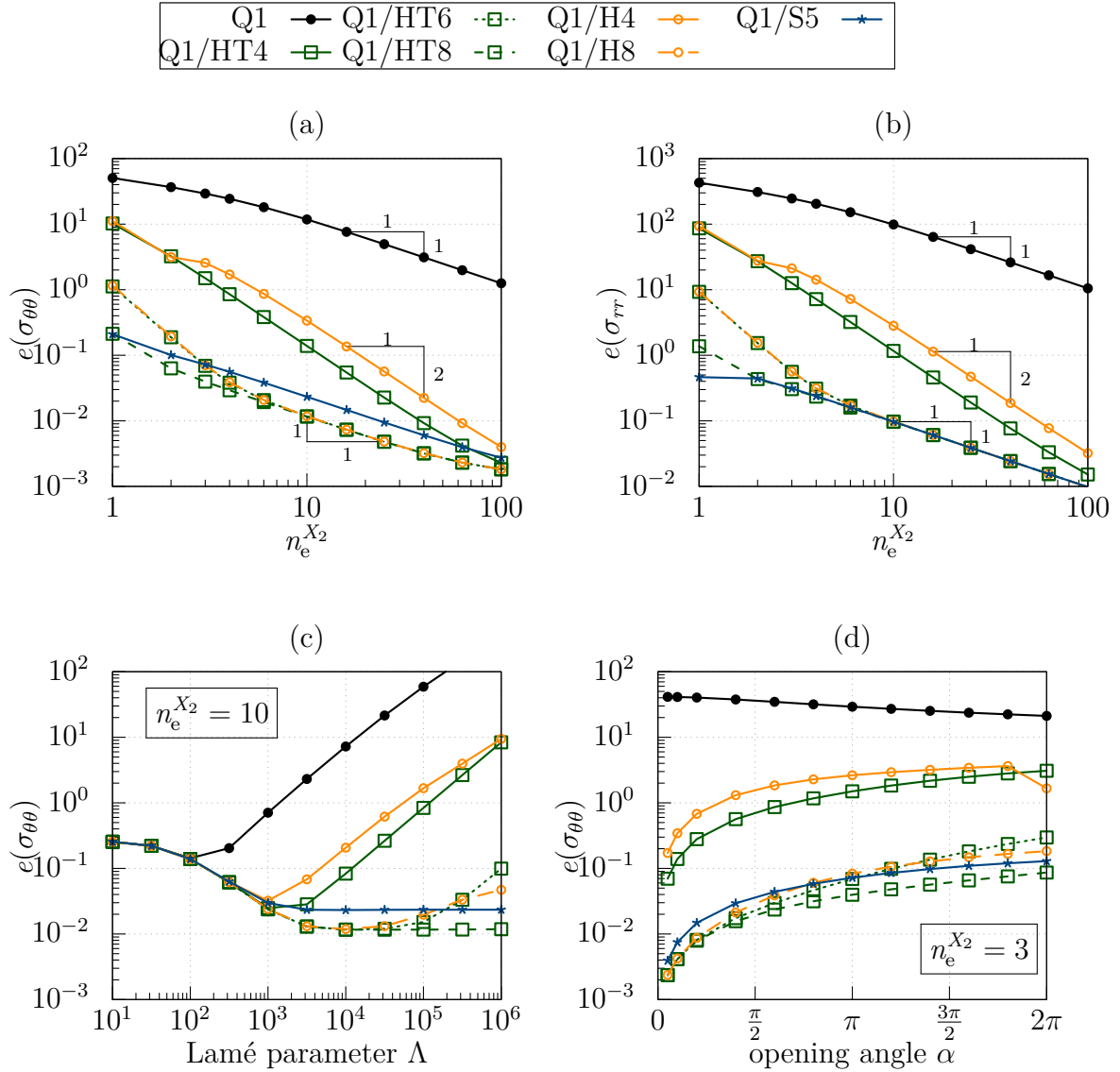


Figure 5.8: Stress convergence; finite bending problem (a,b,c) $\{\alpha = \pi/2, L = 4, T = 1\}$ and (d) $\{L = 8, T = 1\}$.

behaviour contradicts the mathematical definition of locking which constitutes *reduced preasymptotic convergence rates*; see Babuška and Suri 1992.⁵

Figure 5.7 (c) plots the error against an increasing Lamé constant Λ for a fixed (100×10) mesh. First, the error slightly decreases, since the error is dominated by the difference between the compressible (FEM) and incompressible (reference) solutions. Following

⁵A similar preasymptotic behaviour is observed for locking in the context of isogeometric formulations, see Adam et al. 2014.

that, the simulations where volumetric locking becomes dominant branch off from the locking-free curve of Q1/S5.

An interesting feature of nonlinear locking is its deformation dependency, e.g. the larger the (bending-) deformation the stronger is its impact. To analyze this further, a series of simulations is conducted for various opening angles α and fixed geometry parameters $L = 8$ and $T = 1$. For $n_e^{X_2} = 3$, Figure 5.7 (d) shows the error versus increasing values of α .

The plots in Figure 5.8 correspond to the same problems. Here, Q1/H m and Q1/HT m formulations show a similar behaviour than Q1/E m . It is remarked that the difference between Q1/H4 and Q1/HT4 is related to the mixed terms in (5.34).

5.3.2 Slender Beam Problem – Force Controlled

The introductory example of Figure 1.2 is reconsidered. It consists of a slender beam-like block, discretized with a single element layer over the thickness. The Saint-Venant-Kirchhoff material model is used. The tip of the beam is subjected to an end bending moment \hat{M} such that the initially straight configuration coils up to a circle. The results are compared with the analytical thin-beam solution, also valid for compressible materials, see Equation (4.80). Unless otherwise stated, 3×3 Gauss integration is used. As a measure of accuracy, the “coiling ratio” $r_c = \theta/(2\pi)$ is introduced. Here, θ denotes the change of angle of the edge at the tip of the beam with respect to the initial configuration. The thin limit target is $r_c = 1$, i.e., $\theta = 2\pi$. The cases $r_c > 1$ and $r_c < 1$ indicate simulation results that are too soft or too stiff, respectively.

The results for Q1 and Q1/E4 are depicted in Figure 5.9. The stiffness increases with Λ (a) and with the slenderness L/T (b), i.e., for $\Lambda \rightarrow \infty$ (or $\nu \rightarrow 0.5$) and $T \rightarrow 0$. The difference between these curves reflects linear locking, whereas the gap between Q1/E4 and the reference value occurs mainly due to nonlinear locking. It can be observed that the influence of nonlinear locking is less intense than it is for linear locking. Similar to the 2×2 integrated Q1/E4, the novel EAS formulation Q1/E7 performs superior. It is capable of modeling a full coiling of the beam, *independent* of the critical parameters. As shown in Equation (5.22), this enhancement of Q1/E7, in the context of a SVK material, is sufficient to fully remove nonlinear locking. Again, similar results, as with the novel EAS elements, can be obtained by applying 2×2 “reduced integration”.

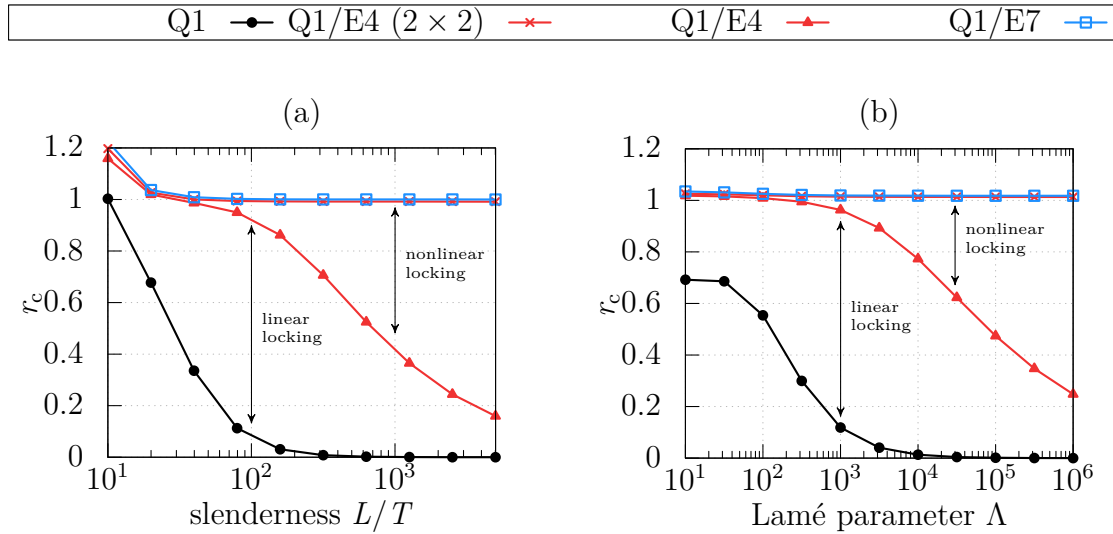


Figure 5.9: Coiling ratio (r_c) in dependence of the Lamé parameter (a) and the slenderness (b). The reference solution for the thin limit is $r_c = 1.0$.

5.3.3 Comment on Further Numerical Results.

It is once again emphasized, that the described nonlinear locking phenomena depend on the *joint interaction* of (i) a critical locking parameter, (ii) the integration scheme and (iii) the presence of large inhomogeneous element deformations. For this reason, the effects of nonlinear locking are negligibly small for a large number of benchmarks. Two main points are of importance: first, mesh refinement will immediately reduce the “amount” of inhomogeneous deformations on element level. This is because the constant strain modes increasingly dominate the element response with (uniform) mesh refinement. Second, many solid mechanic problems, even for coarse meshes, do not involve such severe inhomogeneous deformations as shown in the previous bending experiments. Thus, for problems, as for instance the well-known “Cook’s Membrane” (see for instance Glaser and Armero 1997), with coarse meshes and the presence of (i) and (ii), nonlinear locking has no significant influence on the simulation results.

Chapter 6

Physical and Artificial Instabilities of Nonlinear Finite Elements

This chapter contains further aspects already published in Bieber et al. 2022. The underlying mechanisms of physical and artificial instabilities within a finite element analysis are investigated using simple concepts known from structural mechanics. This provides insights into the causes of hourglassing and is an important step towards understanding possible stabilization strategies. The proposed class of stabilized elements is tested by means of a deformation-dependent eigenvalue analysis and a selected set of benchmarks.

6.1 Literature Review

Due to the extensive literature in this area, the following overview is limited to the most important contributions, primarily related to the enhanced assumed strain (EAS) method. A particular focus lies on two topics: first, works related to the *analysis* of artificial instabilities in finite element analysis, including contributions that deal with the issue of benchmarking against physical instabilities. The second topic focuses on works that deal with potential *remedies*. For further details, reference is made to the textbook by Wriggers 2008, the review article by Pfefferkorn and Betsch 2019 and the introduction in Bieber et al. 2022.

The first study on the hourglassing phenomenon was presented in Wriggers and Reese 1996 and Neto et al. 1995. The source of this pathology was related to large strain compressive element deformations. Herein, the corresponding hourglassing effect is referred to as *geometric hourglassing*. Korelc and Wriggers 1996 determined the necessary conditions for stable EAS elements using a parameter-dependent eigenvalue analysis. The connection of hourglassing under tensile deformations to material instabilities was

addressed in the readable article by Armero 2000. Herein, this pathological phenomenon is referred to as *material hourglassing*. Armero also emphasized the influence of the element's aspect ratio with respect to geometric hourglassing. Interestingly, the obvious analogy to established concepts in structural mechanics received less attention in the aforementioned references. Exceptional contributions are Wall et al. 2000, Sussman and Bathe 2014 and Bieber et al. 2022. All three use the buckling phenomenon of thin structural members to explain geometric hourglassing. As a result of this, the latter reference discovered also a new hourglassing effect for axially compressed thin incompatible mode elements (see Section 6.2 herein).

A decisive topic in the analysis of hourglassing is a thorough benchmarking. The finite element model should accurately capture physical instabilities, without showing unphysical numerical instabilities. A particular focus on that can be found in Auricchio et al. 2005 and Auricchio et al. 2013. Both publications point out the problems of some displacement-pressure type element formulations of showing an accurate stability behavior. Many elements were shown to be numerically stable under tension or compression, with hourglassing in the other case. A further discussion, including a three-dimensional bifurcation benchmark, can be found in Schröder et al. 2017. An analyses with regard to the influence of mesh-distortion can be found in Korelc and Wriggers 1996.

The groups around Peter Wriggers and Stefanie Reese devoted intense research on possible remedies. Within the framework of reduced integrated Q1 elements, they proposed various element formulations with a particular focus on hourglassing-free behavior (both geometric- and material-induced); see for instance Reese and Wriggers 2000 and Reese et al. 2000 for two- and three-dimensional problems, respectively. The elements are based on a physical EAS-derived “stabilization” technique, and thus carry the same hourglassing problem as the corresponding EAS element. A drawback is that the methods require the stabilization matrix to be constant within one load increment in order to preserve quadratic convergence in the Newton-Raphson scheme. This results in an element that is efficient in terms of the required Gauss points but also drastically restricted with respect to the size of the load steps. This obvious disadvantage, however, allows for appropriate modifications of the stabilization matrix, such as enforcing positive definiteness in critical situations or skipping the geometric stiffness to avoid geometric hourglassing (Reese et al. 1999). An elegant way to avoid geometric hourglassing was proposed by Korelc and Wriggers 1996, and relies on a modified shear enhancement of the displacement gradient. By that, destabilizing geometric stiffness terms cancel; see Bieber et al. 2022. However, Glaser and Armero 1997 showed that objectivity requires a modification of the enhancement, yielding, compared to the standard Q1/H4, the more complicated Q1/HT4. A particularly interesting EAS formulation based on an enhancement of the spatial displacement gradient has recently been proposed by Pfefferkorn and Betsch 2022. Numerical evidence has shown that the element is free from geometric and mate-

rial hourglassing. However, this approach results in a more complicated implementation and an unsymmetric stiffness matrix.

6.2 Introductory Example – Ritz Method

The classical method of Ritz 1909 as well as modifications of it are considered. The purpose of this “old-fashioned” method is to illustrate various instability mechanisms and enhance the understanding of the hourglassing phenomena. The bifurcation problem of Section 4.1.3, Figure 4.1, is considered. It is sought for an approximate Ritz solution $\Delta \mathbf{u}^{\text{Ritz}}$ of the incremental eigenvalue problem (4.17), i.e. the criterion for a critical point. A Galerkin approximation of the form

$$\Delta u_1^{\text{Ritz}} = \sum_{A=1}^{n_{\text{R1}}} \Delta c_A R_1^A \quad \text{and} \quad \Delta u_2^{\text{Ritz}} = \sum_{A=n_{\text{R1}}+1}^{n_{\text{R1}}+n_{\text{R2}}} \Delta c_A R_2^A, \quad (6.1)$$

and likewise for $\delta \mathbf{u}^{\text{Ritz}}$, is used. Here, $R_I^A(X_1, X_2)$ denote the *admissible* set of base functions that satisfy the essential boundary conditions (4.19) and $n_{\text{R}I}$ the number of required Ritz coefficients Δc_A for displacement direction Δu_I . An admissible set \mathcal{U}^p from a complete polynomial space up to order p is given by

$$Q_p : \begin{cases} \Delta u_1^{\text{Ritz}} \in \mathcal{U}_1^p = \text{span} (X_1, X_2, X_1 X_2, X_1^2 X_2, \dots, X_1^p X_2^p) \\ \Delta u_2^{\text{Ritz}} \in \mathcal{U}_2^p = \text{span} (\hat{R}, \hat{R} X_1, \hat{R} X_1 X_2, \dots, \hat{R} X_1^p X_2^{p-2}) \end{cases} \quad \text{for } p \geq 2, \quad (6.2)$$

with $\hat{R} = (L_2^2 - X_2^2)$ and thus $n_{\text{R1}} = (p+1)^2 - 1$ and $n_{\text{R2}} = p^2 - 1$. Here, Δu_1^{Ritz} is constrained by the rigid body translation and Δu_2^{Ritz} by the upper and lower roller support. Figure 6.1 sketches the contour plots of the involved Ritz base functions up to cubic order, for a block with $r = 1/2$. In analogy to Section 4.1.3, \mathcal{S}^I and \mathcal{A}^I designate R_1 modes which are symmetric and antisymmetric with respect to the X_I -axis.

The discrete counterpart to criterion (4.17) reads

$$\left(\mathbf{K}_m^{\text{Ritz}} + \mathbf{K}_g^{\text{Ritz}} \right) \Delta \mathbf{c}^{(j)} = \mathbf{0} \quad \text{with } \Delta \mathbf{c}^{(j)} \neq \mathbf{0}, \quad (6.3)$$

where $\mathbf{K}_m^{\text{Ritz}}$ and $\mathbf{K}_g^{\text{Ritz}}$ represent the material and geometric “Ritz stiffness matrices” (consistent unit scaling of (6.1) is assumed), index j denotes the correspondence to the j 'th critical buckling mode and $\Delta \mathbf{c} = \left[\Delta \mathbf{c}_1 \quad \Delta \mathbf{c}_2 \right]^T$ the vector of mode coefficients. Both matrices depend on the homogeneous principal solution, which is explicitly given by (4.5) and (2.63). The ansatz space (6.2) is equivalent to a single compatible quadrilateral Qp

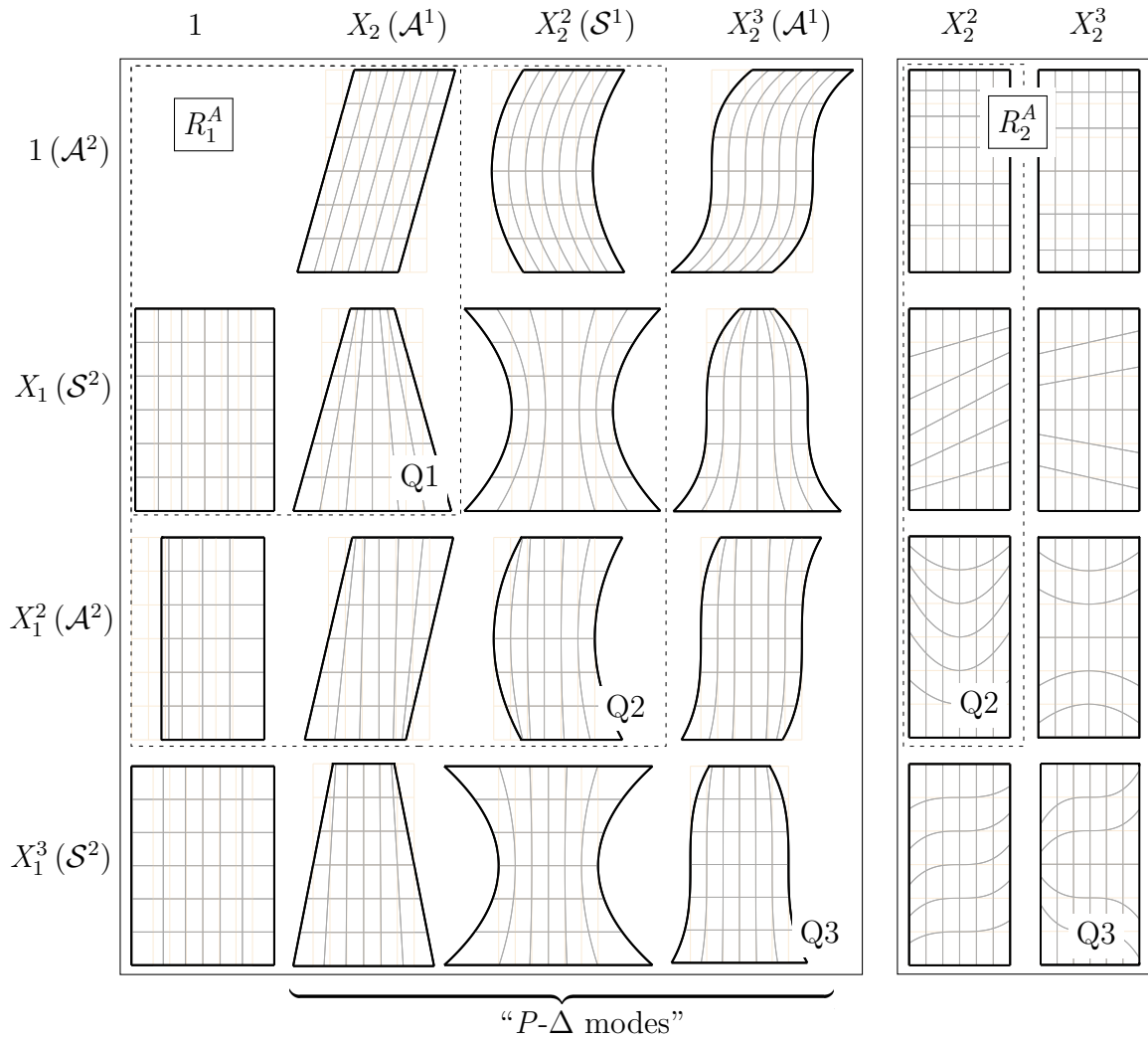


Figure 6.1: Contour plot of Ritz base functions R_1^A superimposed onto a reference grid on a block with aspect ratio $r = 1/2$. The mode designations \mathcal{A}^I and \mathcal{S}^I are only related to the R_1^A modes. The equivalence with a single Q_p element is indicated at the bottom right corner in the respective block group.

element with imposed displacement boundary conditions. Therefore this denomination is adopted herein.

6.2.1 Geometric Instability Mechanisms

A Neo-Hookean (NH) block with $E = 1000$, $\nu = 0.45$ and aspect ratio $r = 1/2$ serves as a model problem. The reference solution and Ritz solutions up to quintic order for the first four critical stretches are provided in Table 6.1. The corresponding reference buckling modes are similar (but not identical, due to a slightly different Poisson's ratio) to the ones in Figure 4.5. The underlying instability mechanism is driven by certain

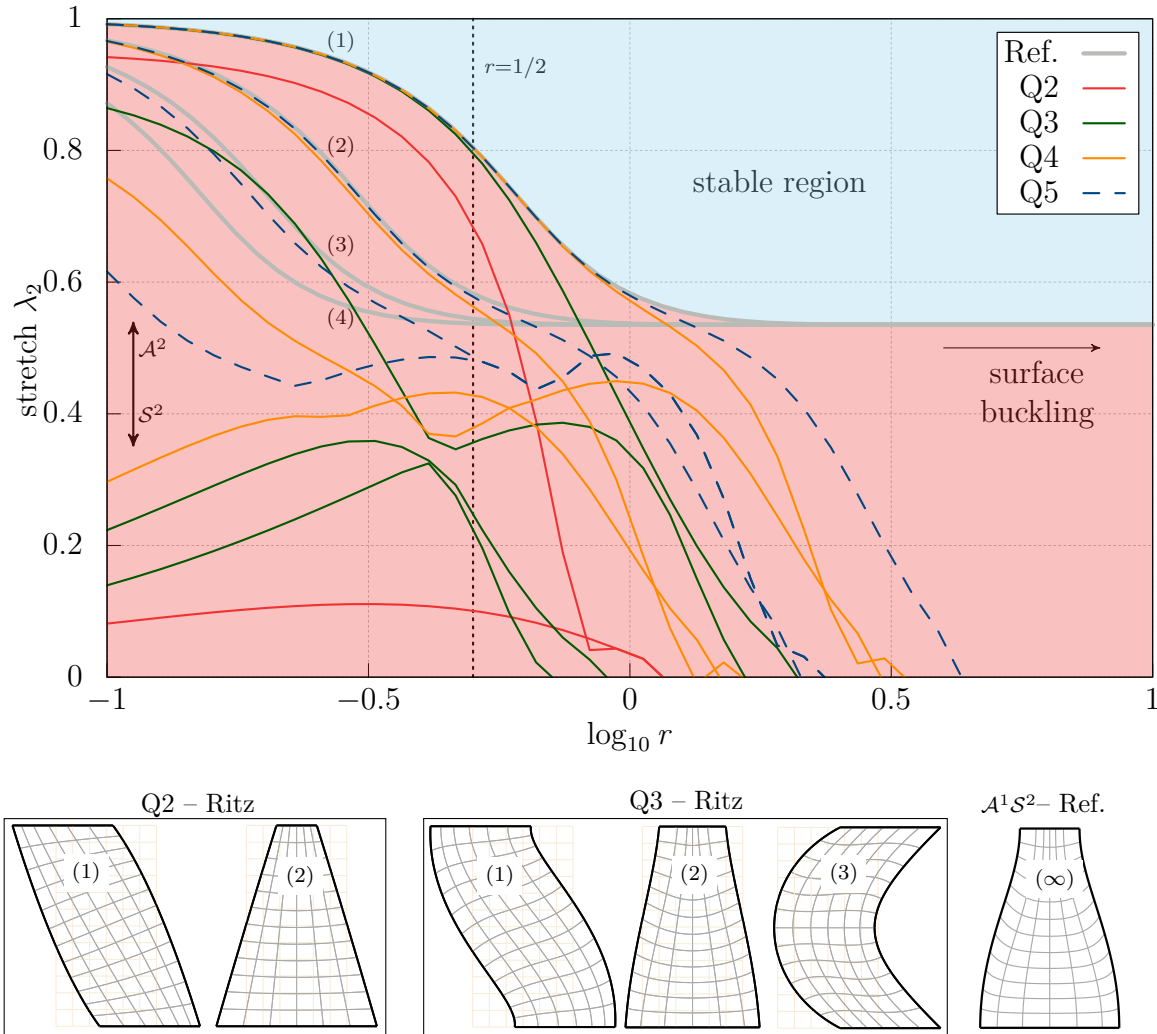


Figure 6.2: Top: stability spectrum of the first four critical stretches $\lambda_c^{(j)}$ of the reference solution and Ritz approximations vs. the aspect ratio. Numbering (j) refers only to the reference branches. Bottom: selected buckling modes superimposed on the undeformed configuration; further reference modes are depicted in Figure 4.5.

terms of the geometric stiffness. To explain this further, a loading program $\gamma = [0, \gamma_c]$ from the undeformed state $\lambda_2 = 1$ until the critical state $\lambda_2 \equiv \lambda_c^{(1)} < 1$ is considered. The material stiffness, obviously present from the start, experiences a slight stiffening during compression due to strain stiffening of the NH material. This positive “stabilizing” material stiffness is opposed by a negative geometric stiffness that accumulates in relation to the uniaxial stress state $\mathbf{S} = \text{diag}(0, S_2)$. For the present uniaxial stress scenario the

	Reference	Q1	Q2	Q3	Q4	Q5
$\lambda_c^{(1)}$	0.806 ($\mathcal{A}^1\mathcal{A}^2, n = 1$)	-	0.688	0.797	0.805	0.806
$\lambda_c^{(2)}$	0.582 ($\mathcal{S}^1\mathcal{A}^2, n = 1$)	-	(0.101)	(0.356)	0.563	0.578
$\lambda_c^{(3)}$	0.544 ($\mathcal{A}^1\mathcal{A}^2, n = 2$)	-	-	0.248	(0.429)	(0.493)
$\lambda_c^{(4)}$	0.537 ($\mathcal{S}^1\mathcal{A}^2, n = 2$)	-	-	-	(0.378)	(0.485)
$\lambda_c^{(\infty)}$	0.386 ($\mathcal{A}^1\mathcal{S}^2, n = 1$)	-	0.101	0.356	0.378	0.386

Table 6.1: Geometric instability; the first four critical stretches $\lambda_c^{(j)}$ for $j = \{1,2,3,4\}$ and the first critical reference stretch $\lambda_c^{(\infty)}$ whose buckling mode is \mathcal{S}^2 symmetric (“ ∞ ” refers to the fact that infinitely many reference \mathcal{A}^2 modes buckle earlier, see Figure 4.3). Critical stretches where the corresponding modes can not – according to the numbering with (j) – be assigned to the reference modes (Figure 4.5) are put in parentheses.

geometric stiffness can be boiled down to

$$\int_{\mathcal{B}_0} (\delta \mathbf{H}^c)^T \Delta \mathbf{H}^c : \mathbf{S} \, dV = \int_{\mathcal{B}_0} \left(\underbrace{\delta H_{12}^c \Delta H_{12}^c}_{(i)} + \underbrace{\delta H_{22}^c \Delta H_{22}^c}_{(ii)} \right) \cdot S_2 \, dV = \delta \mathbf{c}^T \mathbf{K}_g^{\text{Ritz}} \Delta \mathbf{c}. \quad (6.4)$$

Term (i) is the origin of the essential trigger mechanism for geometric instabilities. It is caused by the displacement modes in gradient component H_{12}^c . This corresponds to all X_2 -dependent terms of R_1^A in Figure 6.1. The resulting stiffness is related to the “ P - Δ effect” in structural mechanics. This effect describes the destabilizing lateral stiffness of a truss that is caused by a change in lever arm Δ perpendicular to axial compression forces P . For the corresponding 2d modes, referred to as “ P - Δ modes” in the sequel. The analogy is given by $\Delta \hat{=} \Delta u_1^{\text{Ritz}}$ and $P \hat{=} S_2$. The P - Δ modes can be classified into \mathcal{A}^1 and \mathcal{S}^1 modes; see the corresponding columns in Figure 6.1. However, only the mode combinations that involve \mathcal{A}^2 -bending modes are physically relevant for geometric instabilities, because their material stiffness is significantly lower than that of \mathcal{S}^2 modes.¹ These observations are in full agreement with the analytical results sketched in Figure 4.3. Term (ii) also contributes to the geometric stiffness. The displacement modes involved are all X_2 -dependent terms of R_2^A , i.e., all modes in the right block of Figure 6.1. For geometric instabilities, these modes do not contribute significantly. However, they play a role in “stabilizing” the structure in the context of critical tensile deformation states.

¹Physically “relevant” in the sense that the first upcoming bifurcations correspond all to \mathcal{A}^1 modes. However, this statement is only valid for the present example. For different displacement boundary conditions, the $\mathcal{S}^1\mathcal{S}^2$ modes may also represent critical “bending modes”.

Concrete examples are considered. A bilinear ansatz with $p = 1$ yields

$$Q1 : \begin{cases} \Delta \mathbf{u}_1^{\text{Ritz}} \in \mathcal{U}_1^1 = \text{span}(X_1, X_2, X_1 X_2) \\ \Delta \mathbf{u}_2^{\text{Ritz}} \in \mathcal{U}_2^1 = \emptyset \end{cases} \quad (6.5)$$

For this coarse ansatz no critical deformation state occurs. This is not too much of a surprise, since the reference solution

$$\begin{aligned} \Delta u_1 &= C \sin(0.785 X_2) [0.841 \cosh(1.119 X_1) - 1.472 \cosh(0.785 X_2)] \\ &\approx C \left(-0.496 X_2 + 0.051 X_2^3 + 0.057 X_1^2 X_2 - 0.002 X_2^5 \right), \\ \Delta u_2 &= C \cos(0.785 X_2) [0.869 \sinh(1.119 X_1) - \sinh(0.785 X_1)] \\ &\approx C \left(0.187 X_1 - 0.057 X_1 X_2^2 + 0.122 X_1^3 \right), \end{aligned} \quad (6.6)$$

with the arbitrary constant $C \in \mathbb{R}$, is barely contained in \mathcal{U}_f^1 . A biquadratic ansatz with $p = 2$ is given by

$$Q2 : \begin{cases} \Delta \mathbf{u}_1^{\text{Ritz}} \in \mathcal{U}_1^2 = \mathcal{U}_1^1 + \text{span}(X_2^2, X_1 X_2^2, X_1^2, X_1^2 X_2, X_1^2 X_2^2) \\ \Delta \mathbf{u}_2^{\text{Ritz}} \in \mathcal{U}_2^2 = \text{span}(\hat{R}, \hat{R} X_1, \hat{R} X_1^2) \end{cases} \quad (6.7)$$

Now, two critical deformation states are met. The corresponding buckling modes are given by

$$\left(\Delta \mathbf{u}^{\text{Ritz}} \right)^{(1)} = C \cdot \begin{bmatrix} -0.496 X_2 + 0.122 X_1^2 X_2 \\ 0.352 X_1 - 0.088 X_1 X_2^2 \end{bmatrix} \quad (6.8)$$

and

$$\left(\Delta \mathbf{u}^{\text{Ritz}} \right)^{(2)} = C \cdot \begin{bmatrix} -0.998 X_1 X_2 \\ -0.11 + 0.028 X_2^2 + 0.247 X_2^2 - 0.062 X_1^2 X_2^2 \end{bmatrix}, \quad (6.9)$$

with the arbitrary real constant C . The bottom part of Figure 6.2 shows the corresponding buckling modes for $p = 2$ and $p = 3$. Interesting to observe: for the quadratic and cubic case, the first buckling mode is properly modeled according to the given Ritz ansatz. Surprisingly, the second buckling modes initially correspond to the first \mathcal{S}^2 -symmetric reference mode depicted in Figure 6.2. It is a good approximation to a physically irrelevant mode. In fact, higher-order bifurcation modes do *not necessarily* involve more complex buckling patterns. See also the analytical investigations in Section 4.1.4, in particular Figure 4.3.

This explains the critical branches of the Ritz solutions in the domain $r < 1$ ($\log_{10} r < 0$) in Figure 6.2.² Depending on the approximation power, the first critical reference branches are captured. Followed by that, a gap occurs and the subsequent critical branches are found in severe compression states. The gap indicates a mode shift of the corresponding solutions from \mathcal{A}^2 to \mathcal{S}^2 (indicated by the double arrow). As expected, the surface buckling phenomenon is hardly captured by the considered approximations, since a *global* Ritz ansatz is not suitable to model this *local* phenomenon. Another insight into the problem is that all j 'th reference branches provide an upper bound for the corresponding j 'th branch of the numerical solutions, which is directly related to approximation property (3.29). In other words, the Ritz approximations perform too stiff and consequently, the j 'th branch should not appear above the analytical solution of that branch. This further implies that none of the approximated branches should appear in the stable region. Of course, this also applies for displacement-based finite element solutions.

6.2.2 Geometric Hourglassing Phenomenon

A special “incompatible” Ritz approximation can be used to recover the incompatible mode element from Wilson et al. 1973. Under certain conditions, the latter is also equivalent to the Q1/H4 formulation from Section 3.3.2. The purpose of this approach is to illustrate the mechanism of geometric hourglassing in terms of the Ritz modes from Figure 6.1 and how a simple modification provides a remedy. Similar investigations, all within the framework of a structural instability concepts, are presented in Section 2 of Bieber et al. 2022 as well as Sussman and Bathe 2014 and Wall et al. 2000.

Incompatible Ritz ansatz. A single Q1/H4 element can be mimicked via an *incompatible Ritz ansatz* of the form

$$\text{Q1/H4} : \begin{cases} \Delta \mathbf{u}_1^{\text{IRitz}} & \in \mathcal{U}_1^1 + \text{span}(X_1^2, X_2^2) \\ \Delta \mathbf{u}_2^{\text{IRitz}} & \in \mathcal{U}_2^1 + \text{span}(X_1^2, X_2^2) \end{cases} \quad (6.10)$$

providing

$$\Delta \mathbf{u}^{\text{IRitz}} = \begin{bmatrix} \Delta c_1 X_2 + \Delta c_2 X_1 + \Delta c_3 X_1 X_2 + \Delta c_4 X_1^2 + \Delta c_5 X_2^2 \\ \underline{\Delta c_6 X_1^2 + \Delta c_7 X_2^2} \end{bmatrix} \quad (6.11)$$

Here the underlined terms are introduced, irrespective of the essential boundary conditions. The gradient resembles the EAS ansatz (3.54) with correspondences $\xi \rightarrow X_1$ and

²The graph can be read “from top to bottom” with respect to the vertical axis, i.e., from the undeformed state $\lambda_2 = 1$ to full compression of the block $\lambda_2 \rightarrow 0$.

$\eta \rightarrow X_2$. For the present scenario, modes 6 and 7 violate the displacement constraint at the top and bottom edges. In the context of finite elements, these modes provide a locking-free element, i.e., the material part of the stiffness matrix is improved.³ The focus of the present study lies on the influence of ansatz (6.11) on the geometric stiffness matrix and on the stability behaviour. According to Equation (6.4) only the displacement gradient component

$$\Delta H_{12} = \frac{\partial \Delta u_1^{\text{IRitz}}}{\partial X_2} = \underbrace{\Delta c_1}_{\text{(i)}} + \underbrace{\Delta c_3 X_1}_{\text{(ii)}} + \underbrace{2\Delta c_5 X_2}_{\text{(iii)}} \quad (6.12)$$

contributes to the destabilizing P - Δ stiffness. The three terms in H_{12} fully explain the physical and artificial stability behaviour of the Q1/H4 element:

- Term (i) comes from the compatible linear shear mode $R_1^1 = X_2$. It is the lowest-order \mathcal{A}^1 -antisymmetric P - Δ mode required for modeling $\mathcal{A}^1 \mathcal{A}^2$ buckling modes. In the context of finite elements, this term is essential for modeling physical instabilities, in particular with mesh refinement.
- Term (ii) comes from the compatible bilinear mode $R_1^3 = X_1 X_2$. Its resulting geometric stiffness is responsible for the $\mathcal{A}^1 \mathcal{S}^2$ buckling modes. However, when combined with the incompatible Ritz mode 6, it results in an artificial instability:

Hourglassing effect I: Figure 6.3 (a) depicts a critical buckling mode, caused by geometric stiffness due to (ii). The violation of the kinematic BC is obvious. In the context of finite elements, this yields the well-known hourglassing phenomenon.

- Term (iii) comes from the quadratic mode $R_1^5 = X_2^2$. It is the lowest-order \mathcal{S}^1 -symmetric P - Δ mode, and the geometric stiffness it produces gives rise to the $\mathcal{S}^1 \mathcal{A}^2$ buckling modes. For the classical Euler buckling of an axially loaded beam pinned at both ends, this is the essential trigger mechanism. Because the involved displacement modes necessitate the bilinear mode $R_2 = X_1 X_2$, no related instability appears in this example. However, for other boundary conditions or inside assembled finite element patches, this instability is present and yields an artificial instability:

Hourglassing effect II: Figure 6.3 (b) illustrates a critical buckling mode caused by the geometric stiffness of $R_2^6 = X_1^2$, i.e., the rotated equivalent to term (ii). The violation of the kinematic BC is obvious. In the context of finite elements, this yields an hourglassing phenomenon that was only recently discovered by Bieber et al. 2022.

³Locking phenomena are theoretically present in the Ritz method as well. However, lower-order Ritz base functions are rarely used, and higher ansatz spaces, such as p -refinement, are used to compensate.

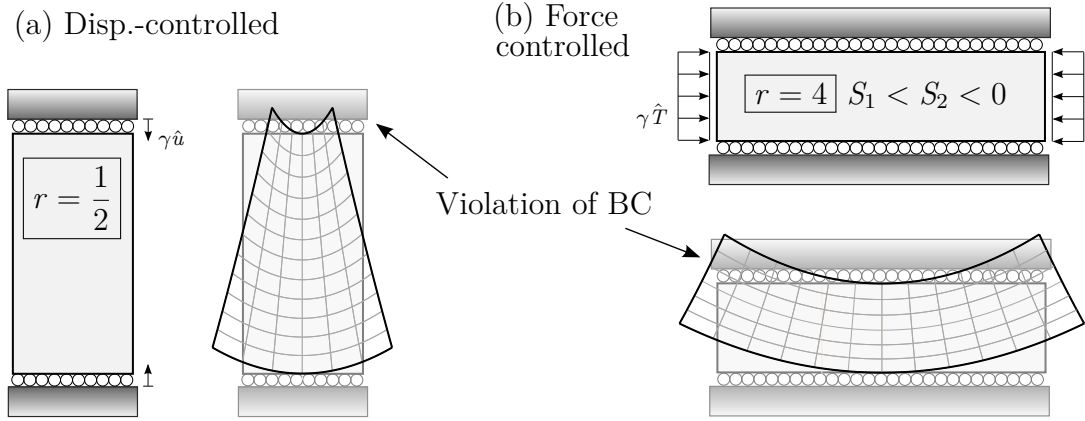


Figure 6.3: Illustration of two geometric hourglassing phenomena via an incompatible Ritz approximation; left: hourglassing effect I; right: hourglassing effect II.

The critical stretch values of the problems in Figure 6.3 are $\lambda_2 = 0.483$ (a) and $\lambda_1 = 0.531$ (b). However, it is remarked that both pathological instabilities strongly depend on the aspect ratio of the block (or the element in the context of hourglassing). The critical stress estimates based on a pre-buckling analysis provide

$$S_2 = \frac{\tilde{E}}{r_e^2} \quad \text{and} \quad S_2 = \frac{\tilde{E}r_e^2}{1+r_e^2} \approx \tilde{E}r_e^2, \quad \text{with } \tilde{E} = E/(1-\nu^2) \quad (6.13)$$

for hourglassing effect I and II, respectively; see Section 2 in Bieber et al. 2022. The former is particularly relevant (in the sense that buckling occurs early, i.e., in small strain regimes) for large aspect ratios, and the latter for small ones.

6.2.3 Material-Induced Structural Instability Mechanisms

A Blatz-Ko (BK) block with $\mu = 100$ and $r = 1/2$ serves as a model problem. The reference solution and some Ritz solutions for the first four critical stretches are provided in Table 6.2. The buckling modes that correspond to the reference solutions are provided in Figure 4.6.

As opposed to geometric instabilities, the underlying instability mechanism is driven by the material part of the stiffness matrix. For the present uniaxial stress scenario, the material stiffness reads

$$\int_{\tilde{B}_0} \delta H_{aB}^c A_{aBcD}^m \Delta H_{cD}^c dV = \int_{\tilde{B}_0} \delta E_{AB}^c C_{ABCD} \Delta E_{CD}^c dV = \delta \mathbf{c}^T \mathbf{K}_m^{\text{Ritz}} \Delta \mathbf{c}. \quad (6.14)$$

	Reference	Q1	Q2	Q3	Q4	Q5
$\lambda_c^{(1)}$	2.285 ($\mathcal{A}^1\mathcal{S}^2, n = 1$)	-	2.286	2.286	2.285	2.285
$\lambda_c^{(2)}$	2.302 ($\mathcal{S}^1\mathcal{S}^2, n = 1$)	-	-	2.314	2.312	2.302
$\lambda_c^{(3)}$	2.328 ($\mathcal{A}^1\mathcal{S}^2, n = 2$)	-	-	-	2.371	2.355
$\lambda_c^{(4)}$	2.363 ($\mathcal{S}^1\mathcal{S}^2, n = 2$)	-	-	-	-	2.459

Table 6.2: Material-induced structural instability; the first four critical stretches $\lambda_c^{(j)}$ for $j = \{1,2,3,4\}$ and the first critical reference stretch.

Here, \mathbb{A}^m is the material part of the constitutive elasticity tensor, defined in Equation (2.46). Certain parts of the material stiffness become negative as the strain softens in the X_2 -direction. The part that primarily contributes to the destabilizing material stiffness can be identified as

$$\int_{\mathcal{B}_0} \delta H_{22}^c A_{2222}^m \Delta H_{22}^c \, dV = \int_{\mathcal{B}_0} \delta H_{22}^c \lambda_2^2 C_{2222}^m \Delta H_{22}^c \, dV. \quad (6.15)$$

Here, C_{2222} is the axial stiffness at the continuum point, which experiences softening. The axial stiffness becomes negative when $\lambda_2 > 2^{3/4} \approx 1.681$. This means that all displacement modes present in the gradient component H_{22}^c contribute to the material stiffness destabilization. This includes all R_2^A modes in Figure 6.1. These modes are referred to as “strain-softening” modes.

Again, concrete examples are considered. The linear Ritz ansatz (6.5) does not provide any instability, because $\mathcal{U}_2^1 = \emptyset$ and thus $H_{22} = 0$. Figure 6.4 shows the buckling modes for a quadratic and cubic approximation. The corresponding critical stretch values in Table 6.2 are in good agreement with the reference solution. It is noted that, similar to the geometric instability problem, higher-order bifurcations as well as bulkier blocks are more poorly approximated as the buckling patterns become more complex.

6.2.4 Material Hourglassing

The incompatible Ritz approximation (6.11) is considered. In contrast to Q1, Q1/H4 is able to capture the stretch that corresponds to the first critical necking mode. Through the incompatible mode $c_7 X_2^2$, the decreasing stiffness of C_{2222} propagates into the material stiffness matrix. In the context of finite elements, this mode is introduced to eliminate volumetric locking. However, as illustrated in Figure 6.4 this goes hand in hand with a severe violation of the kinematic boundary conditions.

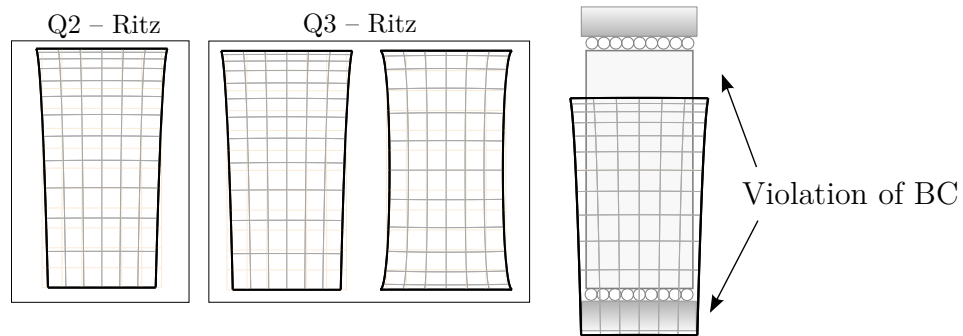


Figure 6.4: Material-induced structural instability; middle-left: selected buckling modes; right: illustration of material hourglassing phenomena via an incompatible Ritz approximation.

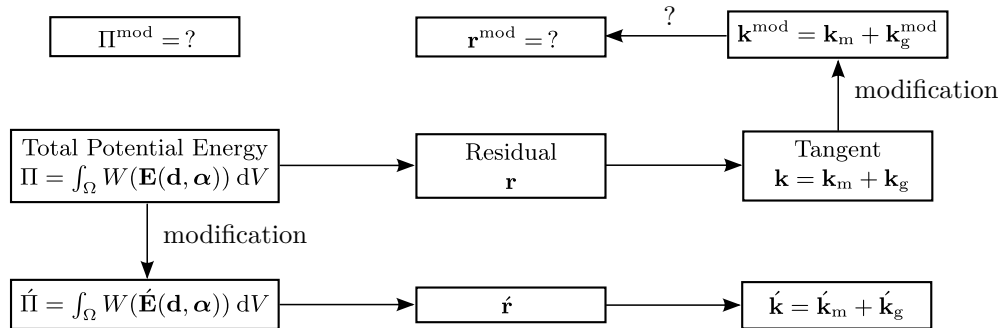


Figure 6.5: Illustration of implications of modifications of a finite element formulation.

6.3 Approach to Avoid Hourglassing

Geometric Hourglassing. In the previous section, it was shown that certain displacement modes are responsible for geometric hourglassing. For the actual finite element implementation, however, it is not efficient to simply skip the corresponding terms from the geometric stiffness matrix. In order to preserve quadratic convergence within the Newton-Raphson scheme or to use explicit solvers, modifications of the residual vector are required. Figure 6.5 shows the inverse problem in the upper row. A possible remedy to that is a (within one load increment) constant stabilization procedure; see for instance Reese et al. 1999. This goes along with an additional implementation effort as well as limitations with respect to the size of the load increment. For a *generally applicable method* it is desired to provide a modified potential of the respective problem, followed by a computation of residual and tangent in a standard manner. The envisaged “one-way street” is shown in Figure 6.5, where the accent denotes the modifications described next.

An efficient way to circumvent these drawbacks is based on the following observation: according to Equation (6.4), only the *quadratic* part $\mathbf{H}^T \mathbf{H}$ of the Green-Lagrange strain

tensor influences the geometric stiffness and thus potentially geometric hourglassing. Remedy provides a modified Green-Lagrange strain expression of the form

$$\boxed{\dot{\mathbf{E}} := \frac{1}{2} \left(\mathbf{H}^T + \mathbf{H} + \mathbf{H}_r^T \mathbf{H}_r + \mathbf{H}_r^T \mathbf{H}_h + \mathbf{H}_h^T \mathbf{H}_r + \beta \mathbf{H}_h^T \mathbf{H}_h \right)} \quad (6.16)$$

with an additive split $\mathbf{H} = \mathbf{H}_r + \mathbf{H}_h$, where \mathbf{H}_h denotes the part that is responsible for geometric hourglassing. For $\beta = 0$, this yields the modified geometric tangent

$$\dot{\mathbf{k}}_g = \int_{\Omega} \frac{1}{2} \left(\mathbf{H}_r^T \mathbf{H}_r + \mathbf{H}_r^T \mathbf{H}_h + \mathbf{H}_h^T \mathbf{H}_r \right)_{,\bar{\mathbf{d}}} : \mathbf{S}(\dot{\mathbf{E}}) \, dV. \quad (6.17)$$

Here, with a slight abuse of notation, $\bar{\mathbf{d}}$ may also represent a more generic element vector of degrees of freedom (e.g. $\bar{\mathbf{d}} = [\mathbf{d} \quad \boldsymbol{\alpha}]^T$) and $\dot{\mathbf{k}}_g$ is the corresponding geometric element stiffness matrix. In addition to that, the material stiffness matrix and the residual vector are also modified. Consistent linearization automatically preserves quadratic convergence. Furthermore, it is efficient to implement since only minor changes to existing element routines are required. The method can be viewed as a self-adaptive stabilization procedure that is only activated for geometric nonlinearity, i.e., when the quadratic part of the Green-Lagrange strain tensor plays a role. In the linear regime, however, the modifications do not affect the element. The fact that $\det \dot{\mathbf{C}} < 0$ (matter penetration) is possible is a critical aspect of the modification (6.16). It can be shown that this corresponds to very large in-plane bending deformations. This is of minor relevance for practical computations and, more importantly, with mesh refinement this defect diminishes.

For details on one possible efficient implementation, it is referred to Bieber et al. 2022. However, this implementation is based on a modification of the shape functions. This approach also modifies the H_{22} -term in Equation (6.4). However, since these terms do not lead to hourglassing, elimination is not necessary. In order to allow simple implementation, these terms are nevertheless included in \mathbf{H}_h . Table 6.4 gives an overview of the modified versions of the original element formulations from Section 3.3.

Material Hourglassing. Avoiding the issue of material hourglassing by means of a similar strategy is substantially more difficult. In terms of the Ritz stiffness, the cause of instability can be traced back to certain parts of the material stiffness matrix in (6.14). In contrast to the geometric instability, the responsible trigger mechanism emanates mainly from the linear part of the Green-Lagrange strain tensor. In analogy to (6.16),

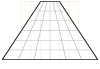
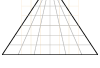
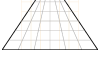
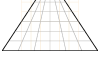

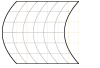
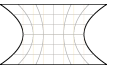
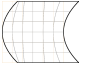
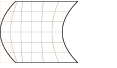
	Modified strain measure	P - Δ modes*
Q1/ME4	$\mathbf{H}_r = \mathbf{H}_0^c, \mathbf{H}_h = \mathbf{H}_1^c$ with $\mathbf{E} = \mathring{\mathbf{E}}^c + \tilde{\mathbf{E}}$	
Q1/MS5	$\mathbf{H}_r = \mathbf{H}_0^c, \mathbf{H}_h = \mathbf{H}_1^c$	
Q1/MH4-I	$\mathbf{H}_r = \mathbf{H}_0^c + \tilde{\mathbf{H}}, \mathbf{H}_h = \mathbf{H}_1^c$	
Q1/MH4-II	$\mathbf{H}_r = \mathbf{H}_0^c, \mathbf{H}_h = \mathbf{H}_1^c + \tilde{\mathbf{H}}$	 
Q2/ME11	$\mathbf{H}_r = \mathbf{H}_0^c + \mathbf{H}_1^c, \mathbf{H}_h = \mathbf{H}_2^c + \mathbf{H}_3^c$ with $\mathbf{E} = \mathring{\mathbf{E}}^c + \tilde{\mathbf{E}}$	   

Table 6.3: Definitions of \mathbf{H}_r and \mathbf{H}_h for various finite element formulations and an illustration of the involved P - Δ modes. Here \mathbf{H}_m^c denotes a multivariate Taylor expansion of order m . *Likewise for the modes in X_2 -direction (not displayed).

a modification of the form

$$\check{\mathbf{E}} := \frac{1}{2} \left(\mathbf{H}_r^T + \mathbf{H}_r + \underbrace{\mathbf{H}_h^T + \mathbf{H}_h}_{:=0} + \mathbf{H}^T \mathbf{H} \right) \quad (6.18)$$

would be required. Here, as before, \mathbf{H}_h represents both compatible hourglass modes. The corresponding element based on Q1/E4 is denoted as Q1/ME4*. Of course, the strain measure $\check{\mathbf{E}}$ is a poor choice, because it does not resemble the strain tensor from linear theory. In addition, the stiffness matrix is singular at the initial state, and artificial stabilization is required. However, numerical experiments have indicated that material hourglassing can be avoided while still capturing material-induced structural instabilities. Potential remedies may be obtained by a modification of the constitutive law of the responsible “strain-stiffening” modes; see Equation 6.15. A principally similar strategy can also be found in Mueller-Hoeppe et al. 2009.

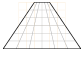
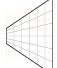
	ω_1^{hg} 	ω_2^{hg} 
Q1	$\frac{1}{3r_e} (A_{11}^n + r_e^2 A_{11}^s)$ $= \frac{\lambda_1^2 (C_{11}^n + r_e^2 C_{12}^s)}{3r_e} + \frac{(r_e^2 S_2 + S_1)}{3r_e}$	$\frac{1}{3r_e} (r_e^2 A_{22}^n + A_{22}^s)$ $= \frac{\lambda_2^2 (r_e^2 C_{22}^n + C_{12}^s)}{3r_e} + \frac{(r_e^2 S_2 + S_1)}{3r_e}$
Q1/E4	$\frac{\lambda_1^2 \det \mathbf{C}^n}{3r_e C_{22}^n} + \frac{(r_e^2 S_2 + S_1)}{3r_e}$	$\frac{r_e \lambda_2^2 \det \mathbf{C}^n}{3C_{11}^n} + \frac{(r_e^2 S_2 + S_1)}{3r_e}$
Q1/E2s	$\frac{\lambda_1^2 C_{11}^n}{3r_e} + \frac{(r_e^2 S_2 + S_1)}{3r_e}$	$\frac{r_e \lambda_2^2 C_{11}^n}{3} + \frac{(r_e^2 S_2 + S_1)}{3r_e}$
Q1/E2n	$\frac{\lambda_1^2 \det \mathbf{C}^n}{3r_e C_{22}^n} + \frac{r_e \lambda_1^2 C_{12}^s}{3} + \frac{(r_e^2 S_2 + S_1)}{3r_e}$	$\frac{r_e \lambda_2^2 \det \mathbf{C}^n}{3C_{11}^n} + \frac{\lambda_2^2 C_{12}^s}{3r_e} + \frac{(r_e^2 S_2 + S_1)}{3r_e}$
Q1/H4	$\frac{\det \mathbf{A}^n}{3r_e A_{22}^n} + \frac{r_e \det \mathbf{A}^s}{3A_{22}^s}$	$\frac{r_e \det \mathbf{A}^n}{3A_{11}^n} + \frac{\det \mathbf{A}^s}{3r_e A_{11}^s}$
Q1/HT4	$\frac{\det \mathbf{A}^n}{3r_e A_{22}^n}$	$\frac{r_e \det \mathbf{A}^n}{3A_{11}^n}$
Q1/ME4	$\frac{\lambda_1^2 \det \mathbf{C}^n}{3r_e C_{22}^n}$	$\frac{\lambda_2^2 r_e \det \mathbf{C}^n}{3C_{11}^n}$
Q1/MH4-I	$\frac{\det \mathbf{A}^n}{3r_e A_{22}^n} + C_{12}^s \left(\frac{r_e \lambda_1^2}{3} + \frac{\lambda_2^2}{3r_e} \right)$ $-\frac{A_{22}^s}{3r_e} - \frac{r_e (A_{12}^s)^2}{3A_{22}^s}$	$\frac{r_e \det \mathbf{A}^n}{3A_{11}^n} + C_{12}^s \left(\frac{r_e \lambda_1^2}{3} + \frac{\lambda_2^2}{3r_e} \right)$ $-\frac{r_e A_{11}^s}{3} - \frac{(A_{12}^s)^2}{3r_e A_{11}^s}$
Q1/MH4-II	$\frac{\lambda_1^2 \det \mathbf{C}^n}{3r_e C_{22}^n}$	$\frac{\lambda_2^2 r_e \det \mathbf{C}^n}{3C_{11}^n}$

Table 6.4: Hourglass eigenvalues of a rectangular-shaped element with aspect ratio $r = L_1^e/L_2^e$ and biaxial stress state $\mathbf{S} = \text{diag}(S_1, S_2)$. Here \mathbf{A}^n , \mathbf{A}^s and \mathbf{C}^s refer to the constitutive targets defined in (2.50) and (2.51).

6.4 Modal Analysis

The eigenvalue monitoring of a fully *unconstrained* tangent stiffness matrix in combination with parameter variations is a crucial tool in the stability analysis of finite elements, see Armero 2000. A single $L_1^e \times L_2^e$ element under plane strain condition is subjected to a homogeneous uniaxial stress state with $\mathbf{S} = \text{diag}(0, S_2(\lambda_2))$. A compressible BK rubber is considered. The hourglass eigenvalues are given as

$$\omega_i^{\text{hg}} = (\Phi_{b,i}^{\text{lin}})^T \mathbf{k}_{\text{red}}(\lambda_1, \lambda_2) \Phi_{b,i}^{\text{lin}} \quad i = 1, 2, \quad (6.19)$$

with the reduced stiffness matrix defined in (3.43) and the normalized hourglass eigenvector $\Phi_{b,i}^{\text{lin}}$ (Equation (5.4)). Closed-form expressions of the hourglass eigenvalues are summarized in Table 6.4. For lower-order Q1 elements, no physically relevant instability can be expected. Thus, a negative hourglass eigenvalue is an indicator that hourglassing is likely to occur. Both are considered separately next.

Geometric Hourglassing. The focus lies only in the compression domain $\lambda_2 < 1$. Figure 6.6 shows the first hourglass eigenvalue for aspect ratios $r_e = 1$, $r_e = 0.2$ (tall skinny element) and $r_e = 5$ (flat bulky element). Both standard EAS formulations Q1/E4 and Q1/H4 as well as Q1/E2s suffer from geometric hourglassing (see Hourglassing effect I in Section 6.2). The critical stretch where $\omega_1^{\text{hg}} = 0$ depends on the aspect ratio, i.e. geometric hourglassing is particularly pronounced for large aspect ratios. In contrast to that, Q1/ME4 and Q1/MH4-I are free from geometric hourglassing and provide similar results as Q1/HT4. Figure 6.7 shows the results for the second hourglass eigenvalue. The only geometric hourglassing defect is observed for the tall skinny element in Figure 6.7 (b). Here Q1/H4 and Q1/MH4-I become unstable due to the quadratic P - Δ mode (Hourglassing effect II in Section 6.2). However, for hyperelastic materials, this hourglassing effect does not occur at more moderate aspect ratios. The reason for that is the strain-stiffening of A_{22}^n under large strain compression.

Material Hourglassing. The focus lies only in the tensile domain $\lambda_2 > 1$. The elements that suffer from volumetric locking⁴, namely Q1 and Q1/E2s, show no material hourglassing. With the exception of Q1/H4 and Q1/MH4-I in Figure 6.7 (b), material hourglassing for ω_1^{hg} and ω_2^{hg} shows up for all other elements. The stability of the former is a pyrrhic victory: the incompatible quadratic P - Δ mode, causing hourglassing in compression, stabilizes both elements under tension. The failure of the other elements is closely related to loss of positive definiteness of \mathbb{A} and \mathbb{C} (Section 2.3.4). For further details it is referred to Section 3.4 in Bieber et al. 2022.

Furthermore, an analysis of elastoplastic materials can be found in the work of Pfeifferkorn and Betsch 2020 and Armero 2000. The former also considered a three-dimensional eigenvalue analysis of brick elements. Here 12 non-constant strain modes appear, i.e. bi- and trilinear perturbations of X_1 , X_2 and X_3 in each spatial direction. The authors have shown that the hourglass mechanisms are similar to those of a two-dimensional analysis. It is expected that the same holds for the present results.

⁴Of course, volumetric locking is only mild for the present BK material, since $\nu = 1/3$.

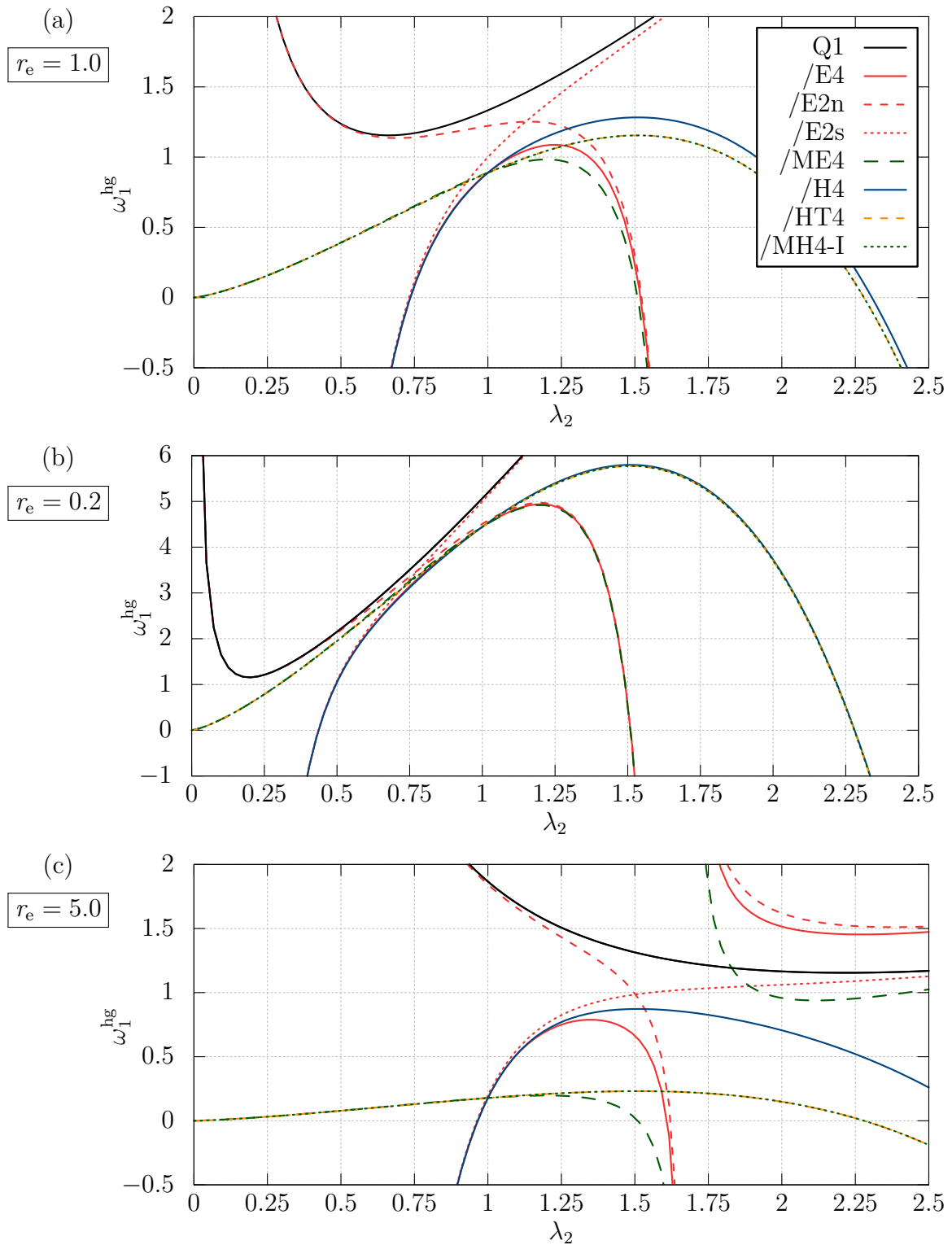


Figure 6.6: Hourglass eigenvalue ω_1^{hg} for a uniaxial stress state $S_1 = 0$.

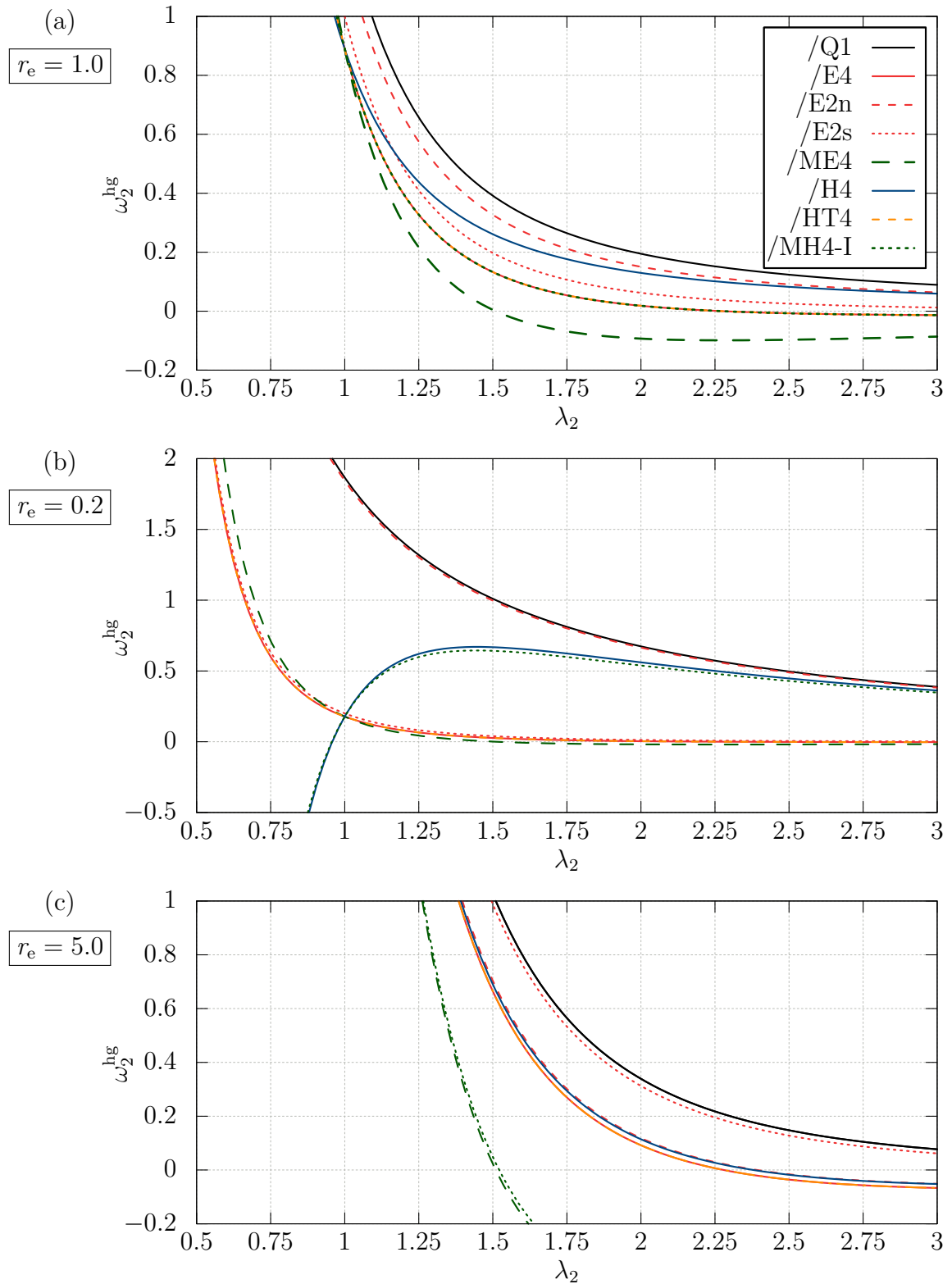


Figure 6.7: Hourglass eigenvalue ω_2^{hg} for a uniaxial stress state $S_1 = 0$.

6.5 Numerical Experiments

The main purpose of this section is to test the newly proposed elements Q1/ME4, Q1/MH4-I, Q1/MS5 and Q2/ME11 for accuracy in terms of modeling physical instabilities. Standard Gauss quadrature is applied, e.g., 2×2 for Q1 and 3×3 for Q2.

6.5.1 Euler Buckling: Coarse Mesh Accuracy

Figure 6.8 (a) depicts a moderately thin beam-like structure with an aspect ratio $r = 1/10$, pinned at both ends, and subjected to uniaxial compression. Using a NH material with $E = 100$ and $\nu = 0$, the critical Euler load $\hat{T}_c^{\text{Euler}} = \pi^2 Er^2/12 \approx 8.22$ provides a thin-limit ($r \rightarrow 0$) reference solution of the underlying buckling problem. The finite element model uses a single element layer in thickness direction. The goal of this benchmark is to evaluate the coarse mesh accuracy in terms of physical stability behavior.

Numerical results are given in Table 6.5. As expected, the models with a single Q1/H4 and Q1/MH4-I element provide a good approximation to the Euler load, since the lion's share of the destabilizing P - Δ mode can be captured with the quadratic incompatible mode, see Figure 6.8 (b). The slight difference between both of them is related to the bilinear bending mode (S^2 -symmetric), which does not contribute to the geometric stiffness in Q1/MH4-I. In contrast to that, Q1/ME4 and Q1/HT4 require at least two elements in thickness direction for a rudimentary modelling of the buckling mode (cf. Figure 6.8 (d,e)). Here the “global” destabilizing P - Δ mode is approximated via an assembly of linear A^2 -antisymmetric P - Δ shear modes.

The softer response of Q1/H4 and Q1/MH4-I, often associated with a “better” element performance, is deceptive. The geometric hourglassing phenomenon II can be triggered with a model where the mesh is refined in the thickness direction, as shown in Figure 6.8 (c). Here, the global (physical) buckling load is larger than the one of a single element and each single element buckles individually.

6.5.2 Block under Compression: Physical vs. Artificial Instabilities

Main results of Bieber et al. 2022. In Section 5 of the respective publication, the authors present an in-depth analysis of the bifurcation problem presented in Section 4.1 (herein). It is described how the block problem can be used as a benchmark: setting $r = r_e$, i.e. having the same aspect ratio for the block and for the element (uniform meshes are assumed), allows investigating the element's stability properties with respect

n_{ele}	Q1/HT4	Q1/H4	Q1/ME4	Q1/MH4-I
1	-	10.00	-	10.10
2	13.33	10.00	13.50	10.10
3	10.00	9.00	10.10	9.08
5	8.80	8.50	8.88	8.57
10	8.36	8.29	8.36	8.29

Table 6.5: Critical buckling load \hat{T}_c of the first critical point. Euler's critical buckling load is $\hat{T} = 8.22$.

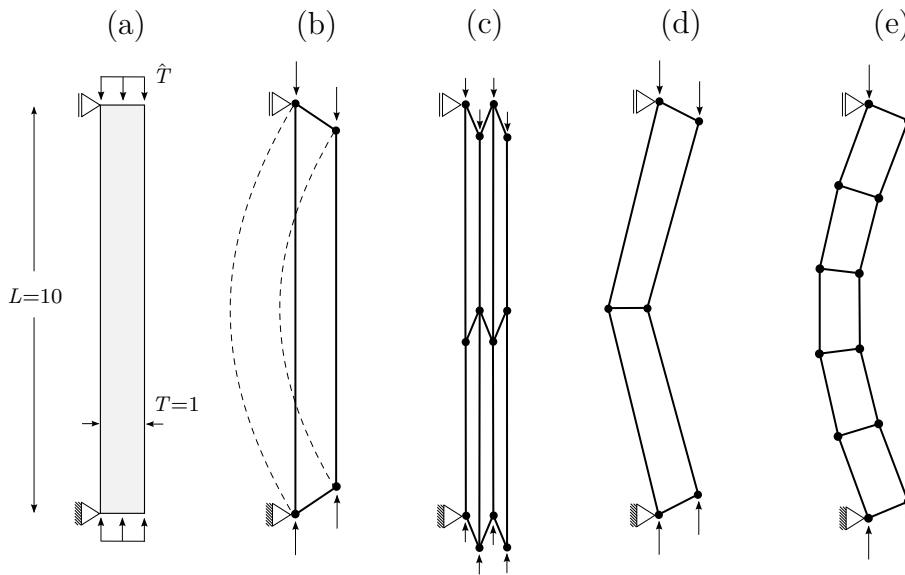


Figure 6.8: Euler buckling; (a) problem setup; (b-e) plots of the first buckling mode; (b, c) is computed with Q1/H4 and (d, e) with Q1/ME4.

to a large set of element aspect ratios. This is essential in a proper analysis of geometric hourglassing defects, since, for certain advantageous mesh configurations, one can always find a case where hourglassing does not occur. A certain set of higher-order bifurcations can be computed and compared with the reference solutions. By that, potential hourglassing issues can be detected and, at the same time, the accuracy in modelling physical instabilities is tested. On the other hand, the authors also investigate the case of undistorted meshes as well as the convergence towards physical instability points.

The results have shown that the modified element formulations Q1/ME4, Q1/ME11 and Q1/MH4-II are free from geometric hourglassing artefacts. Furthermore, the ability to capture physical instability is preserved. To avoid redundancy, those results are not shown here, and the focus is rather on complementary aspects of this benchmark-type.

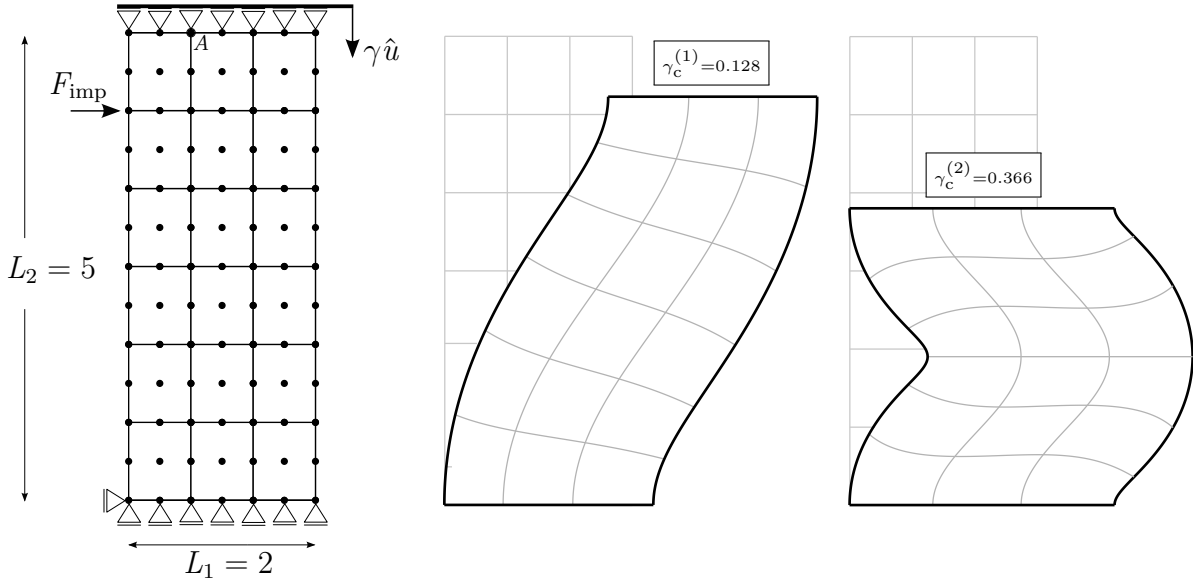


Figure 6.9: Post-bifurcation analysis; left: discrete problem setup (Q2); middle-right: reference buckling modes. In contrast to preceding sections the buckling mode is superimposed on the respective deformed configuration.

Post-bifurcation analysis. The analytical investigations in Section 4.1 as well as the numerical study in Bieber et al. 2022 focus only on the computation of the bifurcation points themselves. Complementing these studies with a post-bifurcation analysis is the purpose of this section. The focus lies on the analysis of imperfection sensitivity as well as the post-critical behavior of the modified elements under severe deformations.

An NH 2×5 block with $E = 1000$, $\nu = 0.45$ and $r = 0.4$ is subjected to a uniaxial compression state. Prescribed is the displacement $\gamma \hat{u} = \gamma 5$ at the upper edge. Figure 6.9 shows a discrete problem setup with Q2 elements. The displacement boundary conditions are slightly different than the ones of the reference problem (cf. Figure 4.1); however, the principal stability behavior remains the same. Furthermore, a small horizontal load imperfection F_{imp} is applied at an upper node on the left side. Perfect ($F_{\text{imp}} = 0$) and imperfect ($F_{\text{imp}} > 0$) finite element models are considered.

Figure 6.10 (a) shows the load-displacement curves for various values of F_{imp} . As an analytical reference solution is not available for the post-bifurcation state, a numerical solution with a 3×6 mesh of bi-quadratic Q2 elements is considered. Of course, this does not provide a converged solution, but rather a target solution for the lower-order locking-free elements (Figure 6.11). The perfect model follows the exact primary solution (homogeneous compression). Bifurcations, i.e., singularities of the stiffness matrix, are indicated with black dots. They are in good correlation with the analytical solution (red triangles). The imperfect structures obviously show a different stability behavior. The equilibrium branch deviates from the principal solution depending on the imper-

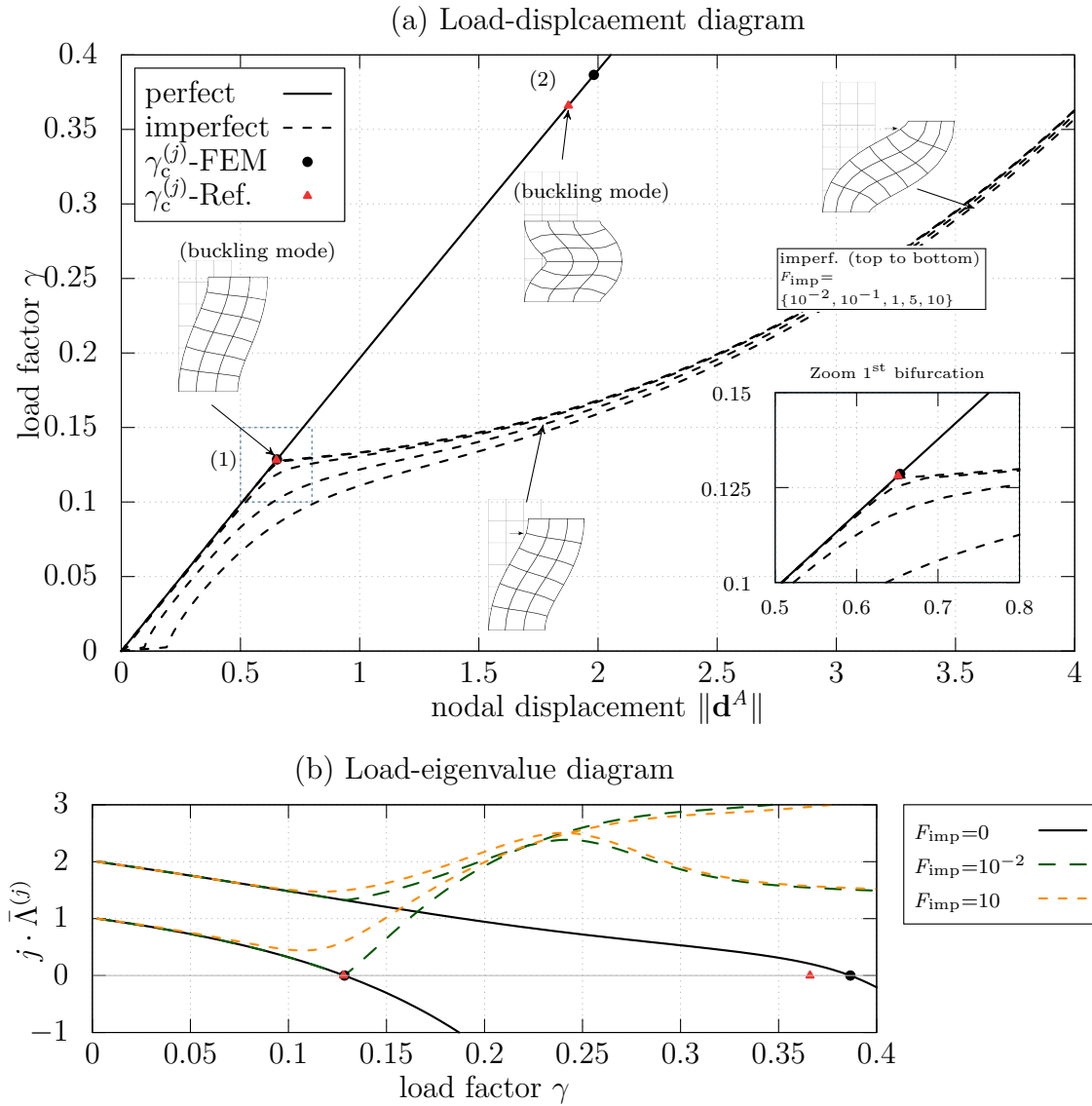


Figure 6.10: Post-bifurcation analysis; Q2 elements; various load-displacement curves for a perfect system (solid) and an imperfection system (dashed) with $F_{\text{imp}} = \{10^{-2}, 10^{-1}, 1, 5, 10\}$; for the perfect structure the bifurcation load γ_c^j is indicated by black dots (FEM, Q2) and red triangles (analytical).

fection load. The block runs into a bending-type deformation in the shape of the first buckling mode. However, for all scenarios, the post-bifurcation path is stable, i.e., the smallest eigenvalue does not become negative; see Figure 6.10 (b). Interestingly, the post-bifurcation behavior for more bulky blocks may also be unstable. For details on post-bifurcation behavior of that problem, it is referred to Section 3.3 in Triantafyllidis et al. 2007.

Ref.	Q2	/E11	/ME11	Q1	/H4	/HT4	/ME4	/MH4-I	/ME4*
-6.6	-6.95	-0.56	-0.438	-38.98	-1.69	-2.16	-1.02	-1.14	-7.46
$+\infty$	∞	10.10	∞	∞	1.88	∞	∞	2.61	0.00

Table 6.6: Critical load factor; top row: tension problem; bottom row: compression problem.

A fixed load imperfection $F_{\text{imp}} = 0.1$ and a set of lower-order Q1 elements are taken into account. Figure 6.11 shows the corresponding load-displacement curves. The principal behavior of all EAS elements is in line with the preceding results. Focusing on the domain around the bifurcation (cf. the enlarged detail), it is observed that the elements with “higher” geometric stiffness perform softer, i.e., Q1/H4 is the softest element, followed by Q1/MH4-I, Q1/HT4 akin Q1/E4 and finally Q1/ME4. However, in view of the overall performance, this difference is of minor relevance.

6.5.3 Compression and Tension of a Constrained Block

The introductory example from Figure 1.2 (b) is reconsidered. The main purpose of this benchmark is to test the coarse mesh accuracy of various elements with respect to geometric and material hourglassing. The 2×2 block consists of the nearly incompressible NH material defined in Equation (2.58). The block’s bottom and lateral edges are fully constrained. In contrast to Auricchio et al. 2005, slightly more “compressible” material parameters are considered: $\mu = 40$ and $\Lambda = \mu \cdot 10^3$ ($\nu = 0.4995$). Two different scenarios for the body load $\hat{\mathbf{B}} = -\gamma\mu\mathbf{E}_2$ are considered; tension ($\gamma < 0$) and compression ($\gamma > 0$). Auricchio et al. 2010 provided a reference value for the fully incompressible tension case of the critical load factor as $\gamma_c^{(1)} = -6.6$. On the other hand, the compression case does not become unstable. Hence, the target load factor value is $\gamma = \infty$. For the numerical computation, stable behavior is assumed when $\gamma = 100$ is reached, see Auricchio et al. 2005.

Tension case. Table 6.6 depicts the critical load factors that are associated with a singular stiffness matrix. Q1 suffers from severe volumetric locking and overestimates the critical tension load by a factor six. In contrast, Q2 and Q1/ME4* (the modification based on the Green-Lagrange strain (6.18)) provide a good approximation to the reference load. The corresponding critical buckling modes are depicted in Figure 6.12 (a,c) and appear to be in good agreement with Auricchio et al. 2010. This is particularly interesting for Q1/ME4*, as it shows (at least conceptually) how to avoid material hourglassing. However, all other elements fail to reproduce the reference load factor value. The elements become more unstable in the range $\gamma \in [-2.16, -0.56]$. Figure 6.12 (b)

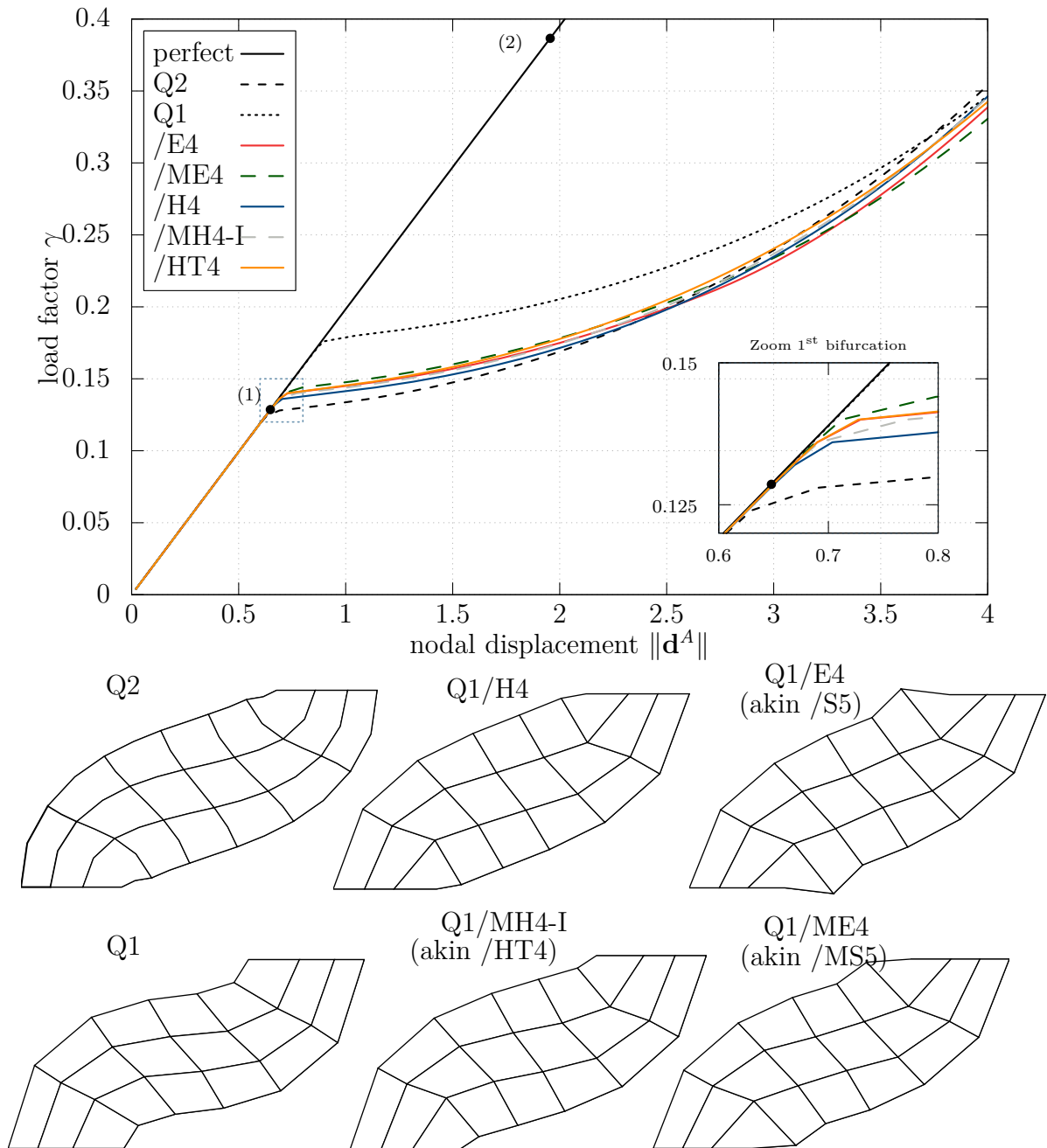


Figure 6.11: Post-bifurcation analysis; top: load-displacement curve with $F_{\text{imp}} = 0.1$; bottom: deformed configurations of the final step in the corresponding load-displacement curve, i.e. $\|\mathbf{d}^A\| = 4$.

depicts the typical hourglassing patterns of the deformed configuration (right) as well as the corresponding buckling mode (left) for Q1/H4. The biaxial stress states of the NH

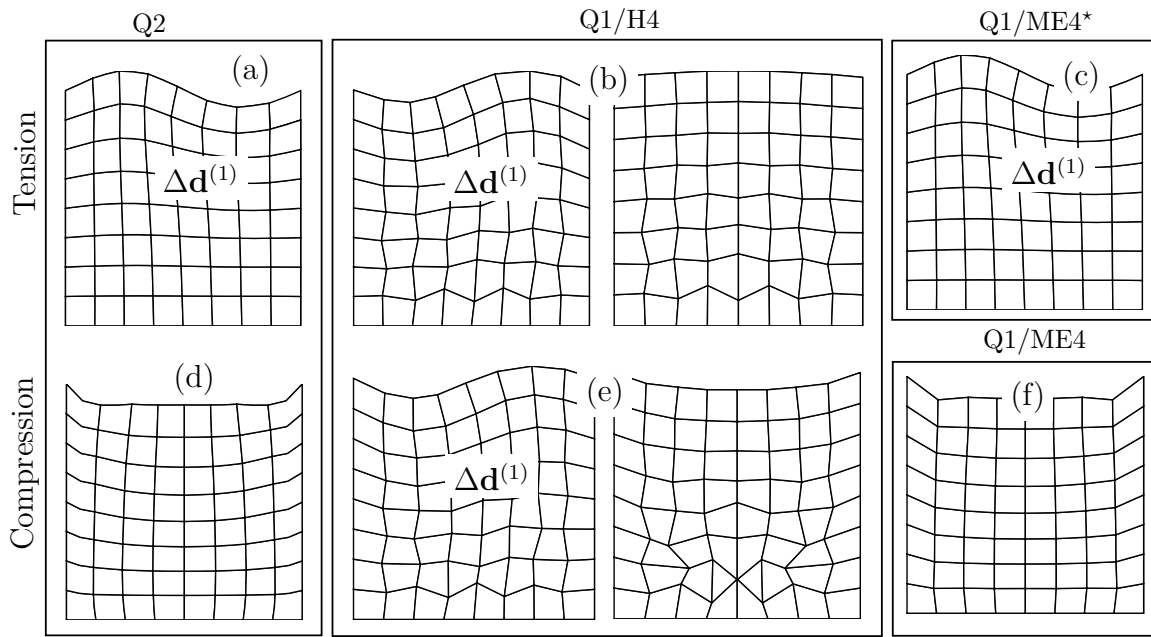


Figure 6.12: Selected plots of deformed mesh configurations at the critical state and critical buckling modes (marked with $\Delta \mathbf{d}^{(1)}$); top: tension instability; bottom: compression instability.

material result in a loss of positive definiteness in the constitutive operators of first \mathbb{C} and then \mathbb{A} , as shown in Figure 2.1. This is especially noticeable in the lower region of the block (where stresses are greatest). As a result, E-enhanced elements become unstable before H-enhanced elements do. Further, the different properties of the (stabilizing) geometric stiffness explain the differences in the critical load values.

Compression case. In contrast to before, the newly proposed elements Q2/ME11 and Q1/ME4 do not suffer from geometric hourglassing. Figure 6.12 (d,f) shows the stable deformed configurations for the final load factor value $\gamma = 100$. Of course, Q1/ME4* becomes immediately unstable. As expected, Q1/MH4-I becomes later unstable than Q1/H4, where the differences is explained by the absence of the destabilizing bilinear P - Δ mode for the former.

Chapter 7

Algorithmic Aspects

7.1 Computational Aspects in the Determination of Critical Points

This section covers algorithms to compute instability points in nonlinear finite element simulations. The intense research on physical and artificial instabilities revealed large numerical difficulties arising in the determination of critical points. Under certain circumstances, tedious and inefficient “trial and error” computations are required, e.g., re-modifying the size of the load steps¹ or implementing problem-specific conditional statements in the code. Difficulties arise in particular in the context of bifurcation problems as well as limit point problems with sharp turns of equilibrium paths, typically present in modified bifurcation problems with relatively small imposed imperfections. In both cases, the onset of instability can appear abruptly without an obvious “announcement”, such as a stiffness softening in the current displacement direction. The principal issues can be described as follows:

1. *Sufficiently small load increments* are desired in order to avoid numerical or algorithmic difficulties in the exact determination of critical points.
2. *Reducing the number of load steps* is desired in order to save computational costs, i.e., avoid an unnecessarily large number of iterations.

The main objective of this section is to find a proper balance between those extremes. At first, the principal stability mechanism of discrete structures and its algorithmic treatment are outlined. Furthermore, a novel *adaptive load control scheme* (ALC) is derived, tailored for the efficient and reliable computation of critical points.

¹With a slight abuse of terminology, this refers also to other control variables, such as the arc-length.

7.1.1 A Short Review On Nonlinear Solution Techniques

Various abbreviations and notational specifications are introduced for ease of readability. A summary is given in Table 7.1. The behavior of nonlinear stability problems is typically illustrated by equilibrium paths; see e.g., Budiansky 1974. Thus, the wording “point” refers to a point on the equilibrium path. Without loss of generality, proportional loading scenarios are assumed throughout this section.

$n \in \mathbb{N}_0$	load step counter	$(\bullet)_n$	“current” quantity (\bullet)
$(\bullet)_{n+1}$	(\bullet) of “next” step	$(\bullet)_{n-1}$	(\bullet) of “previous” step
$\Delta(\bullet)_n = (\bullet)_{n+1} - (\bullet)_n$	increment of (\bullet)	$\mathbf{K}_n = \mathbf{K}(\gamma_n)$	stiffness matrix
$\Lambda^{(j)}$	j 'th eigenvalue of \mathbf{K} (in ascending order)	γ_n	“current” load factor
$\Lambda^{(1)}$	smallest eigenvalue	$D^{(j)}$	j 'th diagonal term (in ascending order)
$\Lambda_0^{(j)}$	initial eigenvalue	$D^{(1)}$	smallest diagonal term
$\bar{\Lambda}^{(j)} = \frac{\Lambda^{(j)}}{\Lambda_0^{(j)}}$	scaled eigenvalue	$D_0^{(j)}$	initial diagonal term
		$\bar{D}^{(j)} = \frac{D^{(j)}}{D_0^{(j)}}$	scaled diagonal term

Table 7.1: Basic variables and notation. Diagonal terms $D^{(j)}$ refer to the entries of the diagonal matrix \mathbf{D} in the Cholesky decomposition $\mathbf{K} = \mathbf{LDL}^T$, see Section 1.3 in Strang 1986.

The computation of critical points has been intensively studied in the literature, see e.g., Chapter 7 in Wriggers 2008 for an overview. For small strain and small displacement problems, a linear pre-buckling analysis is often the way to go. However, this provides only an approximation of the critical load and is less suited for large strain problems. Here, the focus lies on the *exact* determination of critical points and algorithms applicable for general problems, i.e., without limitation to small deformations. In the context of bifurcation problems, Riks 1984 classified two principal approaches: indirect and direct methods. The first one is based on a perturbation approach, where initial geometry, loading or material imperfections provide a slightly modified structure. Hereby, the original problem is, in most cases, transformed into a limit point problem (however, stable bifurcations may also occur, see the numerical experiments in Section 6.5.2). In the pre-critical state, the structural behavior of imperfect structures is often accompanied by a pronounced stiffness reduction, which yields a flattening of the load-displacement curve. The critical point is then characterized by a local load maximum. Tracing these equilibrium paths typically requires continuation methods, like the arc-length method, which are summarized in detail in a recent review article by Leon

et al. 2012. However, the direct approach specifies *a priori* the type of instability and thus may spoil the accuracy compared to the (perfect) mathematical model.² Furthermore, the computation of higher-order bifurcations is not straightforward. In contrast to that, direct methods are based on the original model. Stability is analyzed through an accompanying analysis of the stiffness matrix.

A typical computational approach to detect the first critical points for both direct and indirect methods consists of the following consecutive steps:

1. *Following the principal equilibrium path.* Starting from the undeformed configuration $\gamma_0 = 0$, the deformed structure first follows a stable equilibrium path, controlled by load factor $\gamma \in [0, \gamma_c^{(1)})$.
2. *Isolation of critical point.* The tangent stiffness matrix remains positive definite until, at load increment n , the critical load factor γ_c is exceeded. In case only a single critical point³ is passed, the sufficiently narrow post-critical domain provides

$$\det \mathbf{K}_n < 0 \quad \Leftrightarrow \quad \Lambda_n^{(1)} < 0 \quad \Leftrightarrow \quad D_n^{(1)} < 0. \quad (7.1)$$

Here, $\Lambda_n^{(1)}$ and $D_n^{(1)}$ denote the smallest eigenvalue and smallest diagonal entry, see Table 7.1. It follows that the interval $\mathcal{I}_c^{(1)} = [\gamma_{n-1}, \gamma_n]$ contains $\gamma_c^{(1)}$.

3. *Exact determination of the critical point.* The critical load factor $\gamma_c^{(1)}$ is determined by the criterion

$$\mathbf{K}(\gamma_c^{(1)})\Delta\mathbf{d}^{(1)} = \mathbf{0} \quad \text{with } \Delta\mathbf{d}^{(1)} \neq \mathbf{0}. \quad (7.2)$$

This implies equivalently

$$\det \mathbf{K} = 0 \quad \Leftrightarrow \quad \Lambda^{(1)} = 0 \quad \Leftrightarrow \quad D^{(1)} = 0, \quad (7.3)$$

since

$$\det \mathbf{K} = \prod_{j=1}^{n_{\text{dof}}} \Lambda^{(j)} = \prod_{j=1}^{n_{\text{dof}}} D^{(j)}. \quad (7.4)$$

The eigenvector $\Delta\mathbf{d}^{(1)}$, associated with the zero eigenvalue, represents the incremental buckling mode.

²Of course, imperfections are inherent in real-world structures. However, this does not play a role in the present discussion.

³A special case is the simultaneous vanishing of eigenvalues, implying multiple bifurcations. However, this case is not further considered herein.

A simple method are *bisection methods*. They are simpler to implement but have only a linear convergence behavior. Furthermore, the ill-conditioning of the stiffness matrix close to critical points can lead to severe convergence issues with the Newton-Raphson procedure. Possible remedies are stabilization schemes based on the (computationally expensive) eigenvectors of the stiffness matrix; see e.g., Müller 2007. An alternative tailor-made technique for solving (7.2) is the *method of extended systems*; see Wriggers et al. 1988. The method is quadratically convergent and allows, within a specified numerical tolerance, an *exact* determination of critical points. For problems with inhomogeneous boundary conditions it is referred to the dissertation of Roth 2020. Both methods share the property of being sensitive to the interval $\mathcal{I}_c^{(j)}$, which will be discussed further below.

Remark 7.1.1. This work is restricted to formulations where tangents are solely related to the incremental displacement degrees of freedom. However, it is pointed out that some multi-field mixed formulations, for instance fully incompressible displacement-pressure type formulations or formulations with continuous (e.g., pressure or stress) fields at the element boundary, do not allow static condensation to a pure displacement formulation. These cases require special attention because the criterion (7.1) no longer holds. For further details it is referred to the discussion in Schröder et al. 2017.

7.1.2 Pre- and Post-Critical Behaviour of Discrete Structures

The numerical obstacles that appear in the computation of critical points are discussed in this section. It is anticipated that the overall target in the next section will be to predict the onset of bifurcations. Nevertheless, for the sake of a more general understanding, limit point problems are also discussed herein.

Structural characterization of pre-critical states. The onset of a structural instability is determined by criterion (7.3). Since \mathbf{K} is positive definite in the pre-critical state, it is evident that the scaled determinant $\det \mathbf{K} / \det \mathbf{K}_0$, the scaled eigenvalue $\bar{\Lambda}^{(1)}$ as well as the scaled diagonal entry $\bar{D}^{(1)}$ are continuous functions of γ , which have the value of unity at $\gamma = 0$ and zero at $\gamma = \gamma_c^{(1)}$. In particular, $\det \mathbf{K}(\gamma)$ is a C^∞ -continuous function implying at least C^0 of $\bar{\Lambda}^{(1)}(\gamma)$ and $\bar{D}^{(1)}(\gamma)$; see Strang 1986. The propagation of these quantities during the deformation process can be used to predict the critical point, making them potential candidates to describe the pre-critical behavior of the structure.

However, from criterion (7.3), only the last two, namely $\Lambda^{(1)}$ and $D^{(1)}$ are considered. The reason for that is the infeasible range of $\det \mathbf{K}$. It depends on the mesh size,

material, etc. and usually takes large values.⁴ E.g., while bypassing the first critical point, the determinant typically switches from plus to minus infinity, providing only the information *that* a critical point is passed and not *how*. Thus, the determinant might be useful for structures with few degrees of freedom (e.g., small truss system – omnipresent in pertinent literature on this topic), but not for general finite element models. The post-critical analysis of higher-order bifurcations, i.e., $j > 1$, excludes $\mathbf{D}^{(j)}$. The reason for that is the non-uniqueness of the factorization \mathbf{LDL}^T ; see Strang 1986. For that reason, the eigenvalues are most generally usable.

Four examples of deformation-dependent analyses. Throughout this section the following examples will serve as a benchmark setup.

- Example I: bifurcations of a plane strain Neo-Hookean block ($E = 1000, \nu = 0.45, r = L_1/L_2$) under compression ($\hat{u} = -L_2$), see Section 4.1.4 and Section 6.5.2 for the continuous and discrete problem, respectively.
- Example II: bifurcations of a thin plate under compression; material: $E_1 = 2.1 \cdot 10^5, E_2 = 3.0359 \cdot 10^5, \nu = 0$; geometry: thickness $T = 0.2$, height $L_2 = 24$ and width $L_1 = 5$; boundary conditions: simply supported at the top and bottom, the top edge is subjected to a vertical displacement $u_2 = \gamma \cdot 0.001$; discretization: isogeometric Kirchhoff-Love shell elements based on quadratic B-Splines; mesh: 10×20 .⁵
- Example III: bifurcation problem of a plane strain Blatz-Ko block under tension ($\hat{u} = L_2$), see Section 4.1.5 and Section 6.5.2 for the continuous and discrete problem, respectively.
- Example IV: limit point problem; inhomogeneous compression of a plane strain block, see Example 6.3 in Bieber et al. 2022 (mesh in Figure 21, $n_{\text{ele}} = 198$).

For Example I,III and IV, the graphs in Figure 7.1 show the scaled versions of the first four eigenvalues (left column) and the smallest eigenvalue and diagonal term (right column) versus the load factor.

The graphs on the left show the typical eigenvalue characteristics of discrete stability problems (note the unconventional vertical axis label). The imminent instability is announced by a decrease of the smallest eigenvalue. However, the shape of this curve

⁴This is particularly pronounced in the context of problems involving nearly incompressible materials. Here, in relation to the small ones, very large eigenvalues of volumetric modes occur (physical, not necessarily locking-related). This makes the determinant even less practicable for structures with few degrees of freedom.

⁵All numerical results for this example were calculated by Anika Strauss (IBB, University of Stuttgart). The author is most grateful for this support.

strongly depends on the problem type. While a smooth decrease is observed for (a), the curves in (b,c) show several kinks. These indicate mode swapping, i.e., the branches of individual (not sorted) eigenvalues cross each other. For higher-order bifurcations (a,b), these swaps become more pronounced. For the limit point problem (c), the instability comes without “alert”. Shortly before the first critical point is reached, the eigenvalue experiences an abrupt drop and the stiffness matrix becomes singular.

The graphs on the right show the scaled versions of the smallest eigenvalue and smallest diagonal entry in course of the deformation process. Interestingly, the shape of both curves is similar in the stable domain and, as expected, both values become zero at the critical point. This analogy is exploited in the next section to avoid the more expensive computation of the eigenvalues.

Algorithmic issues. The aforementioned steps to compute instability points are problem-dependent and their numerical treatment often requires a priori knowledge of the problem at hand. Typical issues are:

- (i) Load steps are *too large* and the critical point is *overshooting*. This can give rise to the following problems:
 - Inequalities (7.1) may not be reliable in the broader range of post-critical states. Surpassing the first two bifurcations within one load step can provide, again, a positive $\det \mathbf{K}$. The same applies for negative eigenvalues that turn positive in the post-critical state.
 - Convergence towards a wrong (i.e., not aimed) critical point.
 - The extended systems solver fails to converge.
 - Large number of bisections are required.
- (ii) To avoid the issues in (i), load increments have to be selected sufficiently small. However, when load increments are kept constant, a large number of load steps is required.
- (iii) The search for higher-order bifurcations usually comes along with a non-definiteness of \mathbf{K} and consequently \mathbf{LDL}^T is not unique anymore. This means that techniques based on an accompanying $D^{(j)}$ -observation are only reliable in the pre-critical domain, i.e., for computing only the first bifurcation point.
- (iv) For many problems, the onset of a bifurcated equilibrium branches comes *abruptly*. Often, this onset is followed by a large accumulation of further higher-order bifurcations. Typical examples are the surface buckling phenomenon, buckling of thin walled structures as well as artificial instabilities (hourglassing).

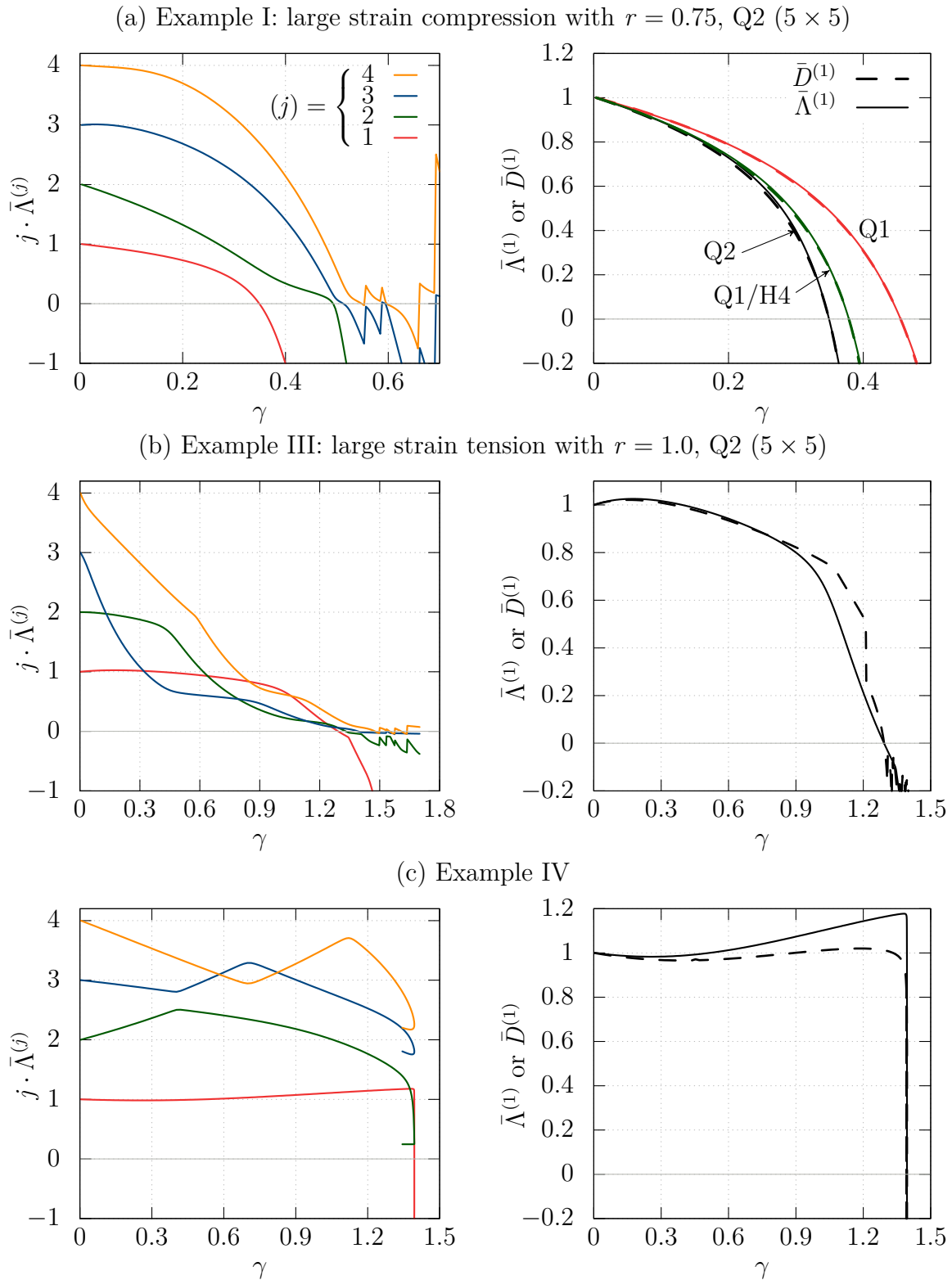


Figure 7.1: Left column: first four scaled (only for illustrative reason) eigenvalues $j \cdot \bar{D}^{(j)}$, versus load factor. Right column: scaled smallest eigenvalue $\bar{\Lambda}^{(1)}$ and smallest diagonal term $\bar{D}^{(1)}$ versus load factor. It is noted that the (c) is a limit point problem, which is why the curves turn back.

In practical applications, a pre-calculation with larger load increments may provide information for specific individual remedies, e.g., conditional load step refinements. Some approaches from the literature, where pre-critical “measures of nonlinearity” are used to adapt the load control, are described next.

Limit point problems: “measures of nonlinearity”. Adaptive path-following schemes often rely on measures that characterize the current degree of “nonlinearity” of the equilibrium path. In the context of the arc-length method, various approaches exist, of which the two most prominent ones are sketched. First, for limit point problems, Bergan et al. 1978 introduced a scalar “current stiffness parameter” S_p to describe the nonlinear behavior. This parameter relates the current stiffness in the (current) displacement-direction to the initial one and provides valuable information on the softening behavior, which is particularly useful to adapt the arc-length. A possible formulation is given by (see Bergan et al. 1978, Eq. (12)). Parameter S_p is equal to one at the initial loading state and zero at the critical point. For a softening/stiffening structural response, S_p becomes smaller/greater. For further details it is referred to Eriksson 1988 as well as the recent discussion in Maghami and Schillinger 2020. Another elegant method was proposed by Ramm 1981. It is based on a simple adjustment of the arc-length by comparing the number of required iterations in the Newton-Raphson scheme.

Bifurcation problems: “measures of nonlinearity”. As opposed to limit point problems, a measure should be related to the properties of the stiffness matrix rather than the displacement increments, since the principal solutions do usually not provide information on forthcoming bifurcations. To the author’s best knowledge, this topic is rarely discussed in literature and approaches do not go beyond a simple accompanying eigenvalue analysis. The approach closest to what comes next can be found in Kouhia 1992. In order to *predict forthcoming critical points*, the author proposed an extrapolation of the load increment in dependence on a scaled determinant of the stiffness matrix (see Equation (24) in Kouhia 1992). However, a modification of the load control is not further discussed.

7.1.3 Adaptive Load Control – Model Problem

Let $M = M(\mathbf{K}(\gamma))$ be a scalar *measure* that quantifies a structural system’s “softening” during deformation. Possible choices for M are discussed later. Assumed are the following properties:

- M becomes zero at the critical point,

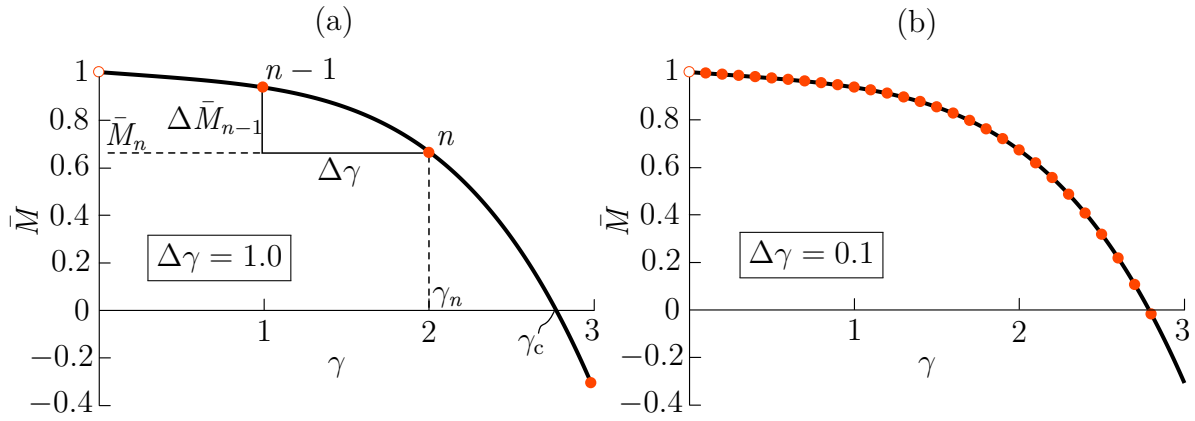


Figure 7.2: Model problem; load-“measure” curve \bar{M} , exemplified for two load incrementations with constant $\Delta\gamma_n = \Delta\gamma$.

- M is monotonously decreasing,
- In analogy to before, the scaled version of M is denoted as $\bar{M} = M/M_0$. At load increment n it takes the form \bar{M}_n .

Model problem. The principal idea of the proposed ALC scheme is explained in terms of a simple model problem. A fabricated $\bar{M} \equiv M$ is introduced as a continuous, monotonously decreasing function of the form

$$\bar{M}(\gamma) = 1 - \frac{1}{70}\gamma^4 - \frac{1}{20}\gamma. \quad (7.5)$$

Each evaluation $\bar{M}(\gamma)$ may be interpreted as the outcome of a nonlinear finite element calculation. The typically employed load factor update is

$$\gamma_{n+1} = \gamma_n + \Delta\gamma, \quad (7.6)$$

with a constant user-defined load increment $\Delta\gamma$. A plot of \bar{M} over load factor γ for a coarse (a) and fine (b) load incrementation is shown in Figure 7.2. The red dots represent discrete \bar{M} evaluations at equidistantly distributed γ_n . Red circles indicate the initial state. Large load increments are obviously more prone to “overshoot” γ_c than small ones, which provide a better interval, $\mathcal{I}_c^{(1)}$. However, the total number of required evaluations increases. This is often unnecessary for trivial principal solutions. A typical example is the bifurcation problem of Section 4.1.3 where the principal solution can even be derived “by hand”.

Principle idea. The main idea of ALC consists of two simple considerations.

- (1) Instead of the conventional load factor incrementation $\Delta\gamma_n = \text{const.}$, the measure increments $\Delta\bar{M}_n$ are prescribed.
- (2) Close to critical points $\Delta\bar{M}$ should be small, otherwise $\Delta\bar{M}$ should be large. Of course, specifying “close, small and large” will require user-defined input parameters.

Consideration (1) bears an obvious obstacle: from the viewpoint of the “current” M_n the future propagation of M is unknown and a result of γ_{n+1} itself. Extrapolation of \bar{M} provides a remedy. A Lagrangian interpolation based on a subset of the preceding (known) discrete values is used

$$\bar{M}_n^{\text{ext}}(\gamma) = \sum_{i=\hat{n}}^n \bar{M}_i L_i \quad \text{with } \hat{n} = n - p, \quad (7.7)$$

with i^{th} Lagrange basis function of degree p

$$L_i(\gamma) = \prod_{i=\hat{n}, i \neq j}^n \frac{\gamma - \gamma_j}{\gamma_i - \gamma_j}. \quad (7.8)$$

The constructed polynomial interpolates the preceding set of (γ_i, \bar{M}_i) and provides an approximation of \bar{M} beyond the current loading state. Exemplified for linear extrapolation with $p = 1$, one obtains

$$\bar{M}_n^{\text{ext}}(\gamma) = \bar{M}_{n-1} L_{n-1} + \bar{M}_n L_n = \bar{M}_{n-1} \frac{\gamma_n - \gamma}{\Delta\gamma_{n-1}} + \bar{M}_n \frac{\gamma - \gamma_{n-1}}{\Delta\gamma_{n-1}}. \quad (7.9)$$

Using $\gamma = \gamma_n + \Delta\gamma_n$, this can also be written as

$$\bar{M}_n^{\text{ext}}(\Delta\gamma_n) = \bar{M}_n + \frac{\Delta\bar{M}_{n-1}}{\Delta\gamma_{n-1}} \underbrace{\Delta\gamma_n}_{\text{unknown}}. \quad (7.10)$$

Technical details on the quadratic extrapolation are given in Appendix A.5. Figure 7.3 shows a sketch of both extrapolation schemes.

The extrapolation (7.7) is used to predict the next load increment $\Delta\gamma_n$. In regard to consideration (2), the activation function $\alpha(\bar{M})$ is introduced. It is a function of \bar{M} that represents the desired (user-defined) incremental decrease of \bar{M} for the next load step. An example is sketched for a constant $\alpha = 0.05$: this means that the upcoming load increment $\Delta\gamma_n$ should be calibrated such that the next load step provides $\Delta\bar{M}_n = \bar{M}_{n+1}(\Delta\gamma_n) - \bar{M}_n = 0.05 = \alpha(\bar{M}_n)$, i.e., the measure decreases by around five percent.

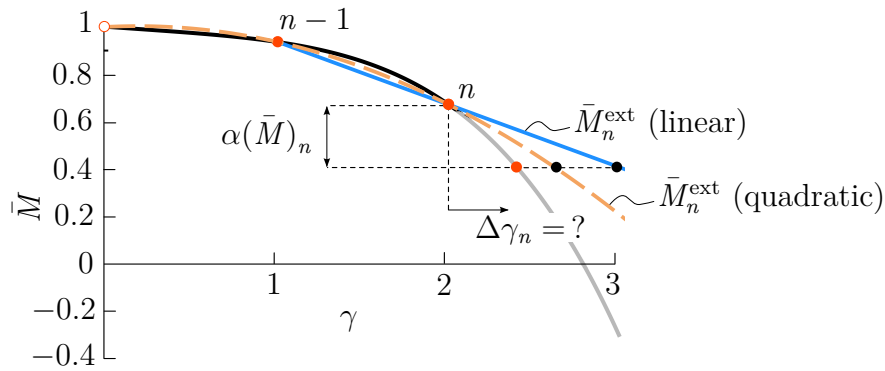


Figure 7.3: Model problem; exemplified extrapolation of \bar{M} at γ_n based of linear and quadratic Lagrange interpolation.

The increment of the extrapolated measure is enforced via

$$\alpha(\bar{M}_n) \stackrel{!}{=} \bar{M}_n^{\text{ext}}(\Delta\gamma_n) - \bar{M}_n. \quad (7.11)$$

Solving for $\Delta\gamma_n$ provides an estimate for the update of the load factor. Exemplified for the linear extrapolation (7.9) this reads

$$\Delta\gamma_n = \frac{\alpha_n}{\Delta\bar{M}_{n-1}} \cdot \Delta\gamma_{n-1} \quad (7.12)$$

and yields a load factor update

$$\boxed{\gamma_{n+1} = \gamma_n + \Delta\gamma_n = \gamma_n + \frac{\alpha_n}{\Delta\bar{M}_{n-1}} \Delta\gamma_{n-1}} \quad (7.13)$$

Here, $\frac{\alpha_n}{\Delta\bar{M}_{n-1}}$ scales the previous (known) load increment by the desired amount.

Estimation of required number of load steps. The activation function α can be interpreted as the “velocity” of \bar{M} in pseudo-time γ .

As a result, the number of required load increments from the initial state $\bar{M}_0 = 1$ to the critical point $\bar{M} = 0$ is given by

$$n_{\text{est}} = \int_0^1 \frac{1}{\alpha} d\bar{M}. \quad (7.14)$$

In case the ALC scheme is not activated at the initial state, e.g., when n_p predictor steps are used, the estimate is

$$n_{\text{est}} = \int_{\bar{M}_{n_p}}^1 \frac{1}{\alpha} d\bar{M} + n_p. \quad (7.15)$$

Of course, due to the extrapolation error, this is only an approximation. Nevertheless, it provides practical guidance on how to choose the activation function. Two possible choices for α are discussed. The most obvious option is to keep $\alpha = \alpha_0$ constant and independent of \bar{M} . The estimate of the required load steps becomes

$$n_{\text{est}} = \frac{1}{\alpha_0}. \quad (7.16)$$

A more advanced choice is the piecewise linear function

$$\alpha = \begin{cases} \alpha_0 + \frac{\alpha_i - \alpha_0}{\bar{M}_i} \bar{M}, & \bar{M} \leq \bar{M}_i \\ \frac{\bar{M}_i \alpha_1 - \alpha_i}{\bar{M}_i - 1} + \frac{\alpha_1 - \alpha_i}{1 - \bar{M}_i} \bar{M}, & \bar{M} > \bar{M}_i \end{cases} \quad (7.17)$$

This function depends on four input parameters: left, right and inner α -values α_0 , α_i and α_1 , respectively, as well as the location \bar{M}_i where both linear functions intersect (however, continuity is not required for α). An estimate of the required steps is given by

$$n_{\text{est}} = \hat{M}_i \frac{\ln \alpha_i - \ln \alpha_0}{\alpha_i - \alpha_0} + (\hat{M}_i - 1) \frac{\ln(-\alpha_1) - \ln(-\alpha_i)}{\alpha_i - \alpha_1}. \quad (7.18)$$

Figure 7.4 depicts the resulting steps for a constant activation function $\alpha_0 = 0.1$ (a,b) and for the linear activation function of (7.17) (c,d) with parameters $\alpha_0 = 0.01$, $\alpha_i = 0.05$, $\alpha_1 = 0.1$ and $\hat{M}_i = 0.1$. The corresponding activation function is sketched on the very left, sharing the same vertical axis. Quadratic extrapolation with two predictor steps $\Delta\gamma = 0.5$ is used. For linear extrapolation, the total number of iterations, using the same predictor steps, is also provided in the graphs. Here, (a,c) represent \bar{M} of (7.5) and (b,d) is a slightly modified function \bar{M} with a steeper initial slope. The main insights of Figure 7.4 may be described as follows:

- For (a,c), the extrapolation error of the third step is larger than for (b,d). This is explained by a sub-optimal predictor which emanates from the linear-dominated part for $\gamma < 1$, whereas the \bar{M} in (b,d) has a smaller curvature and consequently the extrapolation scheme provides better results.

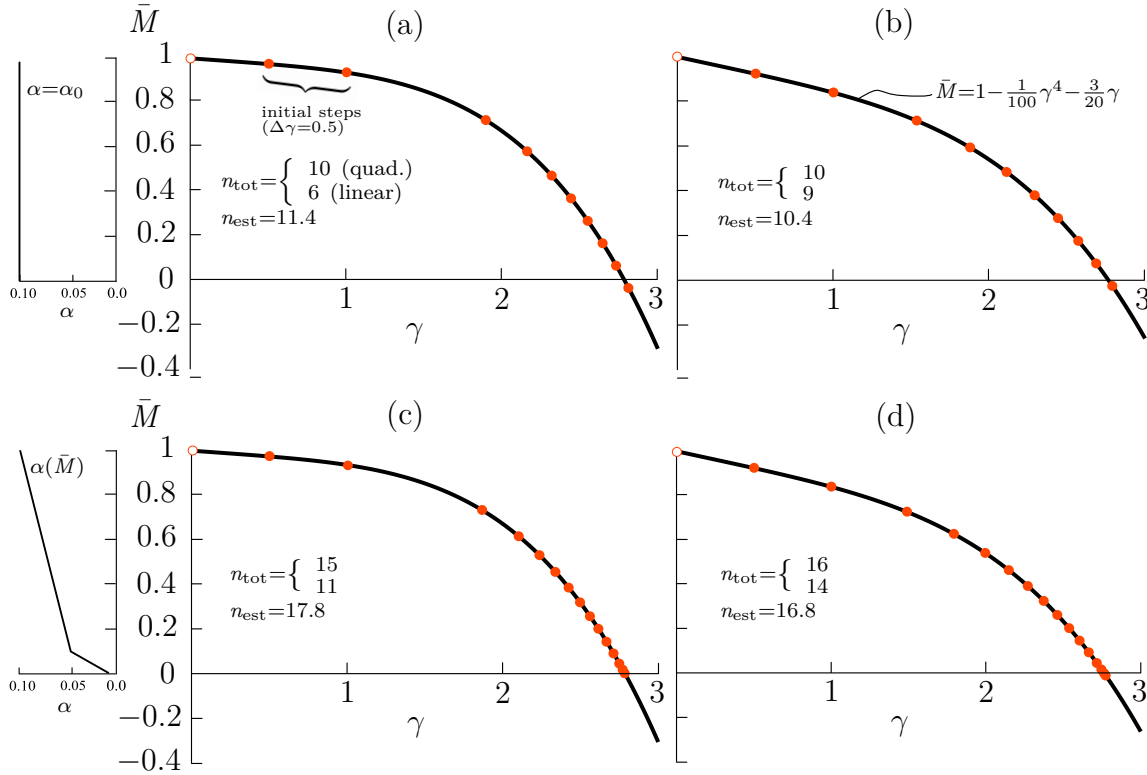


Figure 7.4: Model problem; load-“measure” curve, exemplified for the proposed load incrementation; illustrated are the steps (red dots) using a quadratic interpolation scheme for two different \bar{M} (left and right) and two different α (top and bottom, $\alpha(\bar{M})$ sketched on the very left). Two predictor steps are used.

- The estimate from (7.14) can be used as a criterion for reliability and efficiency of the ALC.
- For convex shapes of \bar{M} ($d\bar{M}/d\gamma < 0$), n_{est} provide an upper bound of n_{tot} .
- For concave shapes of \bar{M} , n_{est} ($d\bar{M}/d\gamma > 0$) provide a lower bound of n_{tot} .

7.1.4 Numerical Experiments

The purpose of this section is to show how the proposed ALC scheme performs in a variety of stability problems. Within this section, the eigenvalues are used as a measure due to the reasons listed in the previous section. The corresponding eigenvalue $\Lambda^{(j)}$ serves for the computation of the j^{th} bifurcation point, i.e.

$$\bar{M}^{(j)} = \frac{\Lambda^{(j)}}{\Lambda_0^{(j)}}. \quad (7.19)$$

This means, that for each critical point, a separate ALC computation is started. With parameters $\alpha_0 = 0.01$, $\alpha_1 = 0.15$, $\alpha_i = 0.05$ and $\hat{M}_i = 0.1$, the piecewise linear activation function (7.17) is used. The estimated number of iterations $n_{\text{est}} = 13.91$ is compared to the number of actually required load steps $\overline{n_{\text{tot}}}$ in $\gamma \in [\gamma_c^{(j-1)}, \gamma_c^{(j)}]$ (of course, $\gamma_c^{(0-1)} = \gamma_0$). It is noted that Equation (7.19) does not cover the case when negative eigenvalues (associated with a preceding critical point) turn back to zero. However, this does not play a role for the present examples. Alternative approaches to suitable measures M are discussed in the next section.

The absence of a reference “target solution” impedes a concrete assessment of the ALC scheme. In the sequel, the step size estimate (7.14) is used to test the performance of ALC and, indirectly, the quality of M . Standard load stepping schemes completely depend on the problem at hand and the chosen $\Delta\gamma = \text{const.}$ is usually determined iteratively. As a result, a comparison with ALC is difficult to measure objectively and therefore not considered in the sequel.

Example I and II: geometric bifurcations of compressed specimens. Figure 7.5 shows the results of various finite element simulations based on ALC. Lines in black, green, and blue are linear interpolants between the discrete set of $\bar{M}^{(j)}$ branches. Again, red dots represent the discrete set $(\gamma_n, \bar{M}_n^{(j)})$. For illustrative purposes these dots are plotted on the eigenvalue branch of the current ALC section (starting with a red circle). Linear extrapolation is used with the piecewise linear activation function (7.17). In contrast to the model problem, a small ghost-predictor (not shown) is used to compute the values for $n = 1$ as well as the second step for the sections of the higher bifurcations.

The deformation-dependent eigenvalue change strongly depends on the problem at hand. Large strain problems (a,b) show large curvature variations, whereas, as expected, the small strain examples (c,d) are nearly linear. As shown for the model problem, extrapolation underestimates the predicted load steps for convex curves (convex side oriented to the origin). This is the reason for the suboptimal performance (in the sense that n_{est} is badly approximated) for $j = 1$ in (a) and particularly (b). However, this is the other way around for $j = (2,3)$ in (b). Here, the concave shape of the branches overestimates the required load steps. In contrast to that, the ALC scheme provides excellent results for the small strain examples (c,d).

Example III: diffuse bifurcations of a block under tension. Figure 7.6 shows the simulation results for a material-induced instability problem. The results are somewhat different than for the preceding problem types. On the one hand, the number of mode jumps, i.e., kinks in the eigenvalue branches, is more pronounced than for the preceding

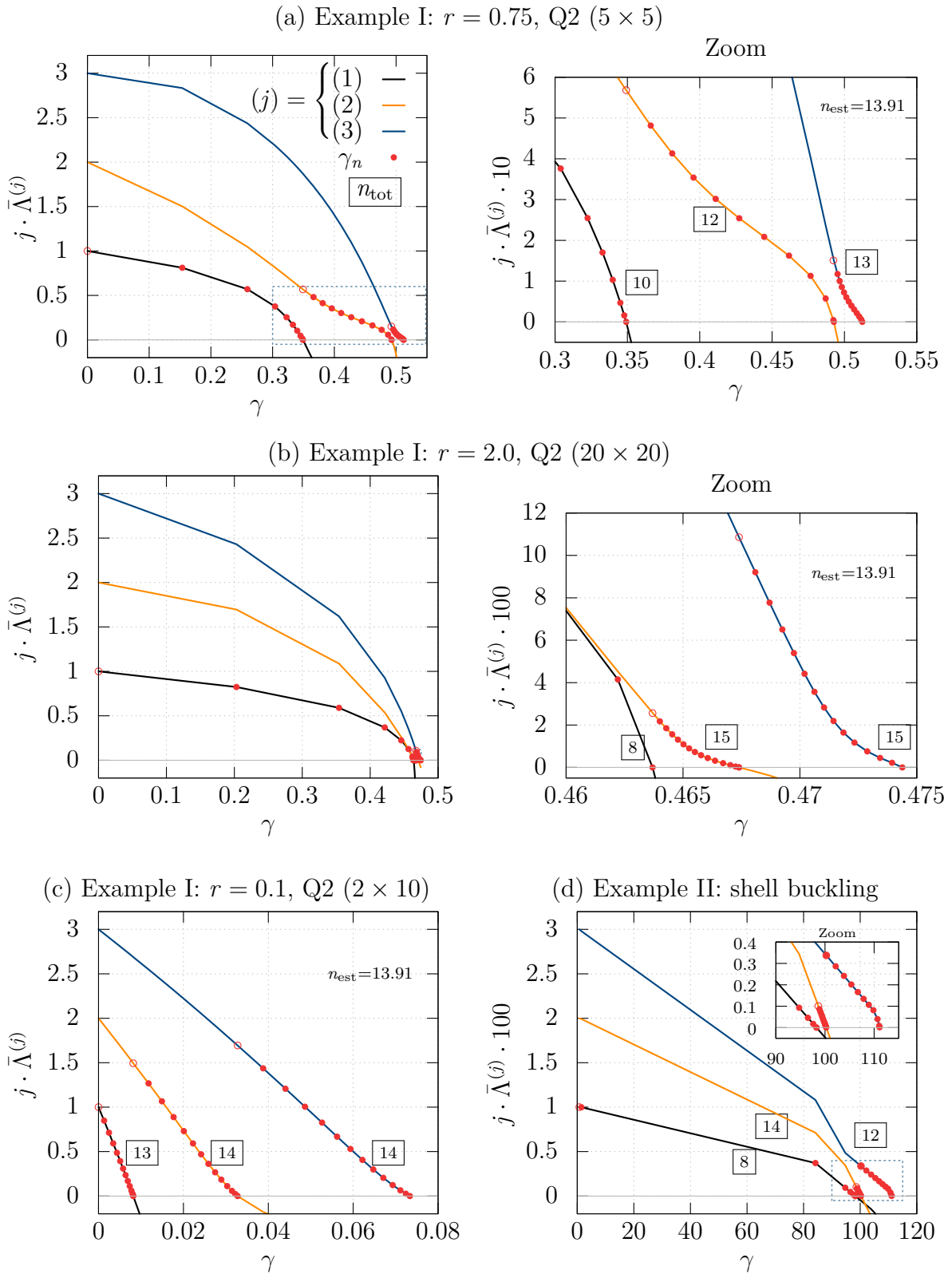


Figure 7.5: ALC scheme for various large strain (a,b) and small strain (c,d) geometric instability problems; linear extrapolation with piecewise linear α .

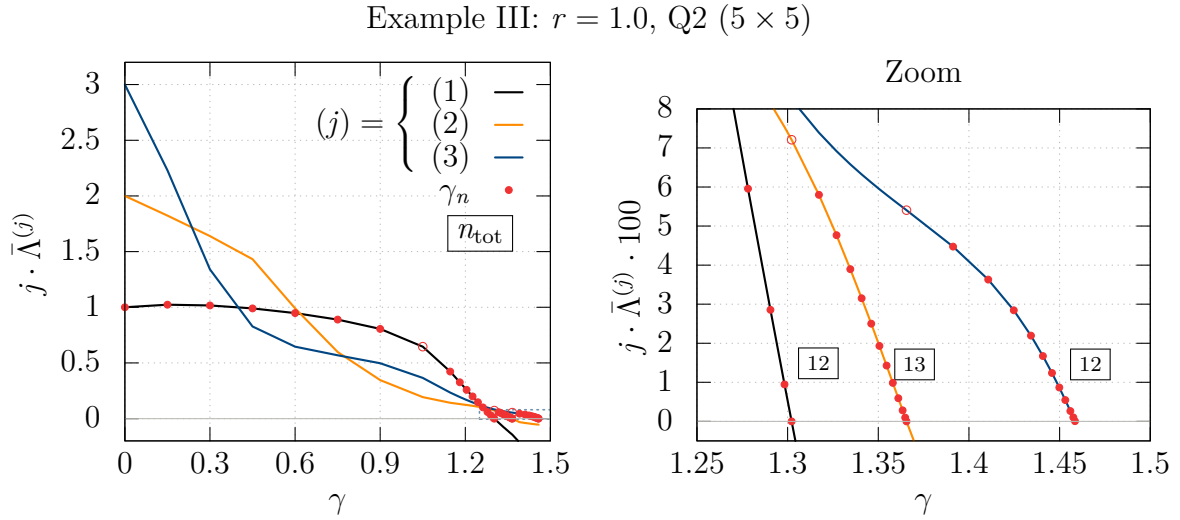


Figure 7.6: ALC scheme for the large strain tension problem; linear extrapolation with piecewise linear α .

compression problems. For the present discrete problem, however, this is not an issue. On the other hand, the value of the smallest eigenvalue increases initially. This is explained by the stiffening (stabilizing) effect of the geometric stiffness due to the tensile stress state. However, at a later loading-state ($\gamma \approx 0.3$), the BK rubber's strain-softening characteristic takes over, and the smallest eigenvalue begins to decrease. The present ALC scheme is designed for a decreasing M . As a result, the computation begins with a standard load incrementation of $\Delta\gamma = 0.15$, and the ALC procedure is activated by a user-defined threshold of $\Delta\bar{M} > 0.1$. For the present example this occurs at $n = 7$ and $\gamma = 1.05$.

Additional comments. The presented results are based on the eigenvalue measure (7.19). Similar results are obtained when $M^{(1)} = D^{(1)}$ is used to compute the first critical point. Furthermore, only minor differences between the ALC results of a linear or quadratic extrapolation are observed. For sake of brevity these results are not shown.

7.1.5 Open Issues

The success of ALC stands or falls with the quality of the measure M . Abrupt curvature variations, kinks, etc., deteriorate the accuracy of the extrapolation and M should preferably be of linear shape.

For some preliminary investigations, Example I and Example III are reconsidered. The left graph in Figure 7.7 (a) and Figure 7.8 (a) show scaled versions of the first 10 eigenvalues. In course of the loading scenario, the eigenvalues become significantly smaller. In fact, this holds not only for the first few but also for the majority of all eigenvalues, see the corresponding full eigenvalue spectrum in Appendix A.3. Numerous mode swappings occur here because the eigenvalues of different modes have different slopes and must inevitably intersect. This shows that only a finite number of eigenvalues of \mathbf{K} represent the *fundamental stability properties* of the discrete structure and that the choice $M = \Lambda^{(1)}$ may not be optimal in general. Initially, higher-order bifurcations can “shoot down” and spoil the smoothness of M .

Deformation-dependent mode tracking, which identifies critical individual eigenvalue branches in the pre-critical state, is an obvious solution. This, however, is not pursued further since the continuous computation of eigenvectors is economically infeasible for larger finite element models.⁶

Ideas for alternative measures. The proposed measure is inspired by the eigenvalue-based representation of the determinant (7.4). However, to avoid the infeasibly large range of $\det \mathbf{K}$, a special minor-type variant of \mathbf{K} is considered. With n_{thr} being a user-defined threshold, defining the number of (smallest) eigenvalues taken into account, the proposed measure reads

$$M(n_{\text{thr}}, \Lambda^{(i)}) = \prod_{i=1}^{n_{\text{thr}}} \ln \left(1 + \frac{\Lambda^{(i)}}{\Lambda_0^{(1)}} \right). \quad (7.20)$$

Here, each eigenvalue of the logarithmic argument is normalized by the *smallest* initial eigenvalue $\Lambda_0^{(1)}$ (not to be confused with the scaled eigenvalue $\bar{\Lambda}$). By that, the magnitude of the eigenvalues becomes (more) independent of the problem at hand, e.g., material or geometry parameters. Furthermore, the natural logarithm reduces the influence of large eigenvalues. In analogy to before, the measure is scaled with its initial value at $\gamma = 0$, i.e.

$$\bar{M} = \bar{M}_n = \frac{M(n_{\text{thr}}, \Lambda_n^{(i)})}{M(n_{\text{thr}}, \Lambda_0^{(i)})}. \quad (7.21)$$

The question that remains to be answered is how to choose the threshold n_{thr} . For the current finite element model (Q2, 5×5) as well as a finer one (20×20), Figure 7.7 (b) and Figure 7.8 (b) shows the eigenmodes which correspond to the respective eigenvalues at the *nearly critical* loading state $\gamma = 1.2$ and post-critical state $\gamma = 0.4$, respectively

⁶However, the issue of efficient mode tracking appears to be relevant in other research fields such as the proper modeling of electromagnetic radiation, see for instance Li et al. 2018.

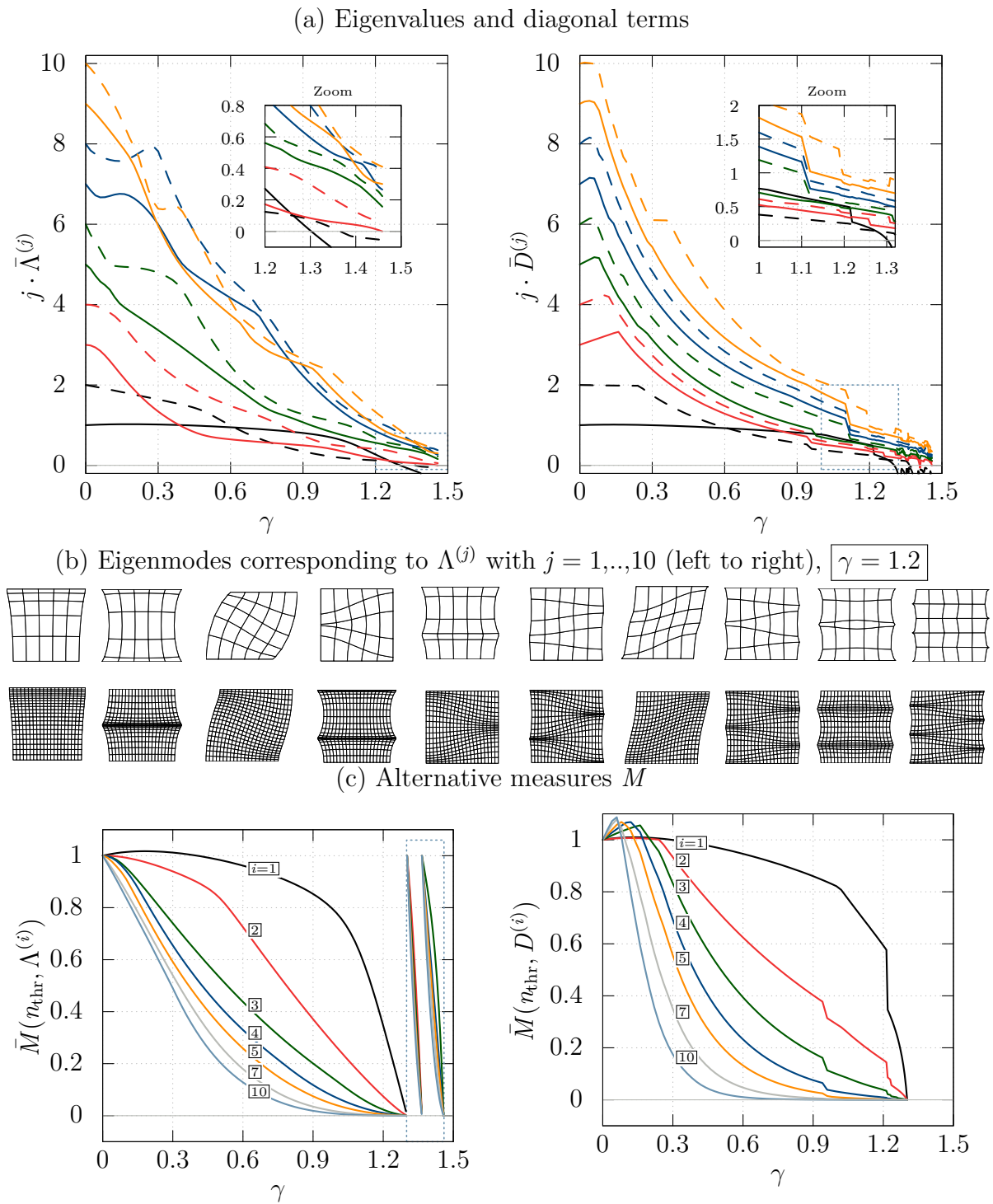


Figure 7.7: Example III; Q2 (5×5); (a) first 10 eigenvalues (left) and diagonal terms (right) over the load factor; (b) first 10 eigenmodes corresponding to $\Lambda^{(j)}$ at $\gamma = 1.2$, Q2 (5×5 (top) and 20×20 (bottom), plotted on the undeformed geometry shortly before the critical reference load $\gamma_c^{(1)} = 1.302$; (c) newly proposed measures.

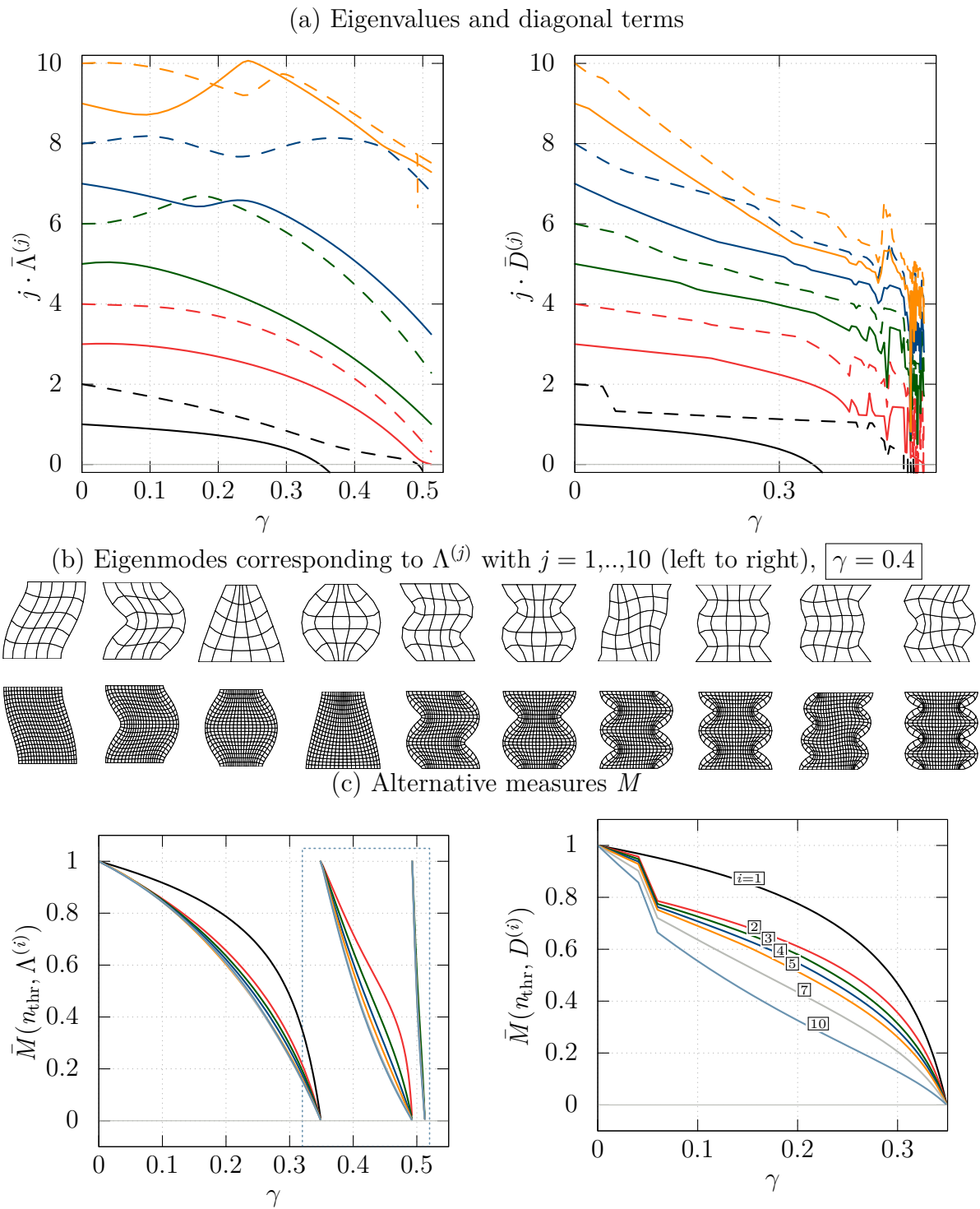


Figure 7.8: Example I; Q2 (5×5); $r = 0.75$, (a) first 10 eigenvalues (left) and diagonal terms (right) over the load factor; (b) first 10 eigenmodes corresponding to $\Lambda^{(j)}$ at $\gamma = 0.4$ – shortly after the first critical reference load $\gamma_c^{(1)} = 0.347$, Q2 (5×5 (top) and 20×20 (bottom), plotted on the undeformed geometry; (c) newly proposed measures.

(recall the critical reference load factor is $\gamma_c^{(1)} = 1.302$ and $\gamma_c^{(1)} = 0.347$). Though the fine model has around 14 times more degrees of freedom (and thus eigenvalues), the 10 lowest modes are very similar. They correspond to the upcoming bifurcation modes, compare the reference modes in Figure 4.8 and Figure 4.5, respectively. For both examples, it is concluded that the lowest set of eigenvalues mainly represents the upcoming structural instability – relatively *independent* of the mesh size. Thus, a single-digit n_{thr} may be sufficient instead of a threshold that is percentage-related to the total number of degrees of freedom. For a set of thresholds n_{thr} up to 10, the left graphs in Figure 7.7 (c) and 7.8 (c) depict the newly proposed measure (7.21). A detailed graph of the higher-order bifurcations is provided in Appendix A.5.2. Good results, in the sense that the slope is “more” linear, are obtained for $n_{\text{thr}} = 2$ and $n_{\text{thr}} = 3$.

For reasons of efficiency, the pre-critical behavior of the diagonal terms is of particular interest. The right graphs in Figure 7.7 (a,c) and 7.8 (a,c) show the behavior of the diagonal entries (a) and, based on $D^{(j)}$, the behavior of the new measure (7.20) (c), i.e., $M(n_{\text{thr}}, D^{(i)})$. Unlike the eigenvalue measure, both sets of diagonal term measures show sharp kinks.

Discussion. Despite the good performance for a selected set of examples, some aspects deserve further attention. Of particular concern are the following questions:

- To what extent is $M^{(j)} = \Lambda^{(j)}$ a reliable choice?
- To what extent is the numerical effort to compute a small set of $\Lambda^{(j)}$ justifiable?
- With respect to the computation of the first critical point: Does the diagonal measure $M = D^{(1)}$ always provide comparable results to $M = \Lambda^{(1)}$?
In other words: is there a relation between the eigenvalues and the diagonal entries?
- Does $D^{(j)}$ admit any physical interpretation?
- With respect to the choice of the activation function α : What is a good shape of $\alpha(\bar{M})$ and what is a good n_{est} ? In other words: What is the best trade-off between small and large load increments in dependence of \bar{M} ?

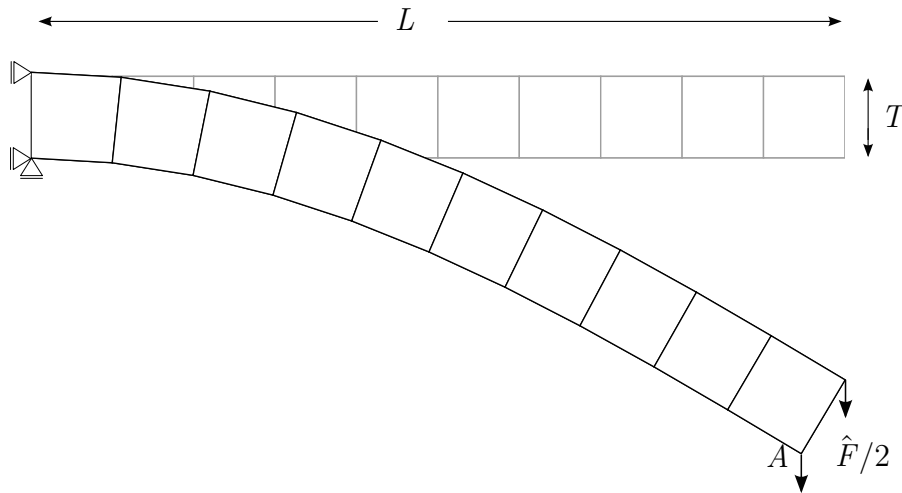


Figure 7.9: Robustness study; problem setup.

7.2 Robustness and Efficiency in the Newton-Raphson Scheme

This section gives a short overview of robustness issues in the Newton-Raphson process in nonlinear finite element analysis. Of concern are two questions:

- Does the strain modification of Q1/ME4 and Q1/MS4 preserve quadratic convergence in the Newton-Raphson process?
- Can, similar to standard EAS elements, the method proposed in Pfefferkorn et al. 2021 be successfully applied to the newly proposed EAS elements Q1/ME4 and Q1/E7?

Figure 7.9 shows the clamped beam problem from Pfefferkorn et al. 2021. The beam-like structure of length $L = 10$ and height $H = 1$ is discretized with a 10×1 mesh. A Saint-Venant Kirchhoff material with $E = 1000$ and $\nu = 0.499$ is used. The beam is subjected to a tip load $\hat{F} = T^3/(1 - \nu^2) \approx 1.3315$. The moderately large deformed configuration is depicted in Figure 7.9.

Table 7.2 shows the number of required iterations for a single load increment as well as the residual norm $\|\mathbf{R}\|$. In analogy to the standard elements Q1/E4 and Q1/S5, a proper asymptotic convergence behavior is observed for all newly proposed formulations. The slightly stiffer behavior, i.e. the smaller tip displacement, of Q1/ME4 and Q1/MS4 is in accordance with the results of Bieber et al. 2022 and related to the strain modification (6.16). This example shows that the newly proposed elements, in particular Q1/ME4, share the same convergence properties as its “parent” Q1/E4, without further

k	Q1/E4	Q1/ME4	Q1/E7	Q1/S5	Q1/MS5
0	$9.416e - 01$	$9.416e - 01$	$9.416e - 01$	$9.416e - 01$	$9.416e - 01$
1	$1.958e + 05$	$1.956e + 05$	$1.958e + 05$	$1.958e + 05$	$1.956e + 05$
2	$2.657e + 04$	$2.652e + 04$	$2.657e + 04$	$1.021e + 04$	$1.021e + 04$
3	$9.305e + 02$	$9.254e + 02$	$9.305e + 02$	$5.202e + 01$	$5.222e + 01$
4	$2.031e + 01$	$2.200e + 01$	$2.016e + 01$	$2.061e - 03$	$2.160e - 03$
5	$2.307e + 01$	$2.436e + 01$	$2.286e + 01$	$3.214e - 10$	$1.534e - 10$
6	$2.247e + 00$	$2.457e + 00$	$2.223e + 00$	-	-
7	$7.268e + 00$	$8.275e + 00$	$7.109e + 00$	-	-
8	$9.827e - 02$	$1.100e - 01$	$9.668e - 02$	-	-
9	$1.258e - 01$	$1.796e - 01$	$1.185e - 01$	-	-
10	$2.950e - 05$	$5.703e - 05$	$2.707e - 05$	-	-
11	$1.281e - 08$	$4.459e - 08$	$1.042e - 08$	-	-
12	$9.059e - 11$	$1.574e - 10$	$1.070e - 10$	-	-
u_2^A	3.443	3.438	3.444	3.444	3.438

Table 7.2: Iteration process of the newly proposed elements based on the residual norm $\|\mathbf{R}\|$.

modifications. However, as described in Pfefferkorn and Betsch 2022, all EAS formulations suffer from suboptimal preasymptotic convergence performance. The strain driven elements require more than twice the number of iterations as the assumed stress elements. This effect is even worsened by an increase of Poisson’s ratio ($\nu \rightarrow 0.5$) as well as more slender elements ($r_e \rightarrow \infty$).

The reason for that discrepancy is related to the strain-driven format of EAS formulation. During the iteration process, stresses are evaluated at non-equilibrated deformation states that degrade from physically meaningful stress. As shown in Kuo-Mo 1987, these stresses can yield a suboptimal geometric stiffness and consequently they significantly spoil the fast convergence within the Newton-Raphson scheme. The number of required iterations can become ineffectively large. It has been shown in Magisano et al. 2017 and Pfefferkorn et al. 2021 that, similar to locking, this effect depends critically on certain parameters, e.g., Poisson’s ratio or the element aspect ratio. This means that, although the nonlinear deformations are similar in size (for a certain set of problem parameters), the number of iterations increases. In contrast to strain-driven formulations, stress-based formulations with an independent pressure or stress fields show an improved behavior. This effect has been observed in Brink and Stein 1996 and Klinkel et al. 2006.

A simple and efficient remedy is the Mixed Integration Point (MIP) method. It has been proposed in Magisano et al. 2017 and further developed by Pfefferkorn et al. 2021 in the context of EAS formulations. The main idea is based on a modified computation

k	Q1/E4-MIP	Q1/ME5-MIP	Q1/E7-MIP
0	$9.416e - 01$	$9.416e - 01$	$9.416e - 01$
1	$1.958e + 05$	$1.958e + 05$	$1.958e + 05$
2	$1.021e + 04$	$2.622e + 04$	$1.021e + 04$
3	$5.206e + 01$	$6.252e + 01$	$5.202e + 01$
4	$2.073e - 03$	$4.979e - 03$	$2.061e - 03$
5	$6.135e - 11$	$1.671e - 10$	$1.194e - 10$
u_2^A	3.443	3.438	3.444

Table 7.3: Iteration process of the newly proposed elements with MIP modification.

of stresses

$$\mathbf{S}_{(k+1)}^{\text{MIP}} = \mathbf{S}_{(k)} + \hat{\mathbf{C}} \left(\mathbf{B}_{(k)} \Delta \mathbf{d}_{(k)} + \mathbf{M}_{\mathbf{E},(k)} \Delta \boldsymbol{\alpha}_{(k)} \right). \quad (7.22)$$

Here, the index k refers to the current iteration step with the Newton-Raphson method and $\mathbf{S}_k = \mathbf{S}(\mathbf{E}_k)$ refers to the “normal” constitutive stresses computed via \mathbf{E} . For the upcoming iteration $k + 1$, stresses (7.22) are then used for the computation of the geometric stiffness matrices (instead of $\mathbf{S}(\mathbf{E}_{k+1})$). Residual quantities are computed in a standard manner and thus convergence towards the original equilibrium state is preserved. The corresponding element formulations are marked with the semi-suffix MIP. Table 7.3 shows the results for MIP-modified EAS formulations. Great improvements, comparable to the assumed stress elements, are obtained. However, an extension to the large strain materials (e.g., Neo-Hooke) is not straightforward; see the discussion in Pfefferkorn et al. 2021.

Chapter 8

Concluding Remarks and Outlook

Several problems that arise in nonlinear finite element analysis were described, analyzed and solved. The investigations were limited to two-dimensional finite elasticity problems. The main findings of this work can be summarized in two main aspects: the development of benchmarks based on existing analytical solutions to finite elasticity problems, as well as the discovery of new issues in nonlinear finite element technology's "old hats", locking and hourglassing, including possible solutions.

Analytical solutions to two nonlinear elasticity problems were presented: large bending of an incompressible rubber block and the underlying bifurcation problem of a compressible block under tension and compression. The problems themselves are simple but still contain important nonlinear phenomena. In the course of the numerical investigations in this thesis, various aspects of their usefulness as finite element benchmarks were demonstrated. While the solutions of the problem's thin-limit cases, namely the bending and buckling of a thin beam, are well-known and widely used in benchmarks, the presented general solutions were, to the best of the author's knowledge, never used in the context of a finite element benchmark. This is remarkable given that the solutions date back more than a half-century to the seminal works by Maurice A. Biot and Ronald S. Rivlin. Both problems enable substantial improvements in reliable benchmarking of nonlinear simulation methods. Future work could complete the large bending benchmark with respect to the underlying stability problem, including an improvement of the observed contradictions between analytical and numerical solutions (cf. Sigaeva et al. 2018). An extension of the bifurcation problem to anisotropic materials, plastic materials as well as three-dimensional problems is evident (cf. Guz 2012, Bigoni 2012). Furthermore, a numerical in-depth analysis of the post-bifurcation problem for a large spectrum of parameters would substantially enhance the overall understanding of the problem.

Two topics related to finite element technology were investigated. Based on the work of Willmann et al. 2022 the issue of volumetric nonlinear locking was further explained in the context of various solid Enhanced Assumed Strain (EAS) finite elements. It was

shown that, for some EAS elements, this stiffening depends on the aspect ratio through a nonlinear effect. However, the special conditions under which the phenomenon occurs, namely higher-order integration and large inhomogeneous element deformations, make it a particularly peculiar occurrence. Possible remedies were presented, including modifications to the strain enhancement of popular EAS formulations. Another topic concerns the issue of artificial instabilities, classified as geometric and material hourglassing. By means of the Ritz method, the results by Bieber et al. 2022 were refined. The trigger mechanisms of geometric- and material-induced instabilities, of both physical and artificial nature, were boiled down into a simple and accessible form. Based on these findings, a potential treatment strategy is straightforward: combat the causes (trigger mechanisms) of hourglassing rather than its symptoms. This deviates from most stabilization methods available in the literature, where artificial instability is alleviated by adding stiffness. Presented were simple modifications of the discrete Green-Lagrange strain tensor at the element level. Numerical examples verify that the method avoids geometric hourglassing with only a slight reduction of accuracy with respect to the modeling of physical instabilities. Future work should focus on an extension into three dimensions as well as a further study on proper selection of the critical deformation modes, including a study on alternative efficient implementations. Based on the present study, the remedies to material hourglassing could be addressed. A future study should include the popular class of displacement-pressure type elements as well as physically more motivated strain-softening materials, such as elastoplastic materials.

A method for the algorithmic treatment of an adaptive load-stepping scheme was presented. It alleviates a major difficulty encountered in the computation of bifurcation points, namely the strongly input-parameter-dependent problem of finding an optimal starting point for the activation of algorithms for the exact determination of critical points (e.g., extended systems or bisection methods). The idea is based on a load-dependent scalar measure, e.g., the smallest eigenvalue of the stiffness matrix, that quantifies a structural system's softening and thus "announces" the upcoming critical point. This measure is used to adapt the load step size appropriately. Numerical examples indicated that the method shows excellent results as long as the measure does not involve large curvatures. Alternative measures were discussed, opening the path for future work.

Appendix A

Appendix

A.1 Technical Aspects of the Finite Element Method

A.1.1 Numerical Quadrature

Table A.1 provides the data of the Gauss-Lobatto and (standard) Gauss-Legendre quadrature. Polynomial of degree $p_{\text{ex}} = 2N_{\text{QP}} - 3$ (Gauss-Lobatto) and $p_{\text{ex}} = 2N_{\text{QP}} - 1$ (Gauss-Legendre) are computed exact for a given number of quadrature points N_{QP} .

N_{QP}	Gauss-Lobatto			Gauss-Legendre		
	p_{ex}	abscissas $\{\pm\xi_i\}$	weights $\{\omega_i\}$	p_{ex}	abscissas $\{\pm\xi_i\}$	weights $\{\omega_i\}$
2	1	1.0000000000	1.0000000000	3	0.5773502692	1.0000000000
3	3	0.0000000000	1.3333333333	5	0.7745966692	0.5555555556
		1.0000000000	0.3333333333		0.0000000000	0.8888888889
4	5	0.4472135954	0.8333333333	7	0.8611363116	0.3478548451
		1.0000000000	0.1666666667		0.3399810436	0.6521451549
5	7	0.0000000000	0.7111111111	9	0.9061798459	0.2369268851
		0.6546536707	0.5444444444		0.5384693101	0.4786286705
		1.0000000000	0.1000000000		0.0000000000	0.5688888889
6	9	0.2852315164	0.5548583770	11	0.2386191861	0.4679139346
		0.7650553239	0.3784749562		0.6612093865	0.3607615730
		1.0000000000	0.0666666666		0.9324695142	0.1713244924

Table A.1: Numerical data for quadrature rules adopted from Zwillinger 2003.

A.1.2 Sobolev Spaces

The presented function norms and spaces are exemplified for a vector-valued function $\mathbf{u} : \Omega_0 = \Omega \rightarrow \mathbb{R}^2$. The energy norm is defined as

$$\|\mathbf{u}\|_E = \sqrt{a(\mathbf{u}, \mathbf{u})} \quad (\text{A.1})$$

and corresponds to twice the strain energy of the body. The space of square integrable functions in Ω is introduced as

$$L_2(\Omega) = \left\{ \mathbf{u} \in L_2 : \int_{\Omega} \mathbf{u} \cdot \mathbf{u} \, d\Omega = \|\mathbf{u}\|_{L_2}^2 < \infty \right\}. \quad (\text{A.2})$$

Here $\|\mathbf{u}\|_{L_2}$ denotes the L_2 -norm of \mathbf{u} , i.e. the generalization of the Euclidean vector norm to functions. The Sobolev norms are denoted as $\|\mathbf{u}\|_{\mathcal{H}^s}$. They are defined via the sum of the L_2 -norm of function \mathbf{u} and its (square integrable) s spatial derivatives, i.e.

$$\|\mathbf{u}\|_{\mathcal{H}^s} = \left(\|\mathbf{u}\|_{L_2}^2 + \left\| \frac{\partial \mathbf{u}}{\partial \mathbf{X}} \right\|_{L_2}^2 + \dots + \left\| \frac{\partial^s \mathbf{u}}{\partial \mathbf{X}^s} \right\|_{L_2}^2 \right)^{\frac{1}{2}}. \quad (\text{A.3})$$

The collected functions \mathbf{u} with a Sobolev norm of order s induce the Sobolev spaces \mathcal{H}^s . Important in linear elasticity is \mathcal{H}^1 in Ω , i.e.

$$\mathcal{H}^1(\Omega) = \left\{ \mathbf{u} \in \mathcal{H}^1 : \|\mathbf{u}\|_{\mathcal{H}^1} = \left(\|\mathbf{u}\|_{L_2}^2 + \left\| \frac{\partial \mathbf{u}}{\partial \mathbf{X}} \right\|_{L_2}^2 \right)^{\frac{1}{2}} < \infty \right\}. \quad (\text{A.4})$$

Of course, $L_2(\Omega) = \mathcal{H}^0(\Omega)$. The norms $\|\mathbf{u}\|_{\#}$ and $\|\mathbf{u}\|_b$ are called *equivalent norms* if

$$C_1 \|\mathbf{u}\|_{(b)} < \|\mathbf{u}\|_{(\#)} < C_2 \|\mathbf{u}\|_{(b)}, \quad (\text{A.5})$$

with constants C_1 and C_2 independent of \mathbf{u} . It can be shown that the energy norm is equivalent to all Sobolev norms.

A.2 Supplements to the Bifurcation Problem

A.2.1 Derivation of the Trigonometric Ansatz Functions

As a subsidiary argument concerning Section 4.1.3, the derivation of the specific ansatz functions for the EI and EC cases are provided. The final buckling mode has to be

real, which can be achieved via various technical options. The ansatz functions can be constructed complex such that complex coefficients provide finally a real buckling mode, see e.g Ogden 1997. In contrast to that the ansatz functions here are constructed to be real.

Starting point is the general ansatz (4.26) which can be specified as

$$\Delta u_\alpha = F_\alpha \left(\sum_{j=1}^4 m_\alpha^{(j)} e^{iz_j} \right), \quad (\text{A.6})$$

where F_α denotes a function which arguments contains $z_j = p_1^{(j)} X_1 + p_2 X_2$, where $p_2 \in \mathbb{R}$ is determined by the (odd or even) wave numbers and completes the resulting four solutions $p_1^{(j)}$ of the characteristic equation (4.27). The subsequent derivations make use of Euler's formulae

$$e^{\pm ix} = \cos x \pm i \sin x \quad \text{and} \quad e^{\pm x} = \cosh x \pm \sinh x, \quad x \in \mathbb{R}, \quad (\text{A.7})$$

such that the exponential form can be expressed in a more intuitive trigonometric form.

EI case. The four purely imaginary solutions (4.35) define $z_{(1,2,3,4)} = p_2 \cdot \{\pm\alpha, \pm\beta\}$. Exemplified for the \mathcal{S}^1 case, the ansatz for the *real* incremental displacement field can be derived via

$$\begin{aligned} \Delta u_1 &= \sum_{j=1}^4 m_1^j \left(\frac{e^{iz_j} + \overline{e^{iz_j}}}{2} \right) \\ &= \text{Re} \left[\left(m_1^{(1)} e^{\alpha p_2 X_1} + m_1^{(2)} e^{-\alpha p_2 X_1} + m_1^{(3)} e^{\beta p_2 X_1} + m_1^{(4)} e^{-\beta p_2 X_1} \right) e^{ip_2 X_2} \right] \\ &= [A_1 \cosh(\alpha p_2 X_1) + B_1 \sinh(\alpha p_2 X_1) + C_1 \cosh(\beta p_2 X_1) + D_1 \sinh(\beta p_2 X_1)] \cos(p_2 X_2) \end{aligned} \quad (\text{A.8})$$

and

$$\begin{aligned} \Delta u_2 &= \sum_{j=1}^4 m_2^j \left(\frac{e^{iz_j} - \overline{e^{iz_j}}}{2i} \right) \\ &= \text{Im} \left[\left(m_2^{(1)} e^{\alpha p_2 X_1} + m_2^{(2)} e^{-\alpha p_2 X_1} + m_2^{(3)} e^{\beta p_2 X_1} + m_2^{(4)} e^{-\beta p_2 X_1} \right) e^{ip_2 X_2} \right] \\ &= -[A_2 \sinh(\alpha p_2 X_1) + B_2 \cosh(\alpha p_2 X_1) + C_2 \sinh(\beta p_2 X_1) + D_2 \cosh(\beta p_2 X_1)] \sin(p_2 X_2) \end{aligned} \quad (\text{A.9})$$

where a rearrangement provides the real constants $(A_\alpha, B_\alpha, C_\alpha, D_\alpha)$. It remains to verify (4.36), i.e. that constants (A_α, C_α) are decoupled from (B_α, D_α) . Substituting (A.8) and

(A.9) in one of the incremental equilibrium equations (4.23) demands

$$A_\alpha = B_\alpha \quad \text{or} \quad A_\alpha \neq 0, B_\alpha = 0 \quad \text{or} \quad A_\alpha = 0, B_\alpha \neq 0, \quad (\text{A.10a})$$

$$C_\alpha = D_\alpha \quad \text{or} \quad C_\alpha \neq 0, D_\alpha = 0 \quad \text{or} \quad C_\alpha = 0, D_\alpha \neq 0. \quad (\text{A.10b})$$

Furthermore the incremental boundary conditions (4.20)₁ (or alternatively (4.20)₂) yields

$$\begin{aligned} & \sinh(\alpha p_1 \{\pm L_1\}) [A_{1111} A_1 \alpha + A_{1122} A_2] + \cosh(\alpha p_1 \{\pm L_1\}) [A_{1111} B_1 \alpha + A_{1122} B_2] \\ & + \sinh(\beta p_1 \{\pm L_1\}) [A_{1111} C_1 \beta + A_{1122} C_2] + \cosh(\beta p_1 \{\pm L_1\}) [A_{1111} D_1 \beta + A_{1122} D_2] = 0, \end{aligned} \quad (\text{A.11})$$

showing that the very left relations (A.10) are not compatible for both boundaries in (A.11) in contrast to the middle and left relations (A.10). Consequently only purely symmetric or antisymmetric modes are simultaneously possible.

EC case. The four complex solutions (4.43) define the trigonometric representation. Again exemplified for the \mathcal{S}^1 case, the ansatz for the *real* incremental displacement field can be derived via

$$\begin{aligned} \Delta u_1 &= \sum_{j=1}^4 m_1^j \left(\frac{e^{iz_j} + \overline{e^{iz_j}}}{2} \right) \\ &= \left[A_1 \cosh(\gamma p_2 X_1) \cos(\delta p_2 X_1) + B_1 \sinh(\gamma p_2 X_1) \cos(\delta p_2 X_1) \right. \\ & \quad \left. + C_1 \sinh(\gamma p_2 X_1) \sin(\delta p_2 X_1) + D_1 \cosh(\gamma p_2 X_1) \sin(\delta p_2 X_1) \right] \cos(p_2 X_2) \end{aligned} \quad (\text{A.12})$$

and

$$\begin{aligned} \Delta u_2 &= \sum_{j=1}^4 m_2^j \left(\frac{e^{iz_j} - \overline{e^{iz_j}}}{2i} \right) \\ &= - \left[A_2 \sinh(\gamma p_2 X_1) \cos(\delta p_2 X_1) + B_2 \cosh(\gamma p_2 X_1) \cos(\delta p_2 X_1) \right. \\ & \quad \left. + C_2 \cosh(\gamma p_2 X_1) \sin(\delta p_2 X_1) + D_2 \sinh(\gamma p_2 X_1) \sin(\delta p_2 X_1) \right] \sin(p_2 X_2). \end{aligned} \quad (\text{A.13})$$

Similar considerations as for the EI case (A.10) verify the decoupling.

A.2.2 Elliptic-Complex Case – Coefficients

The coefficients read

$$\begin{aligned}
\mathbf{u} &= A_{1221}A_{2121}(\delta^2 + \gamma^2)^2 A_{1111}^2 + A_{1122}A_{1212}(A_{1122}A_{2112} - A_{1212}A_{2121} + A_{1221}A_{2112}) \\
&\quad + [(-A_{1221}^2 A_{2112} + (-A_{1122}A_{2112} + A_{1212}A_{2121})A_{1221} + 3A_{1122}A_{1212}A_{2121})\gamma^2 \\
&\quad \quad - \delta^2(A_{1221}^2 A_{2112} + (A_{1122}A_{2112} - A_{1212}A_{2121})A_{1221} + A_{1122}A_{1212}A_{2121})]A_{1111} \\
\mathbf{v} &= A_{1221}A_{2121}(\delta^2 + \gamma^2)^2 A_{1111}^2 + A_{1122}A_{1212}(A_{1122}A_{2112} - A_{1212}A_{2121} + A_{1221}A_{2112}) \\
&\quad + [(A_{1221}^2 A_{2112} + (A_{1122}A_{2112} - A_{1212}A_{2121})A_{1221} + A_{1122}A_{1212}A_{2121})\gamma^2 \\
&\quad \quad - 3(-A_{1221}^2 A_{2112}/3 + (-A_{1122}A_{2112}/3 + A_{1212}A_{2121}/3)A_{1221} + A_{1122}A_{1212}A_{2121})\delta^2]A_{1111}.
\end{aligned} \tag{A.14}$$

A.2.3 Bifurcation Modes – Coefficients

Once a critical stretch is calculated the coefficients of the critical mode are

$$\begin{aligned}
A_1 &= -b_1 A_2 \frac{\alpha(A_{1122} + A_{1221})}{A_{1111}\alpha^2 - A_{1212}}, \\
A_2 &= -\hat{C}_2 \frac{\beta t_\beta \cosh(\beta p_2 L_1)(A_{1111}\alpha^2 - A_{1212})}{\alpha t_\alpha \cosh(\alpha p_2 L_1)(A_{1111}\beta^2 - A_{1212})}, \\
C_1 &= -b_1 \hat{C}_2 \frac{\beta(A_{1122} + A_{1221})}{A_{1111}\beta^2 - A_{1212}}, \\
C_2 &= \hat{C}_2.
\end{aligned} \tag{A.15}$$

and

$$\begin{aligned}
B_1 &= -b_1 B_2 \frac{\alpha(A_{1122} + A_{1221})}{A_{1111}\alpha^2 - A_{1212}}, \\
B_2 &= -\hat{D}_2 \frac{\beta t_\beta \sinh(\beta p_2 L_1)(A_{1111}\alpha^2 - A_{1212})}{\alpha t_\alpha \sinh(\alpha p_2 L_1)(A_{1111}\beta^2 - A_{1212})}, \\
D_1 &= -b_1 \hat{D}_2 \frac{\beta(A_{1122} + A_{1221})}{A_{1111}\beta^2 - A_{1212}}, \\
D_2 &= \hat{D}_2.
\end{aligned} \tag{A.16}$$

for the EI case. The EC case yields

$$\begin{aligned}
 A_1 &= -b_1 \chi_1 \frac{2A_{1111}A_2\delta^2\gamma + \hat{C}_2(-2A_{1111}\gamma^2 + \chi_4)\delta + A_2\gamma\chi_4}{4A_{1111}^2\delta^2\gamma^2 + \chi_4^2} \\
 A_2 &= -4\hat{C}_2 \frac{A_{\text{num}}}{A_{\text{denum}}} \quad \text{with:} \\
 A_{\text{num}} &= -c_\delta\delta(-2\gamma^2 A_{1111}^2 A_{2121}\delta^2 + \gamma^2 \chi_1 A_{1111} A_{2112} - \chi_4(A_{2112}\chi_1 + A_{2121}\chi_4)/2)\mathbf{c}_\gamma/2 \\
 &\quad + \gamma A_{1111}(\gamma^2 A_{1111} A_{2121} + \chi_1 A_{2112}/2)\delta^2 + \chi_4(A_{2112}\chi_1 + A_{2121}\chi_4)/4\mathbf{f}_\gamma s_\delta \\
 A_{\text{denum}} &= 4\gamma(A_{1111}(\gamma^2 A_{1111} A_{2121} + \chi_1 A_{2112}/2)\delta^2 + \chi_4 A_{2112}\chi_1 + A_{2121}\chi_4)/4 \cos(\delta p_2 L_1)\mathbf{c}_\gamma \\
 &\quad + 2\delta\mathbf{c}_\gamma(-2\gamma^2 A_{1111}^2 A_{2121}\delta^2 + \gamma^2 \chi_1 A_{1111} A_{2112} - \chi_4(A_{2112}\chi_1 + A_{2121}\chi_4)/2)s_\delta \\
 C_1 &= (2A_1 A_{1111}\delta\gamma + b_1 A_2 \delta\chi_1 - b_1 \hat{C}_2 \gamma\chi_1)/\chi_4 \\
 C_2 &= \hat{C}_2.
 \end{aligned}$$

and

$$\begin{aligned}
 B_1 &= -b_1 \chi_1 \frac{2A_{1111}B_2\delta^2\gamma + \hat{D}_2(-2A_{1111}\gamma^2 + \chi_4)\delta + B_2\gamma\chi_4}{4A_{1111}^2\delta^2\gamma^2 + \chi_4^2} \\
 B_2 &= -4\hat{D}_2 \frac{B_{\text{num}}}{B_{\text{denum}}} \quad \text{with:} \\
 B_{\text{num}} &= \left(\gamma(A_{1111}(\gamma^2 A_{1111} A_{2121} + A_{2112}\chi_1/2)\delta^2 + \chi_4(A_{2112}\chi_1 + A_{2121}\chi_4)/4) \sin(\delta p_2 L_1)\mathbf{c}_\gamma \right. \\
 &\quad \left. - \cos(\delta p_2 L_1)(-2\gamma^2 A_{1111}^2 A_{2121}\delta^2 + \gamma^2 \chi_1 A_{1111} A_{2112} - \chi_4(A_{2112}\chi_1 + A_{2121}\chi_4)/2)\mathbf{f}_\gamma\delta/2 \right) \\
 B_{\text{denum}} &= \left(2 \sin(\delta p_2 L_1)(-2\gamma^2 A_{1111}^2 A_{2121}\delta^2 + \gamma^2 \chi_1 A_{1111} A_{2112} - \chi_4(A_{2112}\chi_1 + A_{2121}\chi_4)/2)\delta \cosh(\gamma p_2 L_1) \right. \\
 &\quad \left. + 4(A_{1111}(\gamma^2 A_{1111} A_{2121} + A_{2112}\chi_1/2)\delta^2 + \chi_4(A_{2112}\chi_1 + A_{2121}\chi_4)/4)\gamma \cos(\delta p_2 L_1)\mathbf{f}_\gamma \right) \\
 D_1 &= b_1 \frac{-B_2\gamma\chi_1 - \hat{D}_2\delta\chi_1 - b_1 B_1\chi_4}{2\gamma A_{1111}\delta} \\
 D_2 &= \hat{D}_2.
 \end{aligned}$$

A.3 Finite Bending Problem – Stress Resultants

The the integral for the bending moment (4.79) can be computed as follow:

$$\begin{aligned}
M &= \int_{\lambda(r_i)}^{\lambda(r_o)} \sigma_{\theta\theta} \underbrace{\left(\frac{L}{\alpha\lambda}\right)}_r \underbrace{\left(-\frac{L}{\alpha\lambda^2}d\lambda\right)}_{dr} = \frac{L^2}{\alpha^2} \int_{\lambda_i}^{\lambda_o} \left(\frac{\tilde{W}'}{\lambda^2} - \frac{\tilde{W}}{\lambda^3} + \frac{\tilde{W}(\lambda_i)}{\lambda^3} \right) d\lambda \\
&= \frac{L^2}{\alpha^2} \left\{ \int_{\lambda_i}^{\lambda_o} \frac{\tilde{W}}{\lambda^3} d\lambda + \int_{\lambda_i}^{\lambda_o} \left(\frac{\tilde{W}'}{\lambda^2} - 2\frac{\tilde{W}}{\lambda^3} \right) d\lambda + \int_{\lambda_i}^{\lambda_o} \frac{\tilde{W}(\lambda_i)}{\lambda^3} d\lambda \right\} \\
&= \frac{L^2}{\alpha^2} \left\{ \int_{\lambda_i}^{\lambda_o} \frac{\tilde{W}}{\lambda^3} d\lambda + \left[\frac{\tilde{W}}{\lambda^2} - \frac{\tilde{W}(\lambda_i)}{2\lambda^2} \right]_{\lambda_i}^{\lambda_o} \right\} \tag{A.17} \\
&= \frac{L^2}{\alpha^2} \left\{ \int_{\lambda_i}^{\lambda_o} \frac{\tilde{W}}{\lambda^3} d\lambda + \tilde{W}(\lambda_i) \frac{\alpha^2}{2L^2} (r_o^2 - r_i^2) \right\} \\
&= \frac{L^2}{\alpha^2} \int_{\lambda_i}^{\lambda_o} \frac{\tilde{W}}{\lambda^3} d\lambda + \frac{LT}{\alpha} \tilde{W}(\lambda_i)
\end{aligned}$$

Here relations (4.60c) and (4.69) are used. In a similar manner the vanishing normalforce (4.78) can be confirmed via

$$\begin{aligned}
N &= \int_{\lambda_i}^{\lambda_o} \left(\frac{\tilde{W}'}{\lambda} - \frac{\tilde{W}}{\lambda^2} + \frac{\tilde{W}(\lambda_i)}{\lambda^2} \right) d\lambda \\
&= \frac{L}{\alpha} \left[\frac{\tilde{W}}{\lambda} - \frac{\tilde{W}(\lambda_i)}{\lambda} \right]_{\lambda_i}^{\lambda_o} = 0
\end{aligned} \tag{A.18}$$

A.4 Constants

Coefficients of isochoric constraints for the model problem for Q1 read

$$\begin{aligned}
A_1 &= c_2^2 c_3^2 + 2c_2^2 c_3 + 2c_2 c_3^2 + c_2^2 + 4c_2 c_3 + c_3^2 + 2c_2 + 2c_3 + 1 \\
A_2 &= 2c_1 (c_2 c_3^2 + 2c_2 c_3 + c_3^2 + c_2 + 2c_3 + 1) \\
A_3 &= c_1^2 (c_3^2 + 2c_3 + 1)
\end{aligned} \tag{A.19}$$

and for Q1/E4 they read

$$\begin{aligned}
 B_2 &= 2(c_1 c_2 c_3^2 + \alpha_2 c_2^2 + 2c_1 c_2 c_3 + c_1 c_3^2 + 2\alpha_2 c_2 + c_1 c_2 + 2c_1 c_3 + \alpha_2 + c_1) \\
 B_3 &= c_1(c_1 c_3^2 + 4\alpha_2 c_2 + 2c_1 c_3 + 4\alpha_2 + c_1) \\
 B_4 &= -4\alpha_3(c_1 c_2 + \alpha_3 + c_1) \\
 B_5 &= -4\alpha_3 c_1^2 \\
 B_6 &= 2\alpha_2 c_1^2
 \end{aligned} \tag{A.20}$$

A.5 Adaptive Load Control – Technical Aspects

A.5.1 Quadratic Extrapolation

Using $\gamma_{n+1} = \gamma_n + x\Delta\gamma_{n-1}$, quadratic extrapolation yields

$$\bar{M}_n^{\text{ext}}(\gamma) = \bar{M}_{n-2}L_{n-2} + \bar{M}_{n-1}L_{n-1} + \bar{M}_nL_n = ax^2 + bx + \bar{M}_n. \tag{A.21}$$

with $\gamma_{n+1} = \gamma_n + \Delta\gamma_n = \gamma_n + x\Delta\gamma_{n-1}$

$$a := \frac{\Delta\bar{M}_{n-1}(\Delta\bar{M}_{n-1}\Delta\gamma_{n-2} - \Delta\bar{M}_{n-2}\Delta\gamma_{n-1})}{\Delta\gamma_{n-2}(\Delta\gamma_{n-2} + \Delta\gamma_{n-1})}, \tag{A.22a}$$

$$b := \frac{\Delta\bar{M}_{n-1} \cdot \Delta\gamma_{n-2}(\Delta\gamma_{n-2} + 2\Delta\gamma_{n-1}) - \Delta\bar{M}_{n-2}\Delta\gamma_n^2}{\Delta\gamma_{n-2}(\Delta\gamma_{n-2} + \Delta\gamma_{n-1})}. \tag{A.22b}$$

Similar to Equation (7.11) this yields

$$ax^2 + bx = \alpha(\bar{M}_n) \quad \Rightarrow \quad x = \frac{-b \pm \sqrt{b^2 - 4a\alpha(\bar{M}_n)}}{2a} \tag{A.23}$$

The correct x can then be used to update the load factor according to Equations (7.13).

A.5.2 Supplements to Figure 7.7 and 7.8

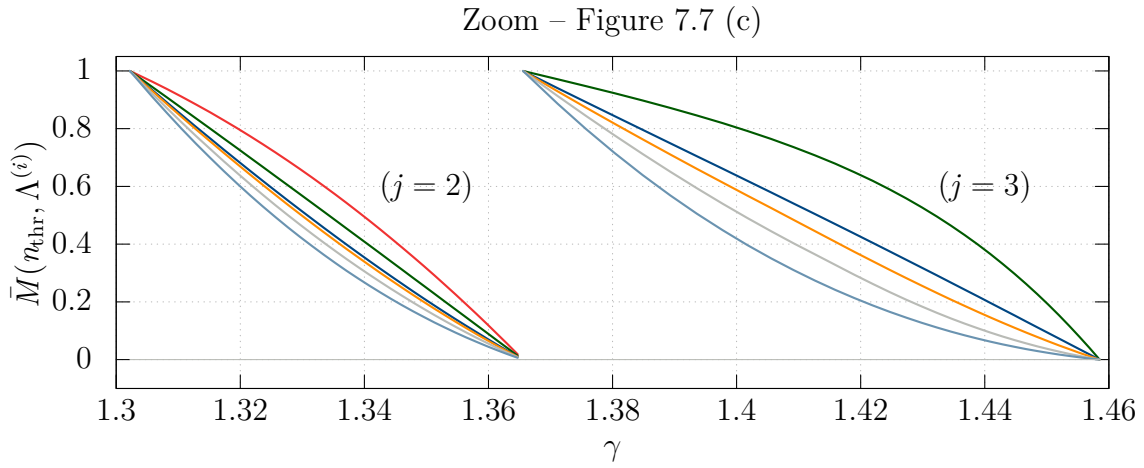


Figure A.1: Example III of Section 7.1.4; BK block with $r = 1.0$ under tension; Q2 (5×5).

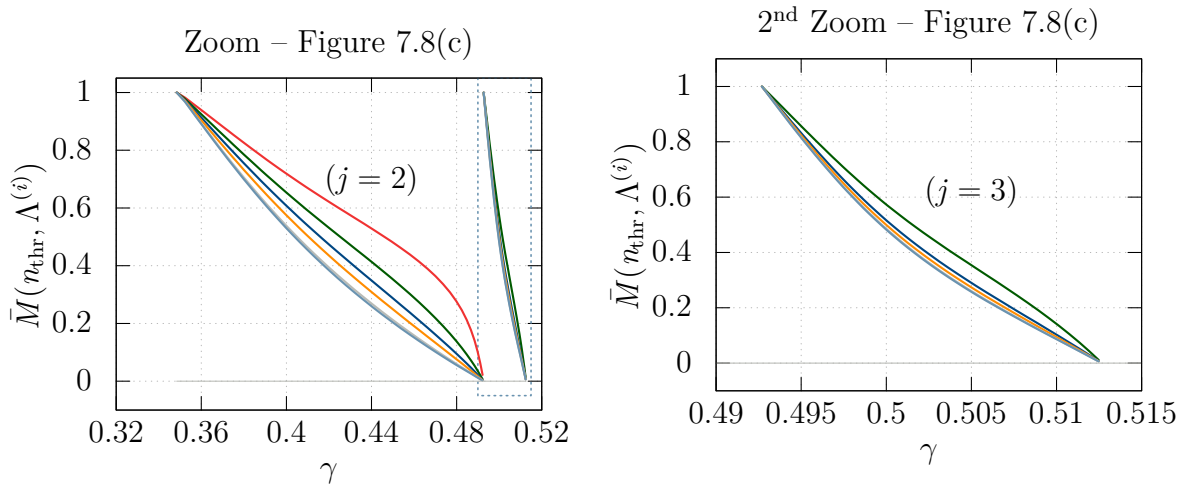


Figure A.2: Example I of Section 7.1.4; NH block with $r = 0.75$ under compression; Q2 (5×5).

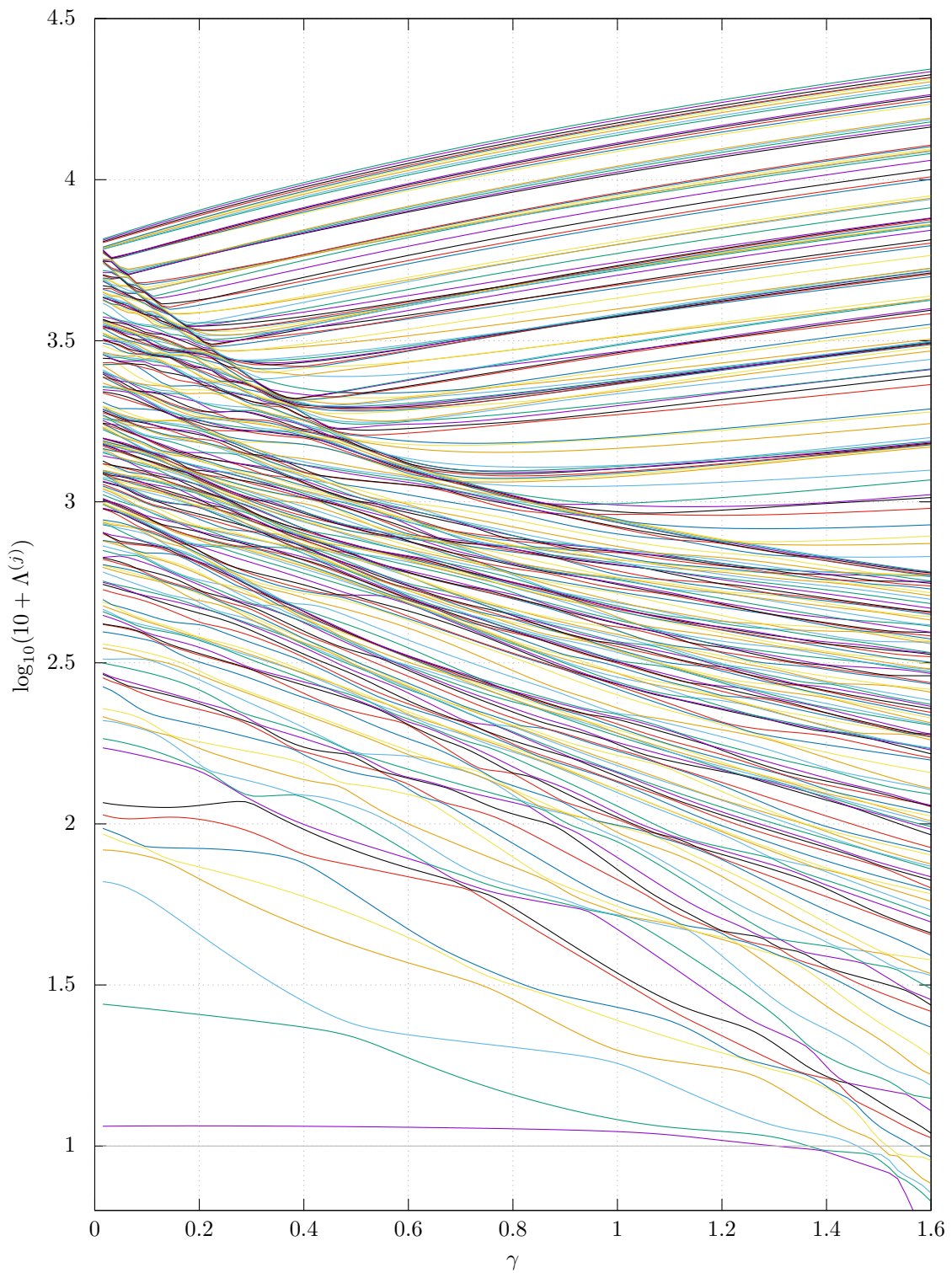


Figure A.3: Eigenvalue spectrum; Example III of Section 7.1.4; BK block with $r = 1.0$ under tension; Q2 (5×5); complete set of all 219 eigenvalues $\Lambda^{(j)}$ over the load factor.

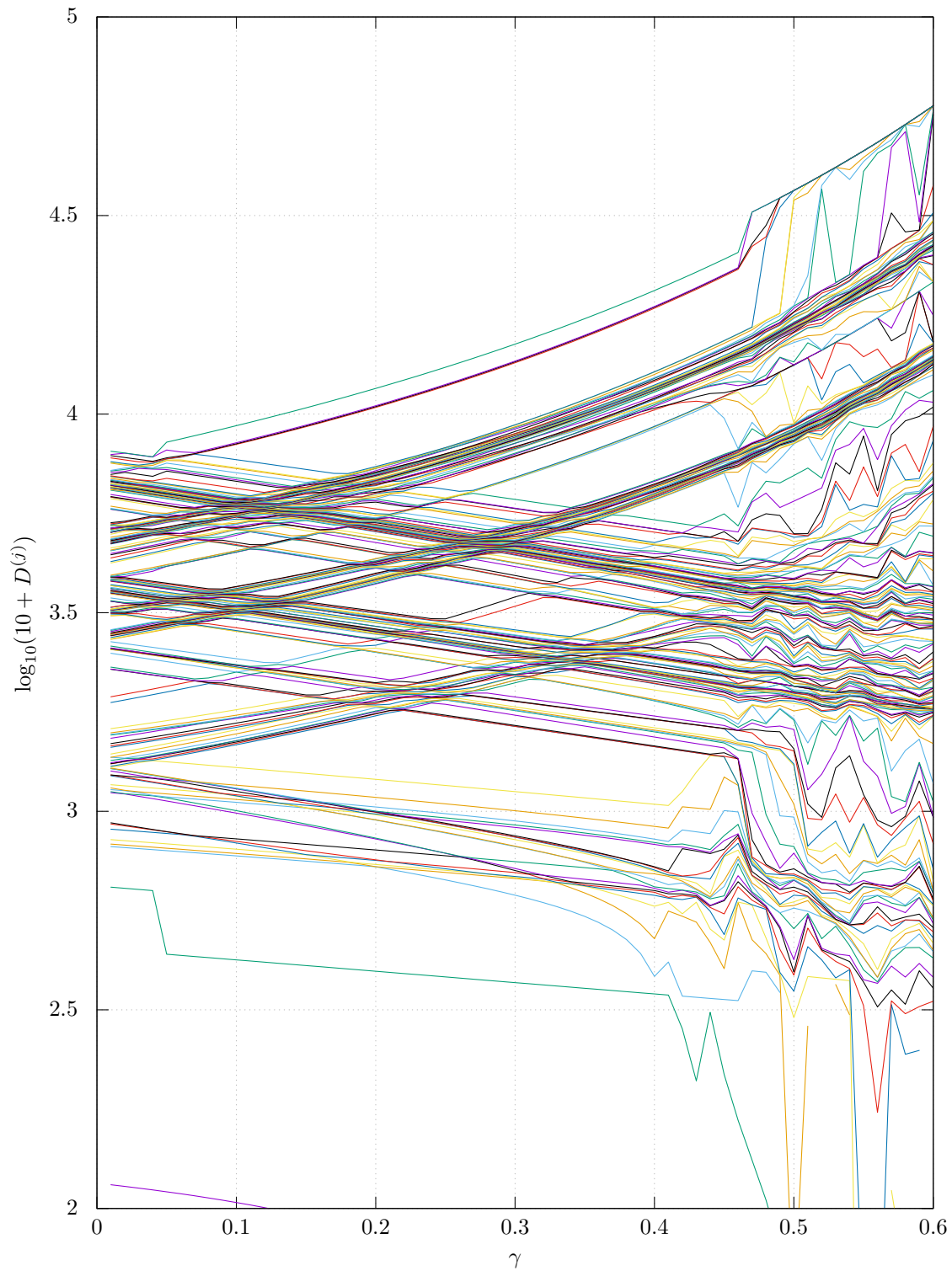


Figure A.4: Diagonal term spectrum; Example III of Section 7.1.4; BK block with $r = 1.0$ under tension; Q2 (5×5); complete set of all 219 diagonal terms $D^{(j)}$ over the load factor.

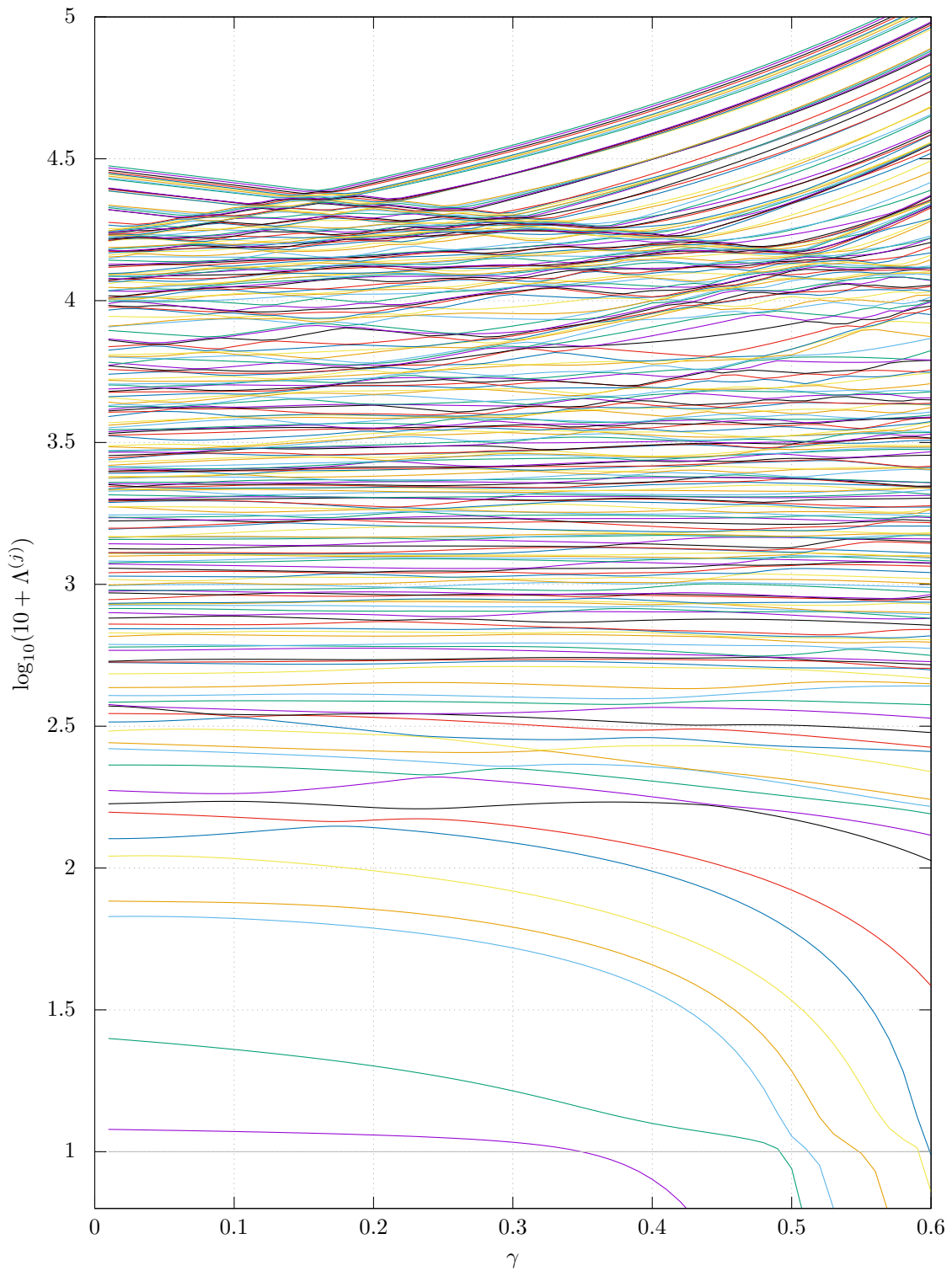


Figure A.5: Eigenvalue spectrum; Example I of Section 7.1.4; BK block with $r = 0.75$ under compression; Q2 (5×5); complete set of all 219 eigenvalues $\Lambda^{(j)}$ over the load factor.

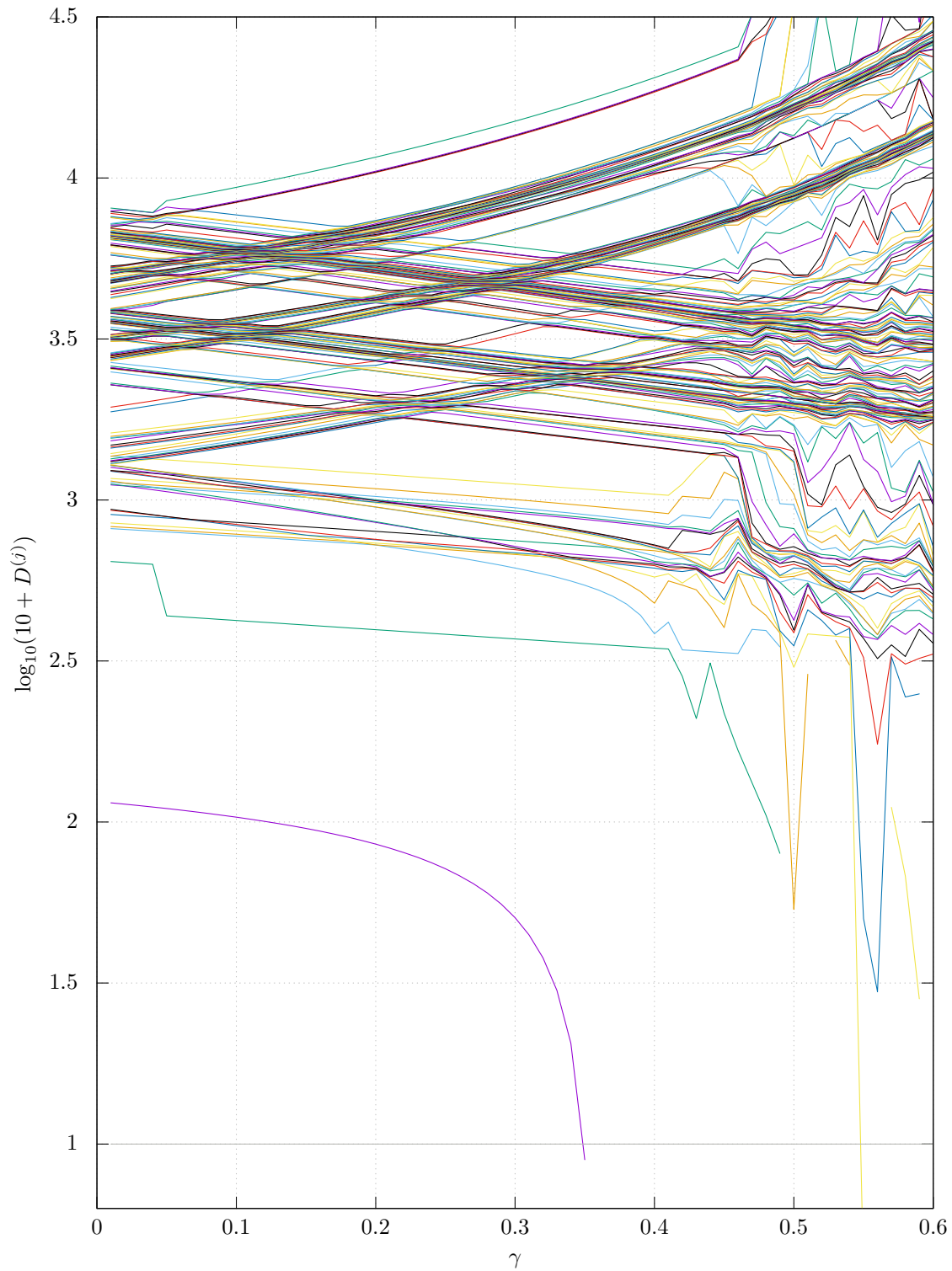


Figure A.6: Diagonal term spectrum; Example I of Section 7.1.4; BK block with $r = 0.75$ under compression; Q2 (5×5); complete set of all 219 diagonal terms $D^{(j)}$ over the load factor.

Bibliography

- Adam, C., S. Bouabdallah, M. Zarroug, and H. Maitournam (2014). “Improved numerical integration for locking treatment in isogeometric structural elements, Part I: Beams”. In: *Comput Methods Appl Mech Eng* 279, pp. 1–28. DOI: <https://doi.org/10.1016/j.cma.2014.06.023>.
- Andelfinger, U. and E. Ramm (1993). “EAS-elements for two-dimensional, three-dimensional, plate and shell structures and their equivalence to HR-elements”. In: *Int J Numer Meth Eng* 36.8, pp. 1311–1337. DOI: <https://doi.org/10.1002/nme.1620360805>.
- Argyris, J. H. and S. Kelsey (1960). *Energy Theorems and Structural Analysis*. Butterworth’s Scientific Publications.
- Armero, F. (2000). “On the locking and stability of finite elements in finite deformation plane strain problems”. In: *Computers & Structures* 75.3, pp. 261–290. DOI: [https://doi.org/10.1016/S0045-7949\(99\)00136-4](https://doi.org/10.1016/S0045-7949(99)00136-4).
- Audoly, B. and J. Hutchinson (2016). “Analysis of necking based on a one-dimensional model”. en. In: *Journal of the Mechanics and Physics of Solids* 97, pp. 68–91. DOI: [10.1016/j.jmps.2015.12.018](https://doi.org/10.1016/j.jmps.2015.12.018).
- Auricchio, F., L. Beirão da Veiga, C. Lovadina, and A. Reali (2005). “A stability study of some mixed finite elements for large deformation elasticity problems”. In: *Comput Methods Appl Mech Eng* 194.9, pp. 1075–1092. DOI: <https://doi.org/10.1016/j.cma.2004.06.014>.
- (2010). “The importance of the exact satisfaction of the incompressibility constraint in nonlinear elasticity: mixed FEMs versus NURBS-based approximations”. In: *Comput Methods Appl Mech Eng*. Computational Geometry and Analysis 199.5, pp. 314–323. DOI: <https://doi.org/10.1016/j.cma.2008.06.004>.
- Auricchio, F., L. Beirão da Veiga, C. Lovadina, A. Reali, R. L. Taylor, and P. Wriggers (2013). “Approximation of incompressible large deformation elastic problems: some unresolved issues”. In: *Computational Mechanics* 52.5, pp. 1153–1167. DOI: <https://doi.org/10.1007/s00466-013-0869-0>.
- Babuska, Ivo, John R. Whiteman, and Theofanis Strouboulis (2011). *Finite Elements: An Introduction to the Method and Error Estimation*. Oxford.
- Babuška, I. and M. Suri (1992). “On Locking and Robustness in the Finite Element Method”. In: *SIAM J. Numer. Anal.* 29.5, pp. 1261–1293. DOI: <https://doi.org/10.1137/0729075>.

- Balbi, V., E. Kuhl, and P. Ciarletta (2015). “Morphoelastic control of gastro-intestinal organogenesis: Theoretical predictions and numerical insights”. In: *Journal of the Mechanics and Physics of Solids* 78, pp. 493–510. DOI: <https://doi.org/10.1016/j.jmps.2015.02.016>.
- Bardet, J. P. (1990a). “Finite element analysis of plane strain bifurcation within compressible solids”. In: *Computers & Structures* 36.6, pp. 993–1007. DOI: [https://doi.org/10.1016/0045-7949\(90\)90206-H](https://doi.org/10.1016/0045-7949(90)90206-H).
- (1990b). “Finite element analysis of surface instability in hypo-elastic solids”. In: *Comput Methods Appl Mech Eng* 78.3, pp. 273–296. DOI: [https://doi.org/10.1016/0045-7825\(90\)90002-4](https://doi.org/10.1016/0045-7825(90)90002-4).
- Bathe, K. (1996). *Finite Element Procedures*. Prentice Hall.
- Beatty, M. F. (1987). “Topics in Finite Elasticity: Hyperelasticity of Rubber, Elastomers, and Biological Tissues—With Examples”. In: *Applied Mechanics Reviews* 40.12, pp. 1699–1734. DOI: <https://doi.org/10.1115/1.3149545>.
- Bergan, P. G., G. Horrigmoe, B. Brakeland, and T. H. Soreide (1978). “Solution techniques for non-linear finite element problems”. In: *Int J Numer Meth Eng* 12.11, pp. 1677–1696. DOI: <https://doi.org/10.1002/nme.1620121106>.
- Betsch, P., F. Gruttmann, and E. Stein (1996). “A 4-node finite shell element for the implementation of general hyperelastic 3D-elasticity at finite strains”. In: *Comput Methods Appl Mech Eng* 130.1, pp. 57–79. DOI: [https://doi.org/10.1016/0045-7825\(95\)00920-5](https://doi.org/10.1016/0045-7825(95)00920-5).
- Bieber, S., F. Auricchio, A. Reali, and M. Bischoff (2022). “Artificial Instabilities of Finite Elements for Nonlinear Elasticity: Analysis and Remedies”. In: *Engineering Archive*. DOI: <https://doi.org/10.31224/2604>.
- Bigoni, D. (2012). *Nonlinear Solid Mechanics: Bifurcation Theory and Material Instability*. Cambridge: Cambridge University Press.
- Biot, M. A. (1963a). “Exact theory of buckling of a thick slab”. en. In: *Applied Scientific Research, Section A* 12.2, pp. 183–198. DOI: <https://doi.org/10.1007/BF03184639>.
- (1963b). “Surface instability of rubber in compression”. In: *Applied Scientific Research, Section A* 12.2, pp. 168–182. DOI: <https://doi.org/10.1007/BF03184638>.
- (1965). *Mechanics of incremental deformations*.
- Bischoff, M. and E. Ramm (1997). “Shear deformable shell elements for large strains and rotations”. In: *Int J Numer Meth Eng* 40.23, pp. 4427–4449. DOI: [10.1002/\(SICI\)1097-0207\(19971215\)40:23<4427::AID-NME268>3.0.CO;2-9](https://doi.org/10.1002/(SICI)1097-0207(19971215)40:23<4427::AID-NME268>3.0.CO;2-9).
- Bischoff, M., E. Ramm, and D. Braess (1999). “A class of equivalent enhanced assumed strain and hybrid stress finite elements”. In: *Computational Mechanics* 22.6, pp. 443–449. DOI: <https://doi.org/10.1007/s004660050378>.
- Blatz, P. J. and W. L. Ko (1962). “Application of Finite Elastic Theory to the Deformation of Rubbery Materials”. In: *Transactions of the Society of Rheology* 6.1, pp. 223–252. DOI: <https://doi.org/10.1122/1.548937>.

- Brezzi, F. (1974). “On the existence, uniqueness and approximation of saddle-point problems arising from lagrangian multipliers”. In: *Revue française d’automatique, informatique, recherche opérationnelle. Analyse numérique* 8 (R2), pp. 129–151. DOI: <https://doi.org/10.1051/m2an/197408R201291>.
- Brink, U. and E. Stein (1996). “On Some Mixed Finite Element Methods for Incompressible and Nearly Incompressible Finite Elasticity”. In: *Comput Mech* 19.1, pp. 105–119. DOI: 10.1007/BF02824849.
- Budiansky, B. (1974). “Theory of Buckling and Post-Buckling Behavior of Elastic Structures”. In: ed. by Chia-Shun Yih. Vol. 14. *Advances in Applied Mechanics*. Elsevier, pp. 1–65. DOI: [https://doi.org/10.1016/S0065-2156\(08\)70030-9](https://doi.org/10.1016/S0065-2156(08)70030-9).
- Calisthanik (2022). <https://www.instagram.com/calisthanik/>.
- Cao, Y. and J. Hutchinson (2012). “From wrinkles to creases in elastomers: the instability and perfection-sensitivity of wrinkling”. In: *Proceedings of the Royal Society* 468, pp. 94–115. DOI: <https://doi.org/10.1098/rspa.2011.0384>.
- Carroll, M. M. (1988). “Finite strain solutions in compressible isotropic elasticity”. In: *Journal of Elasticity* 20, pp. 65–92. DOI: <https://doi.org/10.1007/BF00042141>.
- Chen, G. and G. Baker (2003). “Material Softening and Structural Instability”. In: *Advances in Structural Engineering* 6.4, pp. 353–357. DOI: <https://doi.org/10.1260/136943303322771727>.
- Ciarlet, P. G. (1986). *Mathematical Elasticity - Volume I: Three-Dimensional Elasticity*. Cambridge: North Holland.
- Clough, R. W. (1990). “Original formulation of the finite element method”. In: *Finite Element Analysis and Design* 7, pp. 89–101. DOI: [https://doi.org/10.1016/0168-874X\(90\)90001-U](https://doi.org/10.1016/0168-874X(90)90001-U).
- Coman, C. D. and M. Destrade (2008). “Asymptotic results for bifurcations in pure bending of rubber blocks”. In: *The Quarterly Journal of Mechanics and Applied Mathematics* 61.3, pp. 395–414. DOI: <https://doi.org/10.1093/qjmam/hbn009>.
- Considerè, A (1885). “Mémoire sur l’emploi du fer et de l’acier dans les constructions”. In: *Annales des Ponts et Chaussées* 6, pp. 574–775.
- De Pascalis, Riccardo (2010). “The Semi-Inverse Method in solid mechanics: Theoretical underpinnings and novel applications”. <http://siba-ese.unile.it/index.php/phddepascalis/article/viewFile/11193/10320>. Dissertation. Università del Salento.
- Destrade, M., M. D. Gilchrist, and J. G. Murphy (2010). “Onset of Nonlinearity in the Elastic Bending of Blocks”. In: *Journal of Applied Mechanics* 77.6. DOI: <https://doi.org/10.1115/1.4001282>.
- Ericksen, J. L. (1954). “Deformations possible in every isotropic, incompressible, perfectly elastic body”. In: *Zeitschrift für angewandte Mathematik und Physik* 5.6, pp. 466–489. DOI: <https://doi.org/10.1007/BF01601214>.

- Eriksson, A. (1988). “On some path-related measures for nonlinear structural F. E. problems”. In: *Int J Numer Meth Eng* 26.8, pp. 1791–1803. DOI: <https://doi.org/10.1002/nme.1620260808>.
- Gao, D. Y. and E. Hajilarov (2017). “Analytic Solutions to 3-D Finite Deformation Problems Governed by St Venant–Kirchhoff Material”. In: *Canonical Duality Theory: Unified Methodology for Multidisciplinary Study*. Ed. by D. Y. Gao, V. Latorre, and N. Ruan. Springer International Publishing, pp. 69–88. DOI: <https://doi.org/10.1007/978-3-319-58017-3>.
- Gent, A. N. (2005). “Elastic instabilities in rubber”. In: *International Journal of Non-Linear Mechanics*. Special Issue in Honour of C.O. Horgan 40.2, pp. 165–175. DOI: [10.1016/j.ijnonlinmec.2004.05.006](https://doi.org/10.1016/j.ijnonlinmec.2004.05.006).
- Gent, A. N. and I. S. Cho (1999). “Surface Instabilities in Compressed or Bent Rubber Blocks”. In: *Rubber Chemistry and Technology* 72.2, pp. 253–262. DOI: <https://doi.org/10.5254/1.3538798>.
- Glaser, S. and F. Armero (1997). “On the formulation of enhanced strain finite elements in finite deformations”. In: *Engineering Computations* 14.7, pp. 759–791. DOI: <https://doi.org/10.1108/02644409710188664>.
- Guo, Z.-H. (1980). “The unified theory of variational principles in nonlinear elasticity”. In: *Arch. Mech.* 32.4. https://rcin.org.pl/Content/74758/WA727_89659_P.262_Guo-The-unified.pdf, pp. 577–596.
- Guz, A. N. (2012). “Stability of elastic bodies under uniform compression (review)”. In: *International Applied Mechanics* 48.3, pp. 241–293. DOI: <https://doi.org/10.1007/s10778-012-0520-3>.
- Hartmann, S. and P. Neff (2003). “Polyconvexity of generalized polynomial-type hyperelastic strain energy functions for near-incompressibility”. In: *Int J Solids Struct* 40.11, pp. 2767–2791. DOI: [https://doi.org/10.1016/S0020-7683\(03\)00086-6](https://doi.org/10.1016/S0020-7683(03)00086-6).
- Hill, R. and J. Hutchinson (1975). “Bifurcation phenomena in the plane tension test”. In: *Journal of the Mechanics and Physics of Solids* 23.4, pp. 239–264. DOI: [https://doi.org/10.1016/0022-5096\(75\)90027-7](https://doi.org/10.1016/0022-5096(75)90027-7).
- Hjelmstad, K. D. (2005). *Fundamentals of Structural Mechanics*. Springer.
- Hohlfeld, E. and L. Mahadevan (2011). “Unfolding the Sulcus”. In: *Physical Review Letters* 106.105702. DOI: <https://doi.org/10.1103/PhysRevLett.106.105702>.
- Holzapfel, G. (2010). *Nonlinear solid mechanics: a continuum approach for engineering*. Wiley.
- Horgan, C. O. (1996). “Remarks on ellipticity for the generalized Blatz-Ko constitutive model for a compressible nonlinearly elastic solid”. In: *Journal of Elasticity* 42.2, pp. 165–176. DOI: <https://doi.org/10.1007/BF00040959>.
- Horgan, C. O. and J. G. Murphy (2005). “Plane Strain Bending of Cylindrical Sectors of Admissible Compressible Hyperelastic Materials”. In: *Journal of Elasticity* 81.2, pp. 129–151. DOI: <https://doi.org/10.1007/s10659-005-9010-8>.

- Hughes, T. J. R. (2012). *The Finite Element Method: Linear Static and Dynamic Finite Element Analysis*. Courier Corporation.
- Irons, B. M. (1966). “Engineering applications of numerical integration in stiffness methods.” In: *AIAA Journal* 4.11, pp. 2035–2037. DOI: 10.2514/3.3836.
- Kanner, L. M. and C. O. Horgan (2008). “Plane strain bending of strain-stiffening rubber-like rectangular beams”. In: *Int J Solids Struct* 45.6, pp. 1713–1729. DOI: <https://doi.org/10.1016/j.ijsolstr.2007.10.022>.
- Klinkel, S., F. Gruttmann, and W. Wagner (2006). “A Robust Non-Linear Solid Shell Element Based on a Mixed Variational Formulation”. In: *Comput. Methods Appl. Mech. Engrg.* 195.1, pp. 179–201. DOI: 10.1016/j.cma.2005.01.013.
- Klinkel, S. and W. Wagner (1997). “A geometrical non-linear brick element based on the EAS-method”. In: *Int J Numer Meth Eng* 40.24, pp. 4529–4545. DOI: 10.1002/(SICI)1097-0207(19971230)40:24<4529::AID-NME271>3.0.CO;2-I.
- Knowles, J. K. and E. Sternberg (1975). “On the ellipticity of the equations of nonlinear elastostatics for a special material”. In: *Journal of Elasticity* 5.3, pp. 341–361. DOI: <https://doi.org/10.1007/BF00126996>.
- Korelc, J., U. Šolinc, and P. Wriggers (2010). “An improved EAS brick element for finite deformation”. In: *Computational Mechanics* 46.4, pp. 641–659. DOI: <https://doi.org/10.1007/s00466-010-0506-0>.
- Korelc, J. and P. Wriggers (1996). “Consistent gradient formulation for a stable enhanced strain method for large deformations”. In: *Engineering Computations* 13.1, pp. 103–123. DOI: <https://doi.org/10.1108/02644409610111001>.
- Koschnick, Frank (2004). “Geometrische Locking-Effekte bei Finiten Elementen und ein allgemeines Konzept zu ihrer Vermeidung”. <https://mediatum.ub.tum.de/601060>. Dissertation. Technische Universität München.
- Kosloff, D. and G. A. Frazier (1978). “Treatment of hourglass patterns in low order finite element codes”. In: *International Journal for Numerical and Analytical Methods in Geomechanics* 2.1, pp. 57–72. DOI: <https://doi.org/10.1002/nag.1610020105>.
- Kouhia, R. (1992). “On the solution of non-linear finite element equations”. In: *Computers & Structures* 44.1, pp. 243–254. DOI: [https://doi.org/10.1016/0045-7949\(92\)90243-S](https://doi.org/10.1016/0045-7949(92)90243-S).
- Kuo-Mo, H. (1987). “Nonlinear Analysis of General Shell Structures by Flat Triangular Shell Element”. In: *Computers & Structures* 25.5, pp. 665–675. DOI: 10.1016/0045-7949(87)90159-3.
- Kyriakides, Stelios and Edmundo Corona (2007). Elsevier.
- Leon, S. E., G. H. Paulino, A. Pereira, Ivan F. M. Menezes, and Eduardo N. Lages (2012). “A Unified Library of Nonlinear Solution Schemes”. In: *Applied Mechanics Reviews* 64.4. DOI: <https://doi.org/10.1115/1.4006992>.

- Li, W., J. Zhu, B. Xu, and Z. Zeng (2018). “Fast implementation of characteristic mode tracking”. In: *IET Microwaves, Antennas & Propagation* 12.14, pp. 2179–2183. DOI: <https://doi.org/10.1049/iet-map.2018.5104>.
- Macneal, R. H. (1987). “A theorem regarding the locking of tapered four-noded membrane elements”. In: *Int J Numer Meth Eng* 24.9, pp. 1793–1799. DOI: <https://doi.org/10.1002/nme.1620240913>.
- Maghami, A. and D. Schillinger (2020). “A stiffness parameter and truncation error criterion for adaptive path following in structural mechanics”. In: *Int J Numer Meth Eng* 121.5, pp. 967–989. DOI: <https://doi.org/10.1002/nme.6253>.
- Magisano, D., L. Leonetti, and G. Garcea (2017). “How to Improve Efficiency and Robustness of the Newton Method in Geometrically Non-Linear Structural Problem Discretized via Displacement-Based Finite Elements”. In: *Comput Methods Appl Mech Eng* 313, pp. 986–1005. DOI: 10.1016/j.cma.2016.10.023.
- Miehe, Christian (1988). “Zur Numerischen Behandlung Thermomechanischer Prozesse”. Dissertation. Universität Hannover.
- Moitinho de Almeida, J.P. and E. A. W. Maunder (2017). *Equilibrium Finite Element Formulations*. Wiley.
- Mueller-Hoeppe, D. S., S. Loehnert, and P. Wriggers (2009). “A finite deformation brick element with inhomogeneous mode enhancement”. In: *Int J Numer Meth Eng* 78.10, pp. 1164–1187. DOI: <https://doi.org/10.1002/nme.2523>.
- Müller, M. (2007). “Passing of instability points by applying a stabilized Newton–Raphson scheme to a finite element formulation: Comparison to arc-length method”. In: *Computational Mechanics* 40.4, pp. 683–705. DOI: <https://doi.org/10.1007/s00466-006-0133-y>.
- Needleman, A. (1979). “Non-normality and bifurcation in plane strain tension and compression”. In: *Journal of the Mechanics and Physics of Solids* 27.3, pp. 231–254.
- Neto, E.A.S., D. Perić, G. C. Huang, and D. R. J. Owen (1995). “Remarks on the stability of enhanced strain elements in finite elasticity and elastoplasticity”. In: *Communications in Numerical Methods in Engineering* 11.11, pp. 951–961. DOI: <https://doi.org/10.1002/cnm.1640111109>.
- Ogden, R. W. (1972). “Large deformation isotropic elasticity - On the correlation of theory and experiments for incompressible rubberlike solids”. In: *Proceedings of the Royal Society of London* 326, pp. 565–584. DOI: <https://doi.org/10.1098/rspa.1972.0026>.
- (1997). *Non-linear Elastic Deformations*. Courier Corporation.
- Overvelde, J. T. B., D. M. J. Dykstra, R. de Rooij, J. Weaver, and K. Bertoldi (2016). “Tensile Instability in a Thick Elastic Body”. In: *Physical Review Letter* 117. DOI: <https://doi.org/10.1103/PhysRevLett.117.094301>.

- Petryk, H. (2000). “Theory of Material Instability in Incrementally Nonlinear Plasticity”. In: ed. by H. Petryk, pp. 261–331. DOI: <https://doi.org/10.1007/978-3-7091-2562-5-5>.
- Pfefferkorn, R. and P. Betsch (2019). “On transformations and shape functions for enhanced assumed strain elements”. In: *Int J Numer Meth Eng* 120.2, pp. 231–261. DOI: <https://doi.org/10.1002/nme.6133>.
- (2020). “Extension of the enhanced assumed strain method based on the structure of polyconvex strain-energy functions”. In: *Int J Numer Meth Eng* 121.8, pp. 1695–1737. DOI: <https://doi.org/10.1002/nme.6284>.
- (2021). “Mesh distortion insensitive and locking-free Petrov–Galerkin low-order EAS elements for linear elasticity”. In: *Int J Numer Meth Eng* 122, pp. 6924–6954. DOI: <https://doi.org/10.1002/nme.6817>.
- (2022). “Hourglassing- and Locking-Free Mesh Distortion Insensitive Petrov-Galerkin EAS Elements for Large Deformation Solid Mechanics”. In: *Int J Numer Meth Eng*. submitted.
- Pfefferkorn, R., S. Bieber, B. Oesterle, M. Bischoff, and P. Betsch (2021). “Improving efficiency and robustness of enhanced assumed strain elements for nonlinear problems”. In: *Int J Numer Meth Eng* 122.8, pp. 1911–1939. DOI: <https://doi.org/10.1002/nme.6605>.
- Pian, T. H. H. and K. Sumihara (1984). “Rational approach for assumed stress finite elements”. In: *Int J Numer Meth Eng* 20.9, pp. 1685–1695. DOI: <https://doi.org/10.1002/nme.1620200911>.
- Ramm, E. (1981). “Strategies for Tracing the Nonlinear Response Near Limit Points”. In: *Nonlinear Finite Element Analysis in Structural Mechanics*. Ed. by W. Wunderlich, E. Stein, and K. Bathe. Springer, pp. 63–89.
- Reese, S., M. Küssner, and B. D. Reddy (1999). “A new stabilization technique for finite elements in non-linear elasticity”. In: *Int J Numer Meth Eng* 44.11, pp. 1617–1652. DOI: [https://doi.org/10.1002/\(SICI\)1097-0207\(19990420\)44:11<1617::AID-NME557>3.0.CO;2-X](https://doi.org/10.1002/(SICI)1097-0207(19990420)44:11<1617::AID-NME557>3.0.CO;2-X).
- Reese, S. and P. Wriggers (2000). “A stabilization technique to avoid hourglassing in finite elasticity”. In: *Int J Numer Meth Eng* 48.1, pp. 79–109. DOI: [https://doi.org/10.1002/\(SICI\)1097-0207\(20000510\)48:1<79::AID-NME869>3.0.CO;2-D](https://doi.org/10.1002/(SICI)1097-0207(20000510)48:1<79::AID-NME869>3.0.CO;2-D).
- Reese, S., P. Wriggers, and B. D. Reddy (2000). “A new locking-free brick element technique for large deformation problems in elasticity”. In: *Computers & Structures* 75.3, pp. 291–304. ISSN: 0045-7949. DOI: [https://doi.org/10.1016/S0045-7949\(99\)00137-6](https://doi.org/10.1016/S0045-7949(99)00137-6).
- Riks, E. (1984). “Some computational aspects of the stability analysis of nonlinear structures”. en. In: *Comput Methods Appl Mech Eng* 47.3, pp. 219–259. DOI: [https://doi.org/10.1016/0045-7825\(84\)90078-1](https://doi.org/10.1016/0045-7825(84)90078-1).

- Ritz, W. (1909). “Über eine neue Methode zur Lösung gewisser Variationsprobleme der mathematischen Physik”. In: *Journal für die Reine und Angewandte Mathematik* 135. http://resolver.sub.uni-goettingen.de/purl?PPN243919689_0135, pp. 1–61.
- Rivlin, R. S. (1948). “Large elastic deformations of isotropic materials. I. Fundamental concepts”. In: *Proceedings of the Royal Society of London. Series A. Mathematical and Physical Sciences* 240.822, pp. 459–490. DOI: <https://doi.org/10.1098/rsta.1948.0002>.
- (1949). “Large elastic deformations of isotropic materials. V. The problem of flexure”. In: *Proceedings of the Royal Society of London. Series A. Mathematical and Physical Sciences* 195.1043, pp. 463–473. DOI: <https://doi.org/10.1098/rspa.1949.0004>.
- Roth, S. (2020). “Algorithmen zur nichtlinearen Stabilitätsanalyse dünnwandiger Strukturen”. Dissertation. Universität Stuttgart. DOI: <https://doi.org/10.18419/opus-11239>.
- Rudykh, S. and M. C. Boyce (2014). “Analysis of elasmoid fish imbricated layered scale-tissue systems and their bio-inspired analogues at finite strains and bending”. In: *IMA Journal of Applied Mathematics* 79.5. Conference Name: IMA Journal of Applied Mathematics, pp. 830–847. DOI: <https://doi.org/10.1093/imamat/hxu005>.
- Sachse, R., A. Westermeier, M. Mylo, and S. Poppinga (2020). *Snapping mechanics of the Venus flytrap (Dionaea muscipula)*. DOI: <https://doi.org/10.1073/pnas.2002707117>.
- Schellbach, K. H. (1851). “Probleme der Variationsrechnung”. In: *Zeitschrift für reine und angewandte Mathematik* 41, pp. 293–363. DOI: <https://doi.org/10.1515/crll.1851.41.293>.
- Schröder, J., N. Viebahn, P. Wriggers, F. Auricchio, and K. Steeger (2017). “On the stability analysis of hyperelastic boundary value problems using three- and two-field mixed finite element formulations”. In: *Computational Mechanics* 60.3, pp. 479–492. DOI: <https://doi.org/10.1007/s00466-017-1415-2>.
- Sigaeva, T. (2018). “Note on the generality of one plane strain bending universal solution”. In: *Mechanics Research Communications* 94, pp. 120–124. DOI: <https://doi.org/10.1016/j.mechrescom.2018.10.005>.
- Sigaeva, T., R. Mangan, L. Vergori, M. Destrade, and L. Sudak (2018). “Wrinkles and creases in the bending, unbending and eversion of soft sectors”. en. In: *Proceedings of the Royal Society A: Mathematical, Physical and Engineering Sciences* 474.2212. DOI: <https://doi.org/10.1098/rspa.2017.0827>.
- Simo, F. Armero, and R. L. Taylor (1993). “Improved versions of assumed enhanced strain tri-linear elements for 3D finite deformation problems”. In: *Comput Methods Appl Mech Eng* 110.3, pp. 359–386. DOI: [https://doi.org/10.1016/0045-7825\(93\)90215-J](https://doi.org/10.1016/0045-7825(93)90215-J).

- Simo and F. Armero (1992). “Geometrically non-linear enhanced strain mixed methods and the method of incompatible modes”. In: *Int J Numer Meth Eng* 33.7, pp. 1413–1449. DOI: <https://doi.org/10.1002/nme.1620330705>.
- Simo and M. S. Rifai (1990). “A class of mixed assumed strain methods and the method of incompatible modes”. In: *Int J Numer Meth Eng* 29.8, pp. 1595–1638. DOI: <https://doi.org/10.1002/nme.1620290802>.
- Simo, R. L. Taylor, and K. S. Pister (1985). “Variational and projection methods for the volume constraint in finite deformation elasto-plasticity”. In: *Comput Methods Appl Mech Eng* 51.1, pp. 177–208. DOI: [https://doi.org/10.1016/0045-7825\(85\)90033-7](https://doi.org/10.1016/0045-7825(85)90033-7).
- Strang, G. (1986). *Introduction to Applied Mathematics*. Wellesley-Cambridge Press.
- Suri, M. (1996). “Analytical and computational assessment of locking in the hp finite element method”. In: *Comput Methods Appl Mech Eng* 133.3, pp. 347–371. DOI: [https://doi.org/10.1016/0045-7825\(95\)00947-7](https://doi.org/10.1016/0045-7825(95)00947-7).
- Sussman, T. and K. Bathe (2014). “Spurious modes in geometrically nonlinear small displacement finite elements with incompatible modes”. In: *Computers & Structures* 140, pp. 14–22. DOI: <https://doi.org/10.1016/j.compstruc.2014.04.004>.
- Treloar, L. R. G. (1944). “Stress-Strain Data for Vulcanized Rubber under Various Types of Deformation”. In: *Rubber Chemistry and Technology* 17.4, pp. 813–825. DOI: [10.5254/1.3546701](https://doi.org/10.5254/1.3546701).
- Triantafyllidis, N., W. M. Scherzinger, and H. -J. Huang (2007). “Post-bifurcation equilibria in the plane-strain test of a hyperelastic rectangular block”. In: *Int J Solids Struct* 44.11, pp. 3700–3719. DOI: <https://doi.org/10.1016/j.ijsolstr.2006.10.012>.
- Turner, M., R. W. Clough, H. C. Martin, and L. J. Topp (1956). “Stiffness and deflection analysis of complex structures”. In: *Journal of the Aeronautical Sciences* 23.9, pp. 805–823. DOI: <https://doi.org/10.2514/8.3664>.
- Viebahn, N., J. Schröder, and P. Wriggers (2019). “An extension of assumed stress finite elements to a general hyperelastic framework”. In: *Advanced Modeling and Simulation in Engineering Sciences* 6.1, p. 9. DOI: <https://doi.org/10.1186/s40323-019-0133-z>.
- Wall, W.A., M. Bischoff, and E. Ramm (2000). “A deformation dependent stabilization technique, exemplified by EAS elements at large strains”. In: *Comput Methods Appl Mech Eng*. IVth World Congress on Computational Mechanics. (II). Optimum 188.4, pp. 859–871. DOI: [https://doi.org/10.1016/S0045-7825\(99\)00365-5](https://doi.org/10.1016/S0045-7825(99)00365-5).
- Washizu, K. (1975). *Variational Methods in Elasticity and Plasticity*. Pergamon Press.
- Willmann, T., S. Bieber, and M. Bischoff (2022). “Investigation and elimination of non-linear Poisson stiffening in 3d and solid shell finite elements”. In: *Int J Numer Meth Eng*. DOI: <https://doi.org/10.1002/nme.7119>.

- Wilson, E. L., R. L. Taylor, W. P. Doherty, and J. Ghaboussi (1973). “Incompatible Displacement Models”. In: *Numerical and Computer Methods in Structural Mechanics*. Ed. by S. J. Fenves, N. Perrone, A. R. Robinson, and W. C. Schnobrich. Academic Press, pp. 43–57. DOI: <https://doi.org/10.1016/B978-0-12-253250-4.50008-7>.
- Wriggers, P. (2008). *Nonlinear Finite Element Methods*. en. Berlin Heidelberg: Springer.
- Wriggers, P. and S. Reese (1996). “A note on enhanced strain methods for large deformations”. In: *Comput Methods Appl Mech Eng* 135.3, pp. 201–209. DOI: [https://doi.org/10.1016/0045-7825\(96\)01037-7](https://doi.org/10.1016/0045-7825(96)01037-7).
- Wriggers, P., W. Wagner, and C. Miehe (1988). “A quadratically convergent procedure for the calculation of stability points in finite element analysis”. In: *Comput Methods Appl Mech Eng* 70.3, pp. 329–347. DOI: [https://doi.org/10.1016/0045-7825\(88\)90024-2](https://doi.org/10.1016/0045-7825(88)90024-2).
- Young, N. J. B. (1976). “Bifurcation phenomena in the plane compression test”. In: *Journal of the Mechanics and Physics of Solids* 24.1, pp. 77–91. DOI: [https://doi.org/10.1016/0022-5096\(76\)90019-3](https://doi.org/10.1016/0022-5096(76)90019-3).
- Zienkiewicz, O. C. and R. L. Taylor (2000). *The Finite Element Method: Solid Mechanics*. Butterworth-Heinemann.
- Zienkiewicz, O. C., R. L. Taylor, and D. D. Fox (2014). *The Finite Element Method for Solid & Structural Mechanics*. 7th ed. Butterworth-Heinemann.
- Zwillinger, D. (2003). *CRC Standard Mathematical Tables and Formulae*. Chapman & Hall/CRC.

Curriculum Vitae

Persönliche Angaben:

Name: Simon Bieber
Geburtsdatum: 27.05.1990
Geburtsort: Backnang
Eltern: Margit Bieber,
Werner Bieber

Schulische Ausbildung:

2000 – 2006 Matern-Feuerbacher-Realschule, Großbottwar
2006 – 2009 Technisches Gymnasium, Carl-Schaefer-Schule,
Ludwigsburg
2009 Allgemeine Hochschulreife

Akademischer Werdegang:

2010 – 2013 Bachelorstudium Bauingenieurwesen an der Uni-
versität Stuttgart
2013 – 2016 Masterstudium Bauingenieurwesen an der Univer-
sität Stuttgart
2014 – 2015 Auslandsstudium an der UPC Barcelona
2016 Masterprüfung
2017 Studienpreis des Freundeskreises Stuttgarter
Statik e.V.
2016 – 2022 Akademischer Mitarbeiter am Institut für Baus-
tatik und Baudynamik der Universität Stuttgart
2019 Forschungsaufenthalt: Università di Pavia

Berichte des Instituts für Baustatik und Baudynamik der Universität Stuttgart

- 1 (1983) **P. Osterrieder:**
Traglastberechnung von räumlichen Stabwerken bei großen Verformungen mit finiten Elementen.
- 2 (1983) **T. A. Kompfner:**
Ein finites Elementmodell für die geometrisch und physikalisch nicht-lineare Berechnung von Stahlbetonschalen.
- 3 (1983) **A. Diack:**
Beitrag zur Stabilität diskret längsversteifter Kreiszylinderschalen unter Axialdruck.
- 4 (1984) **A. Burmeister, F.W. Bornscheuer, E. Ramm:**
Traglasten von Kugelbehältern mit Stützen und Formabweichungen unter Innendruck und Stützenlängskraft.
- 5 (1985) **H. Stegmüller:**
Grenzlastberechnungen flüssigkeitsgefüllter Schalen mit "degenerierten" Schalenelementen.
- 6 (1987) **A. Burmeister:**
Dynamische Stabilität nach der Methode der finiten Elemente mit Anwendungen auf Kugelschalen.
- 7 (1987) **G. Kammler:**
Ein finites Elementmodell zur Berechnung von Trägern und Stützen mit offenem, dünnwandigem Querschnitt unter Berücksichtigung der Interaktion zwischen globalem und lokalem Versagen.
- 8 (1988) **A. Matzenmiller:**
Ein rationales Lösungskonzept für geometrisch und physikalisch nicht-lineare Strukturberechnungen.
- 9 (1989) **D. Tao:**
Die Technik der reduzierten Basis bei nichtlinearen finiten Element-Berechnungen.

- 10 (1989) **K. M. Weimar:**
Ein nichtlineares Balkenelement mit Anwendung als Längssteifen axialbelasteter Kreiszyylinder.
- 11 (1990) **K.-U. Bletzinger:**
Formoptimierung von Flächentragwerken.
- 12 (1990) **S. Kimmich:**
Strukturoptimierung und Sensibilitätsanalyse mit finiten Elementen.
- 13 (1991) **U. Andelfinger:**
Untersuchungen zur Zuverlässigkeit hybrid"-gemischter Finiter Elemente für Flächentragwerke.
- 14 (1992) **N. Büchter:**
Zusammenführung von Degenerationskonzept und Schalentheorie bei endlichen Rotationen.
- 15 (1992) **T. J. Hofmann:**
Beitrag zur verfeinerten Balkentheorie.
- 16 (1994) **D. de Mesquita Roehl:**
Zur Berechnung von großen elastoplastischen Deformationen bei Flächentragwerken und Kontinua.
- 17 (1994) **R. Reitinger:**
Stabilität und Optimierung imperfektionsempfindlicher Tragwerke.
- 18 (1995) **R. L. M. Suanno:**
Ein dreidimensionales Simulationsmodell für Stahlbeton mit Plastizität und Schädigung.
- 19 (1995) **M. Braun:**
Nichtlineare Analysen von geschichteten, elastischen Flächentragwerken.
- 20 (1996) **N. Rehle:**
Adaptive Finite Element Verfahren bei der Analyse von Flächentragwerken.

-
- 21 (1996) **C. Haüßer:**
Effiziente Dreieckselemente für Flächentragwerke.
- 22 (1996) **D. Kuhl:**
Stabile Zeitintegrationsalgorithmen in der nichtlinearen Elastodynamik dünnwandiger Tragwerke.
- 23 (1998) **H. Schmidts:**
Zur effizienten Modellierung und Analyse von Hochhausstragwerken.
- 24 (1998) **H. Wang:**
Interaktion des lokalen und globalen Stabilitätsverhaltens dünnwandiger Stäbe.
- 25 (1998) **K. Maute:**
Topologie- und Formoptimierung von dünnwandigen Tragwerken.
- 26 (1998) **B. Maurer:**
Karl Culmann und die graphische Statik.
- 27 (1998) **F. Cirak:**
Adaptive Finite-Element-Methoden bei der nichtlinearen Analyse von Flächentragwerken.
- 28 (1998) **M. Trautz:**
Zur Entwicklung von Form und Struktur historischer Gewölbe aus der Sicht der Statik.
- 29 (1999) **H. Menrath:**
Numerische Simulation des nichtlinearen Tragverhaltens von Stahlverbundträgern.
- 30 (1999) **M. Bischoff:**
Theorie und Numerik einer dreidimensionalen Schalenformulierung.
- 31 (1999) **W. A. Wall:**
Fluid-Struktur-Interaktion mit stabilisierten Finiten Elementen.
- 32 (2000) **E. Kuhl:**
Numerische Modelle für kohäsive Reibungsmaterialien.

- 33 (2001) A. Maute:**
Fehlerkontrolle bei Finite-Element-Methoden in der linearen Struktur-dynamik.
- 34 (2001) S. Schwarz:**
Sensitivitätsanalyse und Optimierung bei nichtlinearem Strukturverhalten.
- 35 (2001) A. Haufe:**
Dreidimensionale Simulation bewehrter Flächentragwerke aus Beton mit der Plastizitätstheorie.
- 36 (2001) D. P. Mok:**
Partitionierte Lösungsansätze in der Strukturmechanik und der Fluid-Struktur-Interaktion.
- 37 (2002) H. Steeb:**
Fehlerschätzer für FE-Berechnungen bei entfestigenden Materialien.
- 38 (2002) K. Krausz:**
Tragverhalten gemauerter Tonnengewölbe mit Stichkappen.
- 39 (2002) M. Hörmann:**
Nichtlineare Versagensanalyse von Faserverbundstrukturen.
- 40 (2003) V. Gravemeier:**
The Variational Multiscale Method for Laminar and Turbulent Incompressible Flow.
- 41 (2004) R. Kemmler:**
Stabilität und große Verschiebungen in der Topologie- und Formoptimierung.
- 42 (2004) G. A. D'Addetta:**
Discrete Models for Cohesive Frictional Materials.
- 43 (2004) M. Gee:**
Effiziente Lösungsstrategien in der nichtlinearen Schalenmechanik.

-
- 44 (2004) **T. Erhart:**
Strategien zur numerischen Modellierung transienter Impaktvorgänge bei nichtlinearem Materialverhalten.
- 45 (2005) **M. Leukart:**
Kombinierte anisotrope Schädigung und Plastizität bei kohäsiven Reibungsmaterialien.
- 46 (2006) **F. Huber:**
Nichtlineare dreidimensionale Modellierung von Beton- und Stahlbetontragwerken.
- 47 (2007) **A. Lipka:**
Verbesserter Materialeinsatz innovativer Werkstoffe durch die Topologieoptimierung.
- 48 (2007) **A. S. Hund:**
Hierarchische Mehrskalenmodellierung des Versagens von Werkstoffen mit Mikrostruktur.
- 49 (2007) **S. Hartmann:**
Kontaktanalyse dünnwandiger Strukturen bei großen Deformationen.
- 50 (2007) **T. M. Hettich:**
Diskontinuierliche Modellierung zur Versagensanalyse von Verbundmaterialien.
- 51 (2007) **C. Förster:**
Robust methods for fluid-structure interaction with stabilised finite elements.
- 52 (2009) **M. von Scheven:**
Effiziente Algorithmen für die Fluid-Struktur-Wechselwirkung.
- 53 (2010) **J. Kato:**
Material Optimization for Fiber Reinforced Composites applying a Damage Formulation.

- 54 (2010) C. F. Hilchenbach:**
Optimierung von Mehrphasenstrukturen mit lokalem Schädigungsverhalten.
- 55 (2011) I. Bruss:**
Dreidimensionale Schädigungsmodellierung heterogener Materialien.
- 56 (2012) B. J. Schneider:**
Polygonale diskrete Elemente zur Modellierung heterogener Materialien.
- 57 (2012) R. Etlender:**
Modellierung und Simulation der Wellenausbreitung in flexiblen hydraulischen Leitungen.
- 58 (2012) T. Cichosz:**
Stabile und konsistente Kontaktmodellierung in Raum und Zeit.
- 59 (2013) R. Echter:**
Isogeometric analysis of shells.
- 60 (2013) A. Tkachuk:**
Variational methods for consistent singular and scaled mass matrices.
- 61 (2013) J. Irslinger:**
Mechanische Grundlagen und Numerik dreidimensionaler Schalenelemente.
- 62 (2014) T. E. Pohl:**
Adaptive Methoden zur Pfadverfolgung bei Entfestigung.
- 63 (2014) A. Sorg:**
Adaptive diskret-kontinuierliche Modellierung von Materialien mit Mikrostruktur.
- 64 (2015) M. E. Matzen:**
Isogeometrische Modellierung und Diskretisierung von Kontaktproblemen.

-
- 65 (2016) V. M. Effinger:**
Finite nichtlinear viskoelastische Modellierung offenzelliger Polymer-schäume.
- 66 (2017) C. M. Wilking:**
Effiziente Integration und verbesserte Kontaktspannungen für duale Mortar-Formulierungen.
- 67 (2018) B. Oesterle:**
Intrinsisch lockingfreie Schalenformulierungen.
- 68 (2018) F. Neukamm:**
Lokalisierung und Versagen von Blechstrukturen.
- 69 (2019) A.-K. Schäuble:**
Variationally consistent inertia templates for speed-up and customization in explicit dynamics.
- 70 (2019) T. Willerding:**
Multiscale simulation of phase transformation in metals.
- 71 (2020) S. Roth:**
Algorithmen zur nichtlinearen Stabilitätsanalyse dünnwandiger Strukturen.
- 72 (2020) R. Sachse:**
Variational Motion Design for Adaptive Structures.
- 73 (2022) A. Tkachuk:**
Parametrized variational principles in dynamics.
- 74 (2022) F. Geiger:**
Strukturmechanische Charakterisierung von Stabtragwerken für den Entwurf adaptiver Tragwerke.
- 75 (2022) M. Benz:**
Automatisierbare direkte Kalibrierung von Materialmodellen auf Basis digitaler Bildkorrelation.



Simon Bieber

This thesis deals with locking and hourglassing issues that arise in nonlinear finite element analyses of problems in mechanics. The major focus lies on the analysis of these numerical deficiencies, the design of suitable benchmarks and the development of novel remedies.

A new nonlinear locking phenomenon is described. It is caused by parasitic nonlinear strain terms and it is particularly pronounced for large element deformations in combination with higher-order integration and a critical parameter, such as the element aspect ratio or the Poisson's ratio. To avoid this problem within the popular class of enhanced assumed strain formulations, novel strain enhancements are presented. An analytical solution of a tailored finite bending problem is used to benchmark the newly proposed element formulations.

Further, the problem of hourglassing in both compression and tension of solid bodies is analysed. It is shown that the underlying causes of hourglassing can be explained by geometry-induced and material-induced trigger mechanisms of structural instabilities. Crucial for understanding as well as benchmarking is the analytical in-depth analysis of a large strain bifurcation problem. Based on these insights, an obvious remedy for the geometric hourglassing phenomenon is presented.

The last part of this thesis is devoted to the efficient algorithmic treatment of the computation of instability points. The difficulties in choosing a suitable load-stepping approach with methods from the literature are discussed and a methodological idea of an adaptive load-stepping scheme is presented. Efficiency and practicability are demonstrated for several benchmarks.